CWP-517
May 2005

Data Continuation for Data Regularization and Internal Multiples

Alison E. Malcolm

— Doctoral Thesis —
Geophysics

Defended on April 1, 2005

Committee Chair:	Prof. James A. McNeil
Advisor:	Prof. Maarten V. de Hoop
Co-Advisor:	Prof. John A. Scales
Committee members:	Prof. Michael L. Batzle
	Prof. Yaoguo Li
	Prof. Paul A. Martin

Center for Wave Phenomena
Colorado School of Mines
Golden, Colorado 80401
(1) 303 273-3557

Abstract

Seismic data collected in the field are often not ideal for processing. The process known as data continuation computes data not recorded from those that are recorded so that data requirements for processing techniques can be met. Although there are many techniques of data continuation currently used in seismic processing, the majority of these assume that the seismic wave velocity is either constant or varying only with depth. A notable exception is the downward continuation of data, often referred to as survey sinking, for which techniques applicable in most velocity models exist.

We extend data continuation techniques used to fill in missing data to velocity models in which caustics are generated in the wavefield. To do this, we use a method based on the composition of Fourier integral operators. To demonstrate that this method doesn't introduce false reflections, we show that the composite operator is also a Fourier integral operator. We illustrate the utility of this theory with a synthetic example, with caustics, in which we fill in missing traces in a shot record. This method is computationally more expensive than similar methods that assume simple velocity models.

First order internal multiples are a source of errors seismic imaging. Artifacts caused by internal multiples are often similar to true reflectors and thus can be difficult to attenuate. Typically multiples are estimated in the data and then subtracted from the data before an image is created. We propose a method by which artifacts in the image are estimated as part of the imaging process; an integral part of this method is the downward continution of data.

Table of Contents

Acknowledgments

First and foremost I want to express my gratitude to my advisor Martijn without whom this thesis would not have happened. Doing science with Martijn has been a wild ride and though I often felt that I was in over my head he always seemed to know when I really needed help and when to leave me to figure things out on my own. I appreciate not only the direct guidance he gave me for my thesis work, but also the breadth of interests and topics he shared with me in many more general scientific discussions. I am also grateful (and impressed) that he never lost patience with me despite my giving him plenty of reasons to.

For most of my time at Mines I have worked with Henri Calandra at Total. I am grateful to him for all of his help and advice with the practical side of the work in this thesis, organizing the financial support for much of this work, the opportunity to visit and work in France and the French lessons.

I was fortunate to have gone through a comprehensive exam process that required two projects with two different faculty members. The work I did with John Scales in the Physical Acoustics Lab was some of the most exciting times I spent on campus. I feel that sharing in John's enthusiasm, his physical insights and his sense of fun has made me a better scientist.

I am grateful for the assistance I have received at every step of the way from the rest of my committee, Mike Batzle, Paul Martin, Jim McNeil and Yaoguo Li as well as the department head Terry Young. I also wish to thank them for their understanding of the somewhat chaotic way in which my thesis was distributed. I have also appreciated the gallons of red ink from Ken Larner, the helpful advice (and jokes) from Roel Snieder and the coding assistance from Dave Hale.

From the first day I arrived at Mines Jérôme Le Rousseau has helped to smooth the way for me. He, along with Günther Hörmann, really got me started in the theory of microlocal analysis and taught me where to find the information I needed and how to learn it. Jérôme has also been a constant source of support and encouragement to me throughout my time here; he introduced me to Henri, encouraged me to work with Martijn and taught me many of his vast supply of computer tricks.

The comraderie amongst the students in the department and in particular in CWP has helped me to really enjoy my time at Mines. I am grateful to all of the students I have shared space with for their individual insights and for sharing with me a little of their own culture (and to Alex and Nicole for keeping me in touch with my own). There are a few students whose presence really smoothed the way for this thesis, to whom I am particularly grateful: Alex–for great car conversations, David–for his always unique perspectives, Ivan–for sharing his intelligence and sense of humour, Matt R.–for pretending I knew more math than him, Sverre and Stig–for bits and pieces of code, and Tamara–for all the gal stuff. I

am also grateful to Albena, Carlos, Huub, Kasper, Kurang, Mila, Pawan, Petr, Rich, Sarah, Xiaoxia, and Yaping; I am glad to have shared space with them here. I also wish to thank Feng Deng and Linbin Zhang who wrote the propagator used in the second half of this thesis as interns at Total. The staff of the department, in particular Sara, Michelle, and Lela (whose presence is sorely missed) have been ever helpful and Barbara McLenon, aside from helping me with publications stuff, has also been my Colorado Mom.

Of course this thesis would not have happened without much love and support from my parents (and Chris) and all my family (and soon to be family-in-law) who put up with me and helped me keep the thesis in perspective.

Many people thank their boyfriend/girlfriend/husband/wife for all the love and support along the way. Very few are also lucky enough to have someone at home with an incredibly broad mathematical knowledge who could explain the difference between finite difference and finite element to me ten times and derive boundary conditions with me on the blackboard at midnight. For all this and much more I thank Scott for sharing the ride.

Last, but not least, I would like to express my gratitude to Total, and the sponsors of the Consortium Project on Seismic Inverse Methods for Complex Structures at the Center for Wave Phenomena for financial support.

Chapter 1

Introduction

The subject of this thesis is data continuation through operator composition, in the general context of seismic imaging. Two applications are investigated, seismic data regularization and the attenuation of imaging artifacts caused by internal multiples. Each chapter is written to be published independently. As such, each contains its own summary and introduction describing the material contained in it. The purpose of this introduction is to tie the four papers together and to give the reader a general overview of the thesis contents. Rather than explain the basics of seismic processing here, I refer the reader not familiar with exploration seismology to two excellent books on the subject: Claerbout (1985) and Yilmaz (1987). Similarly, the reader not familiar with the techniques of microlocal analysis is referred either to the book by Sjöstrand & Grigis (1994), or Appendix A of Le Rousseau (2001). Some of the theory used for multiple prediction is described in detail in Appendix G.

Because this thesis is a complitation of papers, it is not designed to be read cover-to-cover. Chapters 2 and 3 deal primarily with data regularization, whereas Chapters 4 and 5 deal with estimating imaging artifacts caused by internal multiples. The majority of the appendices are associated to particular chapters, as noted in the footnotes at the beginning of each chapter. Appendices A and B give some constant velocity examples of the theory described in Chapter 2. Appendices C-F give some of the more detailed derivations associated with Chapter 3. Appendix G attempts to describe some of the theory of the Lippmann-Schwinger and Bremmer series, which are used extensively in Chapter 4. Appendix H describes some of the artifacts that caused problems in the algorithm development phase leading up to the examples shown in Chapter 5. In Appendix I the amplitude factors necessary for the imaging procedure performed in Chapter 5 are discussed to bridge the gap between the theoretical development and the implementation of these amplitude factors. The final two appendices, J and K are associated with Chapter 4. Appendix J gives a particularly long proof of one of the results in Chapter 4 and Appendix K compares the approach for suppressing internal multiples discussed here with that of Weglein *et al.* (1997) and ten Kroode (2002).

Data continuation is the process by which data are computed at a location different from that at which they were collected. A typical example from seismic imaging is so called survey-sinking *wave equation*[1] migration (Bevc *et al.*, 2003). In this example, data collected at the surface are used to estimate data that would have been recorded at some depth, say

[1]This type of migration goes by many names, the most common of which is wave equation migration. This name is somewhat misleading, however, as all migration techniques are based on the wave equation.

z, in the subsurface. The portion of this depth-continued data set at zero time and zero offset gives an image of the subsurface at depth z.

Currently, for this procedure to be applied to data they must generally be uniformly sampled in space, with offsets beginning at zero. It is not usually possible to collect such data in the field, requiring techniques to resample data and fill in missing data. The content of the data-regularization part of this thesis, Chapters 2 and 3, describes a theory for filling in missing data and illustrates its application with synthetic data.

The imaging condition (offset and time set to zero) is based on the single scattering assumption. This assumption is violated by internal multiples. Thus, if there are internal multiples in the data set they will be incorrectly imaged in the migration procedure described above, leading to imaging artifacts. Typically, these artifacts are avoided by attempting to attenuate internal multiples in the data before imaging. Although such attenuation can be successful in some situations, for complicated velocity models it can be difficult to distinguish multiples from primaries in the data. The multiple-attenuation portion of this thesis, Chapters 4 and 5, describe a technique by which multiples are estimated as part of the imaging process, through a different method of continuation. In this way, their contribution to the image can be estimated, allowing the attenuation of the imaging artifacts they cause.

Another aspect the two parts of the thesis have in common is the theory of operator composition[2]. For data regularization, two or three Fourier Integral Operators (FIOs) are composed to form a single operator that estimates missing data using the recorded data. For attenuating multiples, the multiples are constructed with a series approach in which each term in the series contains more operators than does the previous term. Thus the multiple estimate comes from the composition of several integral operators; a final imaging operator is then applied to this composite operator to find the image artifacts caused by the multiples.

1.1 Data continuation for regularization

A typical seismic migration algorithm requires data sampled at regular intervals. In addition, many algorithms require knowledge of data that cannot be collected in the field. As in the downward-continuation example discussed above, many processing techniques also require knowledge of zero-offset data. Zero-offset data cannot be collected as geophones are not designed to withstand the forces generated by typical seismic sources. Moreover, data are not usually collected on a regular grid because of obstacles in the acquisition region, instrument failure, etc. The goal of data regularization is to circumvent problems caused by irregular geometries and missing data by computing these missing data points, from available data.

This type of data processing was among the first to become generally used in seismic prospecting. In early examples, data differences in reflection arrival times at different offsets

[2]Operator composition is the combining of two operators into a single operator. For example, an operator mapping a space X into Y ($A : X \mapsto Y$) might be composed with an operator mapping Y into Z ($B : Y \mapsto Z$) to form a single operator mapping X to Z ($C = B \circ A : X \mapsto Z$).

(the distance between the source and receiver) were compensated for (i.e., normal-moveout corrected) with the goal of producing a flat section that could be averaged to give a one-dimensional (1D) estimate of subsurface properties. This is in essence a data regularization as the correction for offset is designed to mimic zero-offset data, which are more easily interpreted than are nonzero-offset data. These first approaches made strong assumptions on Earth structure [see Green (1938) for a list], most of which are not at all valid in areas of current interest for oil exploration. Two of the most fundamental assumptions were that the underlying structure consists of a stack of horizontal layers and that the background velocity is constant or at most varies consistently (e.g., linearly) as a function of depth only.

Accounting for dip came first, before computers were readily available, by adjusting the velocity used in common-midpoint (CMP) stacking[3] to stack to account for dipping layers. This is discussed by Levin (1971), drawing on the derivation of the reflection response to a dipping layer made by Brown (1969). Again the goal is to reduce a common-depth-point (CDP)[4] gather to a set of identical traces to be stacked to determine Earth structure at the shared depth point. Further research along these lines introduced the process known as *Dip moveout* (DMO), described in detail by Hale (1983, 1991). Dip moveout is a method by which zero-offset data are estimated from nonzero-offset data extending normal moveout to dipping reflectors. The strengths of this method are in its relatively weak dependence on the precise subsurface velocity and the speed with which it can be computed. A weakness of the method is its inability to account for lateral velocity variations. This is addressed as part of this thesis.

The data regularization method described in this thesis involves the composition of two (or three) operators. The first is an imaging operator from which an estimate of subsurface properties is obtained. The second is a modeling operator that models output data with the desired acquisition geometry. (The third is a restriction operator, used to set up the desired output geometry; it is discussed in both Chapter 2 and 3.) A similar vein of research has been followed by others, a few of which are described in the following paragraphs.

A recently developed method, similar to DMO is azimuth moveout (AMO), first described by Biondi *et al.* (1998). This technique allows the regularization of a data set from multi-azimuth to a single-azimuth. It has proved particularly useful to do this in marine seismology where data are typically collected with a streamer running behind a boat. In this situation there are not enough data to make a true 3D image, but the data are spread over too large an area in the direction perpendicular to the streamer for 2D processing techniques. The technique works by using DMO to go from the original data set to a zero-offset data set and then inverse DMO to go from this zero-offset data set to a nonzero-offset data set at a chosen azimuth. In a constant-background velocity, these imaging and modeling operators can be composed to form a single operator mapping from one azimuth to another. The constant background assumption is often sufficient provided the true subsurface velocity is not overly complex.

[3]The midpoint is halfway between the source and receiver; stacking is an average over offset.

[4]A CDP gather is a set of traces that are assumed to have scattered from the same point at depth. A CDP gather is often approximated by a common midpoint gather (CMP) in which all of the traces share the same midpoint between the source and receiver; the two are equivalent in horizontally layered media.

Along similar but more general lines, Stolt (2002) describes a general framework for data mapping in a constant background. This method also works by composing an imaging and modeling operator, this time through the method of stationary phase. This is similar to what is done here, though in a simpler background velocity. In addition to its scientific contribution, this paper (Stolt, 2002) gives an excellent description of the need for data regularization and of the history of these techniques.

The work that was most important to the actual development of the ideas in the following two chapters is that of Bleistein *et al.* (2000), which gives an overview of data mapping in general. That book encompasses some, though not all, of the published results on data mapping in this framework (Jaramillo, 1997; Jaramillo & Bleistein, 1998; Sheaffer & Bleistein, 1998; Bleistein *et al.*, 1999; Bleistein & Jaramillo, 2000). That work describes data mapping as the composition of modeling and inversion formulas developed in an inversion approach using what the authors call "Fourier-like" integrals. These operators are known in the mathematical literature as Fourier Integral Operators (FIOs)[5], which play a central role in this thesis. The work of Bleistein & Jaramillo (2000) is quite close to that used here; we have extended it in Chapters 2 and 3 to be applicable in rapidly varying velocity models in the presence of caustics. When caustics are present in the wavefield, the integral setup used in Bleistein *et al.* (2000) is no longer applicable as the Green functions derived there do not take into account the different traveltime branches that occur in the presence of caustics.

The following two subsections briefly describe Chapters 2 and 3.

1.1.1 Theoretical description

Chapter 2 is the mathematical framework for the proposed method of data regularization. The geophysicist with more practical than theoretical interests may wish to move directly to Chapter 3, which contains a description of the theory written with this in mind.

In Chapter 2, it is shown that starting from two (possibly three) FIOs, one for modeling data and one for imaging with data (the third is a restriction operator; see the discussion above), a combined operator can be constructed that is again an FIO. A distinction exists between the composition of operators and the cascading of operators. Cascading two operators is the application of one operator after the other. By contrast, composing two operators combines them into a single operator mapping directly from the desired input parameters to the desired output parameters. It is from such compositions that the data mapping procedures discussed above are derived.

The reader might well wonder why it is important that these compositions are again FIOs. The answer to this question requires a summary of the properties of this type of operator. Fortunately this has been done in Le Rousseau (2001), Appendix A, and so only a few essential points need be discussed here. Fourier integral operators generalize Fourier integrals and arise naturally as the solution operators of wave equations (Treves, 1980a). Ensuring that the composition of the modeling and imaging FIO is again an FIO, allows the

[5]FIOs generalize Fourier integrals; they arise naturally in the solutions to hyperbolic partial differential equations, of which the wave equation is one example.

continuation of data from one source-receiver configuration to another without introducing false reflections. (For a detailed explanation see the discussion around Equation 25.22 of Hörmander (1985a).)

Chapter 2 treats the two special cases of DMO and AMO discussed previously. In Appendix A a number of these results are derived for a constant-background velocity, including the derivation of a closed form expression for the DMO impulse response. Appendix A also includes an explanation as to why not all the phase variables[6] can necessarily be integrated out when applying the method of stationary phase. In Appendix B, we give the AMO impulse response.

1.1.2 Examples and Illustrations

The purpose of Chapter 3 is to explain and illustrate the theory described in Chapter 2 in the context of exploration geophysics rather than mathematics. There is little material directly repeated from the previous chapter, although the derivations in Appendix D are contained also in Appendix A and Appendix B in a slightly different form.

The first sections of this chapter give a physical overview of the theory developed in Chapter 2. As part of this development a number of impulse responses are shown to illustrate the salient points of the theory. These impulse responses are not sufficient to demonstrate the applicability of the theory but they do illustrate the construction of the composite operators and show the extent, both in time and in space, of the resultant operators. Following this, the method is illustrated by estimating missing traces in shot records. A description of the algorithm used to do this is also given in this section.

The algorithm discussed in Chapter 3 works but is not the most computationally efficient algorithm possible. Examples of a more efficient algorithm are the fast marching techniques of Sethian (2002). With these techniques, it is possible to construct the table, which will be described in Chapter 3, relating subsurface and surface parameters, with a single pass through the velocity model. Once the table is constructed, data continuation, velocity model building, and imaging can be performed through direct operations on the table. Another way to get a faster algorithm is to use the curvelet techniques currently being developed by my fellow student Huub Douma.

The data regularization theory described in this thesis extends the family of velocity models in which data regularization techniques can be applied. The cost of this extension is in additional time requirements for computations and the requirement that the velocity model be known.

[6]Phase variables are the variables typically integrated out through the method of stationary phase. They are often, though not always, Fourier variables associated with the space/time variables of the equation. For an operator to be an FIO its phase is required to be homogeneous of degree one in these variables, i.e., $\phi(x, \lambda\theta) = \lambda\phi(x, \theta)$, where θ is the phase variable and the FIO, F, is defined through its action on a test function a by

$$(Fa) = \iint a(x,\theta)u(x)e^{\mathrm{i}\phi(x,\theta)}\mathrm{d}\theta\mathrm{d}x\,.$$

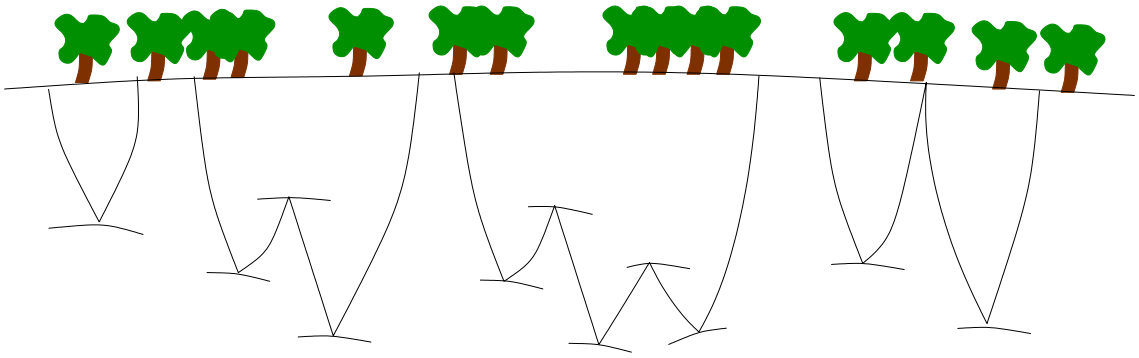

Figure 1.1. From left to right: A primary reflection; a first-order internal multiple; a second-order internal multiple; a surface-related multiple.

1.2 Data continuation for imaging multiples

The subject of Chapters 4 and 5 is the attenuation of imaging artifacts caused by first-order internal multiples. Internal multiples violate the single scattering assumption typical of seismic processing, as they have scattered at least three times, rather than once, in the subsurface. An illustration of the different events discussed in the thesis is given in Figure 1.1. Multiples cause artifacts in imaging with characteristics similar to those of true reflectors. Because of this, they are often misinterpreted as reflectors that are not really present in the subsurface. Surface-related multiples (multiples with at least one reflection at the Earth's surface) are easier to attenuate because the reflection from the surface has a known reflection coefficient (-1) and the data are recorded at the Earth's surface making the estimation of these multiples directly from the data easier. Fokkema & van den Berg (1993) give a complete theory for the attenuation of surface-related multiples. Multiples have been noticed in seismic data for quite some time. Sloat (1948) was perhaps the first to notice them in field data, though the possibility of recording such events was already known at that time.

There are two different categories of approaches to attenuating multiples. One attempts to design filters, using differences in event shape, to attenuate multiples, and the other estimates the multiples and then subtracts them. The work presented in this thesis falls into the second category. In the introduction to Chapter 4, I give an overview of some historical papers; only a few of the references fundamental to this work are discussed in this introduction.

The closest techniques to that discussed in this thesis that are currently in use are extensions of surface-related multiple-attenuation techniques to the internal multiples case. Most of these rely on some sort of series expansion of the wavefield, as is also done in this thesis. Fokkema & van den Berg (1993) develop a theory for multiple attenuation through the principal of reciprocity, resulting in the construction of a Neumann series for surface-related multiple attenuation. Their work is extended to internal multiples by

Fokkema *et al.* (1994); Berkhout & Verschuur (1997); Verschuur & Berkhout (1997) and van Borselen (2002). In some sense, the work presented here is an extension of the surface-related multiples attenuation theory proposed by Aminzadeh & Mendel (1981), who used the Bremmer series to suppress surface multiples. The closest approach to that discussed here, however, is that of Jakubowicz (1998) in which he implicitly uses the Generalized Bremmer series to estimate internal multiples, under the traveltime monotonicity assumption of ten Kroode (2002) (see Figure 1.2). The work of Weglein *et al.* (1997), the mathematical fundamentals of which are presented by ten Kroode (2002), is another series expansion of the wavefield used to estimate internal multiples. Their approach uses a scattering series derived from the Lippmann-Schwinger equation, which will be referred to in what follows as the Lippmann-Schwinger series.

1.2.1 Theoretical description

Chapter 4 describes a theory for attenuating imaging artifacts caused by multiples. This theory involves the development of a hybrid series between the Lippmann-Schwinger and Bremmer series. These two series are discussed in more detail in Appendix G.

The Lippmann-Schwinger series, first proposed by Lippmann (1956) [see also Lippmann & Schwinger (1950); Lippmann (1950)], has been investigated extensively for attenuating internal multiples by Weglein *et al.* (1997, 2003) and ten Kroode (2002). This series is an expansion in the difference between the wave operators in a known reference model and of the unknown true velocity model. Each successive term in the series is of higher order in the difference between the wave operators in these two models. Internal multiples can be estimated from this series, and attenuated through the associated inverse series, which is constructed by assuming that the medium contrast can be expanded in a series with each successive term of higher order in the data. Currently, there are no estimates for convergence on either the forward or inverse seres. With two assumptions on the velocity model, however, this series can be used to attenuate internal multiples without knowledge of the subsurface velocity. The two assumptions are that the wavefield does not contain caustics, and the traveltime monotonicity assumption of ten Kroode (2002), illustrated in Figure 1.2.

The Bremmer series was first developed by Bremmer (1951) for modeling atmospheric phenomena. This series builds up a wavefield by adding together the contributions from successive reflections from different layers in the medium. As constructed by Bremmer, this series is applicable only in a velocity model consisting of a stack of horizontal layers. This series was generalized by de Hoop (1996) to arbitrary reflector geometry and variable background; it is this generalization that is used throughout the thesis. The Bremmer series separates the wavefield into its up- and down-going constituents and as such fits into the framework of a *wave-equation* migration in which an image is formed by propagating the wavefield down into the Earth and extracting the part of the wavefield at zero offset and zero time to be added to the image at each depth. This imaging method works well in the presence of caustics. de Hoop (1996) gives convergence estimates for the Generalized Bremmer series. Drawbacks to the use of this series are that it is not straightforward to

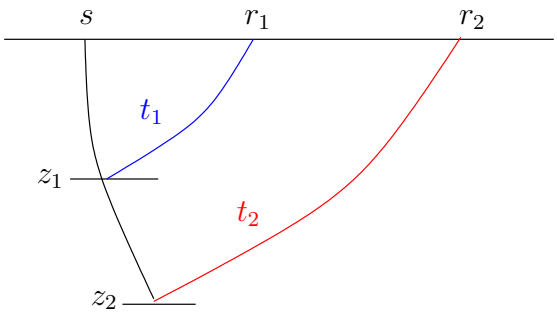

Figure 1.2. The travel time monotonicity condition states that, if $z_1 < z_2$, then $t_1 < t_2$, for waves that share the first portion of their travel path.

construct an inverse series in this framework, and this series requires an estimate of the velocity model.

For the hybrid series, the up/down decomposition of the Bremmer series is used along with the separation of the background medium into two constituents, one known and the other unknown, from the Lippmann-Schwinger series. This combination of the two series is used to enable the construction of an inverse series, while attempting[7] to maintain the convergence properties of the Generalized Bremmer series. Using this hybrid series we construct an algorithm to estimate imaging artifacts caused by internal multiples as part of the imaging process. This allows the estimation of multiples in a larger family of velocity models than do surface methods, but requires an estimate of the velocity model.

1.2.2 Case Study

The goal of Chapter 5 is to illustrate the theory described in Chapter 4 with synthetic and field data examples. The theoretical discussion at the beginning of this chapter is a summary of the most important points of the theory from the previous chapter, designed to give the reader a feel for the theory without the level of detail provided in Chapter 4. This explanation is given in the context of the algorithm used to estimate imaging artifacts caused by internal multiples. To clarify the explanation the algorithm is broken into several steps and each intermediate step is illustrated with a simple synthetic model. Following this, a few more complicated synthetic models are used to demonstrate that the algorithm is not limited to this simple case.

The theory discussed in Chapters 4 and 5 is more general than that used by Weglein *et al.* (1997) and ten Kroode (2002) in that it does not require the traveltime monotonicity assumption and that the velocity model is allowed to contain caustics. To avoid these assumptions knowledge of the velocity model is required to the top of the shallowest reflector

[7] We believe the series to be convergent but have not yet attempted to prove that it is.

involved in the multiple scattering. The computational cost of the algorithm is not prohibitive however; the multiples are estimated with roughly twice the computational cost of a standard migration.

1.3 Acknowledgment

Each chapter of this thesis was written to be published with various co-authors; a full citation of each paper may be found in the footnotes on the title page of the associated chapter. Although each of them was written with the goal of being part of this thesis, much of the work presented was done in close collaboration with Maarten de Hoop, Jérôme Le Rousseau and Henri Calandra. The author gratefully acknowledges their contributions here.

Chapter 2

Seismic wavefield 'continuation' in the single scattering approximation: A framework for Dip and Azimuth MoveOut[1]

2.1 Summary

Seismic data are commonly modeled by a high-frequency single scattering approximation. In this paper we use methods from microlocal analysis and the theory of Fourier integral operators, to study continuation of the seismic wavefield in this single scattering approximation. This amounts to a linearization in the medium coefficient about a smooth background. The discontinuities are contained in the medium perturbation. We use the smooth background to derive the continuation as the composition of imaging, modeling and restriction operators.

2.2 Introduction

In reflection seismology one places point sources and point receivers on the Earth's surface. The source generates acoustic waves in the subsurface, that are reflected where the medium properties vary discontinuously. The recorded reflections that can be observed in the data are used to reconstruct these discontinuities. In principle, the recordings are taken on an acquisition manifold, made up of all source and receiver positions and a time interval. In practice, however, certain subsets in the acquisition manifold are not covered. In this paper, we discuss how, and conditions when, data can be continued from an acquisition submanifold to the complete acquisition manifold.

The data are commonly modeled by a high-frequency single scattering approximation. This amounts to a linearization in the medium coefficient about a smooth background. The discontinuities are contained in the medium perturbation (Beylkin, 1985). Thus a linear operator, the modeling operator, depending on the background, that maps the perturbation to the data is obtained. The smooth background (C^∞) is associated with a computational medium (which can be chosen) rather than a physical one, the distributional ($\mathcal{E}'$) perturba-

[1]This chapter has been published, along with appendices A and B as:
de Hoop, M. V., Malcolm, A. E. and Le Rousseau, J. H. 2003. Seismic wavefield 'continuation' in the single scattering approximation: A framework for dip and azimuth moveout *Can. Appl. Math. Q.*, **10**, 199-238.

tion accounts for geological transitions and the medium's singularities across interfaces and faults. We will consider seismic wavefield continuation in the single scattering approximation and will use an image of the distributional perturbation as an intermediary. We will require some knowledge of the medium properties, viz. the smooth background, but not their discontinuities.

The framework of Fourier integral operators (FIOs) and their composition through the clean intersection calculus (Duistermaat, 1996; Hörmander, 1985a; Treves, 1980a) yield the tools to carry out the following processes: seismic modeling (FIO), acquisition (restriction FIO), imaging (adjoint FIO), resolution (normal operator, the sum of a pseudodifferential operator and a nonlocal FIO)) and inversion (Stolk & de Hoop, 2002).

The wavefront set of the data is, under the so-called Bolker conditions (Guillemin, 1985), a coisotropic submanifold of the acquisition cotangent bundle. It reveals a structure: that of characteristic strips. Restricting in the imaging FIO the seismic data to a common coordinate value on these strips, yields a generalized Radon transform (GRT Beylkin (1985); de Hoop *et al.* (1994); de Hoop *et al.* (1999)) that maps the reflection data into a seismic image. (Under certain conditions the GRT is an FIO (Stolk, 2001).) Collecting these seismic images from the points on the characteristic strips corresponding to available data results in the set of so-called common-image-point gathers (CIGs). In the presence of caustics, a filter needs to be designed and applied prior to extracting a trace from each of the CIGs in the set, to form a model image of the singular component of the medium (Brandsberg-Dahl *et al.*, 2003a; Stolk & de Hoop, 2004b).

From this image, we model seismic data that correspond to a different coordinate value on the characteristic strips. The result of this procedure is a composition of FIOs yielding seismic wavefield continuation, be it in the single scattering approximation. Relevant examples of seismic wavefield continuation are the 'transformation to zero offset' (TZO Hale (1995)) and the 'transformation to common (prescribed) azimuth' (TCA Biondi *et al.* (1998)). The distribution kernel of TZO is called dip moveout (DMO); the distribution kernel of TCA is called azimuth moveout (AMO).

In practice, DMO/AMO is applied to data sets using a constant coefficient model. This is done because, on the one hand, the traditional transforms were derived in constant media, and on the other hand, to make the algorithms which apply DMO/AMO to data simpler and more efficient. Here, we develop a framework for DMO/AMO in heterogeneous, smoothly varying, models allowing the formation caustics. We can thus assess the error in applying DMO/AMO in a simplified model if the 'true' model were to have (strong) variations. (In fact, by composition, the error generating operator can be obtained.)

We mention some of the applications of DMO/AMO: (i) DMO/AMO effectively corresponds to 'partial stacking' of seismic data; such stacking generates reduced data sets viz. on acquisition (zero-offset, common-azimuth) submanifolds. It is important to note that rather than obtaining a reduced dataset from restricting the complete dataset, DMO/AMO will enhance the signal-to-noise ratio by using all available data in the reduction. Under certain conditions addressed in this paper, the reduced data set produces an image consistent with the complete data set. The advantage of using reduced data sets is computational efficiency. (ii) DMO can be employed as a tool for 'velocity analysis', i.e. estimating the

smooth background. (iii) AMO can be employed to carry out approximate (based on a linearized scattering model) seismic data 'regularization'.

The basic idea of investigating the composition of imaging and modeling operators dates back in particular to the work of Goldin (1994).

2.3 High-frequency Born modeling and imaging

We consider the scalar wave equation for acoustic waves in a constant density medium in $\mathbb{R}^n$. We introduce coordinates $x \in \mathbb{R}^n$. The scalar acoustic wave equation is given by

$$Pu = f \ , \quad P = c(x)^{-2}\frac{\partial^2}{\partial t^2} + \sum_{j=1}^{n} D_{x_j}^2, \tag{2.1}$$

where $D_x = -\mathrm{i}\frac{\partial}{\partial x}$. The equation is considered in a time interval $]0, T[$.

If $c \in C^\infty$ the solution operator of (2.1) propagates singularities along bicharacteristics. These are the solutions of a Hamilton system with Hamiltonian given by the principal symbol of P,

$$P(x, \xi, \tau) = -c(x)^{-2}\tau^2 + \|\xi\|^2.$$

The Hamilton system is given by

$$\frac{\partial(x,t)}{\partial\lambda} = \frac{\partial P}{\partial(\xi,\tau)}, \quad \frac{\partial(\xi,\tau)}{\partial\lambda} = -\frac{\partial P}{\partial(x,t)}. \tag{2.2}$$

Its solutions will be parameterized by initial position (x_0), take-off direction ($\alpha \in S^{n-1}$), frequency (τ) and time (t),

$$\boldsymbol{x} = \boldsymbol{x}(x_0, \alpha, \tau, t)$$

and similarly for $\boldsymbol{t}, \boldsymbol{\xi}$; τ is invariant along the Hamilton flow. The evolution parameter λ is the time t.

By Duhamel's principle, a causal solution operator for the inhomogeneous equation (2.1) is given by

$$u(x,t) = \int_0^t \int G(x, t - t_0, x_0) f(x_0, t_0)\, \mathrm{d}x_0 \mathrm{d}t_0, \tag{2.3}$$

where G defines a Fourier integral operator (FIO) with canonical relation, Λ_G, that is essentially a union of bicharacteristics,

$$\Lambda_G = C_+ \cup C_-, \ C_\pm = \{(\boldsymbol{x}(x_0, \alpha, \tau, \pm t), t, \boldsymbol{\xi}(x_0, \alpha, \tau, \pm t), \mp\tau \ ; \ x_0, -\underbrace{\mp(\tau/c(x_0))\alpha)}_{\xi_0}\}.$$

Let

$$(x_I, x_0, \underbrace{\xi_J, \tau}_{\theta}) \quad \text{with} \quad I \cup J = \{1, \ldots, n\} \ , \ N := |J| + 1 \ ,$$

denote coordinates on $C_\pm$. A function S will locally describe C_+ according to

$$\begin{aligned} x_J &= -\frac{\partial}{\partial \xi_J} S \quad , \quad t = -\frac{\partial}{\partial \tau} S \, , \\ \xi_I &= \frac{\partial}{\partial x_I} S \quad , \quad \xi_0 = -\frac{\partial}{\partial x_0} S \, , \end{aligned} \tag{2.4}$$

and generates the non-degenerate phase function

$$\phi_+(x, x_0, t, \xi_J, \tau) = S(x_I, x_0, \xi_J, \tau) + \langle \xi_J, x_J \rangle + \tau t. \tag{2.5}$$

With the canonical relation Λ_G is thus associated the (non-degenerate) phase function ϕ defined by $\phi = \phi_-$ if $\tau > 0$, $\phi = \phi_+$ if $\tau < 0$. The kernel of the mentioned FIO can then be written as a sum of oscillatory integral (OI) contributions

$$G(x, t, x_0) = \sum_i \int_{\mathbb{R}^{N^{(i)}}} a^{(i)}(x, t, x_0, \theta) \, \exp[\mathrm{i}\phi^{(i)}(x, x_0, t, \theta)] \, \mathrm{d}\theta, \tag{2.6}$$

where the $a^{(i)}$ are suitable symbols, see (Duistermaat, 1996, chapter 5).

We adopt the linearized scattering approximation, in which the linearization is in the coefficient c around a smooth background c_0, $c = c_0 + \delta c$. The perturbation δc may contain singularities. In seismology, c_0 is the migration velocity model and δc contains the location of the reflectors. We assume that its support is contained in $X \subset \mathbb{R}^n$. The perturbation in G at (s, r, t) with $s, r \in X$ and $t \in]0, T[$ is given by (cf. (2.3))

$$\delta G(r, t, s) = \int_X \int_0^t G(r, t - t_0, x_0) \, 2c_0^{-3}(x_0) \delta c(x_0) \partial_{t_0}^2 G(x_0, t_0, s) \, \mathrm{d}t_0 \mathrm{d}x_0. \tag{2.7}$$

The singular part of δG is obtained by substituting (2.6) into (2.7). This defines the data modeling map

$$F = F[c_0] \, : \, \delta c \mapsto \mathcal{R} \delta G,$$

where $\mathcal{R}$ is the restriction to the acquisition manifold $Y \ni (s, r, t)$ with $Y = O_s \times O_r \times]0, T[$ subject to $O_s, O_r \subset \partial X$ open. Throughout the paper s, r denote source and receiver position, respectively.

Assumption 1. *[no direct rays, no grazing rays] There are no rays from s to r with travel time t such that $(s, r, t) \in Y$. For all ray pairs connecting r via some $x \in X$ to s with total time t such that $(s, r, t) \in Y$, the rays intersect $O_s \times O_r$ transversally at r and s.*

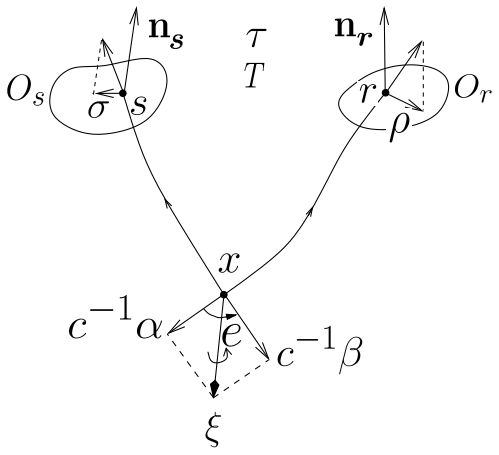

Figure 2.1. Source-receiver bicharacteristics.

Theorem 2.3.1. *(Rakesh, 1988) With Assumption 1 the map F is a Fourier integral operator $\mathcal{D}'(X) \to \mathcal{D}'(Y)$ of order $(n-1)/4$ with canonical relation*

$$\Lambda_F = \{(\boldsymbol{s}(x_0,\beta), \boldsymbol{r}(x_0,\alpha), \overbrace{T(x_0,\alpha)+T(x_0,\beta)}^{T(x_0,\alpha,\beta)}, \boldsymbol{\sigma}(x_0,\beta), \boldsymbol{\rho}(x_0,\alpha), \tau; \\ x_0, -\underbrace{(\tau/c(x_0))\,(\alpha+\beta)}_{\boldsymbol{\xi}(x_0,\alpha,\beta,\tau)}) \mid (x_0,\alpha,\beta) \in K,\ \tau \in \mathbb{R}\backslash 0\} \subset T^*Y\backslash 0 \times T^*X\backslash 0\,, \tag{2.8}$$

where $K \subset \mathbb{R}^n \times \{(\alpha,\beta) \in S^{n-1} \times S^{n-1} \mid \alpha+\beta \neq 0\}$. Here,

$$\underbrace{\boldsymbol{x}(x_0,\alpha,\tau,T(x_0,\alpha))}_{=:\boldsymbol{r}(x_0,\alpha)} \in O_r\,, \quad \underbrace{\boldsymbol{x}(x_0,\beta,\tau,T(x_0,\beta))}_{=:\boldsymbol{s}(x_0,\beta)} \in O_s,$$

which expresses that the time T is locally solved from the equation describing the intersection of the rays with the acquisition manifold, while

$$\boldsymbol{\rho}(x_0,\alpha) = (I - \mathbf{n_r} \otimes \mathbf{n_r})\boldsymbol{\xi}(x_0,\alpha,\tau,T(x_0,\alpha)) \tag{2.9}$$

where $\mathbf{n_r}$ is the unit normal to O_r at $\boldsymbol{r}(x_0,\alpha)$. A similar expression holds for $\boldsymbol{\sigma}(x_0,\beta)$.

The parametrization of Λ_F is illustrated in Figure 2.1. The cotangent vectors σ, ρ can be identified with acquisition 'slopes' p_s, p_r, in accordance with $\boldsymbol{\sigma}(x_0,\beta) = -\tau p_s(x_0,\beta)$ and $\boldsymbol{\rho}(x_0,\alpha) = -\tau p_r(x_0,\alpha)$.

Assumption 1 is microlocal. One can identify the conic set of points $(s,r,t,\sigma,\rho,\tau) \in T^*Y\backslash 0$ where this assumption is violated. If the symbol $\psi = \psi(s,r,t,\sigma,\rho,\tau)$ vanishes on a neighborhood of this set, then the composition ψF of the pseudodifferential cutoff

$\psi = \psi(s, r, t, D_s, D_r, D_t)$ with F is a Fourier integral operator as in the theorem.

We assume also that ψ vanishes outside Y. To image the singularities of δc from the singularities in the data we consider the adjoint $F^*\psi$, which is a Fourier integral operator also.

Assumption 2. *(Guillemin, 1985) The projection of the canonical relation (2.8) on $T^*Y\backslash 0$ is an embedding.*

This assumption is also known as the Bolker condition.

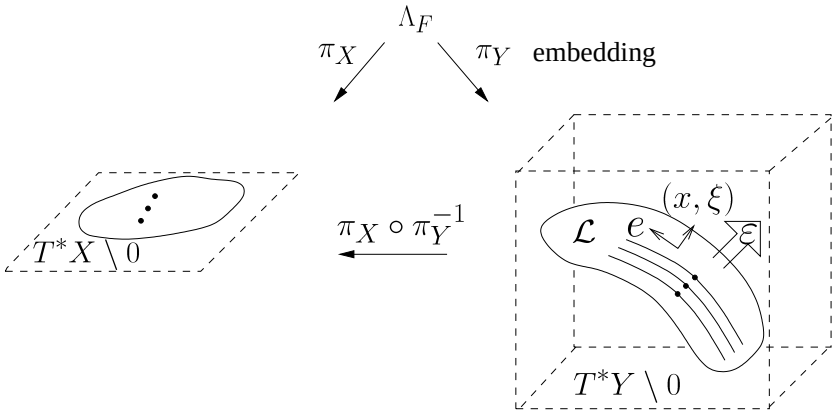

Figure 2.2. Canonical relation and characteristic strips (Stolk & de Hoop, 2002). (Their parametrization is illustrated in Figure 2.1.)

Since (2.8) is a canonical relation that projects submersively on the subsurface variables (x, ξ), the projection of (2.8) on $T^*Y\backslash 0$ is immersive (Hörmander, 1985a, Lemma 25.3.6 and (25.3.4)). Therefore only the injectivity in the assumption needs to be verified (ten Kroode *et al.*, 1998). In fact, it is precisely the injectivity condition that has been assumed in what seismologists call 'map migration'; see Iversen *et al.* (2000) for a recent summary. Figure 2.2 illustrates this schematically.

The following theorem describes the reconstruction of δc modulo a pseudodifferential operator with principal symbol that is nonzero at (x, ξ) whenever there is a point $(s, r, t, \sigma, \rho, \tau; x, \xi)$ in the canonical relation (2.8) with $(s, r, t, \sigma, \rho, \tau)$ in the support of ψ (i.e. whenever there is illumination).

Theorem 2.3.2. *With Assumption 2 the operator $F^*\psi F$ is pseudodifferential of order $n-1$. We denote $F^*\psi F$ by N.*

For the purpose of wavefield continuation within the acquisition manifold Y, we parametrize Λ_F with acquisition coordinates s, r rather than β, α. To describe the kernel of the operator F as an OI on a neighborhood of the point on Λ_F parametrized by $(x_0, \alpha, \beta, \tau)$, the

minimum number of phase variables is given by the corank of the projection

$$D\pi \ : \ T\Lambda \to T(Y \times X)$$

at $(x_0, \alpha, \beta, \tau)$, which is here given by

$$\text{corank } D\pi = 1 + \text{corank } \frac{\partial \boldsymbol{s}}{\partial \beta}(x_0, \beta) + \text{corank } \frac{\partial \boldsymbol{r}}{\partial \alpha}(x_0, \alpha).$$

This corank is > 1 when s or r is in a caustic point relative to x_0. Let

$$\Lambda'_F = \Lambda_F \backslash \{\text{closed neighborhood of } \{\lambda \in \Lambda_F \mid \text{corank } D\pi > 1\}\} \ . \tag{2.10}$$

Λ'_F can be described by phase functions of the 'traveltime' form $\tau\,(t - T^{(m)})$ with the only phase variable being τ. Here, $T^{(m)}$ is the value of the time variable in (2.8). The index m labels the branches of the multi-valued traveltime function. Thus the set $\{T^{(m)}\}_{m\in M}$ describes the canonical relation (2.8) except for a neighborhood of the subset of the canonical relation where the mentioned projection is degenerate. Each $T^{(m)}$ can be viewed as a function defined on a subset $D^{(m)}$ of $X \times O_s \times O_r$. We define $F^{(m)}$ to be a contribution to F with phase function given by $\tau(t - T^{(m)}(x, s, r))$, and symbol $A^{(m)}$ in a suitable class such that on the subset Λ'_F of the canonical relation F is given microlocally by $\sum_{m\in M} F^{(m)}$.

2.4 Generalized Radon transform

We can use $(x, \xi) \in T^*X\backslash 0$ as local coordinates on the canonical relation (2.8) (cf. (Hörmander, 1985b, Prop. C.3.3)). In addition, we need to parameterize the subsets (these are characteristic strips) of the canonical relation given by $(x, \xi) =$ constant; we denote such parameters by e. The canonical relation (2.8) was parameterized by (x, α, β, τ). We relate (x, ξ, e) by a coordinate transformation to (x, α, β, τ): A suitable choice when $\alpha \neq \beta$ is the scattering angles given by de Hoop *et al.* (1999)

$$\boldsymbol{e}(x, \alpha, \beta) = \left(\arccos(\alpha \cdot \beta), \frac{-\alpha + \beta}{2\sin(\arccos(\alpha \cdot \beta)/2)}\right) \in]0, \pi[\times S^{n-2}. \tag{2.11}$$

On $D^{(m)}$ there is a map $(x, \alpha, \beta) \mapsto (x, s, r)$. We define $\boldsymbol{e}^{(m)} = \boldsymbol{e}^{(m)}(x, s, r)$ as the composition of $\boldsymbol{e}$ with the inverse of this map.

In preparation for the generalized Radon transform (GRT) we define the 'angle' transform, L, via a restriction in F^* of the mapping $\boldsymbol{e}^{(m)}$ to a prescribed value e, i.e. the distribution kernel of each contribution $F^{(m)^*}$ is multiplied by $\delta(e - \boldsymbol{e}^{(m)}(x, s, r))$ (which is justified by (Hörmander, 1983, Thm. 8.2.10)). Invoking the Fourier representation of this δ, the kernel of L follows as

$$L(x, e, r, s, t) = \sum_{m\in M} (2\pi)^{-(n-1)} \int \overline{A^{(m)}(x, s, r, \tau)} \exp[\mathrm{i}\Phi^{(m)}(x, e, s, r, t, \varepsilon, \tau)] \, \mathrm{d}\tau \mathrm{d}\varepsilon, \tag{2.12}$$

where $A^{(m)}$ is a symbol for the m-th contribution to F, supported on $D^{(m)}$, and

$$\Phi^{(m)}(x,e,s,r,t,\varepsilon,\tau)=\tau(T^{(m)}(x,s,r)-t)+\langle\varepsilon,e-\boldsymbol{e}^{(m)}(x,s,r)\rangle.$$

In these expressions, ε is the cotangent vector corresponding to e, as in Stolk & de Hoop (2002).

Let $\psi_L=\psi_L(D_s,D_r,D_t)$ be a pseudodifferential cutoff such that $\psi_L(\sigma,\rho,\tau)=0$ on a closed conic neighborhood of $\tau=0$ ($(\sigma,\rho)\neq(0,0)$). Then $\psi_L L$ is a Fourier integral operator (Stolk, 2001) with canonical relation

$$\begin{aligned}\Lambda_L=\cup_{m\in M}\{&(x,\boldsymbol{e}^{(m)}(x,s,r),\boldsymbol{\xi}^{(m)}(x,s,r,\tau,\varepsilon),\varepsilon;\\ &s,r,T^{(m)}(x,s,r),\boldsymbol{\sigma}^{(m)}(x,s,r,\tau,\varepsilon),\boldsymbol{\rho}^{(m)}(x,s,r,\tau,\varepsilon),\tau)\ |\\ &(x,s,r)\in D^{(m)},\ \varepsilon\in\mathbb{R}^{n-1},\ \tau\in\mathbb{R}\backslash 0\}\subset T^*(X\times E)\backslash 0\times T^*Y\backslash 0,\end{aligned}\tag{2.13}$$

where

$$\boldsymbol{\xi}^{(m)}(x,s,r,\tau,\varepsilon)=\partial_x\Phi^{(m)}=\tau\partial_x T^{(m)}(x,s,r)-\langle\varepsilon,\partial_x\boldsymbol{e}^{(m)}(x,s,r)\rangle,\tag{2.14}$$

with similar expressions for $\boldsymbol{\sigma}^{(m)}$ and $\boldsymbol{\rho}^{(m)}$ from $\partial_s\Phi^{(m)}$ and $\partial_r\Phi^{(m)}$.

With the choice (2.11) for $\boldsymbol{e}$, the following assumption is implied. However, for other choices of $\boldsymbol{e}$ it needs to be verified.

Assumption 3. *Consider the mapping*

$$\Xi\ :\ \Lambda_F\to T^*X\backslash 0\times E\ ,\ \lambda(x,\alpha,\beta,\tau)\mapsto(x,\xi,e)\ ,\ \textit{with}\ \xi=-(\tau/c(x))\,(\alpha+\beta).$$

Composing this mapping with the inverse of the mentioned map $(x,\alpha,\beta)\mapsto(x,s,r)$, yields per branch m a mapping $\Xi^{(m)}$ from (x,s,r,τ) to an element of $T^*X\backslash 0\times E$. $\Xi^{(m)}$ is locally diffeomorphic, i.e.

$$\operatorname{rank}\left.\frac{\partial(\boldsymbol{\xi}^{(m)},\boldsymbol{e}^{(m)})}{\partial(s,r,\tau)}\right|_{\varepsilon=0}\quad\textit{is maximal, at given } x \textit{ and branch } m.$$

Let d be the Born modeled data in accordance with Theorem 2.3.1. To reveal any artifacts generated by L, i.e. singularities in Ld at positions not corresponding to an element of $\mathrm{WF}(\delta c)$, we consider the composition $L\,F$. With Assumptions 2 and 3 this composition is equal to the sum of a smooth e-family of pseudodifferential operators and, in general, a non-microlocal operator the wavefront set of which contains no elements with $\varepsilon=0$ (Stolk, 2001, Thm. 6.1). This non-microlocal operator will be a concern in the development of single reflection wavefield continuation. The origin of contributions from $\varepsilon\neq 0$ is illustrated in Figure 2.3. A filter needs to be applied (Brandsberg-Dahl *et al.*, 2003a; Stolk & de Hoop, 2004b) removing contributions from $|\varepsilon|\geq\varepsilon_0>0$: We define the GRT L_U as the FIO, $\mathcal{D}'(Y)\to\mathcal{D}'(X\times E)$, with canonical relation U_L given as a *neighborhood* of $\Lambda_L\cap\{\varepsilon=0\}$ in $\Lambda_L\subset T^*(X\times E)\backslash 0\times T^*Y\backslash 0$. The artifacts in the compose of canonical relations of L

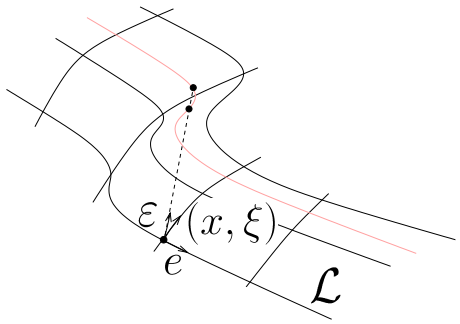

Figure 2.3. The origin of artifacts generated by the GRT. (Inside the $T^*Y\backslash 0$ box of Figure 2.2.)

with F can be evaluated through solving the system of equations

$$\begin{aligned} r &= \boldsymbol{r}(x,\alpha), && (2.15)\\ s &= \boldsymbol{s}(x,\beta), && (2.16)\\ T^{(m)}(z,s,r) &= T(x,\alpha)+T(x,\beta), && (2.17)\\ \boldsymbol{\rho}^{(m)}(z,s,r,\tau,\varepsilon) &= -\tau p_r(x,\alpha), && (2.18)\\ \boldsymbol{\sigma}^{(m)}(z,s,r,\tau,\varepsilon) &= -\tau p_s(x,\beta). && (2.19) \end{aligned}$$

(The frequency is preserved.) Equations (2.15)-(2.17) imply that the image point z must lie on the isochrone determined by (x,s,r). Equations (2.18)-(2.19) enforce a match of slopes (apparent in the appropriate 'slant stacks') in the measurement process,

$$\begin{aligned} -\tau\partial_r T^{(m)}(z,s,r)+\langle\varepsilon,\partial_r \boldsymbol{e}^{(m)}(z,s,r)\rangle &= -\tau p_r(x,\alpha), && (2.20)\\ -\tau\partial_s T^{(m)}(z,s,r)+\langle\varepsilon,\partial_s \boldsymbol{e}^{(m)}(z,s,r)\rangle &= -\tau p_s(x,\beta). && (2.21) \end{aligned}$$

For $\varepsilon\neq 0$ the take-off angles of the pairs of rays at (r,s) following from the right-hand sides of (2.15)-(2.19) may be distinct from those following from the left-hand sides. Equations (2.20)-(2.21) imply the matrix compatibility relation (upon eliminating ε/τ)

$$\begin{aligned} &[\partial_r \boldsymbol{e}^{(m)}(z,s,r)]^{-1}[p_r(x,\alpha)-\partial_r T^{(m)}(z,s,r)]\\ &\qquad = [\partial_s \boldsymbol{e}^{(m)}(z,s,r)]^{-1}[p_s(x,\beta)-\partial_s T^{(m)}(z,s,r)]. \end{aligned} \tag{2.22}$$

The geometrical composition equations determining the artifacts are solved as follows: For each $(x,\alpha,\beta)\in K$ solve the $(3n-2)$ equations (2.15)-(2.17), (2.22) for the $(3n-2)$ unknowns (z,s,r). (From (2.20) we then obtain ε/τ hence ε.)

The GRT reconstructs a distribution in $\mathcal{E}'(X)$ smoothly indexed by $e\in E$. We can trivially extend the domain of modeling operator F from $\mathcal{E}'(X)$ to $\mathcal{E}'(X\times E)$, its action

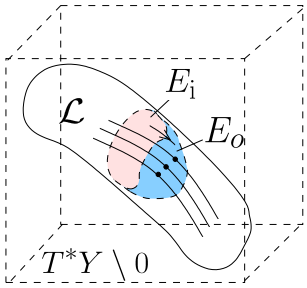

Figure 2.4. Continuation and characteristic strips. (Inside the $T^*Y\backslash 0$ box of Figure 2.2.)

being simply independent of $e \in E$. Hence we can remodel, or what seismologists call 'de-migrate', the image Ld of data d.

2.5 Modeling restricted to an acquisition submanifold

Single reflection seismic wavefield continuation aims at generating from reflection data – through the canonical relation (2.8) – associated with $T^*X\backslash 0 \times E_{\mathrm{i}}$, in which E_{i} is an $(n-1)$-dimensional open neighborhood of e say, reflection data associated with $T^*X\backslash 0 \times E_{\mathrm{o}}$, in which $E_{\mathrm{o}} \supset E_{\mathrm{i}}$. Such continuation, within the acquisition manifold Y, is accomplished through the composition of Fourier integral operators generating an intermediate image of δc. In the previous section, we analyzed a Fourier integral operator, the GRT, that generates δc from data on $T^*X\backslash 0 \times E_{\mathrm{i}}$. In this section we consider, once data are modeled from δc as in Theorem 2.3.1, the restriction to an acquisition submanifold parametrized by (x, ξ, e) through the canonical relation (2.8), such that $e \in E_{\mathrm{o}}$. In the following sections, the restriction, modeling and GRT imaging operators will be composed to yield the continuation. In this composition, the coefficient function c_0 is used, but, naturally, δc does not appear. The continuation is illustrated in Figure 2.4.

A further restriction of the acquisition manifold Y to a submanifold $Y^c = \Sigma^c \times]0, T[$, with $\Sigma^c \stackrel{\imath}{\to} O_s \times O_r$ representing an embedded manifold of codimension $c \geq 0$, yields the following extension of Assumption 1. Let $(y'_1, \ldots, y'_{2n-2-c})$ denote a local coordinate system on Σ^c and $(y'_1, \ldots, y'_{2n-2-c}, y''_{2n-1-c}, \ldots, y''_{2n-2})$ denote a local coordinate system on $O_s \times O_r$ such that Σ^c is given by $(y''_{2n-1-c}, \ldots, y''_{2n-2}) = (0, \ldots, 0)$ locally. (The coordinates on Y are completed by identifying y_{2n-1} with t:

$$(\underbrace{y'_1, \ldots, y'_{2n-2-c}}_{y'}, \underbrace{y''_{2n-1-c}, \ldots, y''_{2n-2}}_{y''}, \underbrace{y_{2n-1}}_{t}). \quad)$$

Assumption 4. *The projection*

$$\Lambda_F \to O_s \times O_r \backslash \Sigma^c \,, \quad (y', y'', t, \eta', \eta'', \tau; x, \xi) \to y''$$

has full rank. In other words

$$\frac{\partial y''}{\partial(x,\alpha,\beta,\tau)} \quad \textit{has maximal rank.}$$

Applying (Duistermaat, 1996, Thm. 4.2.2) to the pair F and the restriction $\mathcal{R}^c$ from $O_s \times O_r \to \Sigma^c$ with Assumption 4 implies that $\mathcal{R}^c F$ is an FIO of order $(n+c-1)/4$ with canonical relation

$$\begin{aligned}\Lambda_F^c = \{(y',t,\eta',\tau;x,\xi) \mid \exists\ (y',y'',\eta',\eta'') \text{ such that} \\ y''=0 \text{ and } (y,\eta;x,\xi)\in\Lambda_F\} \\ \subset T^*Y^c\backslash 0 \times T^*X\backslash 0.\end{aligned} \tag{2.23}$$

We will encounter two examples: Zero offset (ZO), where $c=n-1$ and $\Sigma^c := \Sigma_0 \subset \mathrm{diag}(\partial X)$ (subject to the $n-1$ constraints $r=s$ when $\arccos(\alpha\cdot\beta)=0$ and e_o at x follows from (2.11)), and common azimuth (CA), where $c=1$ and $\Sigma^c := \Sigma_A$ subject to one constraint typically of the form that the $(n-1)$st coordinate in $r-s$ is set to zero, while $E_o \ni e$ at x follows from the mapping $\boldsymbol{e}^{(m)}$. We set $Y_0 = \Sigma_0 \times]0,T[$ and $Y_A = \Sigma_A \times]0,T[$.

The restriction to acquisition submanifolds is placed in the context of inversion in Nolan & Symes (1997).

2.6 Exploding reflector modeling

In this section we introduce a procedure to model zero-offset (ZO) data: data with coinciding sources and receivers. To ensure that the zero-offset experiment can be modeled by an FIO we invoke Assumption 4 with $\Sigma^c := \Sigma_0$. We denote its canonical relation by Λ_0.

For the zero-offset reduction to be 'image preserving', i.e. for the associated normal operator to be pseudodifferential, we mention

Assumption 5. *The projection*

$$\pi_{Y_0} \ : \ \Lambda_0 \to T^*Y_0\backslash 0$$

is an embedding.

(In fact, Assumption 4 with $\Sigma^c = \Sigma_0$ implies that π_{Y_0} is an immersion.) This assumption is most easily verified by checking whether an element (y_0,η_0) in $T^*Y_0\backslash 0$ uniquely determines an element $(x_0, \xi_0 = \partial_{x_0} T_0)$ in $T^*X\backslash 0$ smoothly; here, T_0 is the zero-offset traveltime. (In fact, Assumption 5 implies that the projection π_{Y_0} is a diffeomorphism, which coincides with Beylkin's condition (Beylkin, 1985).)

Remark 2.6.1. Assumptions 4 and 5 precisely allow the introduction of so-called map migration-demigration between the wavefront set of zero-offset data and the wavefront set of the singular medium perturbation.

In the absence of Assumption 5 we introduce the notion of the exploding reflector (ER) model in the following

Lemma 2.6.2. *Let Φ_{ER} be the phase function given by $2S(x_I, x_0, \xi_J, \tau) + 2\langle \xi_J, x_J\rangle + \tau t$ (cf. (2.5)). Let A_{ER} be the symbol given by $[a(x, t, x_0, \xi_J, \tau)]^2$ (cf. (2.6)). A_{ER} and Φ_{ER} generate an oscillatory integral and define an FIO, $\delta G_0 \ : \ \mathcal{E}'(X) \to \mathcal{D}'(X\times]0, T[)$,*

$$\delta G_0(x, t, x_0) = \sum_i \int_X \int_{\mathbb{R}^{N^{(i)}}} A^{(i)}_{\mathrm{ER}}(x, t, x_0, \theta)(-\tau^2)\, \exp[\mathrm{i}\Phi^{(i)}_{\mathrm{ER}}(x, x_0, t, \theta)] \\ 2c_0^{-3}(x_0)\delta c(x_0)\, \mathrm{d}\theta \mathrm{d}x_0.$$

Its canonical relation, $\Lambda_{0,\mathrm{ER}}$, is a scaled version of Λ_G obtained by replacing c in Hamilton system (2.2) by $\frac{1}{2}c_0$.

Proof. Φ_{ER} follows from the nondegenerate phase function ϕ associated with G upon replacing c_0 by $\frac{1}{2}c_0$, and is hence nondegenerate. The source f in (2.3) and (2.6) is replaced by $2c_0^{-3}(x_0)\delta c(x_0)$. □

Let $\mathcal{R}_r$ denote the restriction of $X\times]0, T[$ to $O_r\times]0, T[$. Let $x = (x', x'')$ denote local coordinates on X such that O_r is defined by $x'' = 0$.

Assumption 6. *The intersection of $\Lambda_{0,\mathrm{ER}}$ with the manifold $Y_0 = O_r\times]0, T[$ is transversal. In other words*

$$\frac{\partial x''}{\partial(x_0, \alpha_0, \tau_0)} \text{ has maximal rank.}$$

Corollary 2.6.3. *Subject to Assumption 6, the restriction $F_0 = \mathcal{R}_r\delta G_0$ is a local FIO, $F_0 = F_0[c_0] \ : \ \mathcal{E}'(X) \to \mathcal{D}'(Y_0)$, of order $(n-1)/2$. Its canonical relation is given by*

$$\Lambda_E = \{(\boldsymbol{z}(x_0, \alpha_0), \overbrace{2T(x_0, \alpha_0)}^{T_0(x_0,\alpha_0)}, \boldsymbol{\zeta}(x_0, \alpha_0), \tau_0; \\ x_0, -\underbrace{2\,(\tau/c(x_0))\,\alpha_0)}_{\boldsymbol{\xi}_0(x_0,\alpha_0,\tau_0)} \mid (x_0, \alpha_0) \in K_0,\ \tau_0 \in \mathbb{R}\backslash 0\} \subset T^*Y_0\backslash 0 \times T^*X\backslash 0, \tag{2.24}$$

where $K_0 \subset \mathbb{R}^n \times S^{n-1}$. In the notation of (2.8),

$$\boldsymbol{z}(x_0, \alpha_0) = \boldsymbol{r}(x_0, \alpha_0)\ , \quad \boldsymbol{\zeta}(x_0, \alpha_0) = 2\boldsymbol{\rho}(x_0, \alpha_0)\ .$$

Proof. Let $\Lambda_{\mathcal{R}_r}$ denote the canonical relation of $\mathcal{R}_r$,

$$\Lambda_{\mathcal{R}_r} = \{(x', t, \xi', \tau; (x', x'', t), (\xi', \xi'', \tau)) \in T^*Y_0\backslash 0 \times T^*(X\times]0, T[)\backslash 0 \mid x'' = 0\}.$$

With Assumption 6 it follows that the intersection of $\Lambda_{\mathcal{R}_r} \times \Lambda_{0;\mathrm{ER}}$ with $T^*Y_0\backslash 0 \times \mathrm{diag}(T^*(X\times]0, T[)\backslash 0) \times T^*X\backslash 0$ is transversal. Now apply (Duistermaat, 1996, Thm. 4.2.2) to the pair δG_0 and the restriction $\mathcal{R}_r$. □

Note that canonical relation Λ_E is related to canonical relation Λ_L by fixing the value of e in the latter in accordance with $\beta = \alpha$ (cf. (2.11)). Thus, in the framework of the ER model, the inverse problem is formally determined.

Remark 2.6.4. Subjecting the configuration to Assumption 5, the exploding reflector modeling, F_0, is up to leading order singularities equivalent to restricting the multiple-offset modeling to zero offset, $\mathcal{R}_0\delta G$, where $\mathcal{R}_0$ is the restriction of $X \times X \times]0,T[$ to Y_0. Otherwise, the exploding reflector models only part of the zero-offset data.

2.7 Transformation to zero offset: Dip MoveOut

In applications, the data at zero offset is usually missing: Receivers cannot be placed on top of sources. Hence, as a first example, we analyze the continuation of multiple finite-offset seismic data to zero-offset seismic data. Dip MoveOut is the process following upon composing ER modeling with L_U, the imaging GRT for a neighborhood of a given value of e (conventionally for given value of offset $r-s$); the sing supp of the Lagrangian-distribution kernel of the resulting operator is what seismologists call the DMO 'impulse response'. The compose, F_0L, is a well-defined operator $\mathcal{D}'(Y) \to \mathcal{D}'(Y_0)$. Its wavefront set is contained in the composition of the wavefront sets of F_0 and L (Duistermaat, 1996, Thm. 1.3.7), hence in the composition of canonical relations,

$$\begin{aligned}\Lambda_E \circ \Lambda'_L = \{(z,t_0,\zeta,\tau_0;s,r,t,\sigma,\rho,\tau) \mid \exists\ (x,\xi,\varepsilon) \text{ such that} \\ (z,t_0,\zeta,\tau_0;x,\xi) \in \Lambda_E \text{ and } (x,e,\xi,\varepsilon;s,r,t,\sigma,\rho,\tau) \in \Lambda_L\} \\ \subset T^*Y_0\backslash 0 \times T^*Y\backslash 0\ . \end{aligned} \tag{2.25}$$

with $\Lambda'_L = \{(x,\xi;s,r,t,\sigma,\rho,\tau) \mid \exists\ \varepsilon \text{ such that } (x,e,\xi,\varepsilon;s,r,t,\sigma,\rho,\tau) \in \Lambda_L\}$. Whether the compose is an FIO is yet to be investigated.

Using the parametrization of Λ_E in (2.24) and the parametrization of Λ_L in (2.13), the compose (2.25) can be evaluated through solving a system of equations, the first n being trivial fixing the scattering point $x_0 = x$, the second n equating the cotangent vectors

$$\underbrace{2\tau_0\partial_x T(x_0,\alpha_0)}_{\boldsymbol{\xi}_0(x_0,\alpha_0,\tau_0)} = \underbrace{\tau\partial_x T^{(m)}(x_0,s,r) - \langle\varepsilon,\partial_x \boldsymbol{e}^{(m)}(x_0,s,r)\rangle}_{\boldsymbol{\xi}^{(m)}(x_0,s,r,\tau,\varepsilon)}\,. \tag{2.26}$$

Given x_0, these constitute n equations with the n unknowns (α_0,τ_0). Thus for each (s,r,τ,ε) we need to solve these equations.

Note that, given $e = \boldsymbol{e}^{(m)}(x_0,s,r)$, we can obtain r from s (cf. (2.11)). Thus we can parametrize the composition $\Lambda_E \circ \Lambda'_L$ by (x_0,s,τ,ε). We can interpret the computation of the composition as follows: (i) Given (x_0,s) we compute r and then $T^{(m)}$; (ii) then, given (τ,ε) we compute $\sigma = \boldsymbol{\sigma}^{(m)}$ and $\rho = \boldsymbol{\rho}^{(m)}$; (iii) we solve (2.26) for (α_0,τ_0); (iv) with these initial values, we solve the Hamiltonian flow (with (2.2) in the exploding reflector model) up to its intersection with the acquisition manifold Y_0, from which we deduce t_0 and z, as well as ζ.

Theorem 2.7.1. *With Assumptions 2 and 3 the composition F_0L_U yields a smooth family of FIOs parametrized by e. The compose is called Dip MoveOut. Its canonical relation is given by (2.25)*

$$\Lambda_D = \Lambda_E \circ U_L = \{(z,t_0,\zeta,\tau_0;s,r,t,\sigma,\rho,\tau)\}$$

parameterized by $(x_0, s, \tau, \varepsilon)$, where (s, r, t, σ, ρ) are given in (2.13) subject to the substitution $x = x_0$ and r is obtained from s through $\boldsymbol{e}^{(m)} = e$ which mapping is defined below equation (2.11), and (z, t_0, ζ) are given in Corollary 2.6.3 in which (α_0, τ_0) are obtained by solving (2.26).

Proof. First we extend the operator F_0 to act on distributions in $\mathcal{E}'(X \times E)$ by assuming that the action does not depend on $e \in E$. The calculus of FIOs gives sufficient conditions that the composition of two FIOs, here F_0 and L_U, is again a FIO. The essential condition is that the composition of canonical relations is transversal, i.e. that $\Lambda_E \times U_L$ and $T^*Y_0\backslash 0 \times \mathrm{diag}(T^*(X \times E)\backslash 0) \times T^*Y\backslash 0$ intersect transversally. We have

$$\begin{array}{ccccccc} & & \Lambda_E & & & & U_L & & \\ & \swarrow & & \searrow & & \swarrow & & \searrow & \\ T^*Y_0\backslash 0 & & & & T^*X\backslash 0(\times E) & & & & T^*Y\backslash 0 \end{array} \tag{2.27}$$

where the inner two projections are submersions.

In a neighborhood of a point in Λ_L given by (2.13), Λ_L can be parametrized as in Λ'_F. Using this parametrization one finds that the composition of Λ_E and Λ_L is transversal if and only if the matrix

$$\frac{\partial}{\partial(s, r, \alpha_0, \tau, \varepsilon, \tau_0)} \left(\ \boldsymbol{\xi}_0(x_0, \alpha_0, \tau_0) - \boldsymbol{\xi}^{(m)}(x_0, s, r, \tau, \varepsilon) \ \right)$$

has maximal rank (cf. (2.26)). This follows, for example, just from the $\boldsymbol{\xi}_0$ contribution to this matrix. However, it follows also from the $\boldsymbol{\xi}^{(m)}$ contribution: Parametrizing Λ_L by (x, ξ, ε) and restricting Λ_L to U_L further to $\varepsilon = 0$, results in a parametrization in terms of (x, ξ) (with the artifacts filtered out). Then $\boldsymbol{\xi}^{(m)}$ reduces to ξ and it follows that the composition of Λ_E and U_L is transversal if and only if

$$\mathrm{rank} \ \frac{\partial}{\partial(\xi, \alpha_0, \tau_0)} \left(\ \boldsymbol{\xi}_0(x_0, \alpha_0, \tau_0) - \xi \ \right) \quad \text{is maximal.}$$

This is indeed the case. □

Remark 2.7.2. The Normal MoveOut is the relation obtained by the intersection

$$\Lambda_E \circ (U_L \cap \{\xi / \|\xi\| = (0, \ldots, 0, 1)\})$$

and defines a special case of the time function t_0 which is denoted by t_n. Such a relation accounts for δc with $\mathrm{WF}(\delta c) \subset X \times \{\xi \mid \xi/\|\xi\| = (0, \ldots, 0, 1)\}$ only.

Using all the data (when available), integration over the $(n-1)$ dimensional e removes the artifacts under the Bolker condition, Assumption 2: We obtain the transformation to zero offset (TZO)

Corollary 2.7.3. *Let $\langle N^{-1} \rangle$ denote the regularized inverse of the normal operator in Theorem 2.3.2. With Assumptions 1, 2 and 4 (with $\Sigma^c = \Sigma_0$), the composition $F_0 \langle N^{-1} \rangle F^* =$*

$\int \mathrm{d}e F_0\langle N^{-1}\rangle L$ *is an FIO,* $\mathcal{D}'(Y) \to \mathcal{D}'(Y_0)$. *With Assumption 5 the reduced dataset is image preserving.*

The proof follows that of Theorem 2.3.2 closely (see (Stolk & de Hoop, 2002, Thm. 4.5)).

Remark 2.7.4. The adjoint $(F_0 L_U)^*$ is by Theorem 2.7.1 also an FIO. This operator is called 'inverse' DMO.

2.8 Continuation, transformation to common azimuth

Continuation

We analyze the 'continuation' of multiple finite-offset seismic data.

The compose FL is a well-defined operator $\mathcal{D}'(Y) \to \mathcal{D}'(Y)$. Its wavefront set is contained in the composition of the wavefront sets of F and L (Duistermaat, 1996, Thm. 1.3.7), hence in the composition of canonical relations,

$$\begin{aligned}\Lambda_F \circ \Lambda_L' = \{&(s_2, r_2, t_2, \sigma_2, \rho_2, \tau_2; s_1, r_1, t_1, \sigma_1, \rho_1, \tau_1) \mid \exists\ (x, \xi, \varepsilon) \text{ such that} \\ &(s_2, r_2, t_2, \sigma_2, \rho_2, \tau_2; x, \xi) \in \Lambda_F \text{ and } (x, e, \xi, \varepsilon; s_1, r_1, t_1, \sigma_1, \rho_1, \tau_1) \in \Lambda_L\} \\ &\subset T^*Y\backslash 0 \times T^*Y\backslash 0. \end{aligned} \tag{2.28}$$

Whether the compose is an FIO is yet to be investigated.

Using the parametrizations of Λ_F in (2.8) and Λ_L in (2.13), the compose (2.28) can be evaluated through solving a system of equations, the first n being trivial fixing the scattering point $x_0 = x$, the second n equating the cotangent vectors

$$\underbrace{\tau_2 \partial_x T(x_0, \alpha, \beta)}_{\boldsymbol{\xi}(x,\alpha,\beta,\tau_2)} = \underbrace{\tau_1 \partial_x T^{(m)}(x, s, r) - \langle \varepsilon, \partial_x \boldsymbol{e}^{(m)}(x, s, r)\rangle}_{\boldsymbol{\xi}^{(m)}(x,s,r,\tau_1,\varepsilon)}. \tag{2.29}$$

Given $\boldsymbol{e}(x, \alpha, \beta) = e$ ($n-1$ constraints) these constitute n equations with the $2n-1$ unknowns (α, β, τ_2). (On $D^{(m)}$ the constraints on e can be invoked on s, r instead, viz. via the inverse of the map $(x, \alpha, \beta) \mapsto (x, s, r)$ as before.)

Lemma 2.8.1. *With Assumptions 2 and 3 the composition* FL_U *yields a smooth family of FIOs parametrized by* e. *Their canonical relations are given by*

$$\Lambda_C = \Lambda_F \circ U_L = \{(s_2, r_2, t_2, \sigma_2, \rho_2, \tau_2; s_1, r_1, t_1, \sigma_1, \rho_1, \tau_1)\}$$

parameterized by $(x_0, \alpha, s_1, \tau_1, \varepsilon)$, *where upon substituting* $x = x_0$ *and once* r_1 *is obtained from* s_1 *through the value* e *of* $\boldsymbol{e}^{(m)}$ *(which mapping is defined below equation (2.11)),* $(s_1, r_1, t_1, \sigma_1, \rho_1)$ *are given in (2.13), and, given* (α, ε), $(s_2, r_2, t_2, \sigma_2, \rho_2)$ *are given in Theorem 2.3.1 in which* (β, τ_2) *are obtained by solving (2.29).*

Proof. First we extend the operator F to act on distributions in $\mathcal{E}'(X \times E)$ by assuming that the action does not depend on $e \in E$. The calculus of FIOs gives sufficient conditions that the composition of two FIOs, here F and L_U, is again an FIO. The essential condition

is that the composition of canonical relations is transversal, i.e. that $\mathcal{L} = \Lambda_F \times U_L$ and $\mathcal{M} = T^*Y\backslash 0 \times \mathrm{diag}(T^*(X \times E)\backslash 0) \times T^*Y\backslash 0$ intersect transversally. We have

$$\begin{array}{ccccc} & \Lambda_F & & U_L & \\ \swarrow & & \searrow \quad \swarrow & & \searrow \\ T^*Y\backslash 0 & & T^*X\backslash 0\ (\times E) & & T^*Y\backslash 0 \end{array} \tag{2.30}$$

where the inner two projections are submersions.

On the other hand, in a neighborhood of a point in Λ_F given by (2.13), Λ_F can be parametrized as in Λ_F'. Using this parametrization one finds that the composition of Λ_F and Λ_L is transversal if and only if the matrix

$$\frac{\partial}{\partial(s, r, \alpha, \beta, \tau_2, \varepsilon, \tau_1)} \left(\ \boldsymbol{\xi}(x, \alpha, \beta, \tau_2) - \boldsymbol{\xi}^{(m)}(x, s, r, \tau_1, \varepsilon) \ \right)$$

has maximal rank (cf. (2.29)). This follows, for example, just from the $\boldsymbol{\xi}$ contribution in view of the submersivity of the projection $\pi_X \ : \ \Lambda_F \to T^*X\backslash 0$. However, it follows also from the $\boldsymbol{\xi}^{(m)}$ contribution: Parametrizing Λ_L by (x, ξ, ε) and restricting Λ_L to U_L further to $\varepsilon = 0$, results in a parametrization in terms of (x, ξ) (with the artifacts filtered out). Then $\boldsymbol{\xi}^{(m)}$ becomes ξ and it follows that the composition of Λ_F and U_L is transversal if and only if

$$\text{rank } \frac{\partial}{\partial(\xi, \alpha, \beta, \tau_2)} \left(\ \boldsymbol{\xi}(x, \alpha, \beta, \tau_2) - \xi \ \right) \quad \text{is maximal.}$$

This is indeed the case. □

Subjecting the operator F in the composition to the constraint that $\boldsymbol{e}$ (cf. (2.11)) attains a prescribed value, the parameter α in the lemma will be eliminated.

Remark 2.8.2. Following seismological convention, we have used the terminology wavefield continuation. In fact, this is continuation in the context of continuation theorems also. We consider the continuation of the wavefield in the acquisition manifold from $T^*X\backslash 0 \times E_{\mathrm{i}}$ to $T^*X\backslash 0 \times E_{\mathrm{o}}$. This continuation is unique in the sense that $FL_Ud = 0$ implies $F^*FL_Ud = 0$ and, since $F^*F = N$ is strictly elliptic and pseudodifferential, then $L_Ud = 0$ so that the image of δc vanishes. In the single scattering approximation this implies that $d = F\delta c = 0$, all modulo smoothing contributions.

Remark 2.8.3. The subject of data regularization is the transformation of measured reflection data, sampled in accordance with the actual acquisition, to data associated with a regular sampling of the acquisition manifold Y. In our approach the operator $\mathcal{R}^cF \int \mathrm{d}e\langle N^{-1}\rangle L$ replaces the forward interpolation operator in the usual regularization procedures.

Transformation to common azimuth: Azimuth MoveOut

Azimuth MoveOut is the process following composing $\mathcal{R}^1_A$ restricting Y to Y_A with modeling operator F with the imaging GRT L_U centered at a given value of e (conventionally for given value of offset $r - s$); the sing supp of the Lagrangian-distribution kernel of the

resulting operator is what seismologists call the AMO 'impulse response'. The composition $F\,L_U$ has been addressed in Lemma 2.8.1. The general restriction has been addressed in Section 2.5. Here we combine these results in the following

Theorem 2.8.4. *With Assumptions 2, 3 and 4 with $Y^c = Y_A$, the composition $\mathcal{R}^1_A F\,L_U$ yields a smooth family of FIOs parametrized by e. The resulting operator is called Azimuth MoveOut.*

The following Bolker-like condition ensures that the restriction to common azimuth is 'image preserving'. Let Λ_A denote the canonical relation of $\mathcal{R}^1_A F$ in accordance with the analysis of Section 2.5,

Assumption 7. *The projection*

$$\pi_{Y_A} \;:\; \Lambda_A \to T^*Y_A\backslash 0$$

is an embedding.

This assumption is most easily verified whether an element in $T^*Y_A\backslash 0$ uniquely determines an element in $T^*X\backslash 0$ smoothly given the medium c_0.

Using 'all' the data (when available), integration over the $(n-1)$ dimensional e removes the artifacts under the Bolker condition, Assumption 2: We obtain the transformation to common azimuth (TCA)

Corollary 2.8.5. *Let $\langle N^{-1}\rangle$ denote the regularized inverse of the normal operator in Theorem 2.3.2. With Assumptions 1, 2 and 4 (with $\Sigma^c = \Sigma_A$), the composition $\mathcal{R}^1_A F\langle N^{-1}\rangle F^* = \int \mathrm{d}e \mathcal{R}^1_A F\langle N^{-1}\rangle L$ is an FIO, $\mathcal{D}'(Y) \to \mathcal{D}'(Y_A)$. With Assumption 7 the reduced dataset is image preserving.*

The proof follows that of Theorem 2.3.2 closely (see (Stolk & de Hoop, 2002, Thm. 4.5)).

2.9 Examples

We give a seismologists' perspective on Dip and Azimuth MoveOut. We illustrate their perspective in the constant coefficient c_0 case. This is the common case where the associated transformations are applied. In this paper, however, we have established the methodology to honor the heterogeneity in the subsurface.

The smooth background coefficient function c_0 is called the (seismic) velocity model and characterizes the speed at which waves travel through the medium. Invoking Cartesian coordinates, the acquisition manifold is obtained by setting the nth coordinate of s and r to zero. Then O_s and O_r are open subsets of a plane hypersurface. In seismology, the midpoint in this hypersurface is defined as $y = \frac{1}{2}(s+r)$ and the offset is defined as $h = \frac{1}{2}(r-s)$. In some sense, the midpoint is associated with the direction of ξ while the offset is a particular choice for e. Here, we assume that c_0 is constant. We will illustrate both DMO and AMO, i.e. the singular supports of their respective kernels. In this section, we will highlight the transition from a parametrization including (y,h,t) to a parametrization including (s,e,t) where e relates to the scattering angles.

Dip MoveOut

The dip in Dip MoveOut refers to the direction of the cotangent vector ξ in the canonical relations for modeling or imaging. Here, we illustrate DMO for $n = 2$. For the history of DMO, see Artley & Hale (1994); Black *et al.* (1993); Deregowski & Rocca (1981); Hale (1995); Jakubowicz (1990); Liner (1991); Miller & Burridge (1992); Sorin & Ronen (1989). The relevant phase functions and canonical relations are derived in Appendix A, where also a parametric representation of the impulse response is given.

We first illustrate the (transversal) composition of the canonical relations in a way familiar to seismologists. To this end, we view a canonical relation in X: For each (y, h) (or, equivalently, (s, r)) in the canonical relation Λ_F, an isochron is obtained by fixing the time t. We can, however, also view isochrons for each (s, e) instead, where e is given by (2.11).

The composition of canonical relations that determines the DMO canonical relation, implies the 'matching' in (x, ξ) of exploding reflector (F_0) isochrons with modeling (F) isochrons. Figure 2.5 illustrates this composition in the (y, h, t) parametrization; the finite-offset imaging operator maps data at (y, h, t) to the associated finite-offset isochron (white ellipse), indicated by the two arrows pointing towards the scattering point x. The exploding reflector modeling operator maps the image of the medium perturbation from the zero-offset isochron (white dashed circle) to the acquisition manifold, indicated by an arrow pointing away from the scattering point.

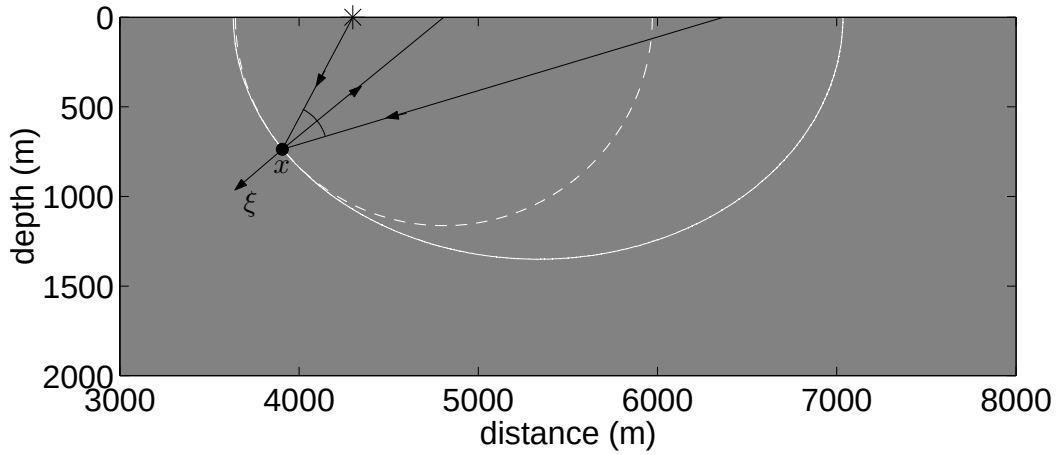

Figure 2.5. Constant velocity medium ($c_0 = 1.7$ km/s) the solid curve is the finite offset isochron, the dashed curve the zero-offset isochron, the black lines are the rays and the dot shows the location of the scattering point, which is the same as that marked by a dot in Figure 2.6.

The analogous construction in the (s, e, t) parametrization is shown in Figure 2.6. Note

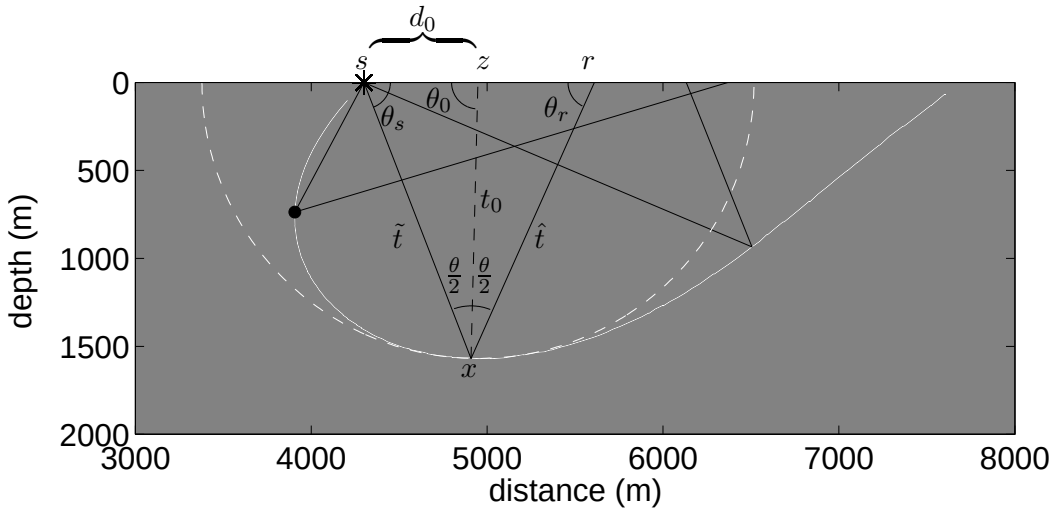

Figure 2.6. Notation for the derivation of the constant medium impulse response (cf. Appendix A). Black lines are rays, the dashed white curve is the zero-offset isochron, the solid white curve is the e 'isochron' and the black dot is the location of the scattering point for the rays shown in Figure 2.5.

that the shape of the finite e 'isochron' differs from the one of the finite h isochron, but that the shapes of exploding reflector model isochrons are the same.

Figure 2.7 shows the 'isochron' in the (s, e, t) parametrization for different values of e. All isochrons, except the exploding reflector one, have two points in common. One of these is the point at which the source ray travels for one time sample less than the full (fixed) time before the ray is scattered and returns to the acquisition surface; the other is the source point.

The impulse response of the DMO operator is the zero-offset traveltime t_0 and the distance d_0 from the source (s) to the exploding reflector source/receiver position (z) both as a function of the direction (θ_s) of the ray at the source (related to σ); all other parameters are fixed. In Figure 2.8 we plot these functions parameterically against one another. They are derived in Appendix A.

Azimuth MoveOut

The azimuth in Azimuth MoveOut Biondi *et al.* (1998) is the polar angle associated with the two-dimensional offset ($n = 3$) in the acquisition manifold. As the key parameter, we will employ the azimuthal angle in e rather than azimuth in h.

The composition of canonical relations that determines the AMO canonical relation, implies the 'matching' in (x, ξ) of two 'isochrons', one associated with the imaging operator L_U and one associated with the modeling operator F. The points at which these two 'isochrons' touch and share the same (co)tangent plane are the points which contribute to

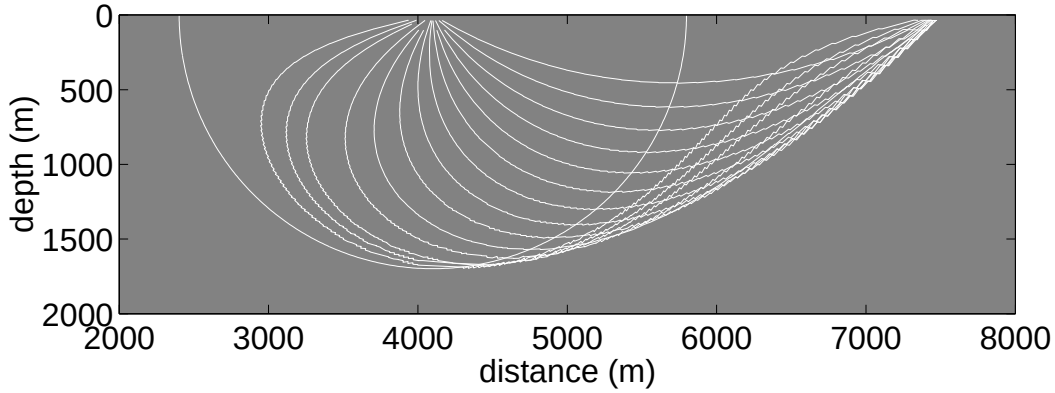

Figure 2.7. Constant velocity medium ($c_0 = 1.7$ km/s) the lines are the locations of the scattering points. Each line represents a different scattering angle, the circular line is $e = 0$, and the other lines are at increments of 0.1 radians from 0.1 radians (leftmost line) to 2.6 radians (shallowest line). All other parameters are the same as Figure 2.6.

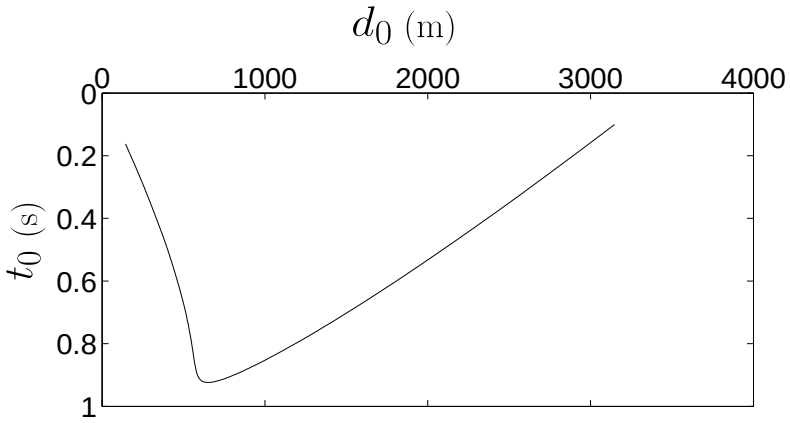

Figure 2.8. Constant velocity medium DMO impulse response, scattering angle 0.7 radians, $c_0 = 1.7$ km/s, $t = 2$ s.

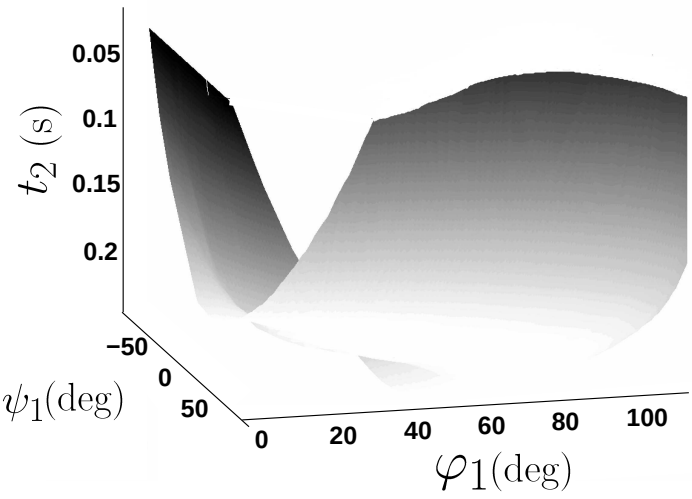

Figure 2.9. Surface plot of the AMO impulse response as a function of input ray directions.

the canonical relation of the AMO operator.

The impulse response of the AMO operator is the traveltime t_2 as a function of the direction $((\theta_s, \psi_s))$ of the ray at the source (related to σ); all other parameters are fixed. In Figure 2.9 we plot this function. The expression is derived in Appendix B.

Chapter 3

The applicability of DMO/AMO in the presence of caustics[1]

3.1 Summary

Reflection seismic data continuation is the computation of data at source and receiver locations that differ from those in the original data, using what data are available. We develop a general theory of data continuation in the presence of caustics and illustrate it with three examples: dip moveout (DMO), azimuth moveout (AMO), and offset continuation. This theory does not require knowledge of the reflector positions. We construct the output data set from the input through the composition of three operators: an imaging operator, a modeling operator, and a restriction operator. This results in a single operator that maps directly from the input data to the desired output data. We use the calculus of Fourier integral operators to develop this theory in the presence of caustics. For both DMO and AMO, we compute impulse responses in a constant-velocity model and in a more complicated model in which caustics arise. This analysis reveals errors that can be introduced by assuming, for example, a model with a constant vertical velocity-gradient when the true model is laterally heterogeneous. Data continuation uses as input a subset (common-offset, common-angle) of the available data, which may introduce artifacts in the continued data. One could suppress these artifacts by stacking over a neighborhood of input data (using a small range of offsets, or angles, for example). We test data continuation on synthetic data from a model known to generate imaging artifacts. We show that stacking over input scattering angles suppresses artifacts in the continued data.

3.2 Introduction

Data collected in the field are often not ideal for processing. For example, zero-offset data are important in seismic data processing but limitations preclude collecting such data in the field. In general, we refer to methods to remedy this problem as *data continuation* or *data mapping*. Stolt (2002) gives an excellent description of why data continuation is necessary, as well as a theory for performing data mapping with a constant-background-velocity model. Patch (2002) gives an example of data continuation in medical imaging.

[1]This chapter has been published, along with Appendices C, D, E, and F as:
Malcolm, A. E., de Hoop, M. V. and Le Rousseau, J. H. 2005. The applicability of DMO/AMO in the presence of caustics. *Geophysics* **70 S1-S17.**

We introduce a theoretical tool to analyze data continuation in the presence of caustics, focusing on the particular examples of dip moveout (DMO) and azimuth moveout (AMO). The mathematical formulation of this tool is given in de Hoop *et al.* (2003a) and de Hoop (2004); the purpose of this paper is to discuss its interpretation, application, and computation. In comparison with previous work, we pay special attention to the case in which caustics are present in the wavefield. Then, the operator becomes, locally, significantly more complicated. The region where the complication occurs depends on the lateral heterogeneity of the velocity model used. Unlike traditional DMO and AMO operators, our operator changes along a profile; thus the computation becomes significantly more complex in regions with complicated velocity structure. The practical value of this tool comes in constructing the near-offset data in regions where the velocity model is complicated.

We use the term *data continuation* to describe any act of computing data that has not been collected in the field. Early examples of data continuation using a partial differential equation can be found in Goldin (1994) and citetgoldin1995. AMO is a special case of data continuation in which the desired output data are common acquisition azimuth data. AMO is described for a constant-velocity model (Biondi *et al.*, 1998) as a transformation of data acquired at a particular offset and acquisition azimuth into (an approximation of) the data that would have been recorded at another offset and acquisition azimuth. Similarly, DMO is a special case of AMO, in which the output offset is simply set to zero, giving normal-incidence, zero-offset data as the output. DMO theory has been developed in constant-velocity media and vertically varying velocity models [see Hale (1991) for an overview]. We will show examples of DMO and more general continuation to illustrate our theory.

In our approach to data continuation, we compose a modeling and imaging/migration operator to construct an operator that computes the desired output data from the available input data. (In a constant velocity model, our continuation operator can be thought of as a solution to the partial differential equation used by Goldin (1994) and Goldin & Fomel (1995).) This approach has been developed in the absence of caustics (e.g., constant-velocity and constant-velocity-gradient media) by Bleistein & Jaramillo (2000), Canning & Gardner (1996) and Stolt (2002). Other related approaches can be found in Hubral *et al.* (1996), Santos *et al.* (1997), and Tygel *et al.* (1998). Our theory extends these results by allowing for both lateral variations in the velocity model and caustics in the ray field. The occurrence of caustics is not uncommon in heterogeneous media (White *et al.*, 1988). Continuation plays the role of forward interpolation in the process of data regularization, as defined by Fomel (1995, 2003) and Stolt (2002), required for imaging-inversion.

To unfold the caustics, implicitly keeping track of the contributions from different branches of the caustic, we use the angle parameterization. In this parameterization the scattering angle, which is the angle between the source and receiver rays, takes the place of offset in the traditional parameterization and the dip angle takes the place of the midpoint. In the absence of caustics a single mapping exists between the traditional parameterization and the angle parameterization. In the presence of caustics a family of maps is required because the caustics do not unfold in the single map traditionally used. This is explained further by de Hoop & Brandsberg-Dahl (2000).

Data continuation is not a stand-alone process but rather exists within a larger framework. Imaging-inversion, migration-velocity-analysis and 'offset' continuation are closely dependent on one another; the operators that connect the three processes are the *annihilators* of the seismic data (Stolk & de Hoop, 2002; Brandsberg-Dahl *et al.*, 2003b).

We first give an outline of how the continuation operators are constructed and then show three examples: DMO, AMO and offset continuation in shot records. To illustrate the properties of the first two operators we compute their impulse responses in both a constant-velocity model and a gas lens model. For the offset continuation section, we demonstrate the applicability of our theory by filling in missing offsets in synthetic shot records. We include three appendices with derivations of certain parts of this theory in constant-velocity media. Appendix A contains the derivation of the impulse responses in closed form. In Appendix B we derive an expression for the amplitudes of the data continuation operator. This result could also be applied in varying velocity models by using the root-mean-square velocity as a local approximation to the true velocity. In Appendix C we show that if the input and output data configurations are the same, the operator does not change the positions of reflections in the data.

3.3 Imaging-Modeling-Restriction

Data continuation is developed from the composition of three processes: imaging/migration, modeling, and restriction. By *composition* we mean applying one operator after another and simplifying the result, by integrating over intermediate phase variables, into a single operator. The continuation process is a single operation that computes data for the desired acquisition geometry from the original data. This is similar to the derivation of AMO (Biondi *et al.*, 1998), in which the observed data are first migrated to form an image of the subsurface (imaging), from which data with another acquisition geometry are modeled (modeling). The output data are assumed to have a certain acquisition azimuth, which is accomplished with the use of a *restriction operator*.

Composing the operators, given the acquisition surface, requires that we impose certain conditions on the velocity model (e.g., removing *grazing caustics*, caustics that are both at and parallel to the acquisition surface). In our scheme, the first operator, the imaging operator, is a Generalized Radon Transform [GRT; Miller *et al.* (1987) and de Hoop & Brandsberg-Dahl (2000)]. The second operator models the data for all possible (continuous) source and receiver positions at the surface, using an image of the subsurface as input. The final operator restricts this modeling operator so that only the desired output data are modeled, rather than the complete data set. Composing the three operators yields a single operator that computes the desired output data directly from the input data. This composition is done in Appendix B, for a general continuation operator, in a constant-velocity (or mildly depth varying) model. All three operators are Fourier integral operators (FIO)[2].

[2]Fourier integral operators, which generalize Fourier integrals, can be used to solve wave equations. These operators are characterized by an amplitude and a phase, but the phase is not necessarily linear in the space variables as it is in Fourier transforms. Stationary phase analysis yields a leading-order asymptotic

Enforcing so-called *transversal composition* of these FIOs results in an FIO for the composite continuation operator (de Hoop *et al.*, 2003a). Such transversal composition may be obtained by imposing conditions (known as the Bolker conditions) on the velocity model, which exclude phenomena such as horizontal wave guiding, and encompass the traveltime injectivity condition of ten Kroode *et al.* (1998). Subject to the Bolker conditions, we can carry out continuation of the reflections without introducing false reflections. The theory of FIOs (Treves, 1980b,a; Duistermaat, 1996; Hörmander, 1985b,a) involves *symplectic geometry* (the geometry of phase space), which is exploited to give the proper geometrical tools to assess these conditions.

Our framework is a generalization of that of DMO, such as in Hale (1991). In fact, in a homogeneous medium the FIOs of this analysis reduce to the Fourier transforms used by Hale to derive DMO. If, however, the velocity model deviates from the constant or constant-gradient cases, several changes in the theory become necessary. In such media, angle parameterization, as opposed to offset parameterization, is preferred, since it allows the unraveling of caustics. Angle parameterization, discussed in de Hoop *et al.* (1999), uses the scattering point, scattering angle, and (in three dimensions) scattering azimuth. Thus, for DMO we replace acquisition offset and acquisition azimuth by scattering angle and scattering azimuth. In two dimensions offset is replaced by scattering angle. This is done because the scattering angle can be used to uniquely specify a pair of rays, given the subsurface point and migration dip (direction normal to the reflector), whereas offset along with the same subsurface parameters does not uniquely determine a pair of rays. Likewise we redefine AMO as a transformation from one acquisition azimuth and subsurface scattering angle to a new acquisition azimuth and new subsurface scattering angle.

To relate this parameterization to the acquisition coordinates, we split the traveltime function into branches, each branch being single-valued, where all branches taken together give the complete set of traveltimes. The suppression of artifacts, or false reflections, in the presence of caustics requires the integration (or stacking) over *neighborhoods* of the scattering angle and scattering azimuth in the input data. By using a neighborhood we are able to discriminate between true features and artifacts through use of multiple samplings of the same subsurface point. Although the data will sample the same subsurface point more than once, the data are not simply redundant; multiple samples, with different scattering angles, are required to suppress artifacts in the final image. In classical DMO, offset, which is used for parameterization, is held constant. In complex media such a parameterization is not only inadequate, it also does not allow a straightforward discrimination between events and artifacts. For examples of procedures to suppress artifacts in imaging, see Brandsberg-Dahl *et al.* (2003a). Artifacts are classified in Stolk (2001).

In order to reduce the amount of numerical computation required, as many phase variables as possible should be integrated out (this is done, for a constant-velocity medium, in Appendix B). In general, at least one phase variable (frequency) will always remain in

contribution of FIOs. For the imaging operator, this yields the rays from the sources to the scattering points and from the receivers to the scattering points. Thus FIOs provide the geometrical insights for scattering and inverse scattering theory.

the final operator. In some cases, for example 3D DMO in constant media (Bleistein *et al.*, 2000, p. 326), additional phase variables must remain in the final operator, as explained in Appendix A of de Hoop *et al.* (2003a).

3.4 DMO

For DMO, finite-offset data are used in the imaging step, after which (normal-incidence) zero-offset data are modeled. When the zero-offset modeling is done by restricting a multiple-offset modeling operator to zero-offset, data from non-normal incidence data will also be modeled. We construct an exploding-reflector (Loewenthal *et al.*, 1976; Claerbout, 1985) modeling operator and use it in place of the restricted modeling operator. The exploding-reflector modeling operator models only a single ray from the scattering point, to the surface point. (From this point onward we will refer to this, single, ray as the zero-offset ray and the associated data as zero-offset data.) This means that for DMO the composition of three operators (imaging, modeling, and restriction) is reduced to a composition of only two (imaging and exploding-reflector modeling).

Using the exploding-reflector modeling operator rather than the full zero-offset modeling operator results in a different amplitude for the final transformation to zero-offset (TZO). A partial explanation for this is that the exploding-reflector operator models the data along a single ray as if the wave speed of the medium were half its true value, while the zero-offset modeling operator models two rays (up- and down-going) in the true medium, with coincident surface and subsurface positions. The amplitude of the exploding-reflector modeling operator differs from that of the restricted multiple-offset modeling operator (RMO); the RMO models a ray that travels from the surface to the subsurface applying geometrical spreading, followed by modeling a ray from the subsurface to the surface applying geometrical spreading once again (thus resulting in the geometrical spreading squared). In contrast, the exploding-reflector modeling operator considers the geometrical spreading for just one ray with half the wave speed along the path.

3.4.1 Homogeneous model

For any operator, we can construct a table relating the input parameters to the output parameters. In migration, for example, this table would relate a point in the subsurface (the output of migration) to the source position, receiver position and two-way travel time (the input to migration). The table can be parameterized in different ways. For example, midpoint and offset, or source position and scattering angle can be used in place of the source and receiver positions. Fixing different sets of these parameters allows us to plot cross-sections of this table. (We use the term cross-section in analogy with the cross-sections of a function; a cross-section of a function of two variables is the function values as a function of one variable with the other variable held fixed.) As a first example, we plot the standard migration ellipse in Figure 3.1; in this case the midpoint, offset and traveltime are fixed giving us a particular cross-section of the table. Similarly we can fix the source point,s, scattering angle, θ, and traveltime giving what we will call an *angle isochron*. An example

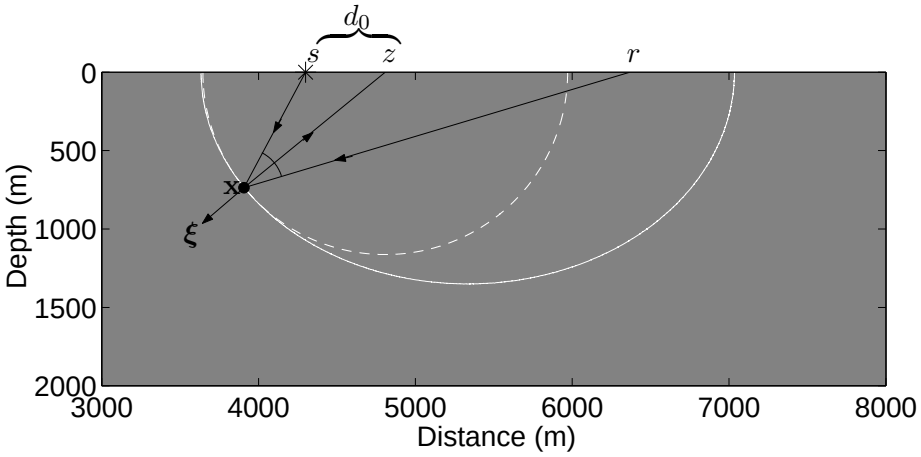

Figure 3.1. Offset DMO in a constant-velocity medium ($v = 1.7$ km/s). The solid curve is a finite-offset isochron (fixed midpoint, offset, and traveltime $t_r + t_s$); the dashed curve is an exploding-reflector isochron (fixed zero-offset surface point z and time t_0); the black lines are the rays; and the dot shows the location of the scattering point, which is the same as that marked by a dot in Figure 3.2. DMO maps from the finite-offset isochron to the exploding-reflector isochron keeping the scattering point and the direction (migration dip), $\boldsymbol{\xi}$, fixed.

of an angle isochron is shown in Figure 3.2. In this construction, the receiver position, and thus the midpoint and offset are variable. By fixing one variable at the surface, s, and another at depth, θ, we look at a different level set of the table; not surprisingly an angle isochron has a different shape than a traditional isochron. Neither of these isochrons illustrates the DMO operator; rather, they show the shape of the migration or imaging operator for the particular velocity model.

The dependence of the shape of the angle isochrons on the scattering angle, θ, is shown in Figure 3.3. The source position and traveltime are the same for each angle isochron. All of the angle isochrons, with the exception of the exploding-reflector isochron ($\theta = 0$, black line), have two points in common: the source point, s, and the rightmost surface point, a. All isochrons reach the point a since this corresponds to a ray that travels horizontally for nearly all of its path before scattering to the surface. Similarly, each angle isochron starts at the source point as this corresponds to a ray that scatters immediately and then travels for all the allowed time horizontally near the surface of the model. While the angle isochrons will approach the exploding-reflector isochron as the scattering angle approaches 0, the angle isochrons will always reach the points s and a whereas the exploding-reflector isochron will not. This highlights a difference between full zero-offset modeling, which can be approximated by the very small scattering angles, and exploding reflector modeling, which uses a single ray.

In Figure 3.3 we show sections of the table for different values of the scattering angle.

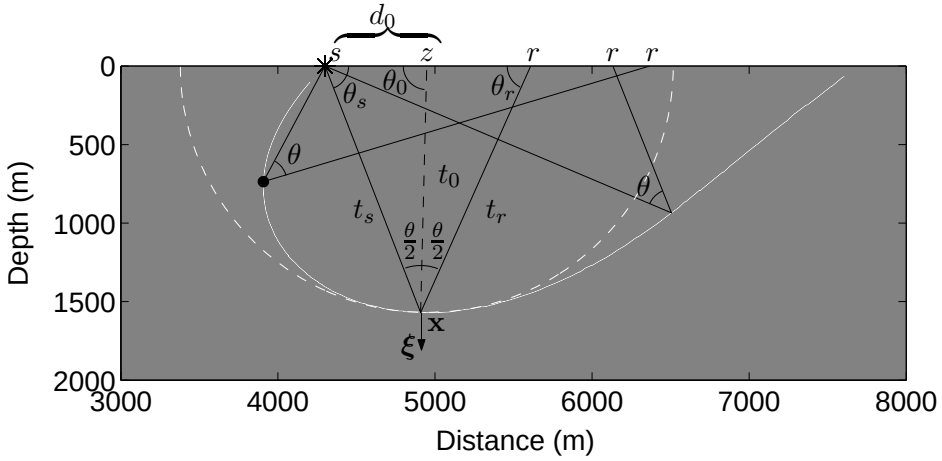

Figure 3.2. Angle DMO, in a constant-velocity medium ($v = 1.7$ km/s). The black lines are rays; the dashed white line is the exploding-reflector isochron; the solid white line is the angle isochron. The black dot is the scattering point from Figure 3.1; this point will have a different contribution to the operator illustrated in this figure than it does to the operator illustrated in Figure 3.1. The angle θ_0, between the zero-offset ray and the surface is variable; it depends on the particular value of the scattering angle. This illustration shows θ_0 close to 90°, which is not generally the case. The notation shown in this figure is used throughout the text and in Appendix A, where the impulse response is computed.

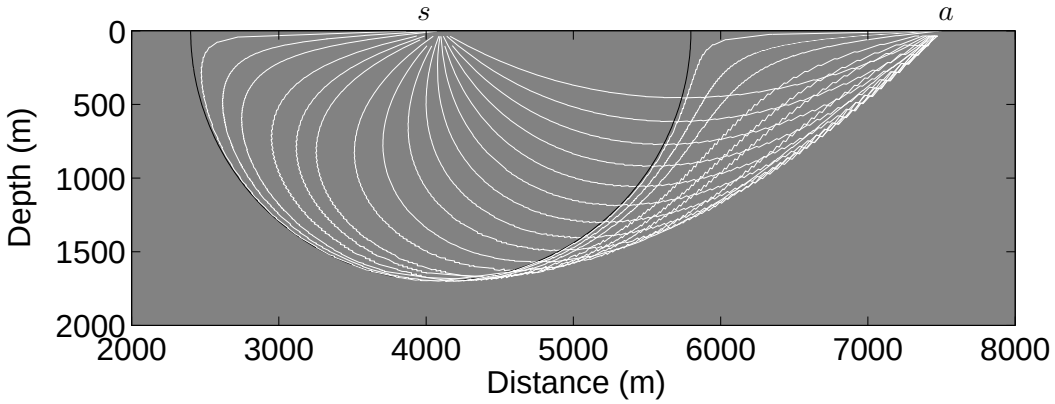

Figure 3.3. Angle isochrons in a constant-velocity medium ($v = 1.7$ km/s), for various scattering angles. All other parameters are the same as in Figure 3.2. The smaller the scattering angle, the deeper the isochron penetrates into the model. The angle isochron for the smallest scattering angle shown, 2.86°, is the closest to the exploding-reflector isochron (black circle), and the angle isochron for the largest scattering angle, 148.97°, is the shallowest line. This plot shows several cross-sections of the migration table described in the text.

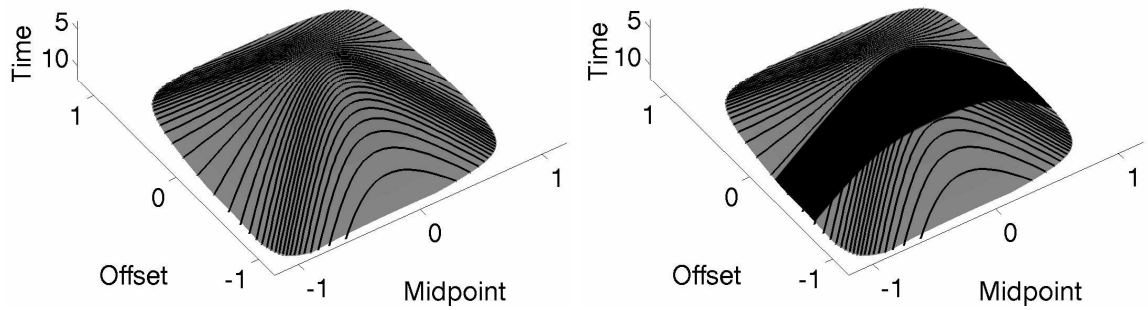

Figure 3.4. Cheops pyramid. The lines represent curves of constant scattering angle. The blacked out region illustrates the removal of some offsets, which will be filled in by the continuation procedure. While Figure 3.3 shows several migration surfaces with fixed source, scattering angle and travel time, this plot shows several data surfaces with fixed depth point $\mathbf{x}$ and scattering angle.

Fomel & Prucha (1999) compute the *Cheops pyramid* in both the offset and angle domains. This is equivalent to fixing $\mathbf{x}$, the subsurface point, in the migration table and then plotting midpoint, offset and traveltime. This pyramid and the common-angle diffraction curves are shown in Figure 3.4. The data continuation discussed involves filling in portions of the pyramid that are missing using the parts that remain. See Fowler (1998) and Sava & Fomel (2003) for more details on the pyramids.

Traditionally, the impulse response of the DMO operator is computed for any midpoint by using common-offset data containing a single Dirac-like impulse as input to the DMO algorithm. This is equivalent to computing from fixed offset, source position (or equivalently midpoint), and traveltime the zero-offset traveltime, as a function of the distance from the source position to the zero-offset source/receiver position (d_0 in Figure 3.1)[3]. Figure 3.1 shows the traditional DMO construction. For the initial source location, offset, and traveltime, we compute an isochron (solid white line). From this isochron, the scattering point $\mathbf{x}$ and migration dip $\boldsymbol{\xi}$ are used to shoot a zero-offset ray. This ray is normal to the exploding-reflector isochron (dashed line), which is a circle centered on the point z. Thus, DMO maps data points from a finite-offset isochron to the exploding-reflector isochron matching the scattering point and migration dip.

[3]Traditionally the DMO operator is plotted as zero-offset traveltime versus the distance between z and the midpoint. We have chosen to use d_0 instead as the source point is fixed in the angle parameterization while the midpoint is not.

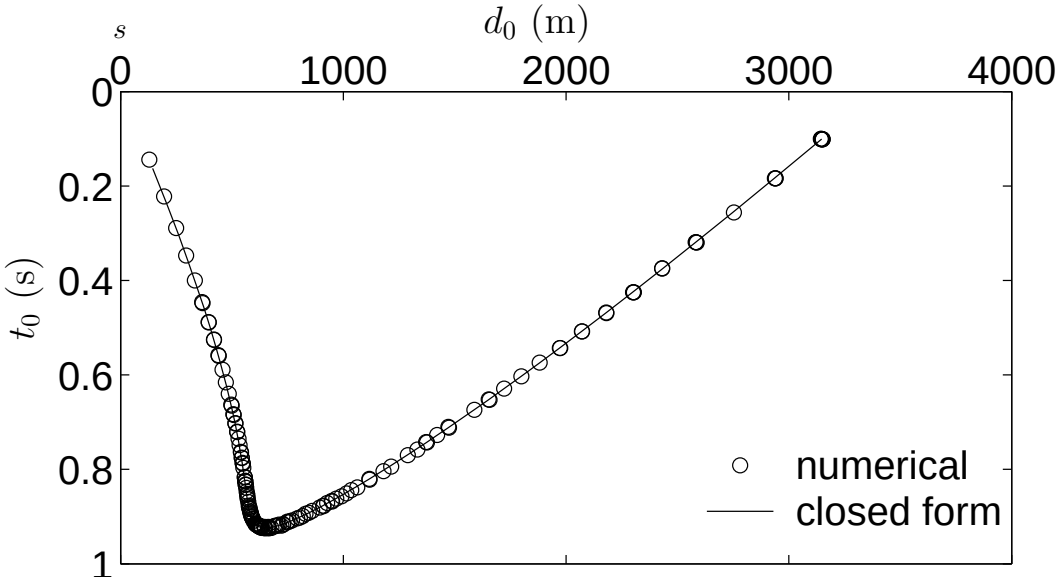

Figure 3.5. DMO impulse response for a constant-velocity medium, for scattering angle 45°, velocity 1.7 km/s, $T = 2$ s. The spacing of the points is constant in take-off angle at the source ray (increments of 5.73°). Areas of the impulse response with denser sampling, which are regions of high curvature, can be expected to have relatively high associated amplitude.

To compute the impulse response in the angle domain (using the notation of Figure 3.2), we fix the scattering angle θ, the source position s, and the traveltime $T = t_s + t_r$, and compute the one-way zero-offset traveltime t_0 as a function of the distance, d_0, from the source position s to the zero-offset source/receiver position z. In a constant-velocity medium, this impulse response can be computed in closed form. This is done in Appendix A. Figure 3.5 shows the impulse response for angle DMO, as derived in Appendix A. This impulse response is the zero-offset traveltime as a function of the distance from the source position to the zero-offset position (the distance d_0 in Figure 3.2). The solid line is the closed-form solution, and the points are computed numerically with ray tracing; the spacing between the points is constant (increment 5.73°) in the take-off angle θ_s (defined in Figure 3.2).

3.4.2 Gas-lens model

The gas-lens model consists of a vertical velocity gradient (0.45 s^{-1}) beginning at 1600 m/s, with a low-velocity circular lens with Gaussian parameter variations (maximum velocity contrast 800 m/s) located at lateral position 4600 m, and depth 600 m, with a diameter (Gaussian standard deviation) of 600 m. This model, introduced by Brandsberg-Dahl *et al.* (2003a), is based on a feature in the BP Valhall field. Throughout this subsection, we compare results for this model with those of a constant-velocity-gradient model (the same as the lens model but without the lens). The background shading of Figures 3.6 and 3.7 depicts the velocity model, with darker shading indicating higher velocity.

In Figure 3.6, we show the relationship between the shape of the angle isochron in the lens model (solid line) and that in the constant-gradient model (dashed line). The

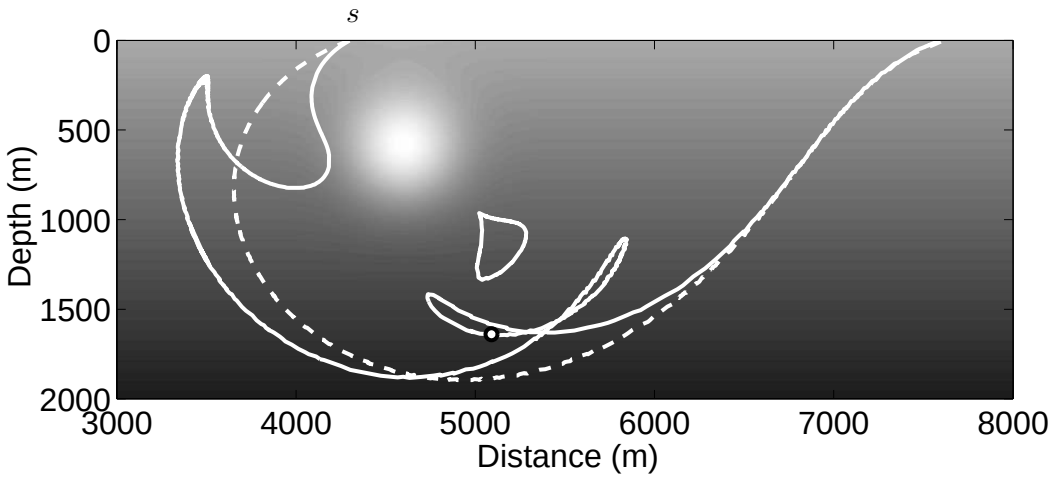

Figure 3.6. Angle isochron in the lens model; scattering angle 45°, $T = 2$ s, source at 4300 m. The solid line uses the lens model, and the dashed line the constant-gradient model without the lens. The background shading portrays the velocity function for the lens model, with darker shading denoting higher velocity.

introduction of the lens adds complicated structures to the isochron not present in the constant-gradient response, but the gross shape of the main branch remains similar. Figure 3.7 illustrates the origin of these features by showing the fixed-scattering-angle rays that build various portions of the isochron. Even this simple velocity variation introduces large complications in these angle isochrons, caused by the complicated geometry of the ray field in the vicinity of the lens.

If traditional DMO were performed on data from this model using the incorrect assumption of a constant velocity gradient, the results could contain significant errors. One source of these errors is that the computed zero-offset time would be calculated for zero-offset rays originating on the dashed curve rather than the more complicated solid one in Figure 3.6. It is possible to create an operator that corrects such an error. By composing inverse DMO in the constant-gradient medium with DMO in the more complicated lens model, an operator can be constructed to re-apply DMO with a more accurate velocity model (e.g., for velocity analysis). The idea of residual DMO was developed by Alkhalifah & de Hoop (2004) in homogeneous anisotropic media. The composed operator is more efficient to apply than inverse DMO in the wrong model followed by DMO in the correct model.

In order to suppress artifacts inherent in the Generalized Radon Transform in the presence of caustics (Brandsberg-Dahl *et al.*, 2003a), it is necessary to stack over a range of scattering angles. To illustrate the cancellation of these artifacts, we plot the impulse response in the lens model for three different scattering angles (40°, 45°, and 50°) in Figure 3.8. For these three scattering angles, the gross structure present in the constant-gradient case

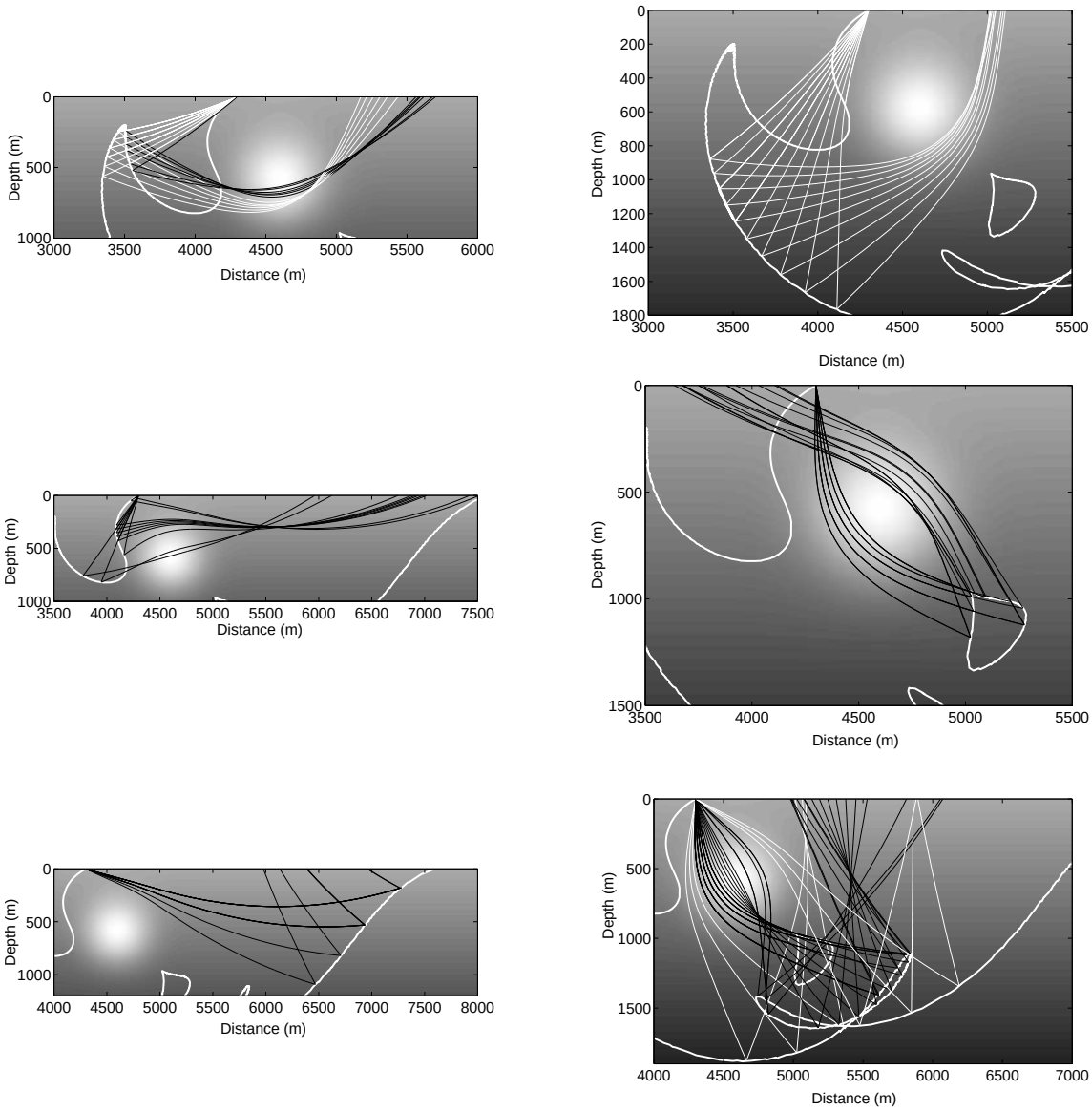

Figure 3.7. Raypaths in the lens model for scattering angle fixed at 45°. This figure illustrates the origin of the complicated structure of the angle isochron by showing the rays that were used to compute it. Where both white and black rays are present, white rays come from the main branch while black rays come from inner (closer to lens) branches. Each panel shows a different region of the same angle isochron.

(dashed line) remains essentially unchanged at the three different angles, while the more complicated structures change more rapidly. Small changes in the scattering angle result in differences in the maximum t_0 and d_0 as well as detailed changes in the small loop structure located at $t_0 \approx 1$ s, $d_0 \approx -700$ m. Because of this, stacking over angle will result in a smaller contribution both at large times and in the loop structure than from regions in which the impulse response does not change.

The composition of the imaging operator with the exploding-reflector modeling operator can be illustrated by again matching the migration dip and scattering point on a finite-offset isochron with those on a conventional exploding-reflector isochron. The counterpart of Figure 3.1 in the presence of a lens is shown in Figure 3.9. For lateral heterogeneity, the shape of the isochron is evaluated for a particular midpoint-offset pair and will change with midpoint, unlike its behavior for a laterally homogeneous medium.

In the lens model (Figure 3.9), the finite-offset isochron exhibits two regions of multipathing, indicated by the triplications in the isochron. The exploding-reflector isochron, which is a snapshot of the wavefront as it passes through the lens, exhibits only a single region of multipathing. The contribution to the DMO operator comes from the points where the two isochrons meet tangentially. The associated rays are the same as those that meet at the point marked with a circle on the angle isochron of Figure 3.6.

3.5 Data Continuation and AMO

In this more general case, we compose the generalized Radon transform (GRT), as the imaging operator, with high-frequency single-scattering modeling and a restriction operator specific to the application. It is this restriction operator that determines the form of the output data. Although the theory applies more generally, the main ideas may be understood based on the calculations in a constant-velocity model given in Appendix B, which also includes a computation of the amplitudes.

When attempting to fill in missing data, it is important that the computed data agree well with the true data. Therefore, the continuation operator must leave the data unchanged if the input and output source-receiver positions are the same. We illustrate that this is the case in Appendix C, by showing that the application of a modeling operator after an imaging operator (for the common-offset case) results in a so-called *pseudodifferential operator*, a partial definition of which is a forward and inverse Fourier transform with an additional multiplication in the Fourier domain.

Data continuation applies in both 2D and 3D. From the 3D case, a transition from 3D to 2.5D is possible, although the 2D case does not follow directly from the 3D theory. The methodology for the transformation to 2.5D in terms of FIOs is discussed in Foss *et al.* (2003).

3.5.1 Homogeneous model

Biondi *et al.* (1998) construct AMO as a mapping of data collected at a given offset and acquisition azimuth to data that would have been collected at a different offset and

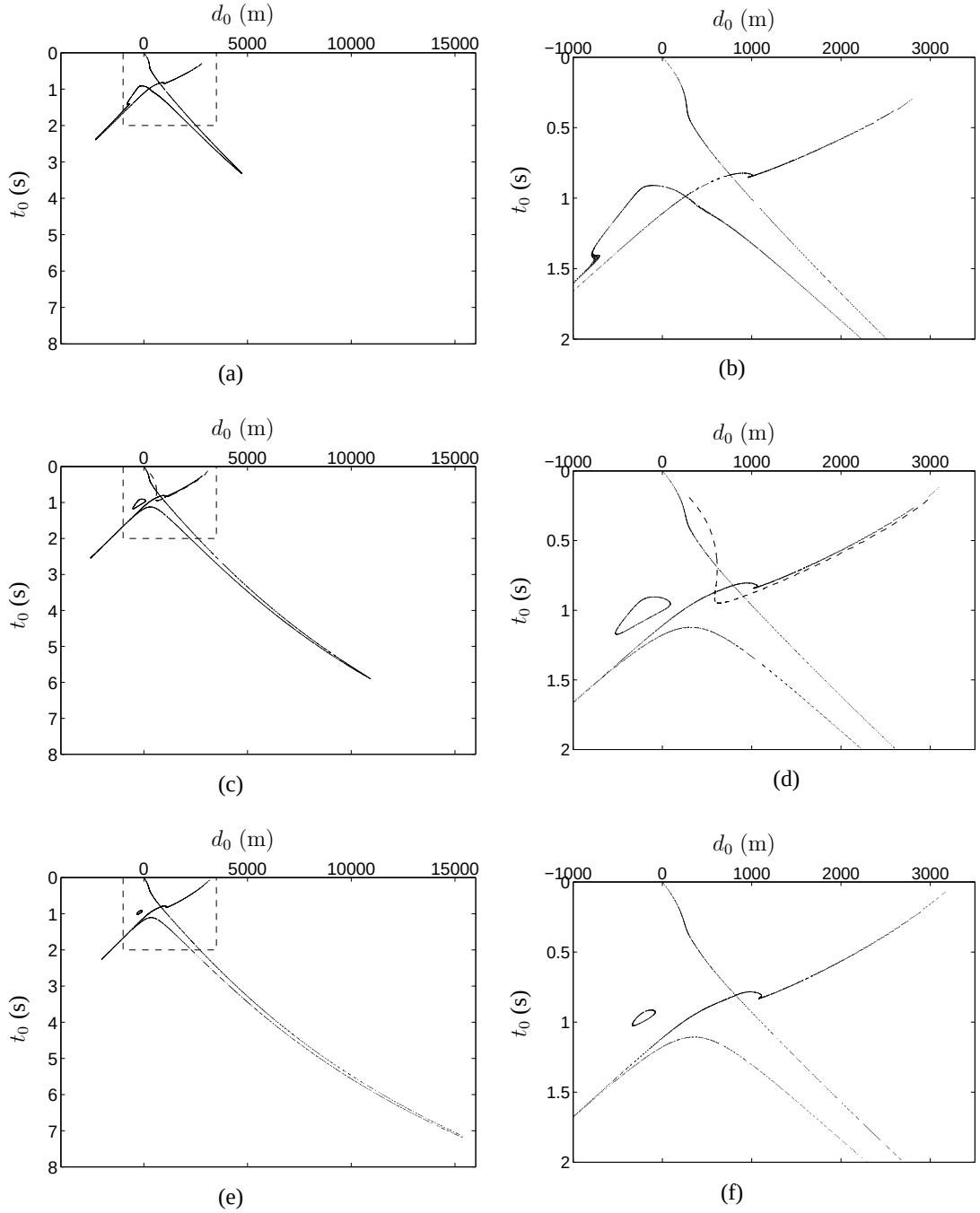

Figure 3.8. Angle DMO impulse responses for the lens model for scattering angles of 40° (a and b), 45° (c and d), and 50° (e and f). The dashed box in a, c, and e outlines the region shown in b, d, and f. The dashed curves in c and d are the impulse responses computed in the constant vertical velocity gradient that makes up the background of the lens model.

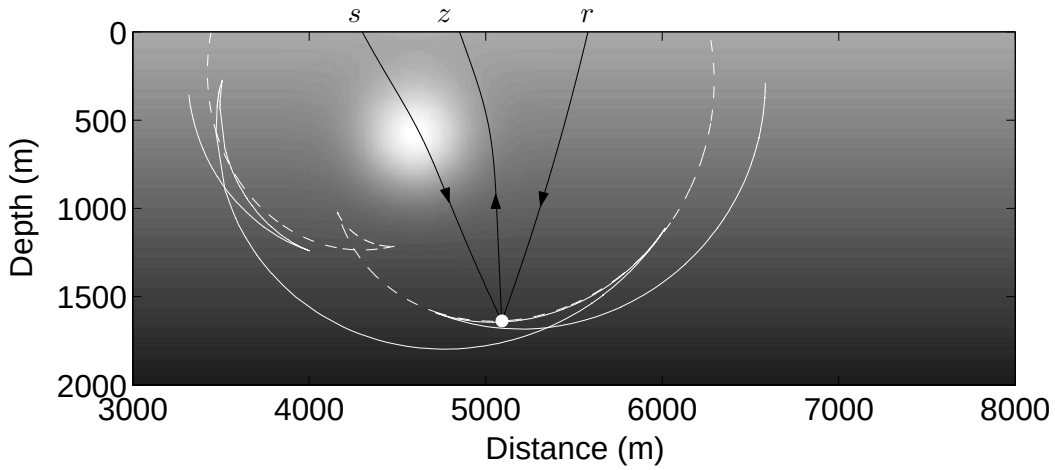

Figure 3.9. Fixed-offset isochrons in the lens model. The solid white line is the finite-offset isochron, and the dashed line is the exploding-reflector isochron; s, r, and z are the source position, receiver position, and the surface point for the zero-offset ray, respectively. Compare this figure with Figure 3.1, which shows the isochrons in the constant-velocity medium.

acquisition azimuth. We construct AMO as a mapping from an input scattering angle and scattering azimuth to an output surface line (acquisition azimuth) and scattering angle.

We compute the angle isochrons, as well as our impulse response, in 3D. In Biondi *et al.* (1998), the impulse response is the output traveltime as a function of the change in midpoint between the input and output data. For our method the impulse response is again the output traveltime but now as a function of the initial direction of the source ray, given in terms of the spherical angles ψ (angle clockwise from x_1) and and φ (angle measured downward from the $x_3 = 0$ plane). The angle isochron, an extension to 3D of the 2D angle isochron (Figure 3.2), is shown in Figure 3.10. The AMO operator takes the initial source and receiver rays and rotates the plane in which they are contained about the zero-offset ray to the desired output direction. The output rays are then computed in this new direction, with a defined scattering angle, keeping the zero-offset ray fixed. Figure 3.11 shows the surface of the impulse response. A closed form expression for this surface is derived in Appendix B of de Hoop *et al.* (2003a).

Gas lens model

To illustrate the complications that arise in a laterally heterogeneous model, we compute the isochron and AMO impulse response for a model containing a low-velocity lens, as was done for the constant-velocity model. The model used is similar to that used in the 2D case; it is scaled down in size due to computation cost. The model consists of a

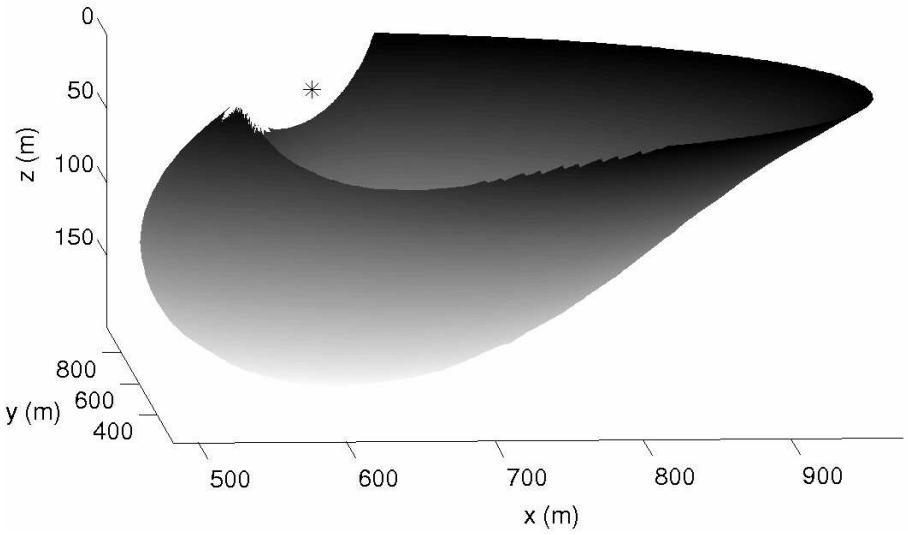

Figure 3.10. 3D angle isochron in a constant-velocity medium, the asterisk indicates the position of the source. This extends to three dimensions the angle isochron shown in 2D in Figure 3.2.

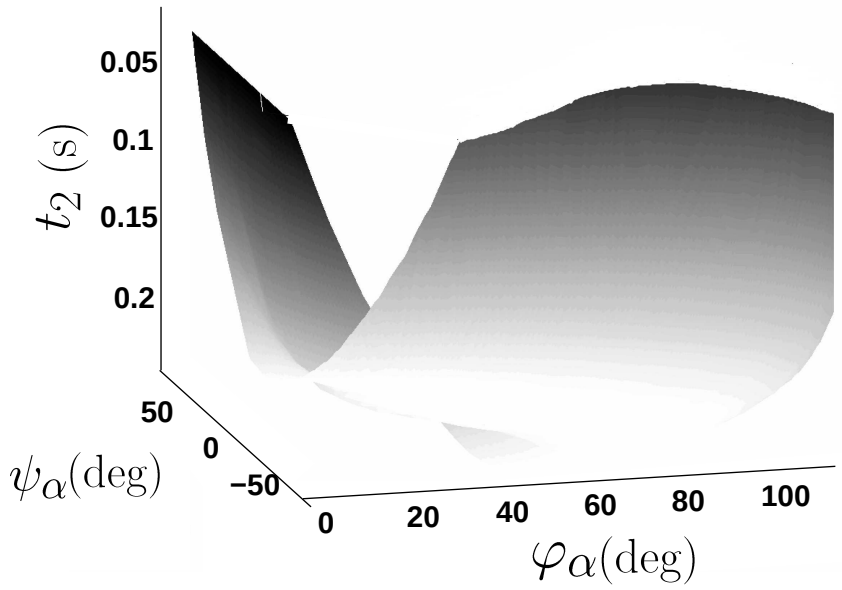

Figure 3.11. AMO impulse response as a function of input ray direction. This is the extension of Figure 3.5 for DMO (2D), to AMO (3D). The angles ϕ_α and ψ_α are the spherical angles, giving the direction of the initial source ray. Cross-sections of this figure at constant ϕ_α give the DMO impulse response.

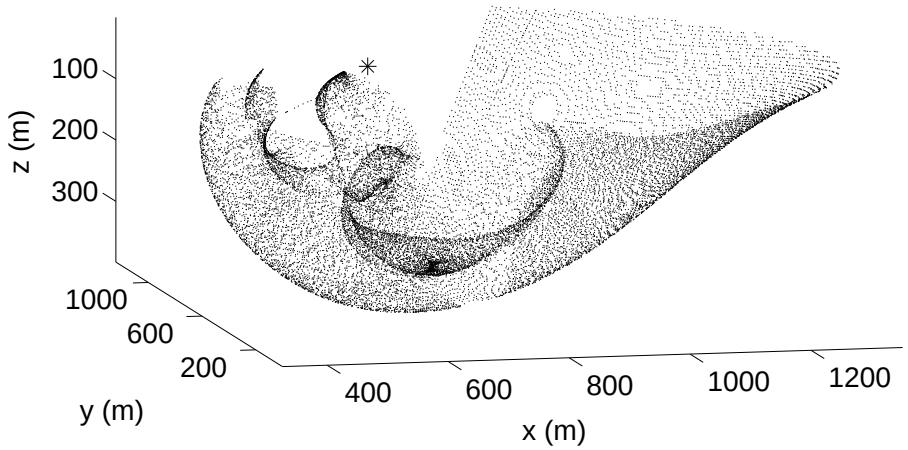

Figure 3.12. Angle isochron in the lens model, for source position indicated by the asterisk. This is an extension to 3D of the angle isochron shown in Figure 3.6.

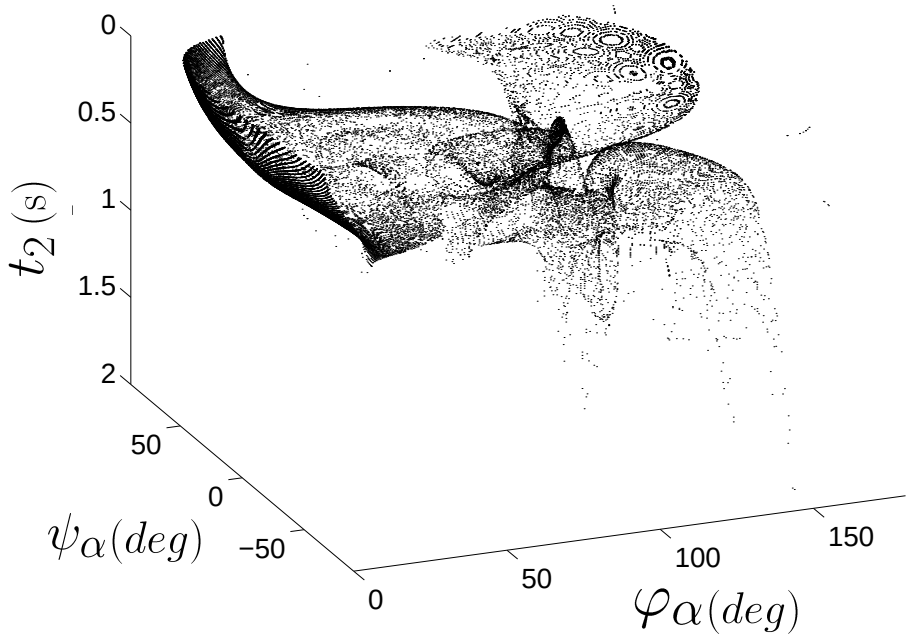

Figure 3.13. AMO impulse response for the lens model. Compared with the impulse response for DMO (2D case) in Figure 3.8, the 3D nature of AMO introduces further complications in this impulse response.

spherical lens with Gaussian parameter variations of 100 m diameter (standard deviation of Gaussian) with center at $x_1 = 600$ m, $x_2 = 600$ m, $x_3 = 100$ m and a maximum velocity contrast of 800 m/s. The model extends to $x_1 = 2400$ m, $x_2 = 2400$ m, $x_3 = 800$ m with an initial velocity of 1600 m/s and a vertical gradient of 0.45 s^{-1}.

The angle isochron, shown in Figure 3.12, exhibits a gross shape similar to that in the constant-velocity case (Figure 3.10). Just as with the 2D angle isochron (Figure 3.6), the 3D version has a complicated shape, in which we recognize the presence of caustics. Figure 3.13 shows the AMO impulse response, which bears little resemblance to that for the constant-velocity model (Figure 3.11). The complications in the AMO impulse response and angle isochrons for the lens model are significantly greater for the 3D problem than for the 2D one.

3.6 Synthetic Data Example

We show an example of data continuation. The example uses the same 2D lens model used for the DMO impulse response calculations, with the addition of a reflector from

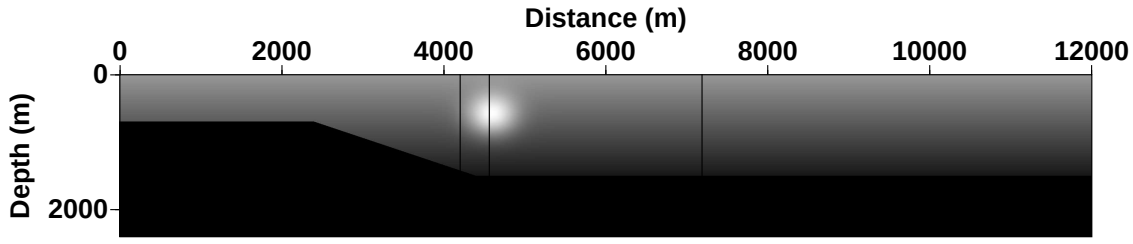

Figure 3.14. Velocity model for synthetic data set. This model is the same as that used for the 2D DMO examples with the addition of the reflector. The vertical lines indicate the location of the shot points for which shot records are shown in Figure 3.15.

which synthetic reflection data are computed. The model is shown in Figure 3.14, and further details on its properties can be found in (Brandsberg-Dahl *et al.*, 2003a).

The goal of this example is to reconstruct data that are missing from the original acquisition. To demonstrate this, we have removed all traces with offsets between 0 and 500 m from the synthetic reflection data set described above. This is illustrated in Figure 3.4 in which we have deleted a set of offsets from the pyramid. The algorithm works in the angle domain but reconstructs missing offsets.

We then use equation (E.27), for general continuation to fill in the data that has been removed. Although the theory is developed in the common-shot domain, the algorithm accesses the traces at random. The 2D algorithm is as follows:

```
for each subsurface point x
    for each migration dip direction ξ/‖ξ‖
        for each input scattering angle θ_i
            shoot scattering rays to surface
            if the rays reach surface within the data range
                get data sample at this position
                for each output scattering angle θ_o
                    shoot scattering rays to surface
                    if these rays are in missing data range
                        add contribution to this point in missing data
```

Although this algorithm works, it is far from the most efficient one possible. For example, we shoot many of the rays more than once, repeating for the output data computations already done for the input data. An example of a more efficient way to do the computations

is based on the escape equations developed by Sethian (2002).

Figure 3.15 shows the results of this procedure applied to the data in three synthetic shot records for the model in Figure 3.14. The top panels show a shot record reconstructed away from the influence of the lens. At this position the event is filled in correctly. Because the event is so simple at this point, interpolation would work just as well. The second panels down show the reconstruction of a shot record on the edge of the lens. Traces with events from both the dipping and flat portions of the reflector are missing, making the reconstruction more difficult. The reconstruction is reasonably successful although there are some amplitude errors. The next panel down shows a shot record for the shot right over the lens. We have removed the traces containing the caustic and are attempting to fill them in with the algorithm. Again the reconstruction is not perfect but it is considerably better than what would have been achieved using conventional interpolation schemes. The data shown have been bandpass filtered to match the frequency content of the original data. We expect some amplitude inaccuracies because the amplitudes are obtained from equation (E.27) which are for a constant velocity model, whereas this model is clearly more complicated. In these examples we have corrected for only the obliquity factor ($|\cos\theta_i|^2$).

The single shot record in Figure 3.16 shows the same computation as above it with a range of only 2° in scattering angle for the input data (compared with the section above it which uses all the available data). A particularly high amplitude artifact appears just below the latest true event in this section. This example can be generated much more quickly than the other images because so few input angles are used. The other panels most likely use more angles than necessary and so the optimal data quality and computational time trade-off is probably somewhere in between the two.

Finally, to mimic the DMO discussion above, we show in Figure 3.17 the exploding reflector data computed from the original data set (with offsets from -6 to 7 km) while removing offsets from -100 m to 100 m. The smallest offset data (offset of 6 m) from the true data set are shown for comparison. This illustrates the difference between zero-offset modeling and exploding reflector modeling.

3.7 Conclusions

We have described and illustrated a method for source-receiver continuation of seismic data in the presence of caustics. In the absence of caustics the method reduces to a form of offset continuation. The computational complexity of this method depends on the geologic complexity and varies in space as the geology changes. In the most complex situation a table must be constructed relating the subsurface and surface parameters, and a search performed in this table; the computational complexity depends on the algorithms used to perform these steps. Both DMO and AMO are examples of data continuation that can be obtained from the continuation framework presented here. It is possible to continue data only when the subsurface point and reflector orientation generating the data point are sampled in the original data set. Thus, the issue of illumination is directly related to data continuation. Similarly, data continuation provides a framework for estimating the smallest necessary data set, by using a combination of acquisition and data continuation

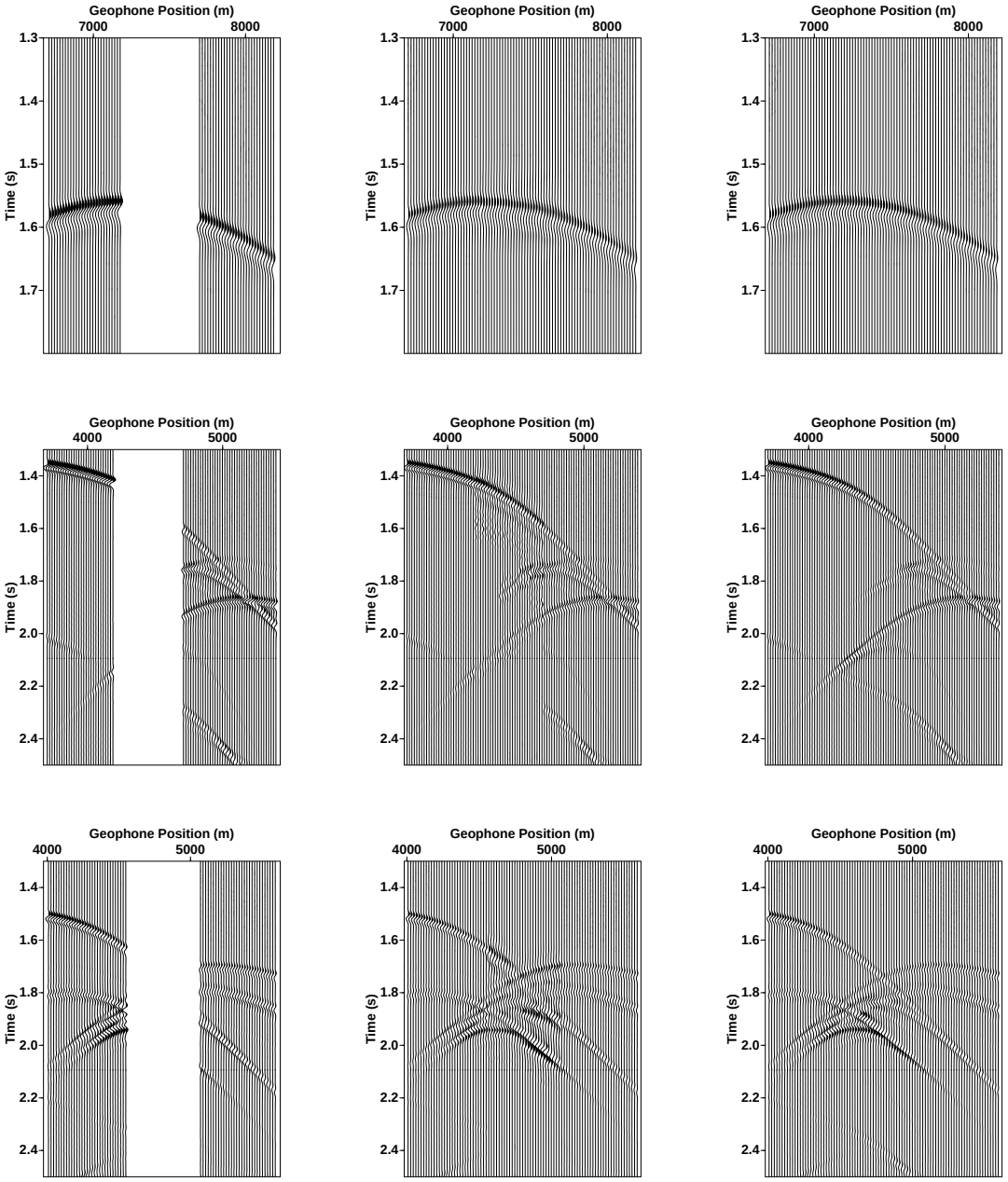

Figure 3.15. In each row of this figure a different shot record has a block of traces removed and then reconstructed. The left column shows the input data, the middle column is the reconstructed data and the right column is the actual full synthetic shot record. The position of the first shot record is at $s = 7188$ m, the second at $s = 4200$ m and the third is at $s = 4560$ m. These locations are denoted with vertical lines in the velocity model, Figure 3.14.

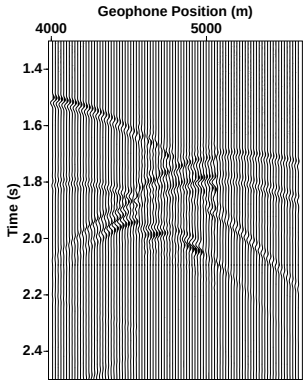

Figure 3.16. This extra section shown at the bottom illustrates the presence of artifacts when insufficient stacking is done over the input scattering angle. It is the shot record at $s = 4560$ m, with only a 2° range of input scattering angle.

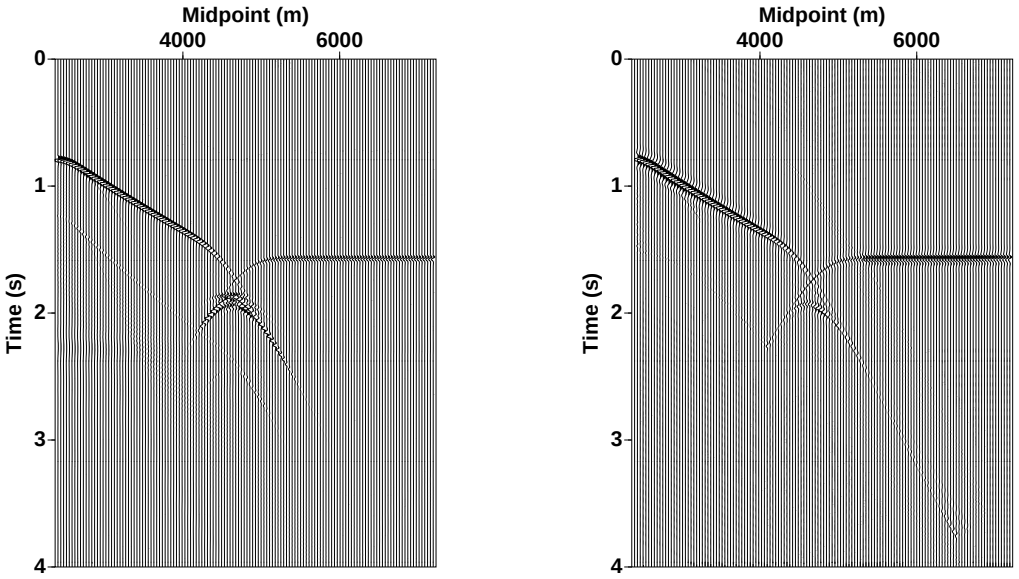

Figure 3.17. The left panel shows the smallest offset available in the synthetic data set (6 m offset). The right panel is the exploding reflector data computed from the portion of the synthetic data set with offsets between -100 m and 100 m removed.

to construct data needed for migration. The general theory of data continuation and the precise conditions when it applies are discussed by de Hoop (2004). An example of when a general data continuation theory is important is in reducing a multi-azimuth data set, with AMO, to a common azimuth data set for efficient migration through downward continuation.

3.8 Acknowledgments

We would like to thank Henri Calandra for his help in writing the first version of the continuation code. We are also grateful to Stig-Kyrre Foss and Sverre Brandsberg-Dahl who provided some of the subroutines in the continuation code used to generate the examples shown. We would also like to thank both Ken Larner and John W. Stockwell for their assistance in the preparation of this manuscript as well as Sergey Fomel and the four anonymous reviewers who all gave excellent suggestions for enhancing the relevance of the results presented in this paper. In particular, the equations in Appendix A for the symmetric impulse response were suggested by Sergey Fomel. This work was supported by the sponsors of the Consortium Project on Seismic Inverse Methods for Complex Structures at the Center for Wave Phenomena, by CRDF grant RG1-2362-NO-02, and by Total.

Chapter 4

A method for inverse scattering based on the generalized Bremmer coupling series[1]

4.1 Summary

Imaging with seismic data is typically done under the assumption of single scattering. Here we formulate a theory that includes multiply scattered waves in the imaging process. We develop both a forward and an inverse scattering series derived from the Lippmann-Schwinger equation and the Bremmer coupling series. We estimate leading-order internal multiples explicitly using the third term of the forward series. From the inverse series, two images are constructed, one formed with all the data, the other with the estimated leading-order internal multiples; the final image is formed from the difference of these two images. We combine the modeling of the leading-order internal multiples with the construction of the second image resulting in one two-part imaging step.

4.2 Introduction

A seismic experiment is typically modeled as a set of sources at the Earth's surface that generate waves that are reflected once from medium discontinuities in the subsurface and recorded at a set of receivers again located on the surface. The goal of this paper is to move beyond the single-reflection assumption to allow for multiply scattered waves. We consider only scalar waves and assume that the sources and receivers are on the same horizontal surface. A finite collection of scatterers with a separation large compared to the wavelength is also assumed, so that each reflection may be treated separately.

Fokkema & van den Berg (1993) developed a rigorous theory for the suppression of surface-related multiples. A surface-related multiple is a wave that has been reflected at least three times, with at least one reflection at the surface. Their analysis is derived from the reciprocity theorem in integral form and results in a Neumann series representation to predict surface-related multiples. If assumptions allowing the construction of data at zero-offset, such as those given by de Hoop *et al.* (2003a) are satisfied, then, in theory, Fokkema and van den Berg's theory solves the surface-related multiple attenuation problem. This

[1]This chapter has been accepted, along with Appendices J and K to Inverse Problems as:
Malcolm, A. E. and de Hoop, M. V. A method for inverse scattering based on the generalized Bremmer coupling series.

paper provides a theory for the suppression of leading-order internal multiples, which are waves that have been reflected three times with no reflections from the Earth's surface.

The work presented here is motivated by the series solutions to inverse scattering problems developed by Moses (1956), Prosser (1969), and Razavy (1975), as well as the Bremmer series approach to multiple attenuation discussed by Aminzadeh & Mendel (1981). Moses constructed a series to represent the quantum scattering potential in terms of measured reflection coefficients. Prosser discusses this methodology from the algorithm-construction viewpoint and touches on convergence issues. Razavy extends this work to recovering the velocity from the reflection coefficient via the scalar wave equation. These three papers use the Lippmann-Schwinger series (Lippmann, 1956), which is a pair of series for the forward and inverse scattering problem. This series representation has been used in exploration seismology by Weglein *et al.* (1997, 2003). The Bremmer series was introduced by Bremmer (1951) to solve the wave equation in a horizontally layered medium. The convergence of this one-dimensional series is discussed by Atkinson (1960) and Gray (1983). Aminzadeh used the Bremmer series to model the seismic wavefield (Aminzadeh & Mendel, 1980) and construct filters to attenuate surface-related multiples (Aminzadeh & Mendel, 1981), both in horizontally layered media. The Bremmer series was extended to two-dimensional problems by Corones (1975); the convergence of this series is discussed by McMaken (1986). de Hoop (1996) introduces a generalization of the Bremmer series to multi-dimensional laterally varying media. This generalization is a Neumann series for forward scattering, which motivates its use here.

From these two series, we develop a hybrid series that uses the directional decomposition (into up- and down-going constituents) of the Bremmer series along with the Lippmann-Schwinger medium decomposition into a known, smooth reference velocity model and unknown, singular perturbation or contrast. Using this hybrid series allows us to trace waves through their up and down scatters while still preserving the contrast-source formulation of the Lippmann-Schwinger construction.

We develop an explicit scheme for modeling and imaging with the triply scattered wave constituent that can be extended to higher-order scattering. This triple scattering scheme is naturally integrated in the downward continuation approach to inverse scattering in the Born approximation. This scheme requires knowledge of the velocity model only to the depth of the shallowest reflector involved in the triple scattering.

In reflection seismology, two distinct methods have been used to attenuate multiples to obtain an approximation of singly scattered data. The first predicts the triply scattered data and then subtracts it from the data set. The second filters out multiples, using filters designed to exploit the differences in moveout (change in arrival time with source-receiver separation) between primaries and multiples. The work discussed in this paper falls into the first category.

In the prediction approach, Kennett (1974, 1979b) used the Thomson-Haskell (Kennett, 1983) method in horizontally layered media to model synthetic seismograms containing both surface and internal multiples. In Kennett (1979a), he uses this theory to suppress surface-related multiples in plane-layered elastic media. There are several extensions of the surface-related multiple attenuation theory of Fokkema & van den Berg (1993) to internal

multiples (Fokkema *et al.*, 1994; Berkhout & Verschuur, 1997; Verschuur & Berkhout, 1997; van Borselen, 2002). In these methods, a particular layer is identified as the multiple generator (i.e. the layer where the second reflection occurs) and the surface-related multiple attenuation is adapted to be applied at that layer. Dragoset and Jeričević give a practical algorithm for attenuating surface-related multiples in (Dragoset & Jericević, 1998); an algorithm such as that discussed by Dragoset and Jeričević could be used for internal multiples in any of the mentioned extensions. Weglein and others (Weglein *et al.*, 1997) have used the Lippmann-Schwinger series to model and process seismic data, including the suppression of both surface-related and internal multiples, without knowledge of the velocity model. In ten Kroode (2002) the mathematical theory behind that approach is given in both one and two dimensions. He shows that internal multiples can be estimated without knowledge of the velocity model if the velocity model satisfies two conditions: ten Kroode's traveltime monotonicity assumption (this condition is described in Appendix K), and the condition that the wavefield contains no caustics. When the two assumptions of ten Kroode are satisfied, our method can be rewritten in a form consistent with the method of Weglein *et al.* (1997); this is discussed further in Appendix K. Jakubowicz (1998) proposes a method for modeling internal multiples by correlating one primary reflection with the convolution of two other primary reflections; his approach implicitly uses the Bremmer series and is similar to the work presented here under ten Kroode's traveltime monotonicity assumption. Kelamis *et al.* (2002) use an approach similar to that of Jakubowicz, in which the multiples are constructed from a combination of different data sets, both at the surface and in the subsurface. In any method that predicts internal multiples and subtracts them, an adaptive subtraction technique such as that suggested by Guitton & Verschuur (2004) must be used.

Aside from reflection seismology, there are other applications in which multiply scattered waves are important. In earthquake seismology, Burdick & Orcutt (1979) investigate the truncation of the generalized ray sum, from which they find earth models in which the inclusion of internal multiples becomes important. Revenaugh & Jordan (1987) observe both internal and surface-related multiples and use them to estimate the attenuation quality factor, Q, of the mantle. In (Revenaugh & Jordan, 1989, 1991), the same authors use multiples to investigate layering in the mantle. Bostock *et al.* (2001) use incident teleseismic P-waves scattered from a free surface and then subsurface structure before being recorded in an inversion scheme in which the teleseismic P-wave coda is used to invert for subsurface structure. For synthetic aperture radar (SAR) data, Cheney & Borden (2002) derive a theory to relate the singular structure (wavefront set) of the object to the singular structure of the multiply scattered data.

In the next section we describe the techniques of the directional decomposition used in the Bremmer series. In the third section, we describe some of the details of the construction of one-way Green functions. This is followed by a description of the contrast-source method used for the Lippmann-Schwinger series. In the fifth section, we construct the hybrid series. In the sixth section we use the hybrid series to model data, giving the first of our three main results in (4.84). The proof of this result is given in Appendix J. Following this, we summarize a method of constructing an inverse to the modeling operator. We then describe, through a series of results in Section 4.9, a method to estimate artifacts in the

image caused by leading-order internal multiples. Appendix K shows the correspondance between the theory described here and that of ten Kroode (2002) and Weglein *et al.* (1997) under certain assumptions.

4.3 Directional decomposition

In the Bremmer series formulation of scattering, the wavefield is split into up- and down-going constituents. This is done by separating the vertical, z, derivative from the horizontal, x, derivatives, and then writing the wave equation as a first-order system of partial differential equations in z. This system is then diagonalized completing the separation into up- and down-going constituents. We begin with the scalar acoustic wave equation

$$\left[-c(z,x)^{-2}D_t^2 + \sum_{j=1}^{n-1} D_{x_j}^2 - \partial_z^2\right] u = f, \tag{4.1}$$

where $x_1, \ldots, x_{n-1}$ denote the horizontal coordinates and $D_{x_j} \equiv -\mathrm{i}\partial_{x_j}$, $D_t \equiv -\mathrm{i}\partial_t$; $c(z,x)$ is the isotropic velocity function, and f is a source density of injection rate. This theory does not allow for attenuation in the medium. We first write the wave equation as a first-order system of equations,

$$\partial_z \begin{pmatrix} u \\ \partial_z u \end{pmatrix} = \begin{pmatrix} 0 & 1 \\ -A(z,x,D_x,D_t) & 0 \end{pmatrix} \begin{pmatrix} u \\ \partial_z u \end{pmatrix} + \begin{pmatrix} 0 \\ -f \end{pmatrix}, \tag{4.2}$$

where A is the transverse Helmholtz operator, with symbol[2] $A(z,x,\xi,\tau) = c(z,x)^{-2}\tau^2 - \|\xi\|^2$. In general, we use Greek letters for cotangent variables, dual to the space/time variables (ξ is the horizontal wave number, dual to x, and τ is radial frequency, the dual of time, t). This notation is consistent with Stolk & de Hoop (2004a,b) as this work builds upon these papers. To correspond with the notation of exploration seismology, τ is typically denoted as ω, ξ as k_x and ζ as k_z. The notation $\|\cdot\|$ indicates the norm of a vector.

To simplify the notation in (4.2), we re-write it in matrix form

$$\partial_z D = \mathsf{A}D + M\,, \tag{4.3}$$

where

$$D = \begin{pmatrix} u \\ \partial_z u \end{pmatrix},\ \mathsf{A} = \begin{pmatrix} 0 & 1 \\ -A(z,x,D_x,D_t) & 0 \end{pmatrix} \text{ and } M = \begin{pmatrix} 0 \\ -f \end{pmatrix}. \tag{4.4}$$

We diagonalize the operator matrix A, which can be done microlocally[3], away from the zeros of $A(z,x,\xi,\tau)$ modulo a smoothing operator. In this framework, there is a z-family

[2]The symbol of the differential operator, $P(x,D_x)$, is defined as $P(x,\xi)$ in which the D_x has been simply replaced with the ξ variable dual to x. The principal symbol, is the highest order component of the symbol and is generally denoted with the same symbol in lower case, i.e., $p(x,\xi)$.

[3]A statement is true microlocally if it is true in a neighborhood of a point in phase space. See Sjöstrand & Grigis (1994) for an introduction to microlocal analysis.

of pseudodifferential operator matrices $\mathsf{Q}(z)$ such that microlocally,

$$U = \begin{pmatrix} u_+ \\ u_- \end{pmatrix} = \mathsf{Q}(z)D\,, \qquad X = \begin{pmatrix} f_+ \\ f_- \end{pmatrix} = \mathsf{Q}(z)M\,. \tag{4.5}$$

The diagonalization procedure requires that cut-offs be applied to U to remove constituents of the wavefield that propagate anywhere horizontal; these cut-offs are described in the following section. We have omitted any indication that these cut-offs are not present in this section to keep the notation in this section consistent with the notation in the remainder of the paper, in which the cut-offs are assumed to have been applied. In this notation, $u_\pm$ satisfy the one-way wave equations

$$\left(I\partial_z + \mathsf{Q}(z)\partial_z\mathsf{Q}^{-1}(z) - \mathsf{B}\right)U = X\,, \tag{4.6}$$

where I is the identity matrix, introducing

$$\mathsf{B} = \mathsf{Q}(z)\mathsf{A}\mathsf{Q}^{-1}(z) = \begin{pmatrix} \mathrm{i}B_+(z,x,D_x,D_t) & 0 \\ 0 & \mathrm{i}B_-(z,x,D_x,D_t) \end{pmatrix}, \tag{4.7}$$

where $B_\pm$ has principal symbol $b_\pm(z,x,\xi,\tau) = \pm\tau\sqrt{c(z,x)^{-2} - \tau^{-2}\|\xi\|^2} = \pm b(z,x,\xi,\tau)$, which corresponds with k_z in the seismological notation.

With the conventions used here, u_+ represents downward propagating waves and u_- represents upward propagating waves. (As is standard in geophysics, we have chosen the positive z-axis downward.) The columns of the Q operator matrix are an operator generalization of eigenvectors and we are free to choose their normalization in the operator sense. We choose the vertical power flux normalization of de Hoop (1996) so as to make $B_\pm$ in (4.6) self-adjoint (the normalization changes the sub-principal part of the operator). In this normalization, the composition and decomposition operators are

$$\mathsf{Q} = \frac{1}{2}\begin{pmatrix} (Q_+^*)^{-1} & -\mathcal{H}Q_+ \\ (Q_-^*)^{-1} & \mathcal{H}Q_- \end{pmatrix}, \qquad \mathsf{Q}^{-1} = \begin{pmatrix} Q_+^* & Q_-^* \\ \mathcal{H}Q_+^{-1} & -\mathcal{H}Q_-^{-1} \end{pmatrix}, \tag{4.8}$$

where * denotes the adjoint of the operator, $\mathcal{H}$ is the Hilbert transform in time, and the principal symbol of both $Q_\pm$ is given by $\left(\frac{\tau^2}{c(z,x)^2} - \|\xi\|^2\right)^{-1/4}$. From these expressions we find that

$$u = Q_+^*u_+ + Q_-^*u_-, \text{ and } f_\pm = \pm\tfrac{1}{2}\mathcal{H}Q_\pm f. \tag{4.9}$$

The $Q_\pm$ operators act in the time variable as time convolutions.

In the flux normalization, the term $\mathsf{Q}^{-1}\partial_z\mathsf{Q}$ in (4.6) is of lower-order in the singularities (i.e. the operator is smoothing in comparison with other terms), thus we omit it. If required, its contribution can be accounted for by including it in the B matrix. We introduce the propagators for the one-way wave equations (4.6) as

$$(\partial_z + \mathsf{B})\,\mathsf{L} = I\delta, \quad \mathsf{L} = \begin{pmatrix} G_+ & 0 \\ 0 & G_- \end{pmatrix}. \tag{4.10}$$

We will denote $\partial_z + \mathsf{B}$ by P. We can now write the solution of (4.6) as $U = \mathsf{L}\ X$, using Duhamel's principle, L is the forward parametrix of P. In integral form this is

$$u_+(z,\cdot) = \int_{-\infty}^{z} G_+(z,z_0) f_+(z_0,\cdot)\ \mathrm{d}z_0 \qquad u_-(z,\cdot) = \int_{z}^{\infty} G_-(z,z_0) f_-(z_0,\cdot)\ \mathrm{d}z_0\,. \quad (4.11)$$

To make a connection to ray theory, the propagation of singularities by the one-way wave equations (4.6) is governed by their principal symbols. These yield the Hamiltonians, $\zeta \mp b$, for the system describing the rays in phase space; the evolution parameter along the rays is then depth, z. In the following section we use this analogy to subject $u_\pm$ and $G_\pm$ to cut-offs removing horizontally propagating constituents of the wavefield.

4.4 The Green functions

In the previous section we diagonalized the wave equation into two first-order equations. In doing this, we implicitly assume that the diagonal system is equivalent to the original system. This is nearly the case, but the choice of a principal direction alters the ability of the system to propagate singularities in directions orthogonal to this preferred direction. Here, we have chosen the vertical direction as the principal direction. To ensure that the diagonal system does not propagate singularities incorrectly, singularities that propagate somewhere horizontally must be attenuated. The details of the method are given in Stolk & de Hoop (2004a); we give only a brief description here to introduce the double-square-root (DSR) assumption used by Stolk & de Hoop. This assumption states that there are no wave constituents that propagate horizontally at any time. At the end of this section, we give a brief summary of the essential properties of the Green functions.

In order to identify horizontal propagation, we work in the high frequency limit, i.e. we develop these ideas via ray theory. Thus we define the phase angle

$$\theta = \arcsin(c(z,x)\|\tau^{-1}\xi\|), \quad (4.12)$$

where (ζ,ξ) is the cotangent vector associated with (z,x) and $c(z,x)$ is the velocity. Note that if the angle θ, is less than $\pi/2$ on a ray segment, the vertical velocity $\frac{\mathrm{d}z}{\mathrm{d}t}$ does not change sign, allowing the parameterization of the ray segment by z. Thus, for any ray segment and any given angle $\theta < \pi/2$, we can define a maximal interval,

$$(z_{\min\pm}(z,x,\xi,\tau,\theta), z_{\max\pm}(z,x,\xi,\tau,\theta))\,, \quad (4.13)$$

for which the propagation away from a particular point (z,x,ξ,τ) can be parameterized by z. In Figure 4.1, the interval $(z_{\min-}, z_{\max-})$ is illustrated; it is the maximal interval such that a bicharacteristic passing through the point (z,x), with direction (ζ,ξ) propagates in a direction such that the angle of the ray with the vertical, θ, does not exceed a given value; in the figure this value is θ_2.The angle θ can be given physical meaning by looking at the ray picture, in Figure 4.1.

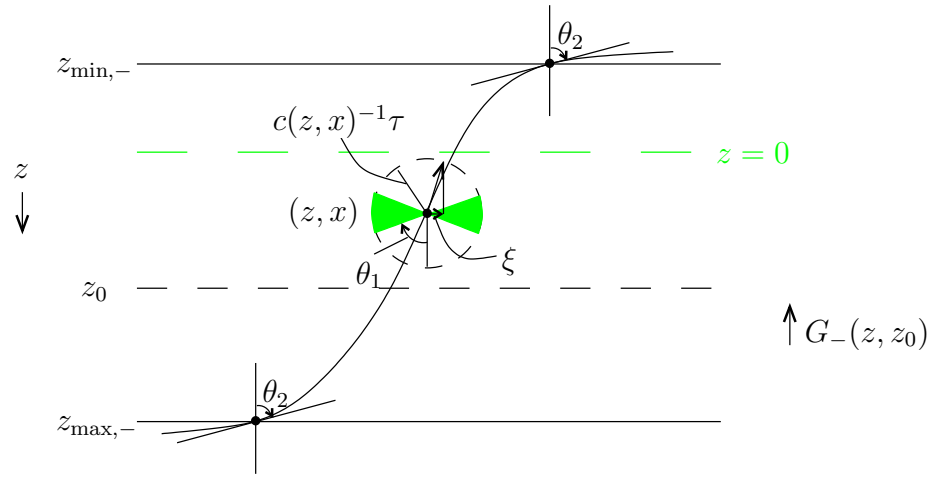

Figure 4.1. Removing horizontal propagations. The symbol of the cut-off operator ψ is one up to an angle θ_1 and then decays smoothly to zero at the angle θ_2. This removes all propagation at angles larger than θ_2, i.e., the region within the gray wedges.

In phase space, we introduce the set

$$I_\theta = \{(z,x,t,\zeta,\xi,\tau) \,|\, \arcsin(c(z,x)\|\tau^{-1}\xi\|) < \theta, |\zeta| < C|\tau|\}, \tag{4.14}$$

illustrated in Figure 4.2, where C is the maximum slowness. Finally, we construct the sets

$$J_-(z_0,\theta) = \{(z,x,t,\zeta,\xi,\tau) \in I_\theta \,|\, \tau^{-1}\zeta < 0 \text{ and } z_{\max-}(z,x,\xi,\tau,\theta) \geq z_0\}, \tag{4.15}$$

and

$$J_+(z_0,\theta) = \{(z,x,t,\zeta,\xi,\tau) \in I_\theta \,|\, \tau^{-1}\zeta > 0 \text{ and } z_{\min+}(z,x,\xi,\tau,\theta) \leq z_0\}. \tag{4.16}$$

Figure 4.1 illustrates the set $J_-(z_0,\theta_2)$, considering the shaded region as excluded from the set.

The sets $J_\pm$ encompass the regions of phase space that must be excluded in order to remove horizontally propagating singularities while analyzing $G_\pm(z,z_0)$. To actually remove singularities from these regions, we define a pseudodifferential cutoff
$\psi_- = \psi_-(z,z_0,x,D_x,D_t)$ with symbol satisfying

$$\psi_-(z,x,\xi,\tau) \sim 1 \text{ on } J_-(z_0,\theta_1), \tag{4.17}$$

$$\psi_-(z,x,\xi,\tau) \in S^\infty \text{ outside } J_-(z_0,\theta_2), \text{ if } z - z_0 > \delta > 0; \tag{4.18}$$

here $0 < \theta_1 < \theta_2$. Singularities propagating at an angle less than θ_1 are unaffected by the

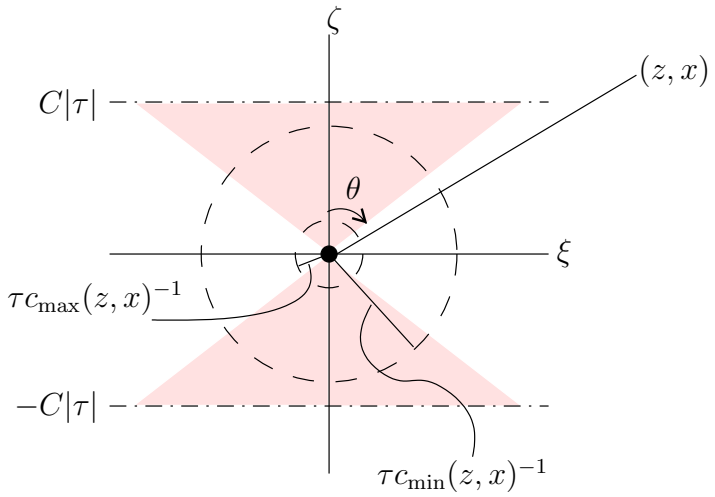

Figure 4.2. Illustration of I_θ. The shaded region represents the ray directions in the set. The minimum velocity in the region is c_{min} and the maximum is c_{max}.

cutoff; at angles greater than θ_2, the operator is smoothing. We then redefine u_- as

$$u_- \equiv \psi_- u'_-, \tag{4.19}$$

where u'_- is the wavefield u_- of the previous section. In u_- the the singularities outside of J_- have been suppressed. There are equivalent expressions for the + constituents. We now rewrite the operators defined above with the singularities outside of J_- (or J_+) suppressed. It is shown in Stolk & de Hoop (2004a) and references therein that the solution operator L to P is

$$\mathsf{L} = \begin{pmatrix} G_+ & 0 \\ 0 & G_- \end{pmatrix}, \tag{4.20}$$

redefining $G_\pm = \psi G'_\pm$ where $G'_\pm$ is the propagator described in the previous section. The operator P is the wave operator defined in the previous section with a dissipative term added to suppress singularities which are anywhere horizontal.

The condition $z_{\max-}(z, x, \xi, \tau, \theta) \geq z_0$, in the definition of J_- combined with the implicit requirement that $z_{\min-} < 0$ ensure that the two points between which one propagates the wavefield are within the allowed propagation interval $(z_{\min-}, z_{\max-})$. From this point onward we will assume that the above procedure has been followed and will be reapplied if necessary.

Remark 4.4.1. We denote the kernel of $(G_-(z_0, z))$ as $(G_-(z_0, z))(x_0, t_0 - t, x) = G_-(z_0, x_0, t_0 - t, z, x)$. The adjoint propagator $(G_-(z_0, z))^*(x, t - t_0, x_0) =$

$G_-^*(z_0, x_0, t_0 - t, z, x)$ follows from

$$\begin{aligned} & \int \mathrm{d}s_0\, \mathrm{d}t_0\, v(z_0, s_0, t_0) \left(\int \mathrm{d}s\, \mathrm{d}t\, G_-(z_0, s_0, t_0 - t, z, s) u(z, s, t) \right) \\ = & \int \mathrm{d}s\, \mathrm{d}t \left(\int \mathrm{d}s_0\, \mathrm{d}t_0\, v(z_0, s_0, t_0) G_-(z_0, s_0, t_0 - t, z, s) \right) u(z, s, t) \\ = & \int \mathrm{d}s\, \mathrm{d}t \left(\int \mathrm{d}s_0\, \mathrm{d}t_0 (G_-(z_0, z))^*(s, t - t_0, s_0) v(z_0, s_0, t_0) \right) u(z, s, t) \end{aligned} \tag{4.21}$$

Using the self-adjoint property of B, $G_-(z_0, s_0, t_0 - t, z, s) = G_+(z, s, t - t_0, z_0, s_0)$, microlocally so that $(G_-(z_0, z))^* = G_+(z, z_0)$. A similar result holds with + and − interchanged. Note that $G_\pm$ are causal.

Remark 4.4.2. The $G_\pm$ propagators obey the reciprocity relation (of the time convolution type)

$$Q_+^*(z) G_+(z, z_0) Q_+(z_0) = -Q_-^*(z_0) G_-(z_0, z) Q_-(z)\,. \tag{4.22}$$

This reciprocity relation is derived from the reciprocity of the full-wave Green propagator.

Remark 4.4.3. We have

$$G_-(z, z') G_-(z', z'') = G_-(z, z'')\,, \tag{4.23}$$

for $z < z' < z''$; this property is known as the semi-group property. The same property holds for G_+.

In the above, we have nowhere assumed the absence of caustics in the wavefield. This section has addressed the necessary assumption that rays are nowhere horizontal: the double-square-root DSR assumption (Stolk & de Hoop, 2004a, Assumption 2).

4.5 Scattering: Contrast source formulation

The Bremmer formulation assumes a degree of smoothness in the velocity model. In the contrast formulation of the Lippmann-Schwinger approach, the velocity, c, is split into a background, c_0, which is here assumed to be smooth (C^∞) and a singular contrast, δc, which is here assumed to be a superposition of conormal distributions. A series is then constructed with terms of increasing order in δc. We use a hybrid of the two approaches; the contrast-source integral equation (Lippmann-Schwinger) subjected to a directional decomposition (Bremmer). We begin with the wave equation in the smooth background and in the true medium respectively

$$(\partial_z + \mathsf{A}_0) D_0 = M, \qquad (\partial_z + \mathsf{A}) D = M, \tag{4.24}$$

where the subscript 0 indicates that an operator is using the smooth background parameters and no subscript indicates an operator acting on the full medium. Subtracting the equation

in the smooth background from that in the true medium gives the contrast equation

$$(\partial_z + \mathsf{A}_0)\delta D = -\delta\mathsf{A}\ D, \tag{4.25}$$

where $D = D_0 + \delta D$ and $\mathsf{A} = \mathsf{A}_0 + \delta\mathsf{A}$. The right hand side of (4.25) is the so-called contrast source. We have (cf. (4.4))

$$\delta\mathsf{A} = \begin{pmatrix} 0 & 0 \\ \delta A & 0 \end{pmatrix} \quad \text{where} \quad \delta A(z, x, D_t) = -2c_0^{-3}\delta c(z, x)D_t^2 = -a(z, x)D_t^2\,, \tag{4.26}$$

defining the contrast a. We insert the Bremmer formulation into that above by diagonalizing the A_0 matrix operator. We apply the (smooth background) diagonalizing Q operator matrices to transform the system in (4.25). Using the diagonalization procedure of section 4.3, equation (4.7) in particular, we find

$$(\partial_z + \mathsf{B}_0)\delta U = -\mathsf{Q}(z)\partial_z\mathsf{Q}^{-1}(z)\delta U - \mathsf{Q}(z)\delta\mathsf{A}\ \mathsf{Q}^{-1}(z)U\,, \tag{4.27}$$

recalling, from section 4.3, the definition of U

$$U = \mathsf{Q}D \tag{4.28}$$

while,

$$U_0 \ := \mathsf{Q}D_0\,, \tag{4.29}$$

$$\delta U \ := \mathsf{Q}\delta D. \tag{4.30}$$

The Q operator matrix is common in all the transformations. Note that $\delta\mathsf{A}$ will not, in general, be diagonalized by Q as the Q operators diagonalize A_0 in the background velocity model only.

Since we have used the flux normalization, the $-\mathsf{Q}(z)\partial_z\mathsf{Q}^{-1}(z)\delta U$ term is of lower-order as before (discussion above (4.10)). This term could be absorbed in $\delta\mathsf{A}$ by $\delta\mathsf{A} := \delta\mathsf{A} + I\partial_z$. We omit this contribution so that

$$(\partial_z + \mathsf{B}_0)\delta U = -\mathsf{Q}(z)\delta\mathsf{A}\mathsf{Q}^{-1}(z)U\,, \tag{4.31}$$

where $\mathsf{Q}(z)\delta\mathsf{A}\mathsf{Q}^{-1}(z)$ is given explicitly as

$$\mathsf{Q}(z)\delta\mathsf{A}\mathsf{Q}^{-1}(z) = \tfrac{1}{2}\mathcal{H}\begin{pmatrix} Q_+(z)\ a\ Q_+^*(z) & Q_+(z)\ a\ Q_-^*(z) \\ -Q_-(z)\ a\ Q_+^*(z) & -Q_-(z)\ a\ Q_-^*(z) \end{pmatrix} D_t^2\,. \tag{4.32}$$

In (4.31), we make the analogy with (4.6) where δU plays the role of U and $-\mathsf{Q}(z)\delta\mathsf{A}\ \mathsf{Q}^{-1}(z)U$ that of X, which is now the contrast source.

We make the comparison between the elements of V and the reflection and transmission

operators of de Hoop (1996) viz,

$$V = \mathsf{Q}\delta\mathsf{A}D_t^2\mathsf{Q}^{-1} = \tfrac{1}{2}\mathcal{H}\begin{pmatrix} Q_+\ a\ Q_+^* & Q_+\ a\ Q_-^* \\ -Q_-\ a\ Q_+^* & -Q_-\ a\ Q_-^* \end{pmatrix} D_t^2 = \begin{pmatrix} S_{++} & S_{-+} \\ S_{+-} & S_{--} \end{pmatrix} D_t^2\,. \quad (4.33)$$

Here, S_{++} and S_{--} are interpreted as transmission operators since they govern scatterings between singularities traveling in the same principal direction before and after scattering. In contrast, S_{+-} and S_{-+} are interpreted as reflection operators because they govern scatterings that result in a change of principal direction; from up-going to down-going and down-going to up-going, respectively.

To simplify the notation, we define

$$P_0 = \partial_z + \mathsf{B}_0\,, \quad (4.34)$$

and its forward parametrix,

$$\mathsf{L}_0 = \begin{pmatrix} G_+ & 0 \\ 0 & G_- \end{pmatrix}. \quad (4.35)$$

Recall also that $V = \mathsf{Q}(z)\ \delta\mathsf{A}\ \mathsf{Q}^{-1}(z)$ from (4.33). In this notation, (4.31) reduces to

$$P_0\ \delta U = -VU\,, \quad (4.36)$$

or

$$\delta U = -\mathsf{L}_0(VU)\,. \quad (4.37)$$

The V operator is a distributional multiplication along with a second time derivative, whereas L_0 is the forward parametrix of a partial differential operator. Writing $U = U_0 + \delta U$ gives

$$\delta U = -\mathsf{L}_0(VU_0) - \mathsf{L}_0(V\delta U)\,, \quad (4.38)$$

or equivalently,

$$(I + \mathsf{L}_0\ V)\ \delta U = -\mathsf{L}_0(VU_0)\,. \quad (4.39)$$

As was done in (4.26), we take out the time derivative in the formulation of V. Thus we introduce $\widehat{V}$, the matrix of $S_{\pm\pm}$ operators (cf (4.33)), viz,

$$V(z, x, D_t) = \widehat{V}(z, x)D_t^2, \quad (4.40)$$

which results in

$$(I + D_t^2\mathsf{L}_0\ \widehat{V})\ \delta U = -D_t^2\mathsf{L}_0(\widehat{V}U_0)\,, \quad (4.41)$$

where $\widehat{V}\delta U$ and $\widehat{V}U_0$ are products of distributions (subject to the condition that their wavefront are favorably oriented (Friedlander & Joshi, 1998, proposition 11.2.3), (Hörmander, 1983, Theorem 8.2.10)). This is the resolvent equation in our hybrid Lippmann-Schwinger-Bremmer formulation for scattered waves. (See Yosida (1995) for details on resolvent equations.)

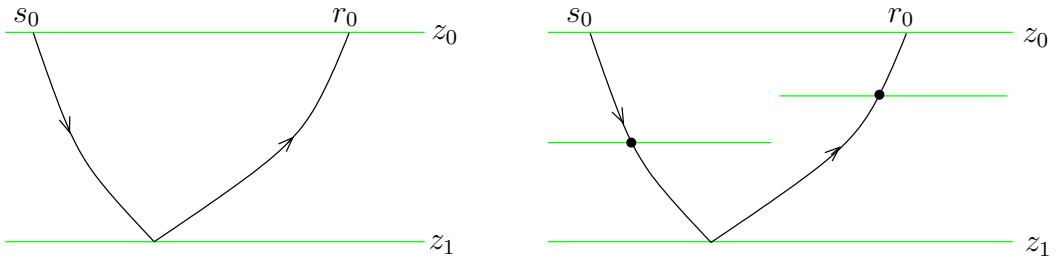

Figure 4.3. Single scattering (left panel) versus primary reflection (right panel). The black dots indicate transmission scatterings.

4.6 Scattering series

4.6.1 Forward scattering series

In this section, we describe the construction of the forward scattering series for δU in terms of $\widehat{V}$, based on the discussion of the previous section. We arrive at expressions (4.43), (4.46) and (4.47) below, through which data are modeled.

Here, we define a singly scattered wave as a wave that has been reflected or transmitted once, such as that shown on the left in Figure 4.3. The term primary reflection is associated with any 'ray-path' (more accurately wave-path since we use wave solutions rather than ray theory) that has reflected only once but may have gone through several transmission, or scatterings where the direction of the wave does not change. This type of contribution is depicted in the right panel of Figure 4.3. Primary reflections have the same traveltime as singly scattered waves but will have amplitude scaled by additional factors of S_{--} or S_{++} because of the transmissions. The same distinction can be made between leading-order internal multiples and triply scattered waves. The diagram on the right of Figure 4.3 is a triply scattered event. The third-order contributions that we take into account are those for which each scattering event is a reflection, i.e., after the scattering the singularities propagate in the opposite direction to that in which they were propagating before the scattering. We refer to contributions such as these, where none of the three scattering events occurs at the acquisition surface, as leading-order internal multiples. The goal of this section is to develop a method for modeling such scattered wave constituents in the data.

Having identified (4.41) as a resolvent equation, we set up the recursion

$$\delta U = \sum_{m=1}^{M} (-1)^m \delta U_m(\widehat{V}) \,, \tag{4.42}$$

where

$$\delta U_1(\widehat{V}) = D_t^2 \mathsf{L}_0(\widehat{V} U_0), \text{ and } \delta U_m(\widehat{V}) = D_t^2 \mathsf{L}_0(\widehat{V}\delta U_{m-1}(\widehat{V})), \ m = 2, 3, \ldots . \tag{4.43}$$

Each subsequent term in the series is a multilinear operator of higher order than previous terms.

To compare the Bremmer series formulation ((VII.1)-(VII.22) of de Hoop (1996)) to the recursion in (4.42) we first make the following identifications. From (VII.1) and (VII.12) we note that W_0 of de Hoop (1996) corresponds to δU_1. From this formulation we note that $-D_t^2 \mathsf{L}_0 \widehat{V}$ corresponds with K of equation (VII.15) in de Hoop (1996) and (4.42) corresponds to equation (VII.22). The major difference between this hybrid series and the Bremmer series is in that the coupling of the different components is different. In the Bremmer series the reflection and transmission operators come from derivatives of the medium contrast whereas in the hybrid series they come from difference between the reference and true model. We use this hybrid formulation to derive operators that model both 'singly' and 'triply' scattered waves.

The expressions in (4.42) and (4.43) are not quite in the form of observables, however; data are acquired only at the Earth's surface, but the L_0 operator models data at all depths. We therefore define a restriction operator, R, which restricts a distribution to the acquisition surface, $z = 0$. This operator does not account for the free-surface boundary condition, thus we assume a homogeneous medium (with no reflectors) above the acquisition surface. In this we way have excluded incoming waves from above the acquisition surface. We assume that there are no reflectors at or near this surface, i.e., we assume that the support of the medium contrast, a, does not contain source or receiver points. The composition $R\mathsf{L}_0$ is well-defined provided there are no grazing rays (Stolk & de Hoop, 2002), which have been excluded already by the ψ cut-off from section 4.4. The composition with Q^{-1} also does not change the properties of the composite operator provided we satisfy the assumptions in the generalized Bremmer series (de Hoop, 1996). Observable quantities are obtained by applying Q^{-1} to δU, as in (4.30). We thus rewrite (4.42)

$$R\mathsf{Q}^{-1}\delta U(\widehat{V}) = \sum_{m=1}^{M} (-1)^m R\mathsf{Q}^{-1}\delta U_m(\widehat{V}) \, . \tag{4.44}$$

With

$$R\mathsf{Q}^{-1}\delta U_1(\widehat{V}) = D_t^2 R\mathsf{Q}^{-1}\mathsf{L}_0(\widehat{V} U_0) \, , \tag{4.45}$$

we introduce the operator

$$\mathsf{M}_0 = R\mathsf{Q}^{-1}\mathsf{L}_0 \, . \tag{4.46}$$

We then have,

$$R\mathsf{Q}^{-1}\delta U(\widehat{V}) \;\; = \;\; -D_t^2 \mathsf{M}_0 \left(\widehat{V} \left(U_0 + \sum_{m=1}^{M} (-1)^m \delta U_m(\widehat{V}) \right) \right) \, , \tag{4.47}$$

where δU_m is defined in (4.43). The first term on the right-hand side of (4.47) is the Born approximation. Using the notation introduced in (4.4) we have, from the leading order term, an expression for the singly scattered data,

$$\delta D = \begin{pmatrix} d \\ \partial_z d \end{pmatrix} = -R\mathsf{Q}^{-1}\delta U_1(\widehat{V}) = -D_t^2\mathsf{M}_0(\widehat{V}U_0)\,. \tag{4.48}$$

From this term the singly scattered data are modeled in section 4.7.1. In section 4.7.2 the second term of (4.47) is used to model internal multiples by examining the $m = 2$ term of the summation. Note that the recursion in (4.47) gives an expression for the data at the surface in terms of the unrestricted field from the previous step; the restriction is applied as a last step after the recursion is completed.

4.6.2 Inverse scattering series using all the data

The forward scattering series (4.47) models the data, given a representation of the medium as the sum of a smooth background and singular contrast. The inverse series estimates the medium contrast from the data. In this section we derive this inverse series, arriving at a recursion for the medium contrast in (4.61).

To motivate the inverse series, we return to (4.41) and write it as an equation for $\widehat{V}$ in terms of δU

$$D_t^2\mathsf{L}_0(\widehat{V}(U_0 - (-\delta U))) = -\delta U\,, \tag{4.49}$$

or, returning to observables via the $R\mathsf{Q}^{-1}$ operator,

$$D_t^2\mathsf{M}_0(\widehat{V}(U_0 - (-\delta U))) = -\delta D\,. \tag{4.50}$$

We then set up an inverse series, by assuming that the medium contrast can be represented in terms of a series of operators,

$$\widehat{V} = \sum_{m=1}^{M} \widehat{V}_m \tag{4.51}$$

where m indicates the order of $\widehat{V}_m$ in the data. This series representation is suggested for quantum mechanical problems by Moses (1956), where the analogue of (4.51) is his equation (3.12). It is also suggested by Razavy (1975) for wave problems, in which the analogue of (4.51) is his equation (33). Perhaps the closest analogue to what is done here is given by Prosser (1969), equations (7) and (8). It is this theory, for the Lippmann-Schwinger series, that is used extensively by Weglein *et al.* (1997).

Substituting (4.51) into (4.42) yields a recursion for $\widehat{V}_m$ in terms of δU

$$\begin{aligned}
\delta U &= -D_t^2\mathsf{L}_0(\widehat{V}_1U_0) && (4.52)\\
0 &= -D_t^2\mathsf{L}_0(\widehat{V}_2U_0) + D_t^4\mathsf{L}_0(\widehat{V}_1\mathsf{L}_0(\widehat{V}_1U_0)) && (4.53)\\
0 &= -D_t^2\mathsf{L}_0(\widehat{V}_3U_0) + D_t^4\mathsf{L}_0(\widehat{V}_2\mathsf{L}_0(\widehat{V}_1U_0)) + D_t^4\mathsf{L}_0(\widehat{V}_1\mathsf{L}_0(\widehat{V}_2(U_0))) && (4.54)\\
&\quad -D_t^6\mathsf{L}_0(\widehat{V}_1\mathsf{L}_0(\widehat{V}_1\mathsf{L}_0(\widehat{V}_1U_0)))
\end{aligned}$$

etc.

These equations are assumed to hold anywhere in the interior of the scattering region. Restricting δU to the surface and transforming it into observables by applying $R\mathsf{Q}^{-1}$ to (4.52-4.54) yields a recursion for $\widehat{V}_m$ in terms of the data d,

$$\begin{aligned}
\delta D &= -D_t^2\mathsf{M}_0(\widehat{V}_1U_0) && (4.55)\\
0 &= -D_t^2\mathsf{M}_0(\widehat{V}_2U_0) + D_t^4\mathsf{M}_0(\widehat{V}_1\mathsf{L}_0(\widehat{V}_1U_0)) && (4.56)\\
0 &= -D_t^2\mathsf{M}_0(\widehat{V}_3U_0) + D_t^4\mathsf{M}_0(\widehat{V}_2\mathsf{L}_0(\widehat{V}_1U_0)) + D_t^4\mathsf{M}_0(\widehat{V}_1\mathsf{L}_0(\widehat{V}_2(U_0))) && (4.57)\\
&\quad -D_t^6\mathsf{M}_0(\widehat{V}_1\mathsf{L}_0(\widehat{V}_1\mathsf{L}_0(\widehat{V}_1U_0)))
\end{aligned}$$

etc.

These equations hold on the acquisition surface, $z = 0$. In general, $\partial_z d$ (the second component of δD) is not recorded. We assume that we record only the up-going field, d_-, from $z > 0$. With this assumption, $d = Q_-^* d_-$ and $\partial_z d = -\mathcal{H}Q_-^{-1}d_-$ allowing $\partial_z d$ to be estimated directly from d.

The first term in the series, given in (4.55), models singly scattered data. The third term, in (4.57), models leading-order internal multiples as well as other primary events such as the one shown on the right in Figure 4.3. (The second term, given in (4.56), models events which have scattered twice, including primary events with one transmission and one reflection.)

Equation (4.57) can be simplified using (4.53). This is done by noting that the distributions $D_t^2\mathsf{L}_0(\widehat{V}_2U_0)$ from the second term of (4.57) and $D_t^4\mathsf{L}_0(\widehat{V}_1\mathsf{L}_0(\widehat{V}_1U_0))$ from the third term are identical by (4.53) and $D_t^2\mathsf{M}_0\widehat{V}_1(\cdot)$, which acts on these distributions (again in the second and third terms) is a linear operator. With this simplification we have, for (4.57)

$$D_t^2\mathsf{M}_0(\widehat{V}_3U_0) = D_t^4\mathsf{M}_0(\widehat{V}_2\mathsf{L}_0(\widehat{V}_1U_0))\,. \tag{4.58}$$

The general equation in the recursion follows from the fact that higher order terms are built from lower-order terms through the application of $D_t^2\mathsf{M}_0\widehat{V}_i$ to $(j-i)^{\text{th}}$-order terms to form terms of order j. For example, terms of order 4 are formed by subtracting $D_t^2\mathsf{M}_0\widehat{V}_1$ applied to (4.54), $D_t^2\mathsf{M}_0\widehat{V}_2$ applied to (4.53), and $D_t^2\mathsf{M}_0\widehat{V}_3$ applied to the right side of (4.52), from $D_t^8\mathsf{M}_0\widehat{V}_4U_0$. In general terms of order j will contain sub-series of the form

$$D_t^2\mathsf{M}_0\widehat{V}_1(\text{sum of terms of order } j-1 \text{ from (4.52)-(4.54)}), \tag{4.59}$$

$$D_t^2\mathsf{M}_0\widehat{V}_2(\text{sum of terms of order } j-2 \text{ from (4.52)-(4.54)}), \tag{4.60}$$

etc. For $j \geq 2$ the sub-series in parentheses sum to zero because of the zero on the left-hand side of (4.53).

We obtain the final form of the recursion,

$$\begin{aligned}
&D_t^2\mathsf{M}_0(\widehat{V}_jU_0) = D_t^4\mathsf{M}_0(\widehat{V}_{j-1}\mathsf{L}_0(\widehat{V}_1U_0))\,, \quad j \geq 2\,,\\
&\text{while } D_t^2\mathsf{M}_0(\widehat{V}_1U_0) = -\delta D
\end{aligned} \tag{4.61}$$

Solving these recursions for $\widehat{V}$ gives a solution for the medium contrast, $\widehat{V}$ in terms of the data d, as in (4.51). Note the similarity in structure between (4.61) and (4.43); (4.61) constructs the medium contrast in terms of the data, while (4.43) constructs the data in terms of the medium contrast.

Remark 4.6.1. Using (4.61) along with the expression for δU in (4.52), we can write the $\widehat{V}$-series as

$$-D_t^2\mathsf{M}_0(\widehat{V}U_0) = \delta D - \left(\sum_{m=1}^{M} D_t^2\mathsf{M}_0(\widehat{V}_m\delta U)\right) . \tag{4.62}$$

This expresses higher order terms in the series as a correction to the data, d. In what follows, we examine the correction obtained from the sum in (4.62); we specifically examine the $m = 2$ term in the series.

Remark 4.6.2. We verify the compatibility of (4.47) and (4.51) for $M = 2$. To this end we insert,

$$\widehat{V} \approx \widehat{V}_1 + \widehat{V}_2 + \widehat{V}_3 \, , \tag{4.63}$$

into the truncated forward series

$$\delta D \approx -D_t^2\mathsf{M}_0(\widehat{V}U_0) + D_t^4\mathsf{M}_0(\widehat{V}\mathsf{L}_0(\widehat{V}U_0)) - D_t^6\mathsf{M}_0(\widehat{V}\mathsf{L}_0(\widehat{V}\mathsf{L}_0(\widehat{V}U_0))) \, . \tag{4.64}$$

Terms of first, second and third 'order' in the resulting sum cancel. The fourth 'order' term in this truncated sum is

$$\begin{aligned} &D_t^4\mathsf{M}_0(\widehat{V}_1\mathsf{L}_0(\widehat{V}_3U_0)) + D_t^4\mathsf{M}_0(\widehat{V}_2\mathsf{L}_0(\widehat{V}_2U_0)) + D_t^4\mathsf{M}_0(\widehat{V}_3\mathsf{L}_0(\widehat{V}_1U_0)) \\ &-D_t^6\mathsf{M}_0(\widehat{V}_1\mathsf{L}_0(\widehat{V}_1\mathsf{L}_0(\widehat{V}_2U_0))) - D_t^6\mathsf{M}_0(\widehat{V}_1\mathsf{L}_0(\widehat{V}_2\mathsf{L}_0(\widehat{V}_1U_0))) \\ &-D_t^6\mathsf{M}_0(\widehat{V}_2\mathsf{L}_0(\widehat{V}_1\mathsf{L}_0(\widehat{V}_1U_0))) \, , \end{aligned} \tag{4.65}$$

vanishes by (4.61). This implies that the error contains fifth 'order' to ninth 'order' terms.

4.7 Modeling multiply scattered data

This section illustrates the modeling of data based on the hybrid series. We consider two cases: modeling primaries in the single scattering approximation and modeling internal multiples from the third term of the series. Section 4.7.1 derives an representation of d_1 from the first term in (4.47). Section 4.7.2 derives a representation of internal multiples, d_3 using the $m = 2$ term of the sum in (4.47). In both of these sections, we track the wavefield from the source, through the scattering(s) to the receiver. The results of this section are the expression for modeling singly scattered data given in (4.76) and that for modeling triply scattered data in (4.81).

4.7.1 Single scattering

The first term in the forward scattering series given in (4.42) is used to construct data in the Born approximation in accordance with equation (3.10) of Stolk & de Hoop (2004a).

We give here an alternate derivation of this equation, resulting in our equation (4.76). We formulate the solution only for the upward propagating constituent of δU_1, which we denote by $\delta u_{-,1}$. We first determine the form of the down-going constituent of U_0, denoted by $u_{+,0}$, which is the down-going wave excited at the surface and arriving at the scattering point. With the expression for the source f_+ in (4.9) and that for u_+ in (4.11) we find that

$$u_{+,0}(z_1,x_1,t_1,z_0,s_0) = \tfrac{1}{2}\int_{-\infty}^{z_1}\mathrm{d}\tilde{z}_0\int\mathrm{d}\tilde{s}_0\int_{\mathbb{R}}\mathrm{d}\tilde{t}_{s_0}G_+(z_1,x_1,t_1-\tilde{t}_{s_0},\tilde{z}_0,\tilde{s}_0) \\ \mathcal{H}Q_{+,\tilde{s}_0}(\tilde{z}_0)f(\tilde{z}_0,\tilde{s}_0,\tilde{t}_{s_0},z_0,s_0)\,, \quad (4.66)$$

where we will adopt the convention that an integral without limits is assumed to be an integration over $\mathbb{R}^{n-1}$. In general, s represents a source position, r represents a receiver position, t is a time variable and z is depth, regardless of subscripts and superscripts. The notation $Q_{-,s}(z)$ is short for $Q_-(z,s,D_s,D_t)$. The t integrations are limited implicitly by the causality of the Green operator, G, discussed in Remark 4.4.1. The operator G_+ in (4.66) propagates between the levels z_0 and z_1, with its action being in the lateral variables $\tilde{s}_0$, and $\tilde{t}_{s_0}$; we will also use the notation $G_+(z_1,z_0)$ for the propagator G_+ when the lateral positions in which it acts are unambiguous. We adopt the standard kernel notation that the input variables to an operator are written to the right of the output variables. We are justified in writing the time dependence of $G_\pm$ as the difference of elapsed time and initial source time as the wave equation is time translation invariant. Expression (4.66) is valid for $z_1 > z_0$. The parameters z_0, s_0 are assumed to be known.

Next, we derive an expression for c_-, the up-going constituent in the contrast source given by,

$$\begin{pmatrix} c_+ \\ c_- \end{pmatrix} = VU_0 = V\begin{pmatrix} u_{+,0} \\ u_{-,0} \end{pmatrix}. \quad (4.67)$$

Using the expression for V in (4.33), and recalling that $u_{-,0} = 0$ for $z > 0$, we obtain an expression for c_-,

$$c_-(z_1,x_1,t_1) = -\tfrac{1}{2}\mathcal{H}D_{t_1}^2Q_{-,x_1}(z_1)a(z_1,x_1)Q^*_{+,x_1}(z_1)u_{+,0}(z_1,x_1,t_1,z_0,s_0)\,. \quad (4.68)$$

Substituting c_- from (4.68) for f_- in (4.11) gives

$$\delta u_{-,1}(z_0,r_0,t_{r_0},z_0,s_0) = -\tfrac{1}{2}\mathcal{H}D_{t_{r_0}}^2\int_{z_0}^{\infty}\mathrm{d}z_1\int\mathrm{d}x_1\int_{\mathbb{R}}\mathrm{d}t_1 \\ G_-(z_0,r_0,t_{r_0}-t_1,z_1,x_1)\underbrace{Q_{-,x_1}(z_1)\;a(z_1,x_1)Q^*_{+,x_1}(z_1)}_{S_{+-}}u_{+,0}(z_1,x_1,t_1,z_0,s_0) \quad (4.69)$$

in the diagonal system without the restriction to the Earth's surface, $z_0 = \tilde{z}_0 = 0$. This is the first term in the series in (4.42)-(4.43). Because a is compactly supported in z_1, the integral over z_1 is actually over a compact set. As in the previous section, we assume that the medium contrast, a, has its support away from $z = 0$. To obtain modeled data, we

apply the $R\mathsf{Q}^{-1}$ operator as in (4.47),

$$\begin{aligned} d_1(s_0,r_0,t_{r_0}) = &\int \mathrm{d}\tilde{s}_0 \int_{\mathbb{R}} \mathrm{d}\tilde{t}_{s_0} \tfrac{1}{4} D^2_{t_{r_0}} \int_0^\infty \mathrm{d}z_1 \int \mathrm{d}x_1 \int_{\mathbb{R}} \mathrm{d}t_1 \\ &Q^*_{-,r_0}(0) G_-(0,r_0,t_{r_0}-t_1,z_1,x_1) Q_{-,x_1}(z_1)\ a(z_1,x_1) Q^*_{+,x_1}(z_1) \\ &G_+(z_1,x_1,t_1-\tilde{t}_{s_0},0,\tilde{s}_0) Q_{+,\tilde{s}_0}(0) f(0,\tilde{s}_0,\tilde{t}_{s_0},0,s_0)\,, \end{aligned} \tag{4.70}$$

yielding the Born modeled data in terms of the $G_\pm$, the solutions of the single square-root equation. This is the first entry in the δD vector, in the series in (4.47).

We apply reciprocity (4.22) to (4.70) to write d_1 in terms of G_- only, giving

$$\begin{aligned} d_1(s_0,r_0,t_{r_0}) = -&\int \mathrm{d}\tilde{s}_0 \int_{\mathbb{R}} \mathrm{d}\tilde{t}_{s_0} f(0,\tilde{s}_0,\tilde{t}_{s_0},0,s_0) \tfrac{1}{4} D^2_{t_{r_0}} \int_0^\infty \mathrm{d}z_1 \int \mathrm{d}x_1 \int_{\mathbb{R}} \mathrm{d}t_1 \\ &Q^*_{-,r_0}(0) G_-(0,r_0,t_{r_0}-t_1,z_1,x_1) Q_{-,x_1}(z_1) Q^*_{-,\tilde{s}_0}(0) \\ &G_-(0,\tilde{s}_0,t_1-\tilde{t}_{s_0},z_1,x_1) Q_{-,x_1}(z_1)\ a(z_1,x_1)\,. \end{aligned} \tag{4.71}$$

To write (4.71) in terms of a single Green function for the source and receiver together, there must be integrations in (x_1,t_1) for each of the Green functions. To introduce these integrations we introduce two extension operators,

$$E_1 : a(z,x) \mapsto \delta(r-s) a(z,\tfrac{r+s}{2})\,,\quad E_2 : b(z,r,s) \mapsto \delta(t) b(z,r,s)\,, \tag{4.72}$$

through their action on the test functions a and b. These operators extend the medium contrast, $a(z,x)$, into fictitious data (now a function of (z,s,r,t)) in the subsurface as illustrated in Figure 4.4. With these operators, we re-write (4.71), now assuming a point source in both space and time. This gives,

$$\begin{aligned} d_1(s_0,r_0,t_{r_0}) = -&\tfrac{1}{4} D^2_{t_{r_0}} \int_0^\infty \mathrm{d}z_1 \int \mathrm{d}s_1 \int \mathrm{d}r_1 \int_{\mathbb{R}} \mathrm{d}t_0 \int_{\mathbb{R}} \mathrm{d}t_1 \\ &Q^*_{-,r_0}(0) G_-(0,r_0,t_{r_0}-t_1-t_0,z_1,r_1) Q_{-,r_1}(z_1) \\ &Q^*_{-,s_0}(0) G_-(0,s_0,t_1,z_1,s_1,0) Q_{-,s_1}(z_1) (E_2 E_1 a)(z_1,s_1,r_1,t_0)\,. \end{aligned} \tag{4.73}$$

We note that the two one-way Green functions are connected through time convolution. To make this explicit we change integration variables from t_1 to $t' = t_1 - \tilde{t}_{s_0}$, giving

$$\begin{aligned} d_1(s_0,r_0,t_{r_0}) = -&\tfrac{1}{4} D^2_{t} \int_0^\infty \mathrm{d}z_1 \int \mathrm{d}s_1 \int \mathrm{d}r_1 \int_{\mathbb{R}} \mathrm{d}t_0 \int_{\mathbb{R}} \mathrm{d}t' \\ &Q^*_{-,r_0}(0) G_-(0,r_0,t_{r_0}-t'-t_0,z_1,r_1) Q_{-,r_1}(z_1) \\ &Q^*_{-,s_0}(0) G_-(0,s_0,t',z_1,s_1) Q_{-,s_1}(0) (E_2 E_1 a)(z_1,s_1,r_1,t_0)\,. \end{aligned} \tag{4.74}$$

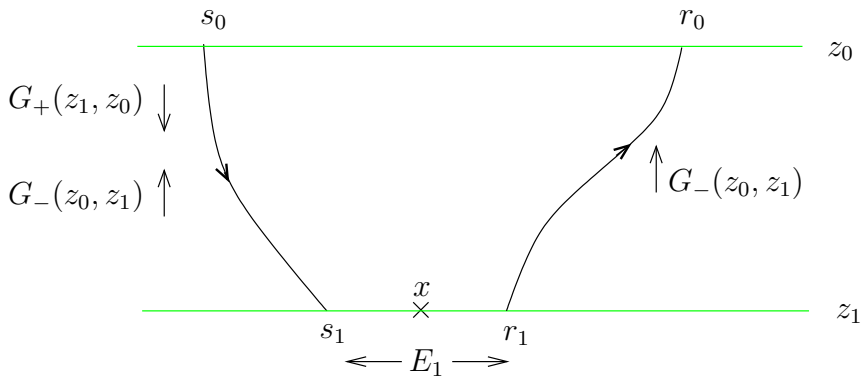

Figure 4.4. Notation for single scattering modeling.

To obtain a more compact expression, we return to operator notation, first introducing

$$(H(z_0, z_1))(s_0, r_0, t - t_0, s_1, r_1) = \int_{\mathbb{R}} (G_-(z_0, z_1))(r_0, t - t' - t_0, r_1)(G_-(z_0, z_1))(s_0, t', s_1)\,\mathrm{d}t', \quad (4.75)$$

the kernel of the propagator $H(z_0, z_1)$ associated with the so-called double-square-root (DSR) equation (Claerbout, 1985), which propagates data from the depth z_1 to the depth z_0. Substituting this expression for the two Green functions in (4.74) gives equation (3.10) of Stolk & de Hoop (2004a, Theorem 5.1),

$$d_1(s_0, r_0, t_{r_0}) = -\tfrac{1}{4} D_t^2 Q^*_{-,r_0}(0) Q^*_{-,s_0}(0) \int_0^\infty \mathrm{d}z_1 \left(H(0, z_1) Q_{-,r_1}(z_1) Q_{-,s_1}(z_1)(E_2 E_1 a) \right)(s_0, r_0, t_{r_0}). \quad (4.76)$$

4.7.2 Leading-order internal multiple scattering

In (4.76), we showed how singly scattered data can be constructed given the medium perturbation. Our ultimate goal is to construct the medium contrast given data containing both primaries and leading-order internal multiples. In this section we establish a relation between the modeling of primaries and internal multiples.

Following the diagram in Figure 4.5, the first scattering of the internal multiple, from s_0 through s_2, r_2 to m_r is nearly identical to the single scattering case. We cannot use the H operator however, because the second leg (from r_2 to m_r) does not reach the surface,

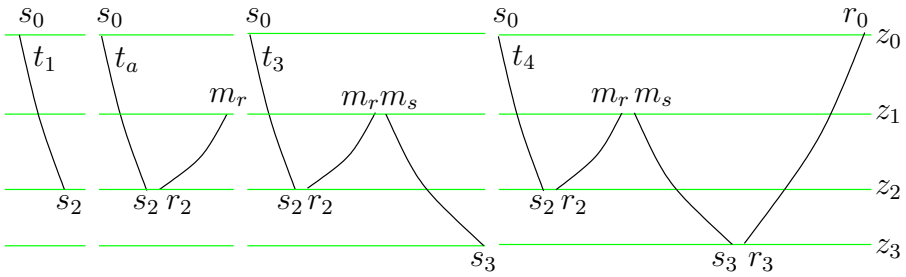

Figure 4.5. Triple scattering notations and conventions. This illustration assumes that the E_2 and E_1 operators have been applied to be clear which variable refers to which leg of the interactions.

$z = 0$. Thus,

$$\delta u_{-,1}(z_1, m, t_a, 0, s_0) = \tfrac{1}{4} D_{t_a}^2 \int \mathrm{d}\tilde{s}_0 \int_{\mathbb{R}} \mathrm{d}\tilde{t}_{s_0} f(0, \tilde{s}_0, \tilde{t}_{s_0}, 0, s_0) Q^*_{-,\tilde{s}_0}(0)$$
$$\int_{z_1}^{\infty} \mathrm{d}z_2 \int \mathrm{d}s_2 \int \mathrm{d}r_2 \int_{\mathbb{R}} \mathrm{d}t_0 \int_{\mathbb{R}} \mathrm{d}t' G_-(z_1, m, t_a - \tilde{t}_{s_0} - t' - t_0, z_2, r_2) G_-(0, \tilde{s}_0, t', z_2, s_2)$$
$$Q_{-,r_2}(z_2) Q_{-,s_2}(z_2)\ (E_2 E_1 a)(z_2, s_2, r_2, t_0)\,, \quad (4.77)$$

where $t' = t_1 - \tilde{t}_{s_0}$ and t_a is the running time variable along the ray (see Figure 4.5). We assume that the three scattering points for multiple scattering are sufficiently far apart. If a is a conormal distribution, its singular support is a countable set of hypersurfaces; thus assuming a to be a conormal distribution is sufficient to satisfy this assumption. This prevents an undefined multiplication of distributions from occurring (see Friedlander & Joshi (1998, Proposition 11.2.3) and Hörmander (1983, Theorem 8.2.10)). In (4.77), we have not returned to observables as the second leg, $G_-(z_1, m, t_a - \tilde{t}_{s_0} - t' - t_0, z_2, r_2)$, does not reach the surface ($z_1 > 0$). The field, $\delta u_{-,1}$ acts as the source of waves propagating from m to s_3, through the contrast source formulation used in the single-scattering case. (The contrast source was explicitly defined in Section 4.5 equation (4.25).) This gives,

$$\delta u_{+,2}(z_3, x_3, t_3, 0, s_0) = \tfrac{1}{2} \mathcal{H} D_{t_3}^2 \int_0^{z_3} \mathrm{d}z_1 \int \mathrm{d}m \int_{\mathbb{R}} \mathrm{d}t_a$$
$$G_+(z_3, x_3, t_3 - t_a, z_1, m) Q_{+,m}(z_1) a(z_1, m) Q^*_{-,m}(z_1) \delta u_{-,1}(z_1, m, t_a, 0, s_0)\,, \quad (4.78)$$

which acts as a contrast source for the final wave, propagating from (z_3, r_3) to $(0, r_0)$,

$$d_3(s_0, r_0, t_4) = -\tfrac{1}{2}\mathcal{H}D_{t_4}^2 Q^*_{-,r_0}(0)\int_0^\infty \mathrm{d}z_3 \int \mathrm{d}x_3 \int_{\mathbb{R}} \mathrm{d}t_3 \\ G_-(0, r_0, t_4 - t_3, z_3, x_3) Q_{-,x_3}(z_3) a(z_3, x_3) Q^*_{+,x_3}(z_3) \delta u_{+,2}(z_3, x_3, t_3, 0, s_0)\,, \quad (4.79)$$

where we have returned to observables through the operator $R\mathsf{Q}^{-1}$, introduced in (4.47). For the above construction to be valid, (z_1, x_1), (z_2, x_2) and (z_3, x_3) cannot be arbitrarily close to one another.

We now apply reciprocity (4.22) to the G_+ occurring in the expression for $\delta u_{+,2}$ in (4.78). We do this by substituting the expression for $\delta u_{+,2}$ in (4.78) into (4.79) to use the Q_+ operators from both expressions combined and introduce the extension operators E_1, E_2. This gives

$$d_3(s_0, r_0, t_4) = -\tfrac{1}{4}D_{t_4}^4 \int_0^\infty \mathrm{d}z_3 \int \mathrm{d}s_3 \int \mathrm{d}r_3 \int_{\mathbb{R}} \mathrm{d}t_3 \int_0^{z_3} \mathrm{d}z_1 \int \mathrm{d}m_s \int \mathrm{d}m_r \int_{\mathbb{R}} \mathrm{d}t_a \\ Q^*_{-,r_0}(0) G_-(0, r_0, t_4 - t_3, z_3, r_3) Q_{-,r_3}(z_3) \\ Q^*_{-,m_s}(z_1) G_-(z_1, m_s, t_3 - t_a, z_3, s_3) Q_{-,s_3}(z_3) \\ (E_1 a)(z_3, s_3, r_3)(E_1 a)(z_1, m_s, m_r) Q^*_{-,m_r}(z_1) \delta u_{-,1}(z_1, m_r, t_a, 0, s_0)\,; \quad (4.80)$$

we have also introduced the extension operator E_1, to split each of the m and x_3 integrations into two.

Identifying the propagator $Q_{-,x_a}(z_a) G_-(z_a, z_b) Q_{-,z_b}(z_b)$ in (4.80) with the function $G(z_a, x_a, t, z_b, x_b)$ in equation (8) of ten Kroode (2002) along with the substitution of the expression for $\delta u_{-,1}$ in (4.77) shows the correspondence of (4.80) with expression (8) in ten Kroode (2002). (Note that $V(x)$ in ten Kroode (2002) is $a(z, x)$ here.)

We interchange the order of integration in t_3 and t_a, and change integration variables from t_3 to $t_3' = t_3 - t_a$, introducing the E_2 operator at the third scatter. This results in

$$d_3(s_0, r_0, t_4) = -\tfrac{1}{4}D_t^4 \int_0^\infty \mathrm{d}z_3 \int \mathrm{d}s_3 \int \mathrm{d}r_3 \int_{\mathbb{R}} \mathrm{d}t_{30} \int_{\mathbb{R}} \mathrm{d}t_a \int_0^{z_3} \mathrm{d}z_1 \int \mathrm{d}m_s \int \mathrm{d}m_r \\ \int_{\mathbb{R}} \mathrm{d}t_3' Q^*_{-,r_0}(0) G_-(0, r_0, t_4 - t_a - t_3' - t_{30}, z_3, r_3) Q_{-,r_3}(z_3) \\ Q^*_{-,m_s}(z_1) G_-(z_1, m_s, t_3', z_3, s_3) Q_{-,s_3}(z_3) \\ (E_2 E_1 a)(z_3, s_3, r_3, t_{30})(E_1 a)(z_1, m_s, m_r) Q^*_{-,m_r}(z_1) \delta u_{-,1}(z_1, m_r, t_a, 0, s_0)\,, \quad (4.81)$$

which is a modeling operator for triply scattered waves. We need not introduce E_2 at the m_s, m_r scattering point here, but it will be required later. Equations (4.81) and (4.78) are expressed entirely in terms of up-going propagators (G_-); they comprise the $m = 2$ term of the forward series, given in the summation in (4.47).

The recursion in equation (4.61) demonstrates that it is possible to express the triply scattered data, d_3, in terms of the singly scattered data d_1. The first step to writing d_3 in

terms of the singly scattered data is to reformulate (4.81) so that propagation is always to the acquisition surface. This idea is motivated by the layer stripping approach proposed by Fokkema *et al.* (1994) to extend the work of Berkhout and Verschuur for surface multiples (Berkhout & Verschuur, 1997; Verschuur & Berkhout, 1997) to the internal multiple case.

Theorem 4.7.1. *Let the data be modeled by (4.47) for $M = 2$. Let*

$$\mathbf{d}_1(z_1; s_0, r_0, t) = \\ -\tfrac{1}{4} D_t^2 Q^*_{-,r_0}(0) Q^*_{-,s_0}(0) \int_{z_1}^{\infty} \mathrm{d}z \left(H(0,z) Q_{-,r}(z) Q_{-,s}(z) (E_2 E_1 a) \right)(s_0, r_0, t) \quad (4.82)$$

represent the single scattered data constituent observed at the surface, but scattered below the depth z_1. Define

$$W(z_1; s_0, m'_r, t, m'_s, r_0) = \int_{\mathbb{R}} \mathrm{d}t_b \, \mathbf{d}_1(z_1; m'_s, r_0, t - t_b) \mathbf{d}_1(z_1; s_0, m'_r, t_b) \,, \quad (4.83)$$

and let d_3 denote the triply scattered field corresponding with the $m = 2$ term in (4.47). Then,

$$d_3(s_0, r_0, t_4) = D_t^2 \int_0^{\infty} \mathrm{d}z_1 \int \mathrm{d}m_s \int \mathrm{d}m_r \int_{\mathbb{R}} \mathrm{d}t_{m_0} (E_2 E_1 a)(z_1, m_s, m_r, t_{m_0}) \\ Q^*_{-,m_s}(z_1) Q^*_{-,m_r}(z_1) H(0,z_1)^* Q^*_{-,m'_r}(0)^{-1} Q^*_{-,m'_s}(0)^{-1} W(z_1; s_0, \overset{m'_r}{\cdot}, t_4 + \overset{t_{m'}}{\cdot}, \overset{m'_s}{\cdot}, r_0) \,. \quad (4.84)$$

The proof is given in Appendix J. The fictitious data $\mathbf{d}_1$ are the singly scattered data constituent predicting reflections below the level z_1. Because W is estimated at $z = 0$ but depends explicitly on z_1, the depth level that generates multiples, we separate z_1 from the other variables with a semi-colon.

Estimating multiples in this way requires knowledge of the velocity model down to depth z_1; we assume instantaneous point sources and receivers. Assuming the traveltime monotonicity assumption as done in ten Kroode (2002), would allow the restriction in z_1 to be translated to a restriction on the time $t - t_s$, allowing $\mathbf{d}_1$ to be computed from d_1 by windowing in time. Expression (4.84) can be viewed as an inner product in the (m_s, m_r, t_{m_0}) variables.

In Appendix K, we write d_3 entirely in terms of the data, completing the correspondance with (4.61) and compare our approach to that of Weglein *et al.* (1997) and ten Kroode (2002).

4.8 Inverse scattering method

Rather than following the approach of attenuating multiples in the data, we estimate and attenuate artifacts in the image caused by leading-order internal multiples. This requires an estimate of the multiples in the image rather than in the data as we have done

thus far. To this end, we now discuss an inverse scattering theory. From the inverse series, constructed in section 4.6.2, we note that only a single-scattering inverse is required, because for each term in the series we estimate $\widehat{V}_j$ from $\mathsf{M}_0(\widehat{V}_j U_0)$ based on the recursion in (4.61).

The Born modeled data, d_1, as given in (4.48), is measured in the field but its vertical derivative is not. A left inverse to the Born modeling operator, the inverse scattering operator, can be constructed under the double-square root (DSR) assumption (see section 4.4 and Stolk & de Hoop (2004a)). This operator gives an estimate of $a(z,x)$ via

$$\langle a_1 \rangle = T d_1 \,, \tag{4.85}$$

where T is the inverse scattering operator and $\langle a_1 \rangle$ is the single scattering estimate of a. Once an estimate of a is obtained, it can be substituted into (4.33) to obtain an estimate of $\widehat{V}$.

Stolk & de Hoop (2004b) give a detailed method for inverse scattering from singly scattered data; here we give a brief summary. The construction involves the depth-to-time conversion operator, $\bar{K}$, defined as

$$\bar{K} : a \mapsto -\int_0^\infty H(0,z)(E_2 a)(z,\cdot,\cdot,\cdot)(s,r,t)\mathrm{d}z \,. \tag{4.86}$$

Stolk and de Hoop show that this operator is an invertible Fourier integral operator. Upon substitution of a point source in (4.76), we obtain

$$d_1 = \tfrac{1}{4} D_t^2 Q^*_{-,s}(0) Q^*_{-,r}(0) \bar{K} J(E_1 a) \,. \tag{4.87}$$

The operator J (denoted V by Stolk & de Hoop (2004b)), has symbol

$$\begin{aligned} &J(z,s,r,\zeta,\sigma,\rho) = \\ &\qquad |\tau|^{-1}(c_0(z,s)^{-2} - \tau^{-2}\|\sigma\|^2)^{-1/4}(c_0(z,r)^{-2} - \tau^{-2}\|\rho\|^2)^{-1/4}|_{\tau=\Theta^{-1}(z,s,r,\zeta,\sigma,\rho)} \,. \end{aligned} \tag{4.88}$$

This operator is related to the $Q_{-,s}(z)Q_{-,r}(z)$ appearing in (4.76); the difference is that J is applied before the E_2 extension operator whereas $Q_{-,s}(z)Q_{-,r}(z)$ is applied after (note that Q and E_2 do not commute). The map Θ is defined by

$$\Theta(z,s,r,\sigma,\rho,\tau) = -b(z,s,\sigma,\tau) - b(z,r,\rho,\tau) \,. \tag{4.89}$$

Stolk & de Hoop (2004a, Lemma 4.1) show that $\tau \mapsto \zeta = \Theta(z,s,r,\sigma,\rho,\tau)$ is a diffeomorphism. The mapping from frequency to vertical wavenumber described by this map is required for J to be applied before the E_2 extension operator.

After defining the adjoint operator in space (restriction to $h=0$) by $R_1 = E_1^*$, the adjoint operator in time (restriction to $t=0$) by $R_2 = E_2^*$, and the normal operator $\bar{\Xi}$ which is equal to the principal part of $\bar{K}^*\bar{K}$ we have

$$\bar{\Phi}(z,x,D_z,D_x)a = R_1 J^{-1} \bar{\Xi}^{-1} \bar{K}^* Q^*_{-,s}(0)^{-1} Q^*_{-,r}(0)^{-1} D_t^{-2} d_1 \,, \tag{4.90}$$

where $\bar{\Phi}$ is shown in Stolk & de Hoop (2004b, Theorem 2.2, Remark 2.4) to be a pseudodifferential operator. It is given by

$$\bar{\Phi} = R_1 J^{-1} \bar{\Xi}^{-1} \bar{K}^* \bar{K} V E_1 \,. \tag{4.91}$$

The operator $\bar{\Phi}$ influences only the amplitudes of the image; its symbol is calculated by Stolk & de Hoop (2004b, Lemma 2.1, Theorem 2.2, Remark 2.4).

From the above discussion, a can be reconstructed under the following assumption, discussed in detail by Stolk and de Hoop. This assumption places a minor restriction on the allowed type of multipathing. It states that, if there are two ray paths through the subsurface such that identical data points are generated (i.e. arriving at the same receiver position and direction, from the same source position and direction, traveling for the same amount of time) then these paths must be somewhere horizontal, violating the first assumption. Under these assumptions we identify, microlocally, $\bar{\Phi}^{-1} R_1 J^{-1} \bar{\Xi}^{-1} K^* Q^*_{-,s}(0)^{-1} Q^*_{-,r}(0)^{-1} D_t^{-2}$, where $\bar{\Phi}^{-1}$ denotes the parametrix of $\bar{\Phi}$, as the inverse of the first entry of $-D_t^2 \mathsf{M}_0(\widehat{V}_1 U_0)$ (cf. (4.47)) from which we compute an estimate of the distribution, a. From (4.61) we then have

$$\langle a_1 \rangle = \bar{\Phi}^{-1} R_1 J^{-1} \bar{\Xi}^{-1} \bar{K}^* Q^*_{-,s}(0)^{-1} Q^*_{-,r}(0)^{-1} D_t^{-2} d \,. \tag{4.92}$$

In (4.92) we have used the single scattering approximation, in which the data in (4.55) are used as an approximation of the data in (4.76). We use the $\langle \cdot \rangle$ notation to indicate that this is an estimate of a rather than its true value; the subscript 1 indicates that this estimate is obtained in the single scattering approximation. From this estimate of a, we obtain an estimate of the operator matrix V_1 using (4.33),

$$\langle \widehat{V}_1 \rangle = \tfrac{1}{2} \mathcal{H} \begin{pmatrix} Q_+ \langle a_1 \rangle Q^*_+ & Q_+ \langle a_1 \rangle Q^*_- \\ -Q_- \langle a_1 \rangle Q^*_+ & -Q_- \langle a_1 \rangle Q^*_- \end{pmatrix} . \tag{4.93}$$

4.9 The downward continuation approach to inverse scattering for internal multiples

The construction of $\mathbf{d}$ with (4.82), at the surface, requires both an estimate of a and the modeling of the wavefield from this estimate; both of these steps are computationally expensive. If the d_3 data set could be computed at the depth z_1 rather than at the surface $z = 0$ this problem can be avoided. In this section, we give three results that form the framework of an algorithm to estimate artifacts caused by internal multiples in imaging. We assume that the DSR assumption (see below Remark 4.4.3) holds throughout this section.

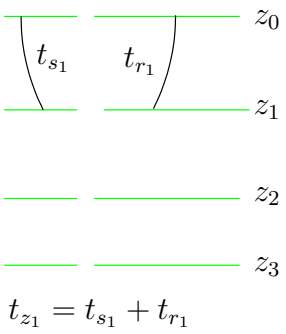

Figure 4.6. Time notations used to estimate d_3 at z_1.

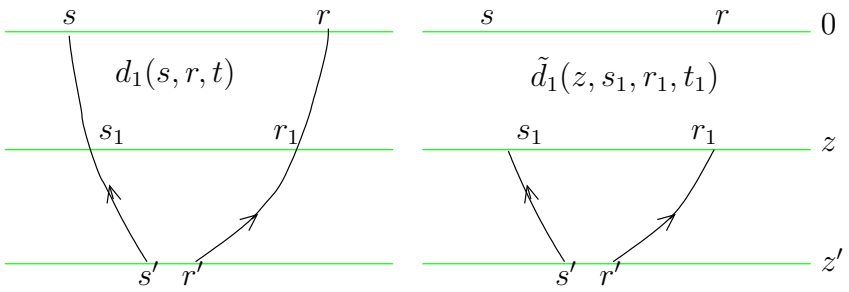

Figure 4.7. Illustration of Lemma 4.9.1; the construction of $\tilde{d}_1$ from d_1.

Lemma 4.9.1. *We define*

$$\tilde{d}_1(z,s,r,t) = -\tfrac{1}{4}D_t^2\int_z^\infty \mathrm{d}z' \left(H(z,z')Q_{-,r'}(z')Q_{-,s'}(z')(E_2E_1a)(z',{}^{s'}_{\cdot},{}^{r'}_{\cdot},{}^{t'}_{\cdot}) \right)(s,r,t)\,. \quad (4.94)$$

For $t > 0$

$$\left(H(0,z)^*Q^*_{-,s}(0)^{-1}Q^*_{-,r}(0)^{-1}d_1\right)(s,r,t) = \tilde{d}_1(z,s,r,t)\,, \quad (4.95)$$

where d_1 *is modeled by (4.76).*

This Lemma is illustrated in Figure 4.7.

Proof. We first define $\bar{a} = \chi a$ where χ is the characteristic function of (z,∞). With this definition we write $\tilde{d}_1$ as

$$\tilde{d}_1(s,r,t) = -\tfrac{1}{4}D_t^2\int_0^\infty \mathrm{d}z' \left(H(z,z')Q_{-,r'}(z')Q_{-,s'}(z')(E_2E_1\bar{a})(z',{}^{s'}_{\cdot},{}^{r'}_{\cdot},{}^{t'}_{\cdot}) \right)(s,r,t)\,. \quad (4.96)$$

We then examine

$$\begin{aligned} & Q^*_{-,s}(0)Q^*_{-,r}(0)H(0,z)\tilde{d}_1 - d_1 \qquad (4.97)\\ &= -\tfrac{1}{4}D_t^2 Q^*_{-,s}(0)Q^*_{-,r}(0) \\ &\qquad \int_0^\infty \left(H(z,z')Q_{-,r'}(z')Q_{-,s'}(z')(E_2E_1(\chi-1)a)(z',\overset{s'}{\cdot},\overset{r'}{\cdot},\overset{t'}{\cdot}) \right)(s,r,t) \\ &= -\tfrac{1}{4}D_t^2 Q^*_{-,s}(0)Q^*_{-,r}(0)\int_0^z \left(H(z,z')Q_{-,r'}(z')Q_{-,s'}(z')(E_2E_1a)(z',\overset{s'}{\cdot},\overset{r'}{\cdot},\overset{t'}{\cdot}) \right)(s,r,t)\,. \end{aligned}$$

Applying $H(0,z)^*Q^*_{-,s}(0)^{-1}Q^*_{-,r}(0)^{-1}$ to both sides of (4.97) gives

$$\begin{aligned} & \tilde{d}_1 - H(0,z)^*Q^*_{-,s}(0)^{-1}Q^*_{-,r}(0)^{-1}d_1 \qquad (4.98)\\ &\quad = -\tfrac{1}{4}D_t^2\; H(0,z)^*\int_0^z \left(H(z,z')Q_{-,r'}(z')Q_{-,s'}(z')(E_2E_1a)(z',\overset{s'}{\cdot},\overset{r'}{\cdot},\overset{t'}{\cdot}) \right)(s,r,t)\,. \end{aligned}$$

The composition $H(0,z)^*H(0,z')$ is zero for $t \le 0$ because from the DSR assumption we have that if z increases t increases and vice-versa. Because $z > z'$, $H(0,z)^*$ propagates for a longer (negative) time than does $H(0,z')$ resulting in no contribution for $t > 0$. □

Equation (4.95) describes a method of estimating (for single scattering) the data that would have been recorded had the experiment been performed at depth z from the data recorded at the surface; this is downward continuation.

We now define the convolution of the $\tilde{d}_1$ data sets, for $t > 0$ at the depth z, of the second scattering point for leading order internal multiples

$$\begin{aligned} \tilde{d}_3(z,s,r,t) = D_t^2 \int \mathrm{d}s' \int \mathrm{d}r' Q^*_{-,s'}(z)(E_1a)(z,s',r')Q^*_{-,r'}(z) \\ \tilde{d}_1(z,s',r,\overset{t}{\cdot}) \overset{(t)}{*} \tilde{d}_1(z,s,r',\overset{t}{\cdot})\,. \qquad (4.99) \end{aligned}$$

The operator E_1 contains $\delta(s'-r')$, thus the integral in (4.99) is over all possible scattering points along with a procedure to connect the two $\tilde{d}_1$ data sets.

Remark 4.9.2. If we replace $D_t^2 a$ in (4.99) with -1 and the second scattering point is at the surface $z = 0$ then (4.99) becomes,

$$\begin{aligned} \tilde{d}_3^S(0,s,r,t) = -Q^*_{-,s}(0)Q^*_{-,r}(0) \int \mathrm{d}s' \int \mathrm{d}r' Q^*_{-,s'}(0)Q^*_{-,r'}(0) \\ \tilde{d}_1(0,s',r,\overset{t}{\cdot}) \overset{(t)}{*} \tilde{d}_1(0,s,r',\overset{t}{\cdot})\,, \qquad (4.100) \end{aligned}$$

returning to observables via $Q^*_{-,s}(0)Q^*_{-,r}(0)$. Noting that $Q^*_{-,s}(0)Q^*_{-,r}(0)\tilde{d}_1(0,s,r,t) = d_1(s,r,t)$ gives

$$d_3^S(s,r,t) = -\int \mathrm{d}s' \int \mathrm{d}r' d_1(s',r,\overset{t}{\cdot}) \overset{(t)}{*} d_1(s,r',\overset{t}{\cdot})\,. \qquad (4.101)$$

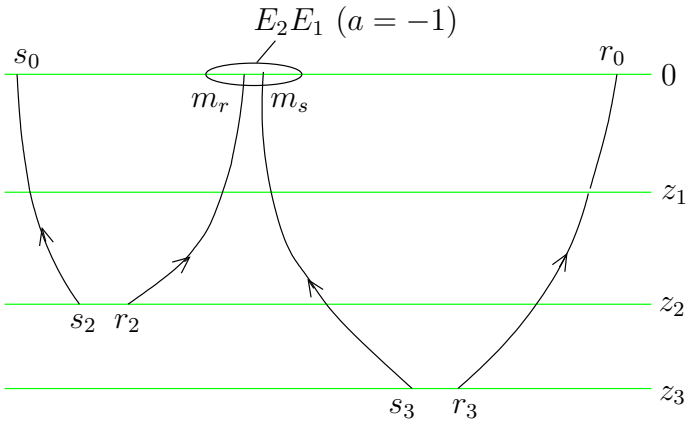

Figure 4.8. Illustration of the surface-related multiple case (SRME).

relating our method to the surface-related multiple elimination (SRME) procedure of Fokkema & van den Berg (1993, chapter 12). This is illustrated in Figure 4.8.

The following theorem describes the relation between the internal multiple estimated at the surface through (4.84) given in Theorem 4.7.1 and the estimate of $\tilde{d}_3$ defined in (4.99).

Theorem 4.9.3. *Let the data be modeled by the forward scattering series (4.47) for $M = 2$. Then there is the following correspondance between the leading-order internal multiple modeled at the surface and $\tilde{d}_3$*

$$d_3(s_0,r_0,t_0) = Q^*_{-,r_0}(0)Q^*_{-,s_0}(0)\int_0^\infty \mathrm{d}z_1 \left(H(0,z_1)\tilde{d}_3(z_1,\overset{s}{\cdot},\overset{r}{\cdot},\overset{t}{\cdot})\right)(s_0,r_0,t_0)\,. \tag{4.102}$$

The theorem is illustrated in Figure 4.9.

Proof. We begin by returning to (4.77),

$$\begin{aligned}\delta u_{-,1}(z_1,m,t_a,0,s_0) = \\ -\tfrac{1}{4}D^2_{t_a}Q^*_{-,s_0}(0)\int_{z_1}^\infty \mathrm{d}z_2 \int \mathrm{d}s_2 \int \mathrm{d}r_2 \int_{\mathbb{R}}\mathrm{d}t_0 \int_{\mathbb{R}}\mathrm{d}t' G_-(z_1,m,t_a-t'-t_0,z_2,r_2) \\ \int \mathrm{d}s_1 \int_{\mathbb{R}}\mathrm{d}t_{s_1} G_-(0,s_0,t_{s_1},z_1,s_1)G_-(z_1,s_1,t'-t_{s_1},z_2,s_2) \\ Q_{-,r_2}(z_2)Q_{-,s_2}(z_2)(E_2E_1a)(z_2,s_2,r_2,t_0)\,,\end{aligned} \tag{4.103}$$

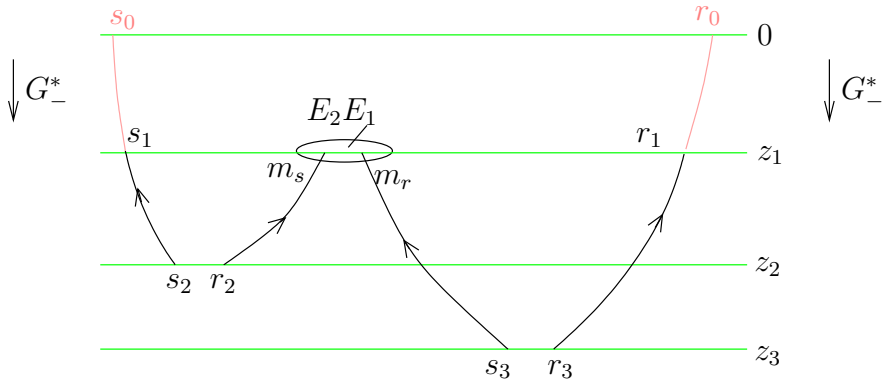

Figure 4.9. The d_3 data set at the depth z_1. The ellipse illustrates the application of the E_2E_1 operators to join the two data sets at m_s, m_r, t_{m_0}. This diagram illustrates the downward continuation of d_3 to form $\tilde{d}_3$ at depth z_1 as in Theorem 4.9.3. The gray paths extending from z_1 to the surface illustrate the modeling of d_3 from $\tilde{d}_3$ with $\tilde{d}_3$ acting as a contrast source or the estimation of $\tilde{d}_3$ from d_3.

assuming a point source and using relation (4.23). We then change the order of integration in preparation of substituting H,

$$\begin{aligned}\delta u_{-,1}(z_1, m, t_a, 0, s_0) = -\tfrac{1}{4} D_{t_a}^2 Q_{-,s_0}^*(0) \int \mathrm{d}s_1 \int_{\mathbb{R}} \mathrm{d}t_{s_1} G_-(0, s_0, t_{s_1}, z_1, s_1) \\ \left\{ \int_{z_1}^{\infty} \mathrm{d}z_2 \int \mathrm{d}s_2 \int \mathrm{d}r_2 \int_{\mathbb{R}} \mathrm{d}t_0 \int_{\mathbb{R}} \mathrm{d}t' G_-(z_1, m, t_a - t' - t_0, z_2, r_2) \right. \\ \left. G_-(z_1, s_1, t' - t_{s_1}, z_2, s_2) Q_{-,r_2}(z_2) Q_{-,s_2}(z_2) (E_2E_1 a)(z_2, s_2, r_2, t_0) \right\} . \quad (4.104)\end{aligned}$$

Substituting H (cf. (4.75)), for the two $G_-(z_1, x_2)$ propagators leads to the simplification

$$\begin{aligned}\delta u_{-,1}(z_1, m, t_a, 0, s_0) = -Q_{-,s_0}^*(0) \int \mathrm{d}s_1 \int_{\mathbb{R}} \mathrm{d}t_{s_1} G_-(0, s_0, t_{s_1}, z_1, s_1) \\ \tilde{d}_1(z_1, s_1, m, t_a - t_{s_1}) , \quad (4.105)\end{aligned}$$

where we have substituted $\tilde{d}_1$ (given in Lemma 4.9.1) for the expression in braces in (4.104).

The same sequence of steps applied to (4.81) gives

$$d_3(s_0,r_0,t_4) = -\tfrac{1}{4}D_t^2\int_0^\infty \mathrm{d}z_1\int \mathrm{d}r_1\int \mathrm{d}t_{r_1} Q^*_{-,r_0}(0)G_-(0,r_0,t_{r_1},z_1,r_1)$$
$$\int \mathrm{d}m_s\int \mathrm{d}m_r Q^*_{-,m_s}(z_1)\int_{\mathbb{R}}\mathrm{d}t_a \tilde{d}_1(z_1,m_s,r_1,t_4-t_a-t_{r_1})$$
$$(E_1a)(z_1,m_s,m_r)Q^*_{-,m_r}(z_1)\delta u_{-,1}(z_1,m_r,t_a,0,s_0)\,, \quad (4.106)$$

where we have also interchanged the order of integration. Substituting the expression for $\delta u_{-,1}$ from (4.105) into (4.106) and re-ordering the Q operators and the G_- propagators results in

$$d_3(s_0,r_0,t_4) =$$
$$D_t^2 Q^*_{-,r_0}(0)Q^*_{-,s_0}(0)\int_0^\infty \mathrm{d}z_1\int \mathrm{d}m_s\int \mathrm{d}m_r Q^*_{-,m_s}(z_1)(E_1a)(z_1,m_s,m_r)$$
$$Q^*_{-,m_r}(z_1)\int_{\mathbb{R}}\mathrm{d}t_a G_-(0,z_1)\tilde{d}_1(z_1,m_s,\overset{r_1}{\cdot},t_4-t_a-\overset{t_{r_1}}{\cdot})G_-(0,z_1)\tilde{d}_1(z_1,\overset{s_1}{\cdot},m_r,t_a-\overset{t_{s_1}}{\cdot})\,. \quad (4.107)$$

Combining the two G_- propagators into a single H operator gives the result.

□

Equation (4.102) is equivalent to (4.76) with $\tilde{d}_3$ taking the place of the contrast source.

Theorem 4.9.4. *Assume the inverse scattering series (4.62) for $M = 2$. If we replace d_1 in (4.95) in Lemma 4.9.1 by d and a in equation (4.99) for $\tilde{d}_3$ by a_1 then*

$$\langle a_3(z,x)\rangle = (\Phi^{-1}R_1J^{-1}\bar{\Xi}^{-1}R_2D_t^{-2}\tilde{d}_3(z,\overset{s}{\cdot},\overset{r}{\cdot},\overset{t}{\cdot}))(x)\,. \quad (4.108)$$

Proof. Recall from the recursion in (4.61) that

$$D_t^2\mathsf{M}_0(\widehat{V}_3U_0) = D_t^6\mathsf{M}_0(\widehat{V}_1\mathsf{L}_0(\widehat{V}_1\mathsf{L}_0(\widehat{V}_1U_0)))\,. \quad (4.109)$$

Theorem 4.7.1 shows that d_3 is third order in $\widehat{V}_1$ and thus third order in d. We then estimate $\widehat{V}_3$ directly from d_3 using (4.92).

$$\begin{aligned}\langle a_3\rangle &= \Phi^{-1}R_1J^{-1}\bar{\Xi}^{-1}K^*D_t^2d_3\\ &= \Phi^{-1}R_1J^{-1}\bar{\Xi}^{-1}R_2H(0,z)^*Q^*_{-,r}(0)^{-1}Q^*_{-,s}(0)^{-1}D_t^{-2}d_3\,. \quad (4.110)\end{aligned}$$

The argument in the proof of Lemma 4.9.1 can be repeated for the expression for d_3 in (4.102), recalling that $\tilde{d}_3$ is defined for $t > 0$ giving

$$\tilde{d}_3(z,s,r,t) = (H(0,z)^*Q^*_{-,s}(0)^{-1}Q^*_{-,r}(0)^{-1}d_3)(z,s,r,t)\,, \quad (4.111)$$

for $t > 0$. We then have

$$\langle a_3(z,x)\rangle = (\Phi^{-1}R_1J^{-1}\bar{\Xi}^{-1}R_2D_t^{-2}\tilde{d}_3(z,\overset{s}{\cdot},\overset{r}{\cdot},\overset{t}{\cdot}))(x)\,. \tag{4.112}$$

□

An estimate of $\widehat{V}_3$ is obtained from $\langle a_3\rangle$ by

$$\langle\widehat{V}_3\rangle = \tfrac{1}{2}\mathcal{H}\begin{pmatrix} Q_+\ \langle a_3\rangle\ Q_+^* & Q_+\ \langle a_3\rangle\ Q_-^* \\ -Q_-\ \langle a_3\rangle\ Q_+^* & -Q_-\ \langle a_3\rangle\ Q_-^* \end{pmatrix}, \tag{4.113}$$

so that the estimate of $\widehat{V}$ becomes

$$\widehat{V} \approx \widehat{V}_1 + \widehat{V}_3\,. \tag{4.114}$$

The estimate $\langle a_3\rangle$ corrects $\langle a_1\rangle$ by estimating and subtracting the erroneous contributions to $\langle a_1\rangle$ due to the single scattering assumption. Thus artifacts in the image, caused by internal multiples, are removed by subtracting an image of the multiples from an image of the full data set. Leading-order internal multiples and primaries have different illumination properties and therefore the estimated image artifacts will never be entirely accurate. We anticipate accounting for these illumination differences as well as errors in the estimate of d_3 via adaptive subtraction.

Remark 4.9.5. To estimate $\tilde{d}_3$ at depth z_1, knowledge of the velocity model is necessary only to the depth z_1; this knowledge is necessary to estimate $\tilde{d}_1$ at z_1. The same part of the velocity model is required to form an image at z_1, $\langle a_1\rangle$ or $\langle a_3\rangle$, from the data. To form a complete image of the subsurface a velocity model is necessary for all depths.

Remark 4.9.6. In this remark, we illustrate the estimation of $\langle a_3\rangle$ with an isochron construction. In Figure 4.10 a contribution to $\langle a_3\rangle$ is shown. If the single scattering inverse is applied to the data d to estimate $\langle a_1\rangle$, the contributions from a particular source, receiver and time would be spread over the single scattering isochron (dashed curve). Although this is correct for a primary reflection, such as that shown with the dot-dash line, it is incorrect for a leading-order internal multiple, such as that shown with the solid rays. To correct these errors, $\langle a_3\rangle$ is estimated and subtracted, adaptively, from $\langle a_1\rangle$. The horizontal gray line in Figure 4.10 shows the depth level z_1 at which d_3 is estimated. The first step in constructing d_3 is to remove the parts of the two data sets in the gray box. This also removes the part of the associated isochron in the gray box. (These isochrons are the solid curves in the figure.) Next the contribution, spread over the remainder of the isochrons is combined through a time convolution, adding the contributions from the two single scattering isochrons. This constructs d_3 at the depth z_1. Applying the single scattering inverse to this data set spreads the contribution from this point along the single scattering isochron (dashed curve), giving $\langle a_3\rangle$. This contribution can then be subtracted from $\langle a_1\rangle$.

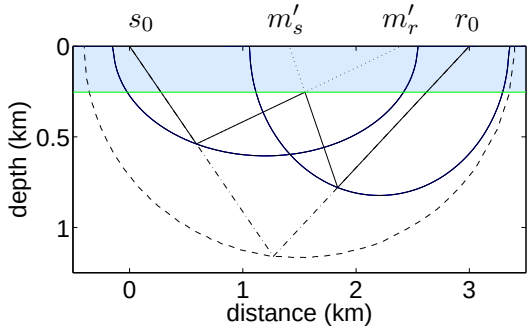

Figure 4.10. A contribution to $\langle a_3 \rangle$. The solid rays are the triply scattered rays. The dash-dot line is the singly scattered contribution with the same source and receiver positions as well as slopes. The dashed curve is the single scattering isochron, for the time t_4 corresponding to the amount of time required to travel along the triply scattered path. The shaded region extends to the depth level z_1 to which the entire wavefield is propagated before generating the image correction via $\langle a_3 \rangle$.

4.10 Discussion

We propose a method for attenuating artifacts in the image generated by leading-order internal multiples. We give two main results: a structure for modeling leading-order internal multiples in (J.8) and (4.84), and a system to estimate leading-order internal multiples as part of the imaging procedure in (4.112). Our suggested algorithm is illustrated by the following flowchart

$$
\begin{array}{ccccccc}
 & & & \overset{(e)}{\curvearrowright} & & & \\
 & & d & & & & \\
 & & \overset{(a)}{\downarrow} & & & & \\
a_1(z.,) & \overset{(d)}{\leftarrow} & \tilde{d}_1(z) & \overset{(b)}{\rightarrow} & \tilde{d}_3(z) & \overset{(d)}{\rightarrow} & a_3(z,.) \\
 & & \overset{(c)}{\downarrow} & & \overset{(c)}{\downarrow} & & \\
 & & \tilde{d}_1(z+\Delta z) & \overset{(+)}{\rightarrow} & \tilde{d}_3(z+\Delta z)\,. & &
\end{array}
$$

In (a) the data are downward continued to the depth z, through Lemma 4.9.1. Following this, in (b) leading-order internal multiples are estimated via (4.99). In (c), both the data and the estimated multiple are propagated to the next depth, again through (4.95) in Lemma 4.9.1. An image is formed, in (d), at this depth via (4.112). The image is also used to obtain an estimate of a used in the estimate of d_3 from (4.99). The theory discussed requires knowledge of the velocity model to the depth z_1 of the up-to-down scatter at which the image is formed. In addition, an adaptive subtraction technique is necessary

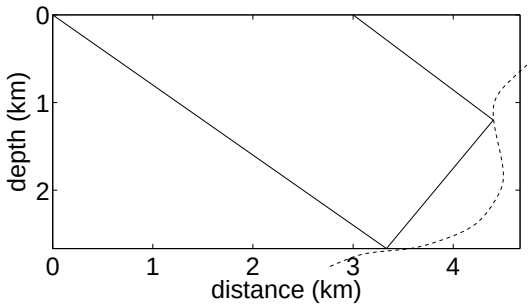

Figure 4.11. A contribution not accounted for by our theory is shown here; this is a doubly scattered event that would be recorded at the surface. The dashed line illustrates a surface that could generate such a scattering.

to compensate for differences in illumination between the singly and triply scattered data. Throughout this paper we have assumed a point source. When this assumption is not satisfied knowledge of the source wavelet is necessary because the source appears twice in the estimated first-order internal multiples and only once in the recorded first-order internal multiples. Under the traveltime monotonicity assumption, in the absence of caustics our theory is in correspondance with the velocity model independent theory of Weglein and ten Kroode . In Figure 4.11, a contribution that is not accounted for by our theory is shown. The event is a doubly scattered event, and thus will contribute to a_2, which is not estimated here. Events like this make an important contribution to seismic data, especially near salt. However, the contribution from the majority of doubly scattered events is lost to the interior of the Earth. Such contributions are therefore more important for transmission experiments than reflection experiments like those studied here.

4.11 Acknowledgments

We would like to thank John W. Stockwell for his assistance in the preparation of this manuscript. We are also grateful to the reviewers for their suggestions. This work was supported by Total and the sponsors of the Consortium Project on Seismic Inverse Methods for Complex Structures at the Center for Wave Phenomena.

Chapter 5

Identification of image artifacts due to leading-order internal multiples [1]

5.1 Summary

First order internal multiples are a source of coherent noise in seismic images. There are a number of techniques to estimate internal multiples in the data, but few methods exist that estimate imaging artifacts caused by internal multiples. We propose a method to do this in which the artifacts are estimated as part of the imaging process. Our technique is based on a hybrid of the Lippmann-Schwinger scattering series and the generalized Bremmer coupling series. Although we require knowledge of the velocity model this allows us to estimate internal multiples without assumptions inherent to other methods.

5.2 Introduction

Internal multiples have been recognized in seismic experiments for a long time (Sloat, 1948). A lot more is known about the attenuation of surface-related multiples (Aminzadeh & Mendel, 1980; Fokkema *et al.*, 1994; Berkhout & Verschuur, 1997; Verschuur & Berkhout, 1997; Weglein *et al.*, 1997), than is known about the attenuation of internal multiples (Weglein *et al.*, 1997; Jakubowicz, 1998; Kelamis *et al.*, 2002; ten Kroode, 2002; van Borselen, 2002). It is still not possible, to estimate multiples in data with sufficient accuracy to remove all the artifacts they introduce in seismic images. In this paper, we propose a technique for estimating imaging artifacts caused by internal multiples as part of the imaging process.

Fokkema & van den Berg (1993) use reciprocity to show the possibility of predicting surface-related multiples through a Neumann series expansion. As a point of departure we use the generalized Bremmer coupling series to model internal multiples, because its behavior and convergence are known (de Hoop, 1996). We then construct a hybrid series, using the contrast source formulation from the Lippmann-Schwinger scattering series (Lippmann, 1956; Weglein *et al.*, 1997), to estimate imaging artifacts caused by leading-order internal multiples. This hybrid series is amenable to the downward continuation approach unlike the Kirchhoff approximation (de Hoop, 2004). Using this method requires knowledge of the velocity model. Technically this knowledge is necessary only to the depth of the shallowest reflector involved in the generation of internal multiples (the depth of the up-to-down reflec-

[1] This chapter is expected to grow into a published paper with co-authors M. V. de Hoop and H. Calandra

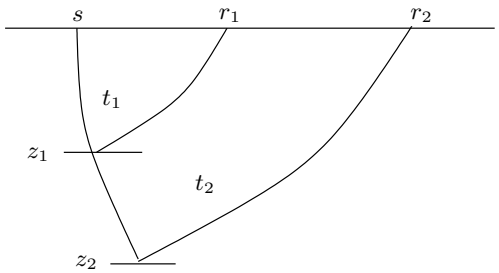

Figure 5.1. Illustration of the traveltime monotonicity assumption. The assumption states that if $z_1 < z_2$ then $t_1 < t_2$.

tion). Our technique is similar to that of Jakubowicz (1998) in that it uses the techniques of so-called wave-equation migration to model internal multiples. Our method differs from Jakubowicz (1998) in that we propose to estimate the artifacts caused by (first-order) internal multiples in the image rather than estimating the multiples in the data and in that we do not require the traveltime monotonicity assumption (ten Kroode, 2002). In addition, Jakubowicz uses implicitly a version of the generalized Bremmer series (de Hoop, 1996) whereas we use a hybrid of the Lippmann-Schwinger and Bremmer series.

The Lippmann-Schwinger series was introduced by Lippmann (1956) to model particle scattering. In the development of this series the wave-equation is solved in a known background model, with successive terms in the series being of successively higher order in the contrast operator. The contrast operator is the difference between the operator in the known background model and the same operator in the true model. This idea is developed further by Moses (1956); Prosser (1969) is developed for the quantum scattering problem and by Razavy (1975) for the wave equation. Weglein *et al.* (1997) use this series for the exploration seismic problem to develop techniques for both surface and internal multiple attenuation; they choose water velocity as the known reference model. Ten Kroode (2002) describes the theoretical foundation of this approach. In particular he notes that the suggested method requires two assumptions. The first assumption is that there are no caustics in the wavefield and the second is the so-called traveltime monotonicity condition. This condition is illustrated in Figure 5.1 and states that a wave excited at s and scattered at depth z_1 will arrive at the surface in less time than a wave following the same path from s to z_1, but scattering at z_2 instead, whenever z_1 is shallower than z_2.

The Bremmer series was introduced for planarly layered (1D) models by Bremmer (1951) and generalized to laterally heterogeneous models by de Hoop (1996). In the Bremmer series, the wavefield is split into up- and down-going constituents; these constituents are then coupled through reflection and transmission operators. Each term involves one more reflection/transmission and propagation step than the previous term. The first term of the series models direct waves, the second models singly scattered (where scattering may be reflection or transmission) waves and so on. The Bremmer series has been applied in

many problems (see van Stralen (1997) for an overview) and the convergence of various generalizations of the original series has also been a subject of interest (Atkinson, 1960; Corones, 1975; Gray, 1983; McMaken, 1986). Aminzadeh & Mendel (1980, 1981) were the first to propose a method using the Bremmer series to attenuate surface-related multiples in a horizontally layered medium.

To estimate artifacts in the image caused by first-order internal multiples (FOIM), we proceed in two steps. We first develop a method to model FOIM, using the hybrid series; this is described in Section 5.3. We circumvent the traveltime monotonicity condition through downward continuation. Following this, we predict internal multiples from downward continued data, to estimate the artifacts they cause in the image, using ideas from the inverse series in Section 5.4. In Section 5.5 we describe an algorithm to perform these two steps at the same time. We illustrate the application of this algorithm to synthetic and field data in Section 5.6.

5.3 The scattering series

We begin by decomposing the pressure wavefield, u, into its up- and down-going constituents, $u_\pm$ ($-$ denotes an up-going constituent and $+$ a down-going constituent). Following Stolk & de Hoop (2004a), we find that

$$\begin{pmatrix} u \\ \partial_z u \end{pmatrix} = \mathsf{Q}^{-1} \begin{pmatrix} u_+ \\ u_- \end{pmatrix} , \tag{5.1}$$

where

$$\mathsf{Q} = \frac{1}{2} \begin{pmatrix} (Q_+^*)^{-1} & -\mathcal{H} Q_+ \\ (Q_-^*)^{-1} & \mathcal{H} Q_- \end{pmatrix} ; \tag{5.2}$$

$\mathcal{H}$ denotes the Hilbert transform in time and * denotes adjoint. From this,

$$Q_-^* G_- \mathcal{H} Q_- ,$$

generates the upgoing constituents of the full-wave Green's function. The Q matrix, along with its inverse, diagonalizes the wave operator written as a first order system and thus splits the wavefield into its up- and down-going constituents.

The hybrid series uses the decomposition discussed above along with the contrast source from the Lippmann-Schwinger series. We use a subscript 0 to indicate the field in the background model and δ to represent a contrast, thus the field U in the unknown true medium is related to that in the known background medium by $U = U_0 + \delta U$. We denote by δU_j the vector of up- and down-going wave constituents scattered j times. The terms in the hybrid forward scattering series are related by

$$\delta U_1(\widehat{V}) = D_t^2 \mathsf{L}_0(\widehat{V} U_0), \quad \text{and} \quad \delta U_m(\widehat{V}) = D_t^2 \mathsf{L}_0(\widehat{V} \delta U_{m-1}(\widehat{V})) , \; m = 2, 3, \ldots \tag{5.3}$$

the full scattered field is related to these constituents by

$$\delta U = \sum_{m\in\mathbb{N}} \delta U_j \,. \tag{5.4}$$

Here

$$\widehat{V} = \tfrac{1}{2}\mathcal{H}\begin{pmatrix} Q_+\ a\ Q_+^* & Q_+\ a\ Q_-^* \\ -Q_-\ a\ Q_+^* & -Q_-\ a\ Q_-^* \end{pmatrix}$$

represents a matrix of reflection (diagonal entries) and transmission (off-diagonal entries) operators. We denote by $a = 2c_0^{-3}\delta c$ the velocity contrast, in which c_0 denotes the smooth background velocity and δc denotes the velocity contrast and by

$$\mathsf{L}_0 = \begin{pmatrix} G_+ & 0 \\ 0 & G_- \end{pmatrix} \tag{5.5}$$

the matrix of one-way propagators evaluated in the background velocity model. Denoting by R the restriction of the wavefield to the acquisition surface (depth $z = 0$), we define $\mathsf{M}_0 = R\mathsf{Q}^{-1}\mathsf{L}_0$. The data are then modeled as

$$\delta D = \begin{pmatrix} d \\ \partial_z d \end{pmatrix} = -D_t^2 \mathsf{M}_0(\widehat{V}(U_0 + \sum_{m\in\mathbb{N}} (-1)^{m+1}\delta U_m(\widehat{V}))). \tag{5.6}$$

The leading order term on the right-hand side represents the singly scattered or Born approximation. This contribution is written explicitly in terms of the propagator

$$(H(z_0,z_1))(s_0,r_0,t-t_0,s_1,r_1) = \int_{\mathbb{R}} (G_-(z_0,z_1))(r_0,t-t'-t_0,r_1)(G_-(z_0,z_1))(s_0,t',s_1)\,\mathrm{d}t', \tag{5.7}$$

of the double-square-root (DSR) (Claerbout, 1985) equation as

$$d_1(s_0,r_0,t) = \tfrac{1}{4}D_t^2 Q_{-,r_0}^*(0)Q_{-,s_0}^*(0) \int_0^\infty \mathrm{d}z H(0,z)Q_{-,r_1}(z_1)Q_{-,s_1}(z_1)(E_2E_1a)(z_1,s_1,r_1,t_0)\,, \tag{5.8}$$

where

$$E_1 : a(z,x) \mapsto \delta(r-s)a(z,\tfrac{r+s}{2}), \quad E_2 : a'(z,r,s) \mapsto \delta(t)a'(z,r,s).$$

Together the E_1 and E_2 operators map the velocity contrast at depth to fictitious data at depth; they can also be interpreted as the kernel of an operator.

5.4 Inverse scattering

In inverse scattering the goal is to solve for $\widehat{V}$ in terms of the data d. To this end, we assume that the contrast operator $\widehat{V}$ can be written as a series

$$\widehat{V} = \sum_{m\in\mathbb{N}} \widehat{V}_m(d)\,, \tag{5.9}$$

where $\widehat{V}_m$ is of order m in the data. Substituting this equation into (5.6) leads to the following relation between the $\widehat{V}_m(d)$,

$$D_t^2\mathsf{M}_0(\widehat{V}_m U_0) = D_t^4\mathsf{M}_0(\widehat{V}_{m-1}\mathsf{L}_0(\widehat{V}_1 U_0))\ \ , m\geq 2\,, \tag{5.10}$$

where

$$\delta D = -D_t^2\mathsf{M}_0(\widehat{V}_1 U_0)\,. \tag{5.11}$$

From this it follows that

$$-D_t^2\mathsf{M}_0(\widehat{V}U_0) = \delta D - \left(\sum_{m\in\mathbb{N}} D_t^2\mathsf{M}_0(\widehat{V}_m\delta U)\right)\,. \tag{5.12}$$

If we ignore the second term on the right-hand side, the problem of expressing $\widehat{V}$ in terms of the data reduces to inverse scattering in the Born approximation (Stolk & de Hoop, 2004b). In the context of wave-equation migration, the inverse scattering procedure is split into two parts: downward continuation and imaging, which are discussed in the next section.

5.5 Artifacts due to internal multiples in imaging

The first step in imaging is downward continuation. To do this, we apply the adjoint propagator $H(0,z)^*$ to the modeled data in (5.8) yielding the downward continued data at depth z,

$$\tilde{d}_1(z) = H(0,z)^* Q^*_{-,s}(0)^{-1} Q^*_{-,r}(0)^{-1} d\,, \tag{5.13}$$

for $t\geq 0$. This downward continuation uses the usual background velocity model to estimate the data that would have been recorded at the depth z. The downward continuated data, $\tilde{d}_1(z)$ is found directly from the medium contrast via

$$\tilde{d}_1(z,s,r,t) = -\tfrac{1}{4}D_t^2\int_z^\infty \mathrm{d}z' \left(H(z,z')Q_{-,r'}(z')Q_{-,s'}(z')(E_2E_1a)(z',\overset{s'}{\cdot},\overset{r'}{\cdot},\overset{t'}{\cdot})\right)(s,r,t)\,. \tag{5.14}$$

Next, we apply the 'true-amplitude' imaging condition, M, to the downward continued data

$$a_1(z,.) = R_1 M R_2 D_t^{-2}\tilde{d}_1(z) \tag{5.15}$$

where $R_1 = E_1^*$ and $R_2 = E_2^*$ are the usual imaging conditions ($t=0$ and $h=0$); this procedure is described in Stolk & de Hoop (2004b). We apply (5.13)-(5.15) to (5.12), from

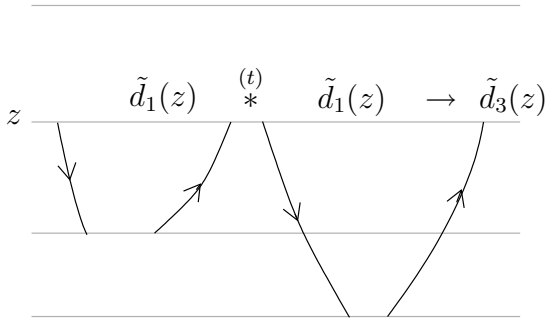

Figure 5.2. Illustration of equation 5.16, the estimation of the multiple at the depth z. The lines represent wavepaths rather than rays and do not connect as the imaging condition has not been applied.

which we obtain an image (first term on the right-hand side of 5.12) minus artifacts (second term on the right-hand side of 5.12).

From chapter 4, we have the following relation between the triply scattered data at depth $\tilde{d}_3(z)$ from the downward continued data $\tilde{d}_1(z)$,

$$\tilde{d}_3(z,s,r,t) = D_t^2 \iint Q^*_{-,s'}(z)(E_1 a)(z,s',r')Q^*_{-,r'}(z)\tilde{d}_1(z,s',r,\cdot) \overset{(t)}{*} \tilde{d}_1(z,s,r',\cdot)\mathrm{d}s'\mathrm{d}r' \,. \tag{5.16}$$

Expression (5.16) is valid upon restricting $\tilde{d}_1$ to $t > 0$ and assumes a point source. If the point source assumption is not satisfied, an estimate of the wavelet should be deconvolved from the estimated multiple. Equation (5.16) is illustrated in Figure 5.2.

To downward continue the multiples, d_3, we make use of the relation

$$d_3(s_0,r_0,t) = Q^*_{-,r_0}(0)Q^*_{-,s_0}(0)\int_0^\infty H(0,z)\tilde{d}_3(z,.)\,, \tag{5.17}$$

which states that the multiple, d_3 can be estimated at the surface, $z = 0$ from the multiple, $\tilde{d}_3$ estimated at the depth z. From the inverse scattering series, we replace the singly scattered downward continuted data (primaries only), $\tilde{d}_1$, with $\tilde{d}$ (all recorded data), the downward continuted data resulting in the following estimate of internal multiples at depth z

$$\tilde{d}_3(z,s,r,t) = D_t^2 \iint Q^*_{-,s'}(z)(E_1 a)(z,s',r')Q^*_{-,r'}(z)\tilde{d}(z,s',r,\cdot) \overset{(t)}{*} \tilde{d}(z,s,r',\cdot)\mathrm{d}s'\mathrm{d}r' \,. \tag{5.18}$$

Note the similarity between this expression and that used in the surface-related multiple elimination (SRME) procedure of Fokkema & van den Berg (1993) and Berkhout & Verschuur (1997).

Using relation (5.17) along with (5.13) we find that artifact in the image caused by FOIM at the depth z can be estimated by

$$a_3(z,.) = R_1 M R_2 D_t^{-2} \tilde{d}_3(z)\,, \tag{5.19}$$

the analog of (5.15).

We propose an algorithm summarized by the following flow chart

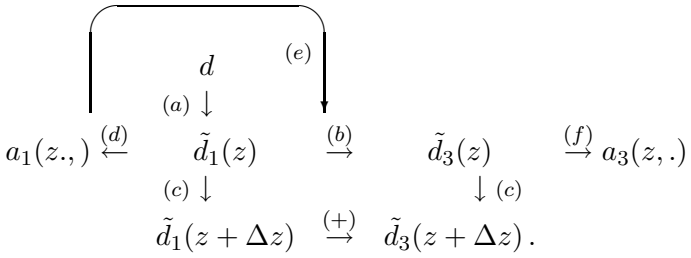

The algorithm can be divided into several steps. First, in (a), we downward continue the data to the depth z. Then in (b), the multiples are estimating using (5.18); this also requires an estimate of the image in (d). An estimate of the artifacts in the image is made in (f). The data and multiples are then downward continued to the next depth in (c).

5.6 Examples

Techniques like the angle-domain filtering proposed by Sava & Guitton (2005) are promising because they attenuate multiples directly in the image as opposed to in the data. In this way, even though the multiples are still not completely removed their location in the image is known. Thus, they are less likely to be misinterpreted as primary reflection energy.

In this section we describe both synthetic and field data results of the technique described above to estimate artifacts from FOIM directly in the image space. Three different synthetic models are presented. A simple flat model illustrates the steps of the algorithm. Following this a more complicated model is used to test the ability of the method to estimate imaging artifacts caused by FOIM in the presence of caustics and to test the sensitvity of the method to the velocity model. The third model shows the techniques applicability in a model with more complicated reflector shapes. The field data example is a 2D line extracted from a 3D survey in the Gulf of Mexico.

The algorithm used to generate the examples shown here falls into the category of a Generalized Screen Propagator. It is implemented as a split step propagator along with an implicit finite difference residual wide-angle correction. The propagator works in the midpoint-offset coordinates, requiring us to use a subset of the available data to obtain an uniformly sampled data set in these coordinates. This algorithm was proposed by Jin *et al.* (1998).

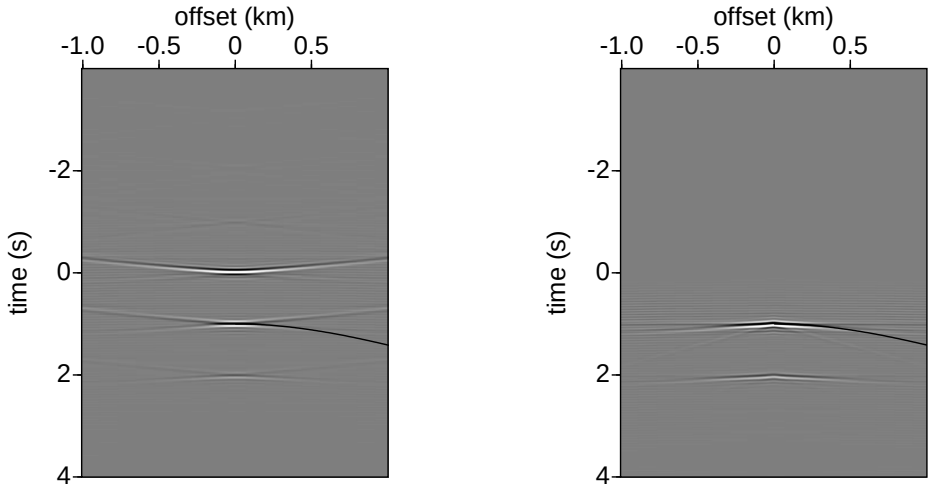

Figure 5.3. Data downward continued to the 1.5 km, the depth of the first reflector. The solid line shows the expected moveout for the reflection from the bottom of the layer. Left: before the removal of the part of the data at $t \leq 0$. Right: after the removal of the part of the data at $t \leq 0$.

The displayed images have had automatic gain control (AGC) applied to enhance the multiple without increasing the noise present around the correctly imaged reflectors. The artifacts that are suppressed in this way are caused by a combination of Fourier wrap-around, aliasing and boundary effects; this error was suppressed in the imaging as much as possible by padding with zeros and tapering the data in both midpoint and offset. In many cases the true reflectors are clipped to show the artifacts more clearly. We have not deconvolved the source wavelet in the estimated artifacts. As a partial compensation we have applied a bandpass filter to match the frequency content of the image and the estimated artifacts.

5.6.1 Flat Model

We begin with a simple, layered, example to illustrate the theory and then proceed to more complicated examples. The first example is a single layer, 1 km thick extending from 1.5 to 2.5 km, with a velocity of 2 km/s embedded in a homogeneous model with velocity 6 km/s. Synthetic data were computed in this model with finite difference modeling, 101 midpoints were generated with 101 offsets at each midpoint and a spacing of 15 m in both midpoint and offset (we define offset as $(s - r)/2$); 4 seconds of data were recorded at 4 ms

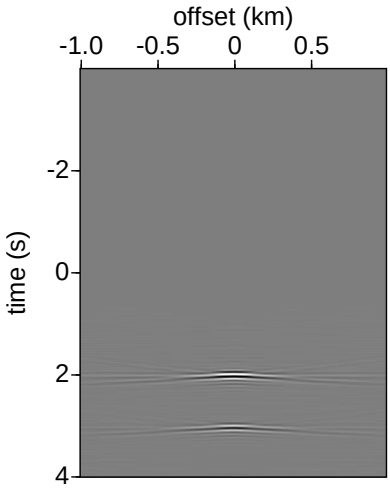

Figure 5.4. The estimated multiple, in the data, at a depth of 1.5 km; note the agreement with the true multiple in Figure 5.3.

sampling.

In our method, the data are first downward continued as part of a standard wave-equation migration technique ((a) in the flowchart). In Figure 5.3 we show $\tilde{d}_1(z = 1.5 \text{ km})$, a single common-midpoint gather (cmp) downward continued to the depth $z = 1.5$ km of the top of the layer. The primary reflected from the top of the layer is located around $t = 0$, the reflection from the bottom of the layer at about $t = 1$ s and the first order internal multiple at about $t = 2$ s.

We now estimate the multiples at depth using equation (5.16). This requires restricting $\tilde{d}_1$ to time $t > 0$. The procedure removes the primary reflection from the current depth (which theoretically arrives at $t = 0$), in this case 1.5 km, before doing the convolution. If this process is not done correctly and energy remains at $t \leq 0$, all primary reflections from deeper depths will be duplicated in the estimated multiples section. In this model a simple time-windowing procedure is sufficient, because the reflections are far apart in time. In some situations, we find a τ-p filter to be more effective. This is because we typically see tails at small positive and negative times caused by the band-limited signal. A τ-p filter is more effective at removing these tails when they are mixed with later reflections. Figure 5.3 show the results of applying the τ-p filter to the data.

Once the negative time contributions to the data have been removed, the multiple is estimated with (5.16), through a convolution. The convolved wavefield is multiplied by an

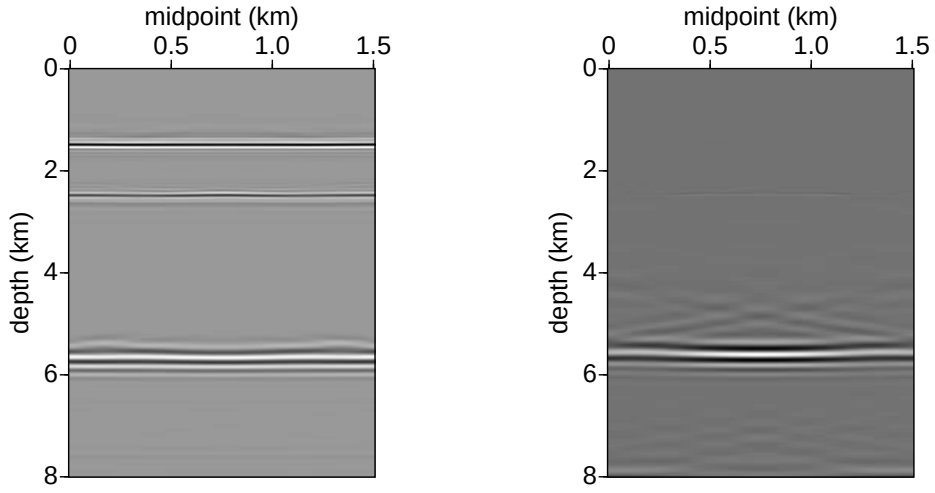

Figure 5.5. On the left is the image with an artifact from a first-order internal multiple at about 5.7 km depth. On the right is the estimated artifact.

estimate of the image at the current depth, in this case $z = 1.5$ km (this is the $(E_1 a)(z, s', r')$ appearing in (5.16)). This completes (b) of the flowchart. The estimated multiple is shown in Figure 5.4. The event at about $t = 3$ s is a second-order internal multiple. This event is formed from the convolution of a primary with a first-order internal multiple. It is not present in the data panel because later arrivals were muted to remove additional artifacts.

We now proceed to (c) of the flowchart and propagate both the data and the estimated multiples to the next depth. From the data, an image at the current depth is formed containing both primaries and multiples using (5.15) ((d) of the flowchart). Another image is also computed at the current depth, containing an estimate of the artifacts caused by FOIM, using (5.19) ((f) of the flowchart). The image containing both primaries and multiples gives the estimate of $a(z, x)$, which feeds back into the estimation of the multiples through (e) of the flowchart.

Figure 5.5 compares the estimated artifact, a_3, with the imaged data, a_1. The estimated artifact overlays the artifact in the data, despite the fact that we have not accounted for the shape of the source wavelet. (Although the wavelet has not been deconvolved, the data have been shifted so that the peak of the source wavelet is at zero time and bandpass filtered to match the frequency content of the two images.)

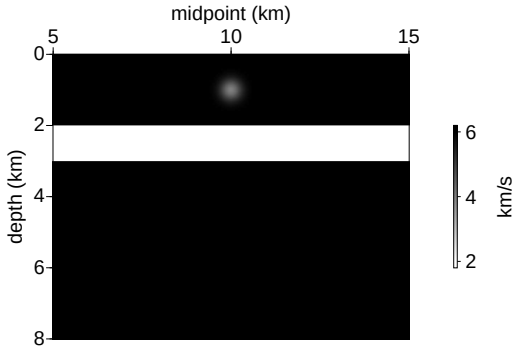

Figure 5.6. Velocity model, similar to the flat layered example discussed previously, with the addition of a low-velocity lens to demonstrate that the method works in laterally heterogeneous velocity models.

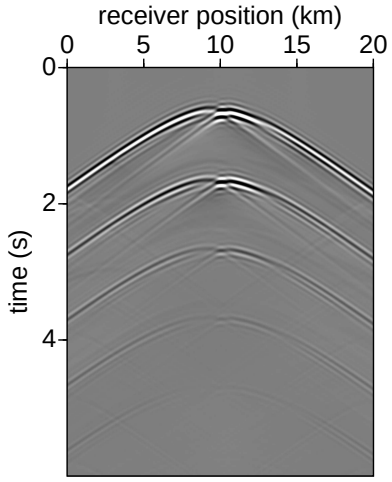

Figure 5.7. Shot record from $s = 9.8$ km, 200 m to the left of the center of the lens. Note the caustic introduced by the lens around zero-offset. The ringing on the second primary (at about 2 s) and the multiple (at about 3 s) is numerical dispersion from the modeling of the data.

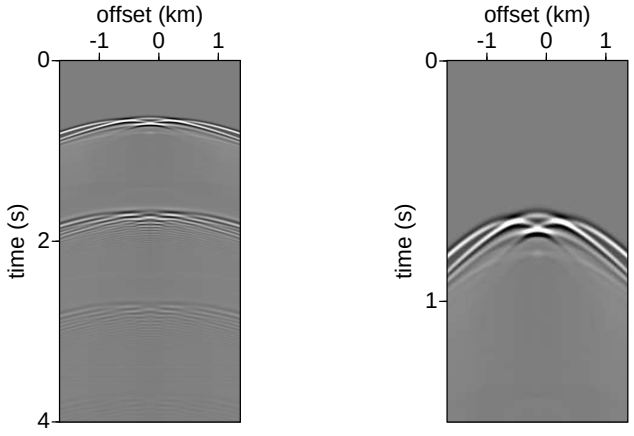

Figure 5.8. Common midpoint gather at 9.8 km and zero depth, with only the offsets used to compute the images shown later. Note the triplications caused by the lens. Left: full gather. Right: zoom of the primary reflection from the top layer.

5.6.2 Lens Model

To illustrate the ability of the method to estimate multiples in more complicated velocity models, we add a low-velocity lens to the model. The resulting velocity model is shown in Figure 5.6. The layer in this model is the same as the layer in the previous model except that it is 0.5 km deeper to allow more space for the low-velocity lens. The lens is located in the center of the model; it is circular with Gaussian velocity variations, a diameter of 600 m and a maximum contrast of -2 km/s. The addition of the lens has a large influence on the recorded data. A shot record directly above the lens is shown in Figure 5.7. Note the ringing, caused by errors in the data modeling, that is particularly strong on the multiple. We use a double-square-root propagator that works in midpoint-offset coordinates rather than shot and receiver. To accommodate this choice, we use a subset of the available offsets so that each midpoint has the same number of offsets. The data from a midpoint of 9.8 km are shown in Figure 5.8. The first arrival is highlighted in this figure to show the triplications caused by the lens more clearly.

To estimate the multiple, we propagate the data to 2 km, the top of the layer, and again show the cmp at midpoint 9.8 km in Figure 5.9 along with the estimated multiples at this depth. Note that the caustic has been removed by the propagation through the lens and that the multiple is accurately estimated. At this point, since we have removed the effects of the lens, the example is essentially the same as the flat case and the multiples are estimated accurately as is shown in Figures 5.10. Once again, the multiple is relatively

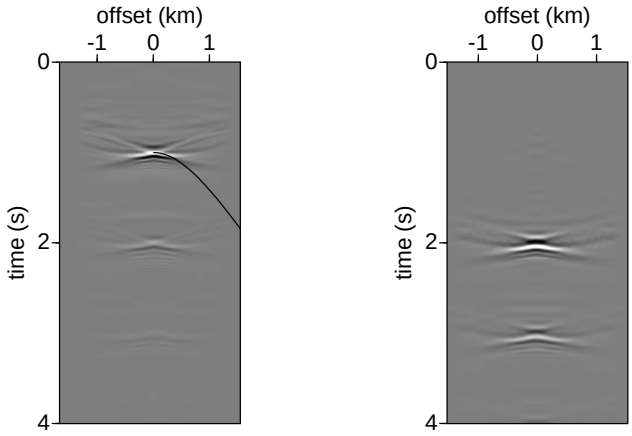

Figure 5.9. Left: Common midpoint gather at 9.8 km and 2 km depth, after the $t \leq 0$ times have been removed. Note the disappearance of the multi-pathing as the data are now below the lens. The solid line shows the expected moveout curve for the reflection from the bottom of the reflector. Right: estimated multiples at this depth.

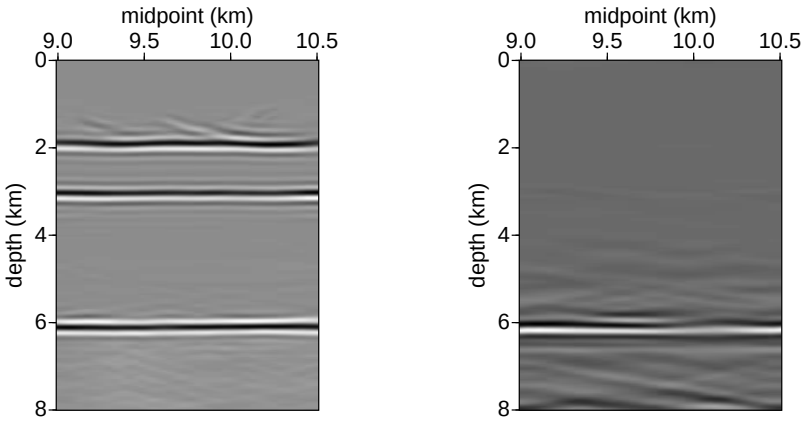

Figure 5.10. Left: Image with an artifact from the first-order internal multiple at approximately 6 km depth. Right: Estimated artifacts from first-order internal multiples.

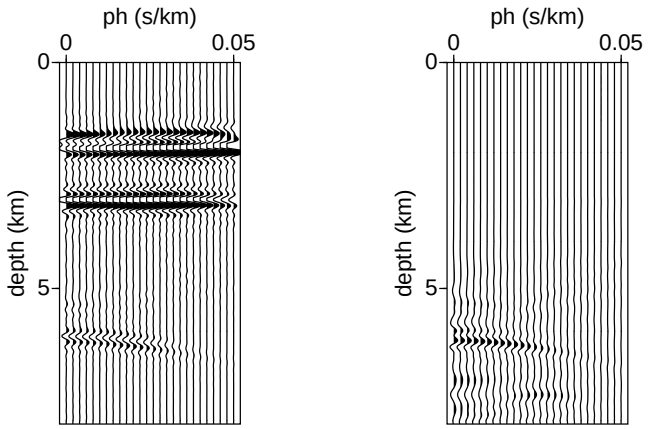

Figure 5.11. Common image gathers for midpoint 9.8 km. Right: image with artifact. Left: estimated artifact.

weak in the estimated image. This is because of the residual moveout on the common image gather, which is shown in Figure 5.11.

To illustrate the dependence of this method on the background velocity model, we perturb the velocity in this section to ascertain the influence of the velocity on the final result. In theory, from equations (5.17) and (5.19), knowledge of the velocity is necessary only to the depth of the shallowest reflection, in this case the top of the layer at 2 km depth. To test this we perturb the model in two ways: first we make the layer thicker, and then we add a second lens, with properties identical to the first lens, below the layer. In the first case, we expect the multiple to be imaged at a shallower depth but otherwise to remain unchanged as the perturbation in the velocity is independent of midpoint. Figure 5.12 shows that we are still able to estimate the artifact accurately despite this error in the velocity model. There is more noise present in the image (left of Figure 5.12) here than in the correct velocity case (Figure 5.10). Part of the reason for this is that we have used a smaller agc window to enhance the image of the bottom of the layer. In the second case, since the perturbation now depends on midpoint the estimated multiple also depends on midpoint. Although the estimated artifact does not match the image artifact as well in this case as when the correct velocity is used, the estimate remains quite good, as shown in Figure 5.13.

The theory presented here does require knowledge of the velocity model to the depth of the up to down reflection (top of layer at 2 km depth). To test the sensitivity of the method to errors in this velocity, we remove the lens and estimate the image and the multiple in this incorrect velocity model. The results are shown in Figure 5.14. Although the estimated

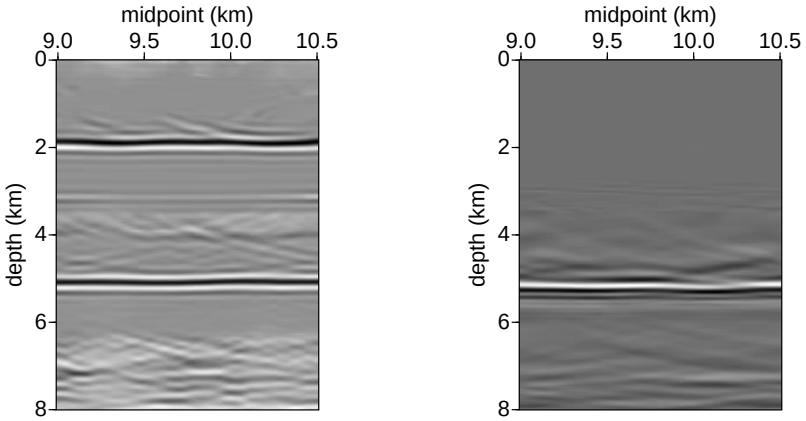

Figure 5.12. In these images, the reflector has been extended to 3.5 km from 3 km to test the sensitivity of the method to the velocity model. Left: Image with artifacts from internal multiples. Right: Estimated artifacts from first-order internal multiples.

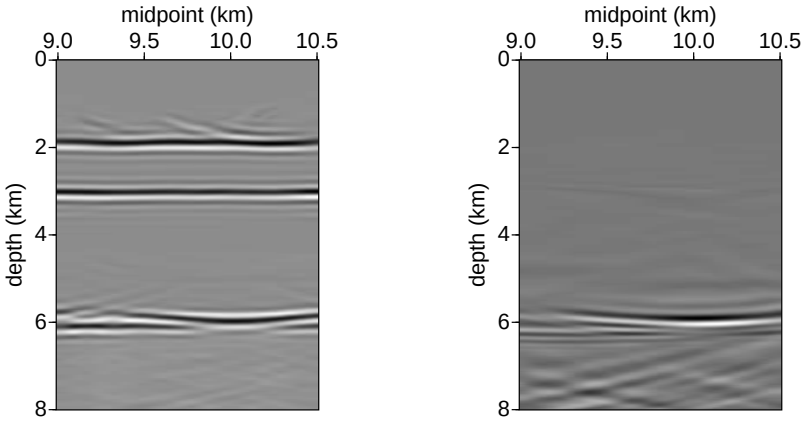

Figure 5.13. In these images, a second lens has been added beneath the layer to introduce a laterally varying velocity perturbation. Left: Image with artifacts from internal multiples. Right: Estimated artifacts from first-order internal multiples.

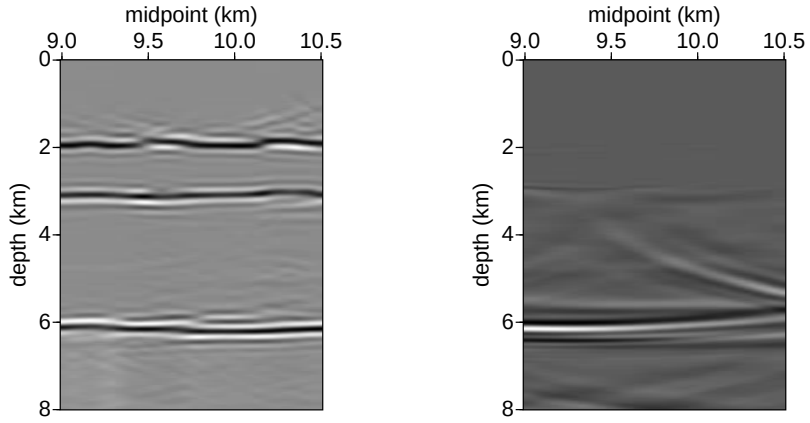

Figure 5.14. The lens was removed from the velocity model before generating these images. Because this perturbation is above the top of the layer, we expect this to have an impact on the estimated multiple. Note the change in the accuracy of the estimate beneath the lens. Left: Image with artifacts from first-order internal multiples. Right: Estimated artifacts from first-order internal multiples.

artifact remains at roughly the correct depth, there is a phase difference between it and the actual artifact and the variation in the image with midpoint is not accurately estimated. Removing the lens entirely is a large change in the model and thus we expect a large change in the image. In Figure 5.15, we demonstrate that we can still estimate the multiple with reasonable accuracy when the velocity perturbation is less dramatic. In this case the lens has been moved 0.2 km shallower than in the true velocity model, and with the exception of the phase change between the artifact and our estimate, the result is still good.

5.6.3 Chalk Model

The next synthetic model is based on a Shell field in the North Sea. The velocity model is a 2D slice of a 3D velocity model with the steeply dipping reservoir interval added manually. The velocity model is shown in Figure 5.16; the chalk layer beginning at about 3 km depth is expected to be the largest generator of internal multiples because of the strong velocity contrast between the chalk and surrounding layers. Some of the layers discussed later are labeled on this figure. The acquisition was designed to simulate a marine experiment. A total of 601 shots were computed with finite differences at a 25 m increment beginning at 15 km and continuing to 30 km. The streamer consists of 241 receivers (hydrophones) spaced at 25 m increments beginning with zero-offset. For the tests

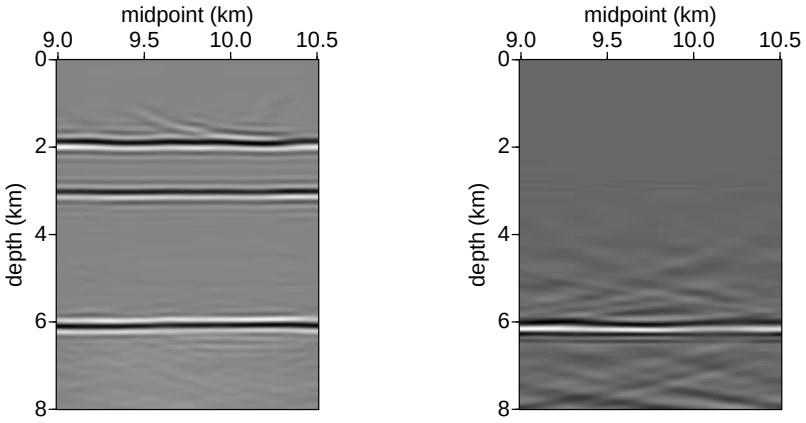

Figure 5.15. In this model the lens was moved 0.2 km deeper than in the correct velocity model. Because this perturbation is above the top of the layer, we expect this to have an impact on the estimated multiple. Note the phase difference between the estimated artifact and the image. Left: Image with artifacts from first-order internal multiples. Right: Estimated artifacts from first-order internal multiples.

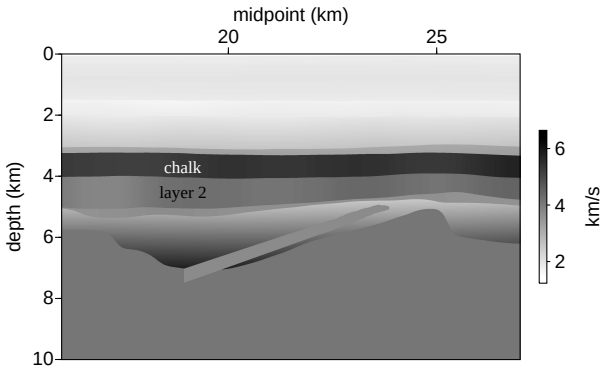

Figure 5.16. Velocity model for the North Sea example.

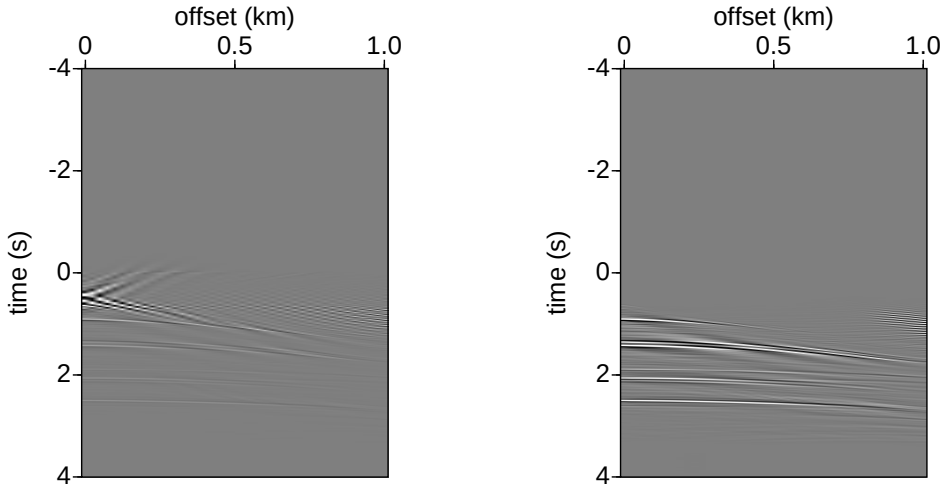

Figure 5.17. Data downward continued to a depth of 2.5 km. Left: before the removal of the part of the data at $t \leq 0$. Right: after the removal of the part of the data at $t \leq 0$ using a τ-p filter.

shown here we use a subset of 241 midpoints, beginning at 15 km with a spacing of 50 m, with 31 offsets at 50 m spacing beginning at zero-offset. A total of 6 s of data were computed with a 4 ms time sampling interval. A small subset of the available offsets were used to avoid imaging refracted waves visible at long offsets, and to avoid to the extent possible numerical dispersion, which is stronger at larger offsets.

In Figure 5.17, the data are shown downward continued to a depth of 2.5 km, just above the top of the chalk (the chalk layer is labeled in Figure 5.16). This figure illustrates that in this instance a simple time windowing is not sufficient. Instead we use a τ-p filter to attenuate the reflection from the top of chalk. By using a τ-p filter rather than a simple time windowing we are also able to apply the filter less frequently as it allows us to remove the entire top of chalk reflection at once, from above the chalk layer.

Figures 5.18 and 5.19 compare the estimated artifacts to the true artifacts in the image. The multiples were estimated in a depth window from 2.5 to 4.2 km depth and the τ-p filter was applied at 2.5 and 3.25 km. Thus we expect to see the multiples from the top and bottom of the chalk layer. The estimated multiples are imaged at approximately the depth expected based on the velocity model. The multiple at about 4.5 km depth is imaged at the depth expected for an internal multiple entirely within the chalk layer extending from approximately 3 to 4 km depth. The multiples at about 5.5 km are either peg-legs from

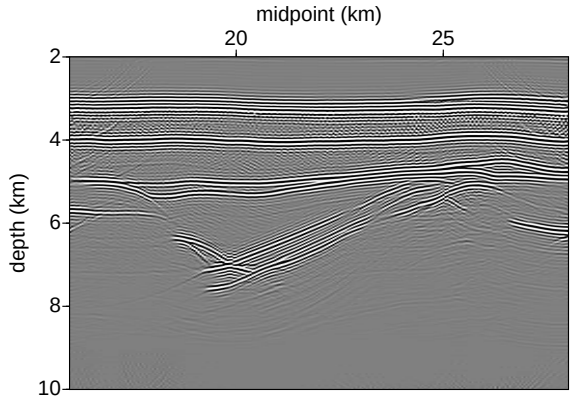

Figure 5.18. The image in the chalk model, with artifacts from a first-order internal multiple at about 4.5 km depth.

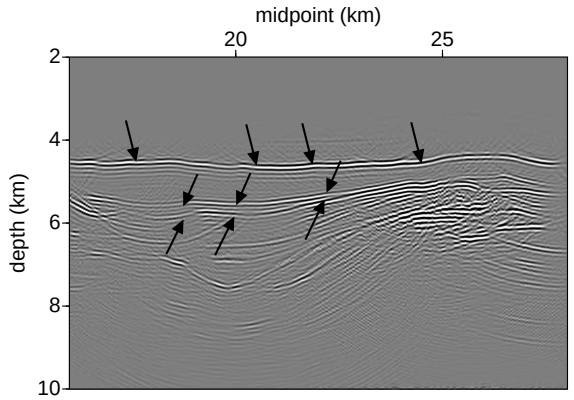

Figure 5.19. This figure repeats the estimated artifacts from internal multiples shown in Figure 5.18, with arrows indicating locations at which multiples can be observed in the results of ten Kroode (2005).

the bottom of the chalk and the bottom of layer 2 or internal multiples with both deeper scattering points at the bottom of the layer 2. The artifacts caused by these multiples in the image are not easy to identify, however, as they are obscured by other ringing in the data. This ringing does not appear in the estimated artifacts because these estimates are made using the primaries, which arrive at earlier times and are thus less strongly influenced by the ringing. To highlight the multiples as much as possible, we have stacked only the smallest p-values (i.e. the first few traces of the common image gather) to make the image and we have low-passed filtered the image to remove as much of the high-frequency noise visible after the chalk layer as possible, without damaging the imaged structure. In Figure 5.19 we compare our estimate to one made by ten Kroode (2005), in which he estimates the multiples from the top of the chalk layer and compares them to the multiples in the data. This is an extremely coarse comparison as it is not possible to show his image, but the arrows indicate several locations at which artifacts from multiples are present in his image.

5.6.4 Field Data

In this section, we present an example of the application of this method to field data. The data, provided by Total, are from The Gulf of Mexico, and contain a large salt body. The strong velocity contrast between the salt and surrounding sediments make imaging in this area challenging. Estimating internal multiples in such an area is also difficult because of the multi-pathing introduced by the salt. The data have had standard pre-processing applied, including surface-related multiple elimination and a radon demultiple; they have also been regularized to a uniform grid in the midpoint-offset coordinates. We show results from a single 2D line extracted from a 3D survey. Because the salt has a complicated 3D geometry, performing 2D imaging on this line is likely to introduce errors. Comparison with the image from a full 3D migration indicates that these effects are not overwhelming for imaging. Despite this, the estimated artifacts are likely to contain errors resulting from applying a 2D multiple estimation algorithm in an area where the geology is 3D.

An image of the line is shown in Figure 5.20; the base of salt is indicated with the white arrows. The circled regions contain events that are suspected to be artifacts caused by internal multiples. Comparing this image with the image of the estimated artifacts shown in Figure 5.21 yields little conclusive results because there seems to be energy in the estimated artifacts section that is not present in the image. A partial explanation for this is the amplitude differences between the two, making the internal multiples difficult to see in the image. To truly compare the estimated artifacts with the artifacts seen in the image space, we show common image gathers from two points in the model, covering the three highlighted areas.

The first image gather, shown in Figure 5.22 is at cmp 150, approximately in the middle of the highlighted region on the left-hand side. There are five areas marked on this image gather at which artifacts are estimated and also occur in the imaged data. Arrow number 4 is the artifact that occurs in the highlighted region of the image, indicating that this event is indeed an artifact caused by first-order internal multiples within the salt body. Arrow number 1 marks a number of estimated artifacts mixed with primaries within and

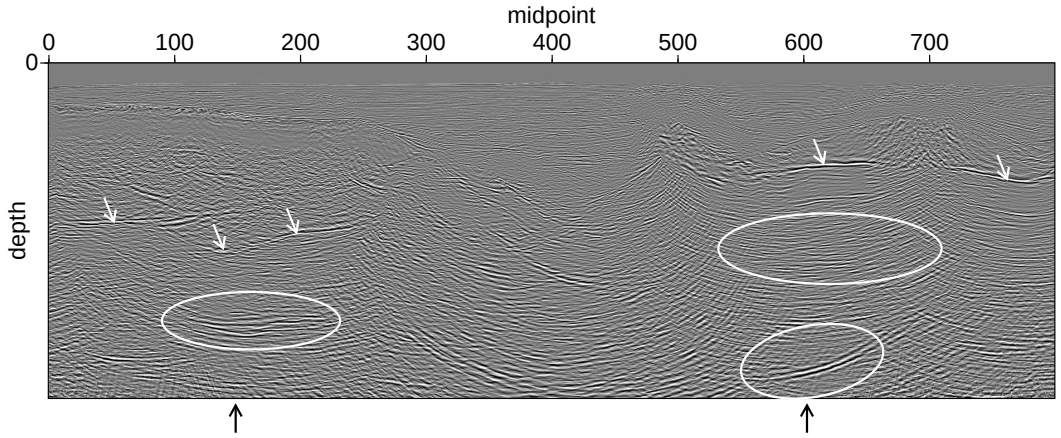

Figure 5.20. Image for the real data example. The base of salt is marked with white arrows and three areas of the image are marked, two of which contain artifacts from internal multiples (left and top right) and one of which does not (bottom right). The locations of the CIGs shown in Figures 5.22 and 5.23 are marked with the black arrows below the image.

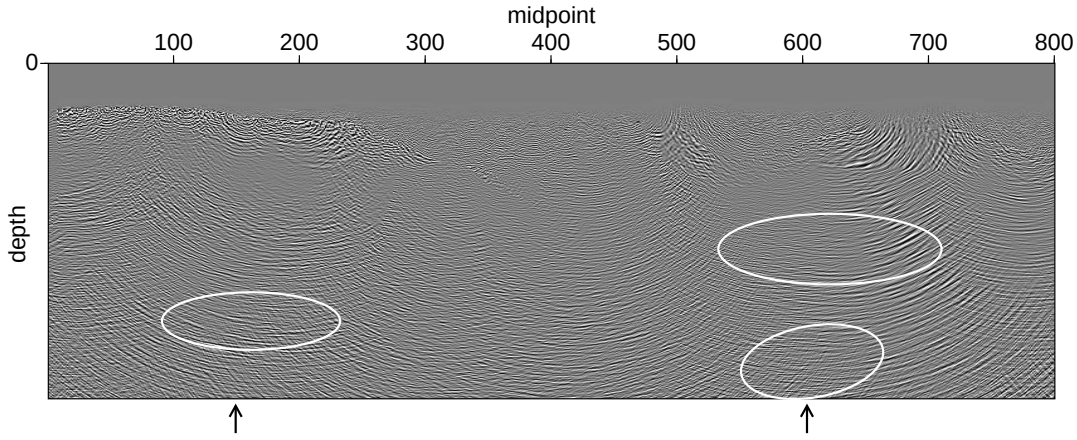

Figure 5.21. Estimated artifacts for the real data example. The three areas marked are the same as those marked on the image above. The locations of the CIGs shown in Figures 5.22 and 5.23 are marked with the arrows below the image.

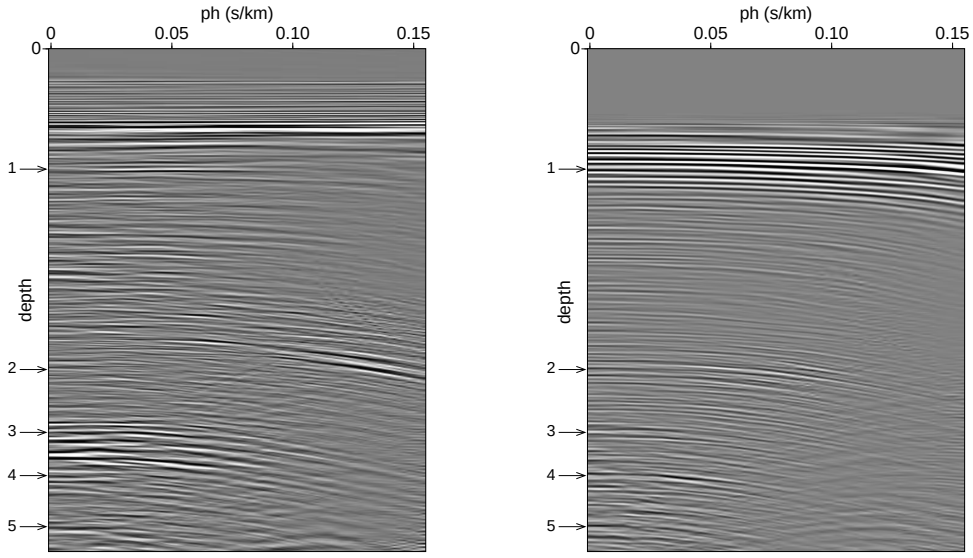

Figure 5.22. Real data example, common image gather at cmp 150. On the left is the standard image gather and on the right are the estimated artifacts from internal multiples. The five arrows indicate the locations of accurately estimated artifacts. Arrow number 4 is the artifact in the left highlighted region on the image shown in Figure 5.20.

above the salt. It is possible that these artifacts are in fact residual energy from $t \leq 0$ that was incompletely removed. Arrow numbers 2, 3, and 5 appear to be correctly estimated internal multiples.

The second image gather, shown in Figure 5.23, is at cmp 600, within the two highlighted regions on the right of the image. First, note that at arrow number 3, there is a strong event in the image gather that does not correspond to an estimated artifact. This is the event in the lower-right highlighted region. The absence of an estimated artifact at this position indicates that this energy is not an imaging artifact caused by internal multiples. It could be, for example, a primary that is migrated poorly due to inaccuracies in the velocity model, or residual energy from a surface-related multiple. Arrows 1 and 2 mark other estimated artifacts in this image gather. Arrow 2 is in the second, shallower highlighted region, indicating that in this area some of the energy does come from internal multiples.

In the CIGs there are many estimated artifacts that are not easily correlated with events in the standard image gather. Some of these estimated artifacts could have been attenuation by the Radon demultiple that has been applied to the data. Other sources of error include 3D effects, both in the image and in the estimation of the multiples, as well as amplitude errors in the estimated artifacts resulting in stronger amplitudes on the estimated artifacts than on the artifacts actually seen in the migration. Much work remains

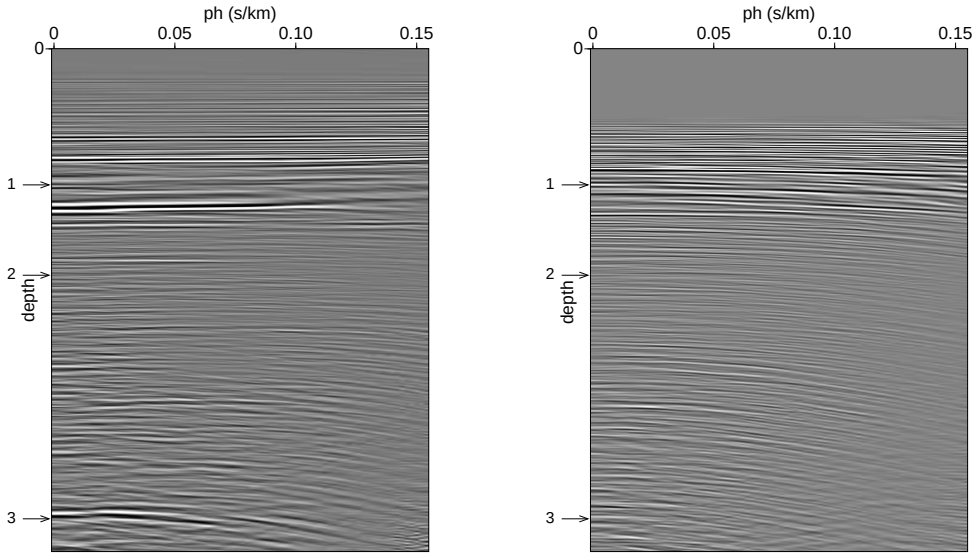

Figure 5.23. Real data example, common image gather at cmp 600. On the left is the standard image gather and on the right are the estimated artifacts from internal multiples. Arrows 1 and 2 indicate the locations of accurately estimated artifacts. Arrow number 2 is within the upper-right highlighted region of the image. Arrow number 3 marks the artifact in the lower right highlighted region on the image shown in Figure 5.20. That this artifact does not appear in the estimated artifacts indicates that this energy does not come from an internal multiple.

to be done to have a robust algorithm for real data applications. This example illustrates that at the least this method can be used to ascertain whether artifacts in the image come from internal multiples or not.

5.7 Discussion

We have described a method to estimate imaging artifacts caused by first-order internal multiples. This method requires knowledge of the velocity model down to the top of the layer that generates the multiple (the depth of the up-to-down reflection). The main computational cost of the algorithm comes from the downward continuation of the data and the internal multiples. Because two data sets are downward continued (the data themselves and the estimated multiples), the cost of the algorithm described here is about twice that of a usual pre-stack depth migration, plus the cost of the removal of negative times. The removal of negatives times can be compuationally expensive because it is necessary to

return all of the data to the time domain to window the data. Using the τ-p filter reduces this cost because the negative times can be removed less frequently, although the cost of the τ-p transform is much higher than that of a simple time windowing. By estimating the multiple on downward continued data, rather than in surface data, we avoid difficulties caused by caustics in the wavefield or the failure of the traveltime monotonicity assumption. In addition, estimating artifacts in the image rather than estimating multiples in the data shows clearly which part of the image has been contaminated by internal multiples, even if those multiples are poorly estimated or incompletely subtracted.

5.8 Acknowledgments

We thank Total for permission to publish the real data example. We are grateful to Fons ten Kroode and Shell for the North Sea synthetic example. We also appreciate the many helpful discussion with Kris Innanen and Ken Larner as well as the coding assistance from Peng Sheng, Feng Deng, Linbin Zhang and Dave Hale. This work was supported by Total and the sponsors of the Consortium Project on Seismic Inverse Methods for Complex Structures at the Center for Wave Phenomena.

Chapter 6

Conclusions and Future Work

6.1 Conclusions

Data continuation has many application in seismology, two of which are discussed in this thesis. By employing the mathematics of Fourier Integral Operators, we are able to extend data regularization or data mapping techniques to situations in which the wavefield contains caustics. In addition, we have shown that techniques for the downward continuation of data allow us to dispence with two commonly made assumptions in multiple attenuation: that the wavefield does not contain caustics and the traveltime monotonicity assumption. We have developed a technique that is able to estimate imaging artifacts caused by first-order internal multiples without these two assumption. Both of these applications also involve operator composition, in which several operators are combined to make a final, single, operator. For data regularization, this composition comes with conditions under which the resulting operator does not introduce false reflections in the data. For multiples the application of successive Green's operators illustrates the need for the traveltime monotonicity assumption used in other multiple attenuation techniques.

For data regularization we have shown that, even in the presence of caustics, it is possible to fill in missing data. We have illustrated this theory by computing impulse responses and by filling in missing data in synthetic shot records. The major limitation of this technique is its computational cost. Although we believe it to be possible to fill in missing data with the cost on the order of a prestack migration that is still expensive as a pre-conditioning step. On the other hand, this technique is designed to be applied in the most complicated geologic structures where traditional, faster techniques fail.

We have developed a theory for multiple attenuation in the presence of caustics, when the traveltime monotoncity condition does not hold. We have begun to illustrate the practical value of the process but a lot of work remains in that direction. First of all, artifacts caused by internal multiples have significantly smaller amplitudes than do primary reflections. This presents problems for accurately modeling data containing multiples, but not containing other artifacts such as aliasing, numerical dispersion, refractions and boundary reflections. Even if such modeled data are available it is also difficult to see the artifacts from internal multiples on synthetic data because of errors in the migration itself, such as wrap-around, aliasing and wide-angle effects that interfere with the low amplitude multiples. The problem of modeling data is removed by application to real data but this comes with its own set of problems as the data contain noise, have been pre-processed introducing other errors that are difficult to assess.

From an algorithm design point of view, the most difficult part of the algorithm used here to estimate artifacts from internal multiples is the removal of the negative time interval. This must be done several times during the multiple estimation process and is both costly and difficult as imperfect data propagation results in significant portions of the data being removed at each step. It is costly because wave equation migration algorithms are typically run in the frequency domain, parallelized over frequency. To return to the time domain and remove negative times requires collecting all frequencies before windowing.

6.2 Future Work

For both examples discussed in this thesis, the major direction of future work is on the practical rather than theoretical side.

For data regularization, the algorithm used to generate the examples shown in chapter 3 is far from the most efficient possible. The fast marching techniques developed by Sethian (2002) allow the construction of the canonical relation or "table" discussed in chapter 3 with only one pass through the velocity model. By contrast, the method we used requires one pass through the velocity model for each input and output ray pair. In addition, our construction for data regularization is velocity model dependent. One can choose to look at this as a disadvantage of the method or equivalently one can think of using the technique as a tool for velocity analysis. Traditional velocity analysis involves assessing the change in the image as a result of perturbing the velocity model. A model dependent data regularization technique could be used in a similar manner to assess improvements (or degradations) in the match between predicted and recorded data resulting from perturbing the velocity model.

The algorithm discussed in this thesis for estimating image artifacts caused by internal multiples is computationally efficient, but has several practical problems. In wave-equation migration, data are traditionally continued into the Earth and an image is formed by taking the zero time and zero offset data point at each depth. The method proposed in this thesis uses the data at each depth, however, and thus requires more of the propagator than is traditionally necessary. Although the propagator used in this thesis has been carefully tested for imaging, it has not been carefully tested to assess its robustness for data propagation, in particular the images shown in chapter 5 required a lot of zero padding to deal with wrap-around and it was also necessary to apply reciprocity to the input data to improve the accuracy of the downward continued data, which doubles the amount of data propagated at each step. In addition, the removal of negative times is a significant computational hurdle. For a perfectly imaged reflection this would be easy as only zero time and offset would need to be removed from the data at each depth. We do not have perfect images due to, among others, errors in the propagation and band limitation. Thus a region around the zero time and offset needs to be removed, which we did with a τ-p transform. A major problem with this transform is that it does not preserve the amplitudes of the input data (in other words it has an adjoint but not an inverse) which destroys any possibility of matching the amplitudes of the predicted artifacts with the amplitudes of the artifacts in the image.

If the above problems can be overcome, the method has the potential to be used for more than just the prediction of artifacts. For example, multiples can interfer in velocity

analysis because they do not satisfy the assumptions of the method; they are triply scattered not singly scattered. Multiples are sensitive to the velocity model, however, in particular they are sensitive to the structure in which they scatter three times rather than the single time primaries are reflected. By estimating the multiples in the image, or preferably in the image gather, the flatness criteria often used in velocity analysis can be replaced with a joint criteria on the flatness of the primaries and the successful prediction of artifacts from internal multiples. In addition the matching between the predicted and true multiple is influenced by the velocity above the shallowest scattering point only, providing an indicator of which parts of the velocity model need to be updated.

Multiples are also more sensitive to reflector positions in the Earth because they scatter three times rather than once. When they are mixed with primaries it is difficult to use this information because whether the recorded energy is a primary scattered deep in the Earth or a multiple scattered shallower is not easily assessed. Seperating the multiples from the primaries opens up the possibility of imaging with multiples as is currently under investigation for surface-related multiples by Brown (2004).

References

Alkhalifah, T., & de Hoop, M. V. 2004. Residual Dip moveout in VTI media. *Geophysical Prospecting, in print*.

Aminzadeh, F., & Mendel, J. M. 1980. On the Bremmer series decomposition: Equivalence between two different approaches. *Geophysical Prospecting*, **28**, 71–84.

Aminzadeh, F., & Mendel, J. M. 1981. Filter Design for suppression of surface multiples in a non-normal incidence seismogram. *Geophysical Prospecting*, **29**, 835–852.

Artley, C., & Hale, D. 1994. Dip-moveout processing for depth-variable velocity. *Geophysics*, **59**, 610–622.

Atkinson, F. V. 1960. Wave propagation and the Bremmer series. *J. Math. Anal. Appl.*, **1**, 225–276.

Berkhout, A. J., & Verschuur, D. J. 1997. Estimation of multiple scattering by iterative inversion, Part I: Theoretical considerations. *Geophysics*, **62**(5), 1586–1595.

Bevc, D., Fliedner, M., Crawley, S., & Biondi, B. 2003. Wave equation imaging comparisons: Survey sinking vs. shot profile methods. *SEG Technical Program Expanded Abstracts*, **22**(1), 885–888.

Beylkin, G. 1985. Imaging of discontinuities in the inverse scattering problem by inversion of a causal generalized Radon transform. *J. of Math. Phys.*, **26**, 99–108.

Biondi, B., Fomel, S., & Chemingui, N. 1998. Azimuth moveout for 3-D prestack imaging. *Geophysics*, **63**, 574–588.

Black, J. L., Schleicher, K. L., & Zhang, L. 1993. True-amplitude imaging and dip moveout. *Geophysics*, **58**, 47–66.

Bleistein, N. 1990. Born DMO revisited. *60th Annual International Meeting, SEG, Expanded Abstracts*, 1366–1369.

Bleistein, N., & Jaramillo, H. 2000. A platform for data mapping in scalar models of data acquisition. *Geophysical Prospecting*, **48**, 135–161.

Bleistein, N., Cohen, J. K., & Jaramillo, H. 1999. True amplitude transformation to zero offset of data from curved reflectors. *Geophysics*, **64**, 112–129.

Bleistein, N., Cohen, J. K., & Stockwell, J. W. Jr. 2000. *Mathematics of multidimensional seismic imaging, migration and inversion*. New York: Springer-Verlag.

Bostock, M. G., Rondenay, S., & Shragge, J. 2001. Multiparameter two-dimensional inversion of scattered teleseismic body waves 1. Theory for oblique incidence. *Journal of Geophysical Research*, **106**, 30771–30782.

Brandsberg-Dahl, S., de Hoop, M. V., & Ursin, B. 2003a. Focusing in dip and AVA compensation on scattering-angle/azimuth gathers. *Geophysics*, **68**, 232–254.

Brandsberg-Dahl, S., Ursin, B., & De Hoop, M. V. 2003b. Seismic velocity analysis in the scattering-angle/azimuth domain. *Geophysical Prospecting*, **51**, 295–314.

Bremmer, H. 1951. The W. K. B. approximation as the first term of a geometric-optical series. *Communications on Pure and Applied Mathematics*, **4**, 105–115.

Brown, M. 2004. *Least-Squares Joint Imaging of Multiples and Primaries*. Ph.D. thesis, Stanford University.

Brown, R. J. S. 1969. Normal-Moveout and velocity relations for flat and dipping beds and for long offsets. *Geophysics*, **34**(2), 180–195.

Burdick, L. J., & Orcutt, J. A. 1979. A comparison of the generalized ray and reflectivity methods of waveform synthesis. *Geophys. J. Int.*, **58**, 261–278.

Burridge, R., & Beylkin, G. 1988. On double integrals over spheres. *Inverse Problems*, **4**(1), 1–10.

Canning, A., & Gardner, G. H. 1996. Regularizing 3-D data sets with DMO. *Geophysics*, **61**, 1103–1114.

Cheney, M., & Borden, B. 2002. Microlocal structure of inverse synthetic aperture radar data. *Inverse Problems*, **19**, 173–194.

Claerbout, J. F. 1985. *Imaging the Earth's Interior*. Blackwell Sci. Publ.

Corones, J. P. 1975. Bremmer series that correct parabolic approximations. *J. Math. Annal. Appl.*, **50**, 361–372.

de Hoop, M. V. 1996. Generalization of the Bremmer coupling series. *J. Math. Phys.*, **37**, 3246–3282.

de Hoop, M. V. 2004. The downward continuation approach to modeling and inverse scattering of seismic data in the Kirchhoff approximation. *in print, Contemp. Math.*

de Hoop, M. V., & Bleistein, N. 1997. Generalized Radon transform inversions for reflectivity in anisotropic elastic media. *Inverse Problems*, **13**, 669–690.

de Hoop, M. V., & Brandsberg-Dahl, S. 2000. Maslov extension of generalized Radon transform inversion in anisotropic elastic media:A least-squares approach. *Inverse Problems*, **16**, 519–562.

de Hoop, M. V., Burridge, R., Spencer, C., & Miller, D. 1994. Generalized radon transform amplitude versus angle (GRT/AVA) migration/inversion in anisotropic media. *Pages 15–27 of: Proc SPIE 2301.* SPIE.

de Hoop, M. V., Spencer, C., & Burridge, R. 1999. The resolving power of seismic amplitude data: An anisotropic inversion/migration approach. *Geophysics*, **64**(3), 852–873.

de Hoop, M. V., Malcolm, A. E., & Le Rousseau, J. H. 2003a. Seismic wavefield 'continuation' in the single scattering approximation: A framework for dip and azimuth moveout. *Can. Appl. Math. Q.*, **10**, 199–238.

de Hoop, M. V., Le Rousseau, J. H., & Biondi, B. 2003b. Symplectic structure of wave-equation imaging: A path-integral approach based on the double-square-root equation. *Geophys. J. Int.*, **153**, 52–74.

Deregowski, S. G., & Rocca, F. 1981. Geometrical optics and wave theory of constant offset sections in layered media. *Geoph. Prosp.*, **29**, 374–406.

Dragoset, W. H., & Jericević, Z. 1998. Some remarks on surface multiple attenuation. *Geophysics*, **63**, 772–789.

Duistermaat, J. J. 1996. *Fourier integral operators.* Boston: Birkhäuser.

Fokkema, J. T., & van den Berg, P. M. 1993. *Seismic applications of acoustic reciprocity.* Amsterdam: Elsevier.

Fokkema, J.T., Van Borselen, R. G., & Van den Berg, P.M. 1994. *Removal of inhomogeneous internal multiples.* Eur. Assn. of Expl. Geophys. Page Session:H039.

Fomel, S. 1995. Amplitude preserving offset continuation in theory, Part 1: the offset continuation equation. *Pages 179–196 of: Stanford Exploration Project Preprint*, vol. SEP-84.

Fomel, S. 2003. Theory of differential offset continuation. *Geophysics*, **68**(2), 718–732.

Fomel, S., & Bleistein, N. 2001. Amplitude preservation for offset continuation: Confirmation for Kirchhoff data. *Journal of Seismic Exploration*, **10**, 121–130.

Fomel, S., & Prucha, M. 1999. Angle-gather time migration. *SEP-100*, 141–150.

Foss, S-K., De Hoop, M. V., & Ursin, B. 2003. Linearized 2.5-D parameter imaging-inversion in anisotropic elastic media. *CWP-431-P.*

Fowler, P. J. 1998. A comparative overview of dip moveout methods. *68th Annual International Meeting, SEG, Expanded Abstracts*, 1744–1747.

Friedlander, F. G., & Joshi, M. 1998. *Introduction to the theory of distributions.* Cambridge university press.

Goldin, S. 1994. Superposition and continuation of transformations used in seismic migration. *Russian Geology and Geophysics*, **35**, 131–145.

Goldin, S., & Fomel, S. 1995. Estimation of reflection coefficient in DMO. *Russian Geology and Geophysics*, **36**(4), 103–115.

Gray, S. H. 1983. On the convergence of the time domain Bremmer series. *Wave Motion*, **5**, 249–255.

Green, C. H. 1938. Velocity determinations by means of reflection profiles. *Geophysics*, **3**(4), 295–305.

Guillemin, V. 1985. *Pseudodifferential operators and applications (Notre Dame, Ind., 1984)*. Providence, RI: Amer. Math. Soc. Chap. On some results of Gel′fand in integral geometry, pages 149–155.

Guitton, A., & Verschuur, D. J. 2004. Adaptive subtraction of multiples using the L_1-norm. *Geoph. Prosp.*, **52**, 27–38.

Hale, D. 1983. *Dip Moveout by Fourier Transform*. Ph.D. thesis, Stanford.

Hale, D. 1991. *Dip Moveout Processing*. course notes series. Tulsa: Society of Exploration Geophysicists.

Hale, D. 1995. *DMO processing*. Geophysics Reprint Series.

Hörmander, L. 1983. *The analysis of linear partial differential operators*. Vol. I. Berlin: Springer-Verlag.

Hörmander, L. 1985a. *The analysis of linear partial differential operators*. Vol. IV. Berlin: Springer-Verlag.

Hörmander, L. 1985b. *The analysis of linear partial differential operators*. Vol. III. Berlin: Springer-Verlag.

Hubral, P., Schleicher, J., & Tygel, M. 1996. A unified approach to 3-D seismic reflection imaging, part I: Basic concepts. *Geophysics*, **61**(3), 742–758.

Iversen, E., Gjøystdal, H., & Hansen, J. O. 2000. Prestack map migration as an engine for parameter estimation in TI media. *Pages 1004–1007 of: 70th Ann. Mtg. Soc. Explor. Geoph., Expanded Abstracts*.

Jakubowicz, H. 1990. A simple efficient method of dip-moveout correction. *Geoph. Prosp.*, **38**, 221–245.

Jakubowicz, H. 1998. Wave equation prediction and removal of interbed multiples. *Pages 1527–1530 of: Expanded Abstracts*. Soc. Explor. Geophys.

Jaramillo, H. 1997. *Seismic Data Mapping*. Ph.D. thesis, Colorado School of Mines.

Jaramillo, Herman, & Bleistein, Norman. 1998. Seismic data mapping. *SEG Technical Program Expanded Abstracts*, **17**(1), 1991–1994.

Jin, Shengwen, Wu, Ru-Shan, & Peng, Chengbin. 1998. Prestack depth migration using a hybrid pseudo-screen propagator. *SEG Technical Program Expanded Abstracts*, **17**(1), 1819–1822.

Kelamis, P., Erickson, K., Burnstad, R., Clark, R., & Verschuur, D. 2002. *Data-driven internal multiple attenuation - Applications and issues on land data*. Soc. of Expl. Geophys. Pages 2035–2038.

Kennett, B. L. N. 1974. Reflections, Rays and Reverberations. *Bull. Seism. Soc. Am.*, **64**, 1685–1696.

Kennett, B. L. N. 1979a. The suppression of surface multiples on seismic records. *Geoph. Prosp.*, **27**, 584–600.

Kennett, B. L. N. 1979b. Theoretical Reflection Seismograms for Elastic Media. *Geoph. Prosp.*, **27**, 301–321.

Kennett, B. L. N. 1983. *Seismic Wave Propagation in Stratified Media*. Cambridge: Cambridge University Press.

Le Rousseau, J. H. 2001. *Microlocal analysis of wave-equation imaging and generalized-screen propagators*. Ph.D. thesis, Colorado School of Mines.

Levin, F. K. 1971. Apparent velocity from dipping interface reflections. *Geophysics*, **36**, 510–516.

Liner, C. L. 1991. Born theory of wave-equation dip moveout. *Geophysics*, **56**(2), 182–189.

Lippmann, B. A. 1950. Variational principles for scattering processes II Scattering of slow Neutrons by Para-Hydrogen. *Phys. Rev.*, **79**(3), 481–486.

Lippmann, B. A. 1956. Rearrangement Collisions. *Phys. Rev.*, **102**(1), 264–268.

Lippmann, B. A., & Schwinger, J. 1950. Variational principles for scattering processes I. *Phys. Rev.*, **79**(3), 469–480.

Loewenthal, D., Lu, L., Roberson, R., & Sherwood, J. 1976. The wave equation applied to migration. *Geophysical Prospecting*, **24**(2), 380–399.

McMaken, H. 1986. On the convergence of the Bremmer series for the Helmholtz equation in 2d. *Wave Motion*, **8**, 277–283.

Miller, D., & Burridge, R. 1992. *Geophysical inversion*. SIAM. Chap. Multiparameter inversion, dip-moveout, and the generalized Radon transform, pages 46–58.

Miller, D., Oristaglio, M., & Beylkin, G. 1987. A new slant on seismic imaging: migration and integral geometry. *Geophysics*, **52**(6), 943–964.

Moses, H. E. 1956. Calculation of scattering potential from reflection coefficients. *Phys. Rev.*, **102**, 559–567.

Nolan, C. J., & Symes, W. W. 1997. Global solution of a linearized inverse problem for the wave equation. *Communications in Partial Differential Equations*, **22**(5-6), 919–952.

Patch, S. K. 2002. Computation of unmeasured thrid-generation VCT views from measured views. *IEEE Transactions on Medical Imaging*, **21**(7), 801–813.

Prosser, R. T. 1969. Formal solutions of inverse scattering problems. *Journal of Math. Phys.*, **10**, 1819–1822.

Rakesh. 1988. A linearised inverse problem for the wave equation. *Comm. in Part. Diff. Eqs.*, **13**, 573–601.

Razavy, M. 1975. Determination of the wave velocity in an inhomogeneous medium from reflection data. *J. Acoust. Soc. Am.*, **58**, 956–963.

Revenaugh, J., & Jordan, T. H. 1987. Observations of first-order mantle reverberations. *Bull. Seism. Soc. Am.*, **77**, 1704–1717.

Revenaugh, J., & Jordan, T. H. 1989. A study of mantle layering beneath the western pacific. *Jour. Geoph. Res.*, **94**, 5787–5813.

Revenaugh, J., & Jordan, T. H. 1991. Mantle Layering From ScS Reverberations 1. Waveform Inversion of Zeroth-Order Reverberations. *Jour. Geoph. Res.*, **96**, 19,749–19,762.

Santos, L. T., Schleicher, J., & Tygel, M. 1997. 2.5-D true amplitude offset continuation. *Journal of Seismic Exploration*, **6**(2/3), 103–116.

Sava, P., & Fomel, S. 2003. Angle-domain common-image gathers by wavefield continuation methods. *Geophysics*, **68**(3), 1065–1074.

Sava, Paul, & Guitton, Antoine. 2005. Multiple attenuation in the image space. *Geophysics*, **70**(1), V10–V20.

Sethian, J. A. 2002. Fast Algorithms for Optimal Control, Anisotropic Front Propagation and Multiple Arrivals. *ICM*, **3**, 735–746.

Sheaffer, Steven D., & Bleistein, Norman. 1998. 2.5D downward continuation using data mapping theory. *SEG Technical Program Expanded Abstracts*, **17**(1), 1554–1557.

Sjöstrand, J., & Grigis, A. 1994. *Microlocal Analysis for Differential Operators : An Introduction*. Cambridge: Cambridge University Press.

Sloat, John. 1948. Identification of echo reflections. *Geophysics*, **13**(1), 27–35.

Sorin, V., & Ronen, S. 1989. Ray-geometrical analysis of dip moveout amplitude distribution. *Geophysics*, **54**, 1333–1335.

Stolk, C. C. 2001 (July). *Microlocal analysis of the scattering angle transform.* Preprint, Dept. of Computational and Applied Mathematics, Rice University, http://www.caam.rice.edu/~cstolk/angle.ps.

Stolk, C. C., & de Hoop, M. V. 2002. Microlocal analysis of seismic inverse scattering in anisotropic elastic media. *Comm. Pure Appl. Math.*, **55**(3), 261–301.

Stolk, C. C., & de Hoop, M. V. 2004a. Modeling of seismic data in the downward continuation approach. *submitted to SIAM J. Appl. Math.* CWP468P.

Stolk, C. C., & de Hoop, M. V. 2004b. Seismic inverse scattering in the downward continuation approach. *submitted to SIAM J. Appl. Math.* CWP469P.

Stolk, C. C., & Symes, W. W. 2004. Kinematic artifacts in prestack depth migration. *Geophysics*, **69**(2), 562–575.

Stolk, C. C., de Hoop, M. V., & Symes, W. W. 2005. Kinematics of shot-geophone migration. *in preparation.*

Stolt, R. H. 1978. Migration by Fourier Transform. *Geophysics*, **43**(1), 23–48.

Stolt, R.H. 2002. Seismic data mapping and reconstruction. *Geophysics*, **67**, 890–908.

ten Kroode, A. P. E. 2002. Prediction of internal multiples. *Wave Motion*, **35**, 315–338.

ten Kroode, A. P. E. 2005. personal communication.

ten Kroode, A. P. E., Smit, D.-J., & Verdel, A. R. 1998. A microlocal analysis of migration. *Wave Motion*, **28**, 149–172.

Treves, F. 1980a. *Introduction to pseudodifferential and Fourier integral operators.* Vol. 2. New York: Plenum Press.

Treves, F. 1980b. *Introduction to pseudodifferential and Fourier integral operators.* Vol. 1. New York: Plenum Press.

Tygel, M., Schleicher, J., Hubral, P., & Santos, L. T. 1998. 2.5-D true-amplitude Kirchhoff migration to zero offset in laterally inhomogeneous media. *Geophysics*, **63**(2), 557–573.

van Borselen, R. 2002. Data-driven interbed multiple removal: Strategies and examples. *In: Expanded Abstracts.* Society of Exploration Geophysicists.

van Stralen, M. J. N. 1997. *Directional decomposition of electromagnetic and acoustic wave-fields.* Ph.D. thesis, Delft University of Technology.

Verschuur, D. J., & Berkhout, A. 1997. Estimation of multiple scattering by iterative inversion, Part II: Practical aspects and examples. *Geophysics*, **62**(5), 1596–1611.

Weglein, A., Gasparotto, F. A., Carvalho, P. M., & Stolt, R. H. 1997. An inverse-scattering series method for attenuating multiples in seismic reflection data. *Geophysics*, **62**, 1975–1989.

Weglein, A., Araújo, F. B., Carvalho, P. M., Stolt, R. H., Matson, K. H., Coates, R. T., Corrigan, D., Foster, D. J., Shaw, S. A., & Zhang, H. 2003. Inverse scattering series and seismic exploration. *Inverse Problems*, **19**, R27–R83.

White, B. S., Nair, B., & Bayliss, A. 1988. Random rays and seismic amplitude anomalies. *Geophysics*, **53**, 903–907.

Yilmaz, O. 1987. *Seismic data processing*. Investigations in Geophysics, vol. 2. Tulsa: Society of Exploration Geophysicists.

Yosida, K. 1995. *Functional Analysis*. Berlin: Springer.

Appendix A

Dip MoveOut: $n = 3$ and constant coefficient[1]

The aim of this appendix is two-fold: (i) to show that the analysis presented in the main text encompasses the usual DMO analysis in the absence of caustics as practiced in seismology, and (ii) to clarify the issue of number of phase variables needed in the OI representation of the DMO kernel for $n = 3$ in the constant coefficient case.

It is noted, that in the case of constant c, e can be chosen to be offset $h = \frac{1}{2}(r - s)$ in the acquisition manifold. We define an acquisition submanifold, Y', by prescribing the value of h. Throughout the analysis, in particular of the operator L, the manifold Y can be replaced by the submanifold Y' and the cotangent bundle $T^*Y\backslash 0$ by $T^*Y'\backslash 0$.

A.1 Modeling and imaging operators

In the case of a medium with constant velocity c, the generating function S in (2.4) is simply given by $-\tau T(x, x_0)$ with $T(x, x_0)$ the traveltime function along the ray connecting x with x_0, viz.

$$T(x, x_0) = \frac{|x - x_0|}{c}\,. \tag{A.1}$$

Since, away from the point source, no caustics occur, the traveltime function is single valued and only one phase variable, namely τ, is required in the phase function. We will use Cartesian coordinates.

The Green's function, G, is given by the OI (cf. (2.6))

$$G(x, t, x_0) = \int \frac{1}{8\pi^2 c^2 |x - x_0|} \exp[\mathrm{i}\tau(t - T(x, x_0))]\,\mathrm{d}\tau,$$

from which the modeling operator kernel of F is derived,

$$F(s_1, s_2, r_1, r_2, t, x_0) = \int \frac{-\tau^2}{16c^7\pi^3 |r - x_0||s - x_0|}\delta c(x_0) \exp[\mathrm{i}\tau(t - T(x_0, s_1, s_2, 0, r_1, r_2, 0))]\,\mathrm{d}\tau,$$

[1]This appendix has been published, along with Chapter 2 and Appendix B in:
de Hoop, M. V., Malcolm, A. E. and Le Rousseau, J. H. 2003. Seismic wavefield 'continuation' in the single scattering approximation: A framework for dip and azimuth moveout *Can. Appl. Math. Q.*, **10**, 199-238.

in which

$$T(x,s,r) = T(x,s) + T(x,r), \tag{A.2}$$

and the acquisition manifold, Y, is given by $(s_3, r_3) = (0,0)$ and X is given by $(x_0)_3 > 0$. The canonical relation of F follows as

$$\begin{aligned}\Lambda_F = \{(&\boldsymbol{s}_{1,2}(x_0,\beta) = (x_0)_{1,2} + cT(x_0,\beta)\beta_{1,2}, \boldsymbol{r}_{1,2}(x_0,\alpha) = (x_0)_{1,2} + cT(x_0,\alpha)\alpha_{1,2},\\ &T(x_0,\beta) + T(x_0,\alpha), \boldsymbol{\sigma}_{1,2}(\beta,\tau) = \tau\beta_{1,2}/c, \boldsymbol{\rho}_{1,2}(\alpha,\tau) = \tau\alpha_{1,2}/c, \tau;\\ &x_0, \tau(\beta+\alpha)/c) \mid (x_0)_3 > 0\ ,\ (\alpha,\beta) \in S^2 \times S^2\ , \alpha_3 > 0, \beta_3 > 0\},\end{aligned}$$

where

$$\begin{aligned} T(x_0,\beta) &= (x_0)_3/(c\beta_3),\\ T(x_0,\alpha) &= (x_0)_3/(c\alpha_3).\end{aligned}$$

The kernel of the exploding reflector modeling operator, F_0, is given by

$$F_0(z_1,z_2,t_0,x_0) = \int \frac{-\tau_0^2}{16c^7\pi^3|z-x_0|^2}\delta c(x_0)\exp[\mathrm{i}\tau_0(t - 2T(z_1,z_2,0,x_0))]\,\mathrm{d}\tau_0,$$

with $z = (z_1, z_2, 0)$. The corresponding canonical relation follows as

$$\begin{aligned}\Lambda_E = \{(&\boldsymbol{z}_{1,2}(x_0,\alpha) = (x_0)_{1,2} + (x_0)_3\alpha_{1,2}/\alpha_3, T_0(x_0,\alpha) = 2(x_0)_3/(\alpha_3 c),\\ &\boldsymbol{\zeta}_{1,2}(x_0,\alpha) = 2\tau_0\alpha_{1,2}/c, \tau_0; x_0, 2\tau_0\alpha/c) \mid (x_0)_3 > 0\ ,\ \alpha \in S^2\ , \alpha_3 > 0\}.\end{aligned}$$

A.2 The Dip MoveOut operator

We compose the exploding reflector modeling operator and the GRT to form the DMO operator. We introduce the midpoint(y)-offset(h) parametrization, i.e., $s = y - h$, $r = y + h$. In the constant coefficient case, in the absence of caustics, we can set $e = h$. Then the GRT, $L = L_U$, is replaced by the 'common-offset imaging' operator. The phase function associated with the common-offset imaging operator is simply given by $\Phi(y,t,x_0,\tau) = \tau(\frac{|x_0-y-h|}{c} + \frac{|x_0-y+h|}{c} - t)$. We choose our coordinates such that $h = (h_1, 0, 0)$.

The phase function associated with the exploding reflector modeling is

$$\Phi_{\mathrm{ER}}(z,t_0,x_0,\tau_0) = \tau_0(t_0 - 2\frac{|x_0 - z|}{c}).$$

The phase function of the DMO operator then becomes

$$\Psi(y,t,z,t_0,x_0,\tau,\tau_0) = \Phi(y,t,x_0,\tau) + \Phi_{\mathrm{ER}}(z,t_0,x_0,\tau_0).$$

(Observe that (x_0,τ,τ_0) are the phase variables.)

Theorem A.2.1. *Ψ is a non-degenerate phase function. The composition of Λ_E and Λ_L*

is transversal.

Proof. The partial derivatives of Ψ with respect to the phase variables are given by

$$\frac{\partial\Psi}{\partial(x_0)_i} = -\frac{2\tau_0}{c}\frac{((x_0)_i - z_i)}{|x_0 - z|} + \frac{\tau}{c}\left(\frac{((x_0)_i - y_i - h_i)}{|x_0 - y - h|} + \frac{((x_0)_i - y_i + h_i)}{|x_0 - y + h|}\right) , \quad \text{(A.3)}$$

$$\frac{\partial\Psi}{\partial\tau} = -t + \frac{1}{c}\left(|x_0 - y - h| + |x_0 - y + h|\right) , \quad \text{(A.4)}$$

$$\frac{\partial\Psi}{\partial\tau_0} = t_0 - \frac{2|x_0 - z|}{c} , \quad \text{(A.5)}$$

$i = 1, 2, 3$. The form of the differentials with respect to all the variables is:

			$\mathrm{d}(\partial_{(x_0)_i}\Psi)$ $(i=1,2,3)$	$\mathrm{d}(\partial_\tau\Psi)$	$\mathrm{d}(\partial_{\tau_0}\Psi)$
(i)	y_j	$(j=1,2)$	$*$	$*$	$*$
(ii)	t		$\boxed{0}$	$\boxed{-1}$	$\boxed{0}$
(iii)	z_j	$(j=1,2)$	$-\frac{2\tau_0}{c}\left(-\frac{\delta_{ij}}{\lvert x_0-z\rvert} + \frac{((x_0)_i-z_i)((x_0)_j-z_j)}{\lvert x_0-z\rvert^3}\right)$	$*$	$*$
(iv)	t_0		$\boxed{0}$	$\boxed{0}$	$\boxed{1}$
(v)	$(x_0)_j$	$(j=1,2,3)$	$*$	$*$	$*$
(vi)	τ		$*$	0	0
(vii)	τ_0		$-\frac{2}{c}\frac{((x_0)_i-z_i)}{\lvert x_0-z\rvert}$	0	0

Because of the entries related to t and t_0 [rows (ii) and (iv)] the rank of the matrix is $2 + \mathrm{rank}(\mathrm{d}(\frac{\partial\Psi}{\partial x_0}))$. Now, $\frac{c}{2\tau_0} \times (iii)_j - \frac{c}{2}\frac{((x_0)_j - z_j)}{|x_0-z|^2} \times (vii)$, for $j = 1, 2$ yields the form of rows (iii) and (vii):

$$\begin{array}{c|ccc} (iii)_1 & \frac{1}{|x_0-z|} & 0 & 0 \\ (iii)_2 & 0 & \frac{1}{|x_0-z|} & 0 \\ (vii) & * & * & -\frac{2}{c}\frac{((x_0)_3-z_3)}{|x_0-z|} \end{array} .$$

Since $|x_0 - z| > 0$, $(0 = z_3 < (x_0)_3)$, $\mathrm{rank}(\mathrm{d}(\frac{\partial\Psi}{\partial x_0})) = 3$. The rank of the differentials is therefore maximal; the phase is nondegenerate. It follows that the composition of the two canonical relations is transversal (Hörmander, 1985b, Thm. 21.2.19). □

Parametrization of the canonical relation

As already mentioned above in the case $e = h$ one can restrict the DMO operation to a constant offset one, replacing Y by Y'. Comparing to the main text, observe that one does not need the cotangent variable ε to parameterize the canonical relation: we make use of only s, x_0, τ here. In this case Λ_D then follows as

$$\Lambda_D = \{(\boldsymbol{z}(s,x_0), \boldsymbol{t}_0(s,x_0), \boldsymbol{\zeta}(s,x_0,\tau), \boldsymbol{\tau}_0(s,x_0,\tau); \boldsymbol{y}(s), \boldsymbol{t}(s,x_0), \boldsymbol{\eta}(s,x_0,\tau), \tau)\} .$$

The midpoint y is $y = s + h$, the receiver location is $r = s + 2h$, and the traveltime is $t = (|x_0 - s| + |x_0 - r|)/c$. Using the phase function Ψ we immediately obtain that

$$\eta_i = \frac{\tau}{c}\left(\frac{s_i - (x_0)_i}{|x_0 - s|} + \frac{r_i - (x_0)_i}{|x_0 - r|}\right) , \quad i = 1, 2 ,$$

We introduce ξ as,

$$\xi = \partial_{x_0}\Psi = \frac{\tau}{c}\left(\frac{(x_0)_i - s_i}{|x_0 - s|} + \frac{(x_0)_i - r_i}{|x_0 - r|}\right) , \quad i = 1, 2, 3 .$$

Observe that, in a constant medium, we naturally have $\xi_i = -\eta_i$ for $i = 1, 2$. According to the main text, we define $\alpha_0 \in S^2$ as

$$(2\tau_0/c)\alpha_0 = \xi ,$$

which yields τ_0. Note that $\sin\theta_0 = (\alpha_0)_3 > 0$ (cf. Figure 3.2). The zero-offset travel time is then given by $t_0 = (x_0)_3/(c\sin\theta_0)$. The zero-offset source location, z, then follows as $z = ct_0\alpha_0 + x_0$.

The 'impulse response', $n = 2$

In the case $n = 2$, and the 'horizontal' acquisition manifold as in the previous subsection, we have $s = (s_1, 0)$, $r = (r_1, 0)$ for source and receiver locations. We parameterize the canonical relation of the DMO operator, Λ_D, with $(x_0, s, \tau, \varepsilon)$, where s is the source, x_0 is the scattering point (cf. Figure 3.2), τ the frequency, and ε the cotangent variable corresponding to e. Here, e is taken to be the scattering angle, θ,

$$\theta = \boldsymbol{\theta}(x_0, s, r) = \arccos\left(\frac{\langle x_0 - r, x_0 - s\rangle}{|x_0 - r||x_0 - s|}\right) .$$

The canonical relation, Λ_D, will then be of the form

$$\begin{aligned}\Lambda_D \;=\; \{&(\boldsymbol{z}(x_0, s, \tau, \varepsilon), \boldsymbol{t}_0(x_0, s, \tau, \varepsilon), \boldsymbol{\zeta}(x_0, s, \tau, \varepsilon), \boldsymbol{\tau}_0(x_0, s, \tau, \varepsilon);\\ &s, \boldsymbol{r}(x_0, s, \tau, \varepsilon), T(x_0, s, \tau, \varepsilon), \boldsymbol{\sigma}(x_0, s, \tau, \varepsilon), \boldsymbol{\rho}(x_0, s, \tau, \varepsilon), \tau)\} .\end{aligned}$$

The zero-offset case corresponds to $\theta = 0$, which we exclude in the neighborhood E_{i} (cf. Figure 2.4). We make use of only one connected component of E_{i} and thus assume that $\theta > 0$ in E_{i}.

To determine the cotangent variables, σ, ρ, ζ and τ_0, we will make use of the derivatives

$$\begin{aligned}\partial_{(x_0)_i}\theta = -\frac{1}{\sin\theta}\Bigg\{&\left(\frac{\delta_{ij}}{|x_0 - r|} - \frac{(x_0)_j - r_j}{|x_0 - r|^3}\right)\left(\frac{(x_0)_j - s_j}{|x_0 - s|}\right)\\ &+ \left(\frac{\delta_{ij}}{|x_0 - s|} - \frac{(x_0)_j - s_j}{|x_0 - s|^3}\right)\left(\frac{(x_0)_j - r_j}{|x_0 - r|}\right)\Bigg\} ,\\ \partial_{s_1}\theta = \frac{1}{\sin\theta}&\left(\frac{\delta_{1j}}{|x_0 - s|} + \frac{(x_0)_j - s_j}{|x_0 - s|^3}\right)\left(\frac{(x_0)_j - r_j}{|x_0 - r|}\right) ,\end{aligned}$$

and a similar expression for $\partial_{r_1}\theta$.

(A.6)

From (x_0, s) we determine the direction of the ray at the source,

$$-\beta = \frac{s - x_0}{|s - x_0|} , \tag{A.7}$$

and the traveltime

$$\tilde{t} = \frac{|s - x_0|}{c} . \tag{A.8}$$

The angle θ_s is defined through

$$\beta = (\cos\theta_s, \sin\theta_s) . \tag{A.9}$$

Using the relation $\theta_r = \theta_s + \theta$ (cf. Figure 3.2) we find the angle θ_r which defines the direction of the ray at the receiver

$$-\alpha = -(\cos\theta_r, \sin\theta_r) . \tag{A.10}$$

The receiver ray traveltime then follows from

$$\sin\theta_r c\hat{t} = \frac{(x_0)_3}{c} . \tag{A.11}$$

Then the receiver position is found to be

$$r = -\hat{t}c\alpha + x_0 . \tag{A.12}$$

The total traveltime is simply given by

$$T = \tilde{t} + \hat{t} . \tag{A.13}$$

The cotangent variables σ and ρ are then given by

$$\sigma = -\frac{\tau}{c}\cos\theta_s - \varepsilon\partial_{s_1}\theta(x_0, s, r) , \tag{A.14}$$

$$\rho = -\frac{\tau}{c}\cos\theta_r - \varepsilon\partial_{r_1}\theta(x_0, s, r) . \tag{A.15}$$

We determine (α_0, τ_0) from the equality

$$\frac{\tau}{c}(\alpha + \beta) - \varepsilon\partial_{x_0}\theta(x_0, s, r) = \xi = 2\left(\frac{\tau_0}{c}\right)\ \alpha_0 . \tag{A.16}$$

The zero-offset traveltime, t_0, thus follows as

$$t_0 = (x_0)_3/(c\ \sin\theta_0) ,$$

with $\sin\theta_0 = (\alpha_0)_3$. The zero-offset source position, z, is then given by

$$z = ct_0\alpha_0 + x_0 \ ,$$

while

$$\zeta = -\xi_1$$

(cf. (A.16)).

For Born modeled data the only contribution comes from $\varepsilon = 0$, in which case these formulae simplify to

$$\begin{aligned} \sigma &= -\frac{\tau}{c}\cos\theta_s \ , \quad \rho = -\frac{\tau}{c}\cos\theta_r \ , \\ \alpha_0 &= (\alpha+\beta)/(|\alpha+\beta|) \ , \\ t_0 &= (x_0)_3/(c\sin\theta_0) = T\sin\theta_r\sin\theta_s/[\sin\theta_0(\sin\theta_r+\sin\theta_s)] \ . \end{aligned}$$

The distance between the source location, s, and the zero-offset source location, z, is given by

$$d_0 = z - s = c(\tilde{t}\beta_1 - t_0(\alpha_0)_1) = cT\sin\theta_r\sin(\theta/2)/[(\sin\theta_s+\sin\theta_r)\sin\theta_0] \ .$$

A.3 Parameterization of the canonical relation by a phase function

In the case $e = h$ discussed above, it is possible that the number of phase variables used in Ψ, here, (x_0, τ, τ_0), is unnecessarily large. Since the canonical relation and the stationary point set are locally diffeomorphic, we can investigate this question on the stationary point set, $S_\Psi = \{(y,t,z,t_0,x_0,\tau,\tau_0) \mid \partial_{x_0}\Psi = 0,\ \partial_\tau\Psi = 0,\ \partial_{\tau_0}\Psi = 0\}$.

Minimum number of phase variables

Let us first project S_Ψ onto the natural base coordinates (y,t,z,t_0). Let

$$\pi : (y,t,z,t_0,x_0,\tau,\tau_0) \mapsto (y,t,z,t_0) \ ,$$

then $\operatorname{rank}(D\pi\,|_{S_\Psi}) = \dim\{(y,t,z,t_0)\} + \operatorname{rank}(\partial_{x_0}f, \partial_\tau f, \partial_{\tau_0}f) - \dim\{(x_0,\tau,\tau_0)\}$, where $f = 0$ is the defining equation for S_Ψ, i.e., $f = (\partial_{x_0}\Psi, \partial_\tau\Psi, \partial_{\tau_0}\Psi)$. Then

$$\operatorname{corank}(D\pi\,|_{S_\Phi}) = \dim\{(x_0,\tau,\tau_0)\} - \operatorname{rank}(\partial_{x_0}f, \partial_\tau f, \partial_{\tau_0}f)$$

is the minimal number of phase variables required to characterize the canonical relation.

Corollary A.3.1. *The minimum number of phase variables that locally parameterizes $\Lambda_D = \Lambda_E \circ \Lambda_L$ is 2.*

Proof. The structure of the differentials of f with respect to (x_0, τ, τ_0) is:

	(a) $\mathrm{d}(\partial_{(x_0)_j}\Psi)$ $(j=1,2,3)$	(b) $\mathrm{d}(\partial_\tau \Psi)$	(c) $\mathrm{d}(\partial_{\tau_0}\Psi)$
$(i)\ (x_0)_i$	$-\frac{2\tau_0}{c}\left(\frac{\delta_{ij}}{\lvert x_0-z\rvert}-\frac{((x_0)_i-z_i)((x_0)_j-z_j)}{\lvert x_0-z\rvert^3}\right)$ $+\frac{\tau}{c}\left(\frac{\delta_{ij}}{\lvert x_0-y-h\rvert}-\frac{((x_0)_i-y_i-h_i)((x_0)_j-y_j-h_j)}{\lvert x_0-y-h\rvert^3}\right)$ $+\frac{\tau}{c}\left(\frac{\delta_{ij}}{\lvert x_0-y+h\rvert}-\frac{((x_0)_i-y_i+h_i)((x_0)_j-y_j+h_j)}{\lvert x_0-y+h\rvert^3}\right)$	$\frac{1}{c}\left(\frac{((x_0)_i-y_i-h_i)}{\lvert x_0-y-h\rvert}+\frac{((x_0)_i-y_i+h_i)}{\lvert x_0-y+h\rvert}\right)$	$\frac{2}{c}\frac{((x_0)_i-z_i)}{\lvert x_0-z\rvert}$
$(ii)\ \ \tau$	$\frac{1}{c}\left(\frac{((x_0)_j-y_j-h_j)}{\lvert x_0-y-h\rvert}+\frac{((x_0)_j-y_j+h_j)}{\lvert x_0-y+h\rvert}\right)$	0	0
$(iii)\ \tau_0$	$-\frac{2}{c}\frac{((x_0)_j-z_j)}{\lvert x_0-z\rvert}$	0	0

with $i=1,2,3$. On the stationary point set, S_Ψ, in view of equation (A.3), rows (ii) and (iii) are linearly dependent and the same holds for columns (b) and (c). Equation (A.3) for $(x_0)_3$ ($(x_0)_3 \neq 0$) gives $-\frac{2\tau_0}{c}\frac{1}{\lvert x_0-z\rvert}+\frac{\tau}{c}\left(\frac{1}{\lvert x_0-y-h\rvert}+\frac{1}{\lvert x_0-y+h\rvert}\right)=0$ and hence a simplification of the upper left 3×3 matrix. Therefore $\mathrm{rank}(\partial_{x_0}f, \partial_\tau f, \partial_{\tau_0} f)$ is that of:

	(a)	(b)
(i)	$2\tau_0\frac{((x_0)_i-z_i)((x_0)_j-z_j)}{\lvert x_0-z\rvert^3}$ $-\tau\frac{((x_0)_i-y_i-h_i)((x_0)_j-y_j-h_j)}{\lvert x_0-y-h\rvert^3}$ $-\tau\frac{((x_0)_i-y_i+h_i)((x_0)_j-y_j+h_j)}{\lvert x_0-y+h\rvert^3}$	$((x_0)_i-z_i)$
(ii)	$((x_0)_j-z_j)$	0

with $i,j=1,2,3$. By subtracting $[2\tau_0\frac{((x_0)_j-z_j)}{\lvert x_0-z\rvert^3}-\tau(\frac{((x_0)_j-y_j-h_j)}{\lvert x_0-y-h\rvert^3}+\frac{((x_0)_j-y_j+h_j)}{\lvert x_0-y+h\rvert^3})]\times(b)$ from $(a)_j$, $j=1,2,3$, and using the fact that $h_2=h_3=0$, $z_3=y_3=0$, and $z_2=y_2$ on S_Φ, the matrix further simplifies to

	(a)	(b)
$(i)_1$	$-\tau\frac{(z_1-y_1-h_1)((x_0)_j-y_j-h_j)}{\lvert x_0-y-h\rvert^3}-\tau\frac{(z_1-y_1+h_1)((x_0)_j-y_j+h_j)}{\lvert x_0-y+h\rvert^3}$	$((x_0)_1-z_1)$
$(i)_2$	0	$((x_0)_2-y_2)$
$(i)_3$	0	$(x_0)_3$
(ii)	$((x_0)_j-z_j)$	0

Performing a similar operation with rows instead yields that the rank is that of $((x_0)_3>0)$

	$(a)_1$	$(a)_3$	(b)
$(i)_1$	$-\tau\frac{(z_1-y_1-h_1)^2}{\lvert x_0-y-h\rvert^3}-\tau\frac{(z_1-y_1+h_1)^2}{\lvert x_0-y+h\rvert^3}$	0	$((x_0)_1-z_1)$
$(i)_3$	0	0	$(x_0)_3$
(ii)	$((x_0)_1-z_1)$	$(x_0)_3$	0

(A.17)

the determinant of which, $\tau(x_0)_3^2\left(\frac{(z_1-y_1-h_1)^2}{|x_0-y-h|^3}+\frac{(z_1-y_1+h_1)^2}{|x_0-y+h|^3}\right)$, is not zero if $h_1 \neq 0$. We conclude that $\text{rank}(\partial_{x_0} f, \partial_\tau f, \partial_{\tau_0} f) = 3$. □

Choice of phase variables

A similar argument as that of the proof of Corollary A.3.1, shows that the corank of the projection on $(y_1, y_2, t, z_1, (x_0)_2, \tau)$ is 0. It makes use of the fact that $h_1 \neq 0$, $(x_0)_3 \neq 0$ as well as that $(x_0)_1 > y_1 \Leftrightarrow (x_0)_1 > z_1$ on S_Ψ. We can therefore use $(x_0)_2$ and τ as phase variables or $\alpha_2 = (z_2 - (x_0)_2)/|z - x_0|$ and τ. Figure A.1 illustrates the need for a second phase variable in addition to τ.

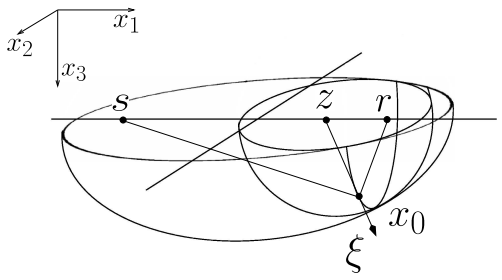

Figure A.1. Isochrones for DMO, $n = 3$ constant coefficient.

The amplitude

We apply the stationary phase formula to achieve the parameterization of the OI representation of the DMO kernel with only $(x_0)_2$ and τ as phase variables. We compute the Hessian of Ψ/τ with respect to $(x_0)_1$, $(x_0)_3$, τ_0, which does not vanish because of the previous remarks. Its evaluation at stationarity yields

$$H = \left|\frac{\partial^2 \Psi/\tau}{\partial^2((x_0)_1, (x_0)_3, \tau_0)}\right| = \frac{4}{\tau^2 c^3}\frac{(x_0)_3^2}{|x_0 - z|^2}\left(\frac{(z_1 - y_1 - h_1)^2}{|x_0 - y - h|^3} + \frac{(z_1 - y_1 + h_1)^2}{|x_0 - y + h|^3}\right) .$$

We can relate this Hessian geometrically to the curvatures of the finite-offset and zero-offset isochrons. In this form, the Hessian simplifies, using the law of sines, to

$$H = \frac{-4(x_0)_3^2}{\tau^3 c^2}(\kappa_O - \kappa_I) K \frac{1}{h_1}\left(\frac{1}{\sin(\theta_r)} + \frac{1}{\sin(\theta_s)}\right)\frac{1}{\sin(\theta/2)}\frac{1}{\sin^2(\theta_0)} ,$$

where the κ_O is the curvature of the zero-offset isochron, κ_I is the curvature of the constant-offset isochron, and $K = -\frac{2\tau \sin^2(\theta/2)\cos(\theta/2}{c|x-z|}$ as defined in (Bleistein *et al.*, 2000, (7.6.10)-(7.6.13)).

The signature of the second order differential $(\partial^2\Psi/\tau)/(\partial^2((x_0)_1,(x_0)_3,\tau_0))$ is constant. It is easy to compute it at a point x_0 half-way between source and receiver. The signature is then -1.

At stationarity the phase function simplifies to

$$\tau(\frac{|x_0-y-h|}{c}+\frac{|x_0-y+h|}{c}-t)\ ,$$

and the entire amplitude of the associated oscillatory integral representatio becomes

$$\frac{\tau^{1/2}\tau_0^2}{32c^{14}(2\pi)^{3/2}|z-x_0|^2|y+h-x_0||y-h-x_0|}\exp(-\mathrm{i}\pi/4)\frac{1}{|H|^{1/2}}\ .$$

Appendix B

Azimuth MoveOut: $n = 3$ and constant coefficient[1]

In a constant velocity medium, it is possible to derive an expression for the impulse response in closed form. In Biondi *et al.* (1998) the impulse response of AMO was derived as the time t_2 as a function of translation in midpoint location, $\frac{1}{2}(r_2 + s_2) - \frac{1}{2}(r_1 + s_1)$ for given offsets $\frac{1}{2}(r_1 - s_1)$ and $\frac{1}{2}(r_2 - s_2)$. Here, we determine time t_2 as a function of ray direction at s_1 (associated with σ_1) for given e_1 and (subsurface) scattering angle from e_2 and (acquisition surface) azimuth direction, i.e. direction of $\frac{1}{2}(r_2 - s_2)$.

We derive the impulse response in two steps. First, we determine the three-dimensional DMO zero-offset traveltime (t_0) from (s_1, r_1, t_1), and then we determine the AMO time (t_2) by performing inverse DMO from the zero-offset ray to (s_2, r_2, t_2). Since the zero-offset ray will always be in the plane defined by the source and receiver rays, we need only compute the scattering angle in that plane, as a function of the initial ray angles at the source s_1. We apply the DMO formula derived in Appendix A.

In Figure B.1 we introduce the unit vectors

$$\tilde{\alpha}_1 = (\cos(\varphi_1)\cos(\psi_1), \cos(\varphi_1)\sin(\psi_1), \sin(\varphi_1)) , \tag{B.1}$$

$$\Xi = (\cos(\varphi_2)\cos(\psi_2), \cos(\varphi_2)\sin(\psi_2), \sin(\varphi_2)) . \tag{B.2}$$

($\tilde{\alpha}_1$ determines σ_1 and Ξ determines ξ.) We observe that $w = \tilde{\alpha}_1 - \lambda\Xi$, while also w lies in the $x_3 = 0$ plane. We evaluate λ by setting $w_3 = 0$,

$$\lambda = \frac{\sin(\varphi_1)}{\sin(\varphi_2)} . \tag{B.3}$$

Then

$$w = \begin{pmatrix} \cos(\varphi_1)\cos(\psi_1) - \frac{\sin(\varphi_1)}{\sin(\varphi_2)}\cos(\varphi_2)\cos(\psi_2) \\ \cos(\varphi_1)\sin(\psi_1) - \frac{\sin(\varphi_1)}{\sin(\varphi_2)}\cos(\varphi_2)\sin(\psi_2) \\ 0 \end{pmatrix} \tag{B.4}$$

with

$$\|w\|^2 = \cos^2(\varphi_1) + \frac{\sin^2(\varphi_1)}{\tan^2(\varphi_2)} - \frac{\sin(2\varphi_1)}{\tan(\varphi_2)}\cos(\psi_1 - \psi_2) . \tag{B.5}$$

[1]This appendix has been published, along with Chapter 2 and Appendix A in:
de Hoop, M. V., Malcolm, A. E. and Le Rousseau, J. H. 2003. Seismic wavefield 'continuation' in the single scattering approximation: A framework for dip and azimuth moveout *Can. Appl. Math. Q.*, **10**, 199-238.

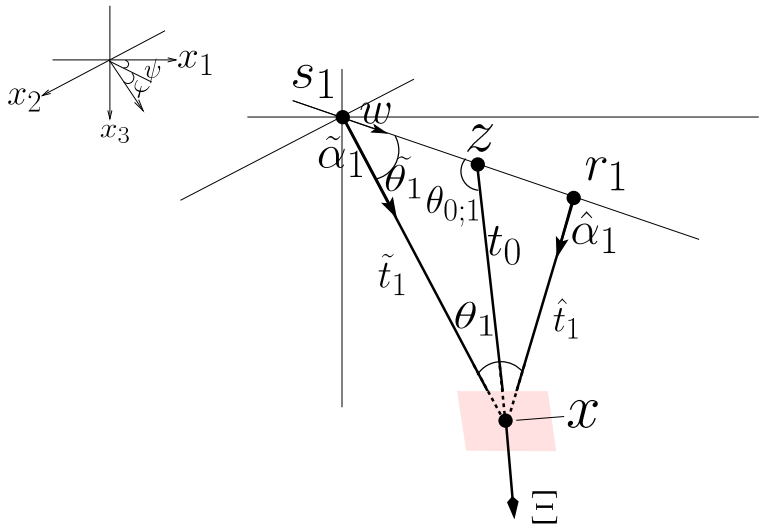

Figure B.1. DMO geometry and notation related to $(s_1, r_1, t_1, \sigma_1, \rho_1, \tau_1)$.

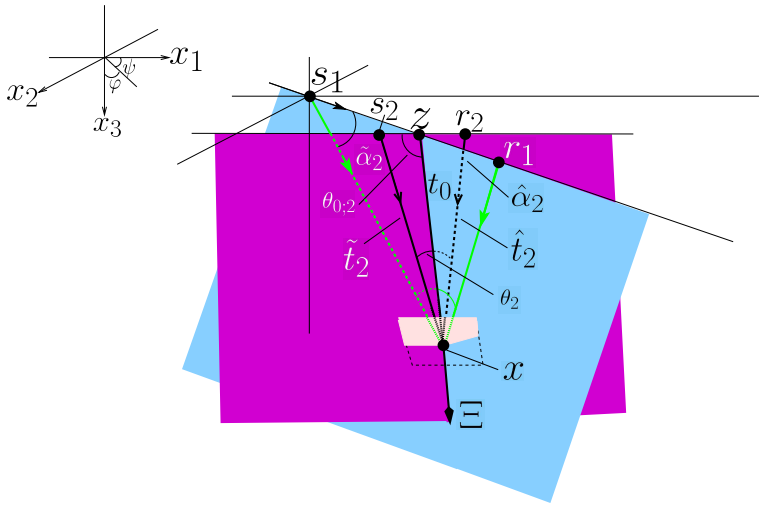

Figure B.2. Rotation to set azimuth showing the notation for the output (black) rays. The input rays are shown in gray. The plane which contains the output rays (dark gray) is the result of rotating the plane which contains the input rays (light gray) about the Ξ vector.

The angle $\tilde{\theta_1}$ is defined in Figure B.1 and is given by

$$\tilde{\theta_1} = \text{acos}\left(\frac{\tilde{\alpha}_1 \cdot w}{\|w\|}\right) . \tag{B.6}$$

With $\tilde{\theta_1}$ we derive the zero-offset time t_0 using (A.17),

$$t_0 = \frac{t_1 \sin(\tilde{\theta_1}) \sin(\hat{\theta}_1)}{(\sin(\tilde{\theta_1}) + \sin(\hat{\theta}_1)) \sin(\theta_{0;1})} . \tag{B.7}$$

We now rotate this DMO ray geometry about the Ξ axis to obtain the desired azimuthal orientation. We have chosen our coordinates such that this orientation coincides with the 1 axis, which implies that $w := (1, 0, 0)$. We determine the time t_2 by applying inverse DMO to the rotated geometry. Thus,

$$\theta_{0;2} = \text{acos}(\Xi \cdot (1, 0, 0)) = \text{acos}(\cos(\varphi_2) \cos(\psi_2)) , \tag{B.8}$$

and it follows that

$$t_2 = \tilde{t}_2 + \hat{t}_2 = \frac{t_0(\sin(\tilde{\theta}_2) + \sin(\hat{\theta}_2)) \sin(\theta_{0;2})}{\sin(\tilde{\theta}_2) \sin(\hat{\theta}_2)} . \tag{B.9}$$

Appendix C

Table of Symbols for Appendix D, E, F and Chapter 3[1]

Table C.1. Table of symbols. In general quantities with a sub or super-script s refer to source quantities, with r to receiver quantities. Bold symbols are vectors and an underlined symbol is a function of other variables.

symbol	in or near	meaning
θ	p. 37	scattering angle
s	p. 38	source position
a	p. 38	rightmost surface position in Figure 3.3
d_0	p. 40, Figure 3.2	distance from source to zero offset surface position
$\mathbf{x}$	p. 40, Figure 3.2	subsurface position
$\boldsymbol{\xi}$	p. 40, Figure 3.2	migration dip
z, $\mathbf{z}$	p. 40, Figure 3.2	surface position of zero-offset ray
T	p. 41	two-way time
t_s	p. 41 Figure 3.2	time along source ray
t_0	p. 41 Figure 3.2	one-way zero-offset time
θ_s	p. 41, Figure 3.2	angle between surface and source ray
φ_α	p. 46	spherical angle measured clockwise from x
ψ_α	p. 46	spherical angle measured downward from $x-y$ plane
θ_0	Eqn D.2, Figure 3.2	angle from zero-offset ray to surface
y	p. 140	midpoint
h, $\mathbf{h}$	Eqn. D.8	half-offset
F	Eqn. E.1	modeling operator
δc	Eqn. E.1	velocity contrast
c	Eqn. E.1	smooth background velocity
$G(\mathbf{r},t,\mathbf{x})$	Eqn. E.1	Green's function for singularities from $\mathbf{x}$ to $\mathbf{r}$ in time t
X	Eqn. E.1	set of subsurface scattering points

[1]This appendix has been published, along with Chapter 3 and Appendices D, E, and F as: Malcolm, A. E., de Hoop, M. V. and Le Rousseau, J. H. 2005. The applicability of DMO/AMO in the presence of caustics. *Geophysics* **70 S1-S17.**

symbol	in or near	meaning
$T(\mathbf{x},\mathbf{y})$	Eqn E.2	traveltime function for ray travelling from $\mathbf{x}$ to $\mathbf{y}$
ω	Eqn E.2	angular frequency
F^*	Eqn. E.5	imaging/migration operator
$O_r \times O_s$	Eqn. E.5	set of source and receiver positions
N	Eqn. E.6	normal operator F^*F
$A(\mathbf{s},\mathbf{x},\mathbf{r})$	Eqn. E.6	amplitude of the Green's function
$\boldsymbol{\alpha}^s$	Eqn. E.8	source ray direction
S_s^2	Eqn. E.9	sphere of source ray directions
$\boldsymbol{\Gamma}$	Eqn. E.10	spatial gradient of traveltime function
$\boldsymbol{\nu}$	Eqn. E.10	normalized $\boldsymbol{\Gamma}$ (migration dip)
μ_{LS}	Eqn. E.11	amplitude factor for normal operator
ψ	Eqn. E.12	scattering azimuth
E_ν, E_θ, E_ψ	Eqn. E.12	set of ν, θ, ψ values
Λ	Eqn. E.13	full amplitude of normal operator
$P(\mathbf{x},\mathbf{y})$	Eqn. E.14	parametrix (approximate inverse) of normal operator
$\mathbf{v}$	Eqn. E.16	$\boldsymbol{\nu}$ in input variables rather than output variables
I	Eqn. E.18	left inverse of modeling operator
σ_1', σ_2'	Eqn. E.22	coordinates on level set of T
τ'	Eqn. E.22	parameter to fix which level set of T we are on
$\boldsymbol{\psi}$	Eqn. E.23	azimuthal vector
Φ	Eqn. E.24	phase function
$\mathbf{H}$	p. 147	Hessian of second derivatives for stationary phase
$\mathbf{B}_{kl}$	p. 147	2^{nd} fundamental tensor
$\mathbf{x}_0$	Eqn. E.27	stationary point for x integration
$\boldsymbol{\eta}'$	Eqn. F.3	Fourier variable associated to midpoint
ω^0	Eqn. F.6	stationary point in ω
$\mathbf{J}$	Eqn. F.15	jacobian of the variable transformation $x_1, x_2 \to \eta_1', \eta_2'$
$\mathbf{p}$ ($\mathbf{q}$)	Eqn. F.15	vectors from scattering point to source (receiver)
k_1	Eqn. F.18	symbol to simplify calculations in appendix C

Appendix D

Impulse Responses[1]

D.1 DMO

For a constant-velocity model one can derive, in closed form, the shape of the angle-domain DMO impulse response. To do this, we fix the source position, s, the scattering angle, θ, and the two-way traveltime T, and compute the output time t_0 and the source to zero-offset distance, d_0. We use the notation defined in Figure 3.2.

Since we assume the traveltime to be fixed and the medium to have a constant velocity (straight rays), we have the following three relations (see Figure 3.2):

$$\theta_r = \pi - \theta - \theta_s \tag{D.1}$$

$$\theta_0 = \pi - \frac{\theta}{2} - \theta_s \tag{D.2}$$

$$T = t_s + t_r. \tag{D.3}$$

From the law of sines we derive the following relationships:

$$t_0 = \frac{T \sin\theta_s \sin\theta_r}{(\sin\theta_s + \sin\theta_r)\sin\theta_0} \tag{D.4}$$

$$d_0 = \frac{vT \sin\theta_r \sin(\frac{\theta}{2})}{(\sin\theta_s + \sin\theta_r)\sin\theta_0}, \tag{D.5}$$

which gives both the one-way zero-offset travel time t_0 and the distance d_0 between the source and the zero-offset source/receiver as a function of the source angle θ_s. Figure 3.5 shows this impulse response (t_0 as a function of d_0). In these expressions, θ and T are fixed, while the other angles vary.

Although equations (D.4), (D.5) are given in terms of θ_s, θ_r and θ_0, it is possible to fully determine both t_0 and d_0 in terms of only two angles. Using equation (D.1) to substitute for θ_r and (D.2) for θ_s, equation (D.4) simplifies to

$$t_0 = \frac{\sin^2\theta_0 - \sin^2(\frac{\theta}{2})}{2\sin^2\theta_0 \cos(\frac{\theta}{2})}. \tag{D.6}$$

[1]This appendix has been published, along with Chapter 3 and Appendices C, E, and F as:
Malcolm, A. E., de Hoop, M. V. and Le Rousseau, J. H. 2005. The applicability of DMO/AMO in the presence of caustics. *Geophysics* **70 S1-S17.**

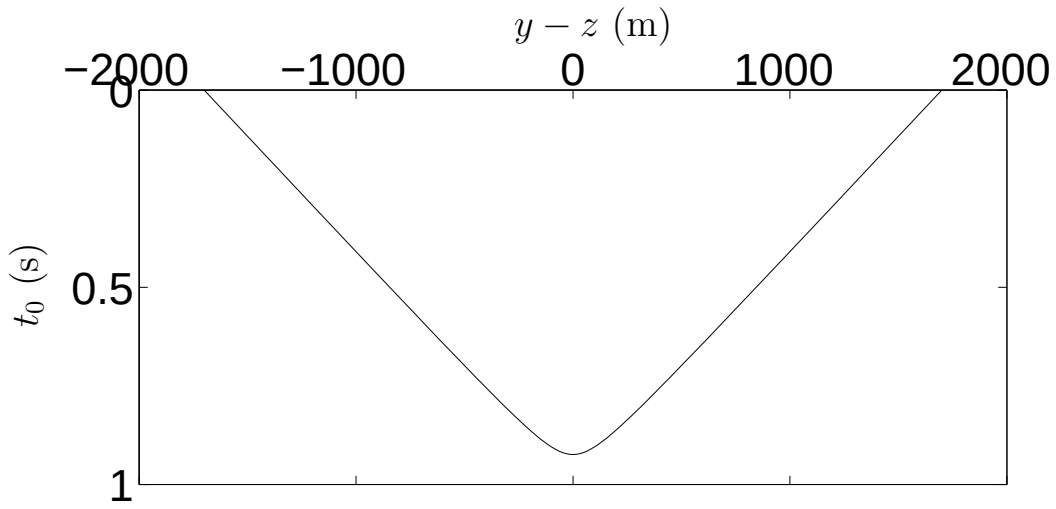

Figure D.1. DMO impulse response showing the zero-offset travel time as a function of the distance from the midpoint to the surface position of the zero-offset ray. Cross plotting these quantities makes the impulse response symmetric in a constant-velocity model. This symmetry disappears if the velocity model is not symmetric.

Using equations (44-46) of Fomel (2003) along with (D.6) allows us to arrive at the expression

$$y - z = \frac{vT \cos\theta_0 \sin^2(\frac{\theta}{2})}{2\sin^2\theta_0 cos(\frac{\theta}{2})}, \tag{D.7}$$

where $y = \frac{s+r}{2}$ is the midpoint. The relation between our notation and Fomel's is $\gamma = \frac{\theta}{2}$, $y - z = y - y_0$, $\alpha = \frac{\pi}{2} - \theta_0$. Using (D.6) and (D.7) for the impulse response rather than (D.4) and (D.5) results in a symmetric impulse response, shown in Figure D.1. The symmetry disappears in a non-symmetric heterogeneous velocity model such as the lens model. Also, plotting $s - z$ rather than $y - z$ highlights the fact that we keep the source position s fixed (i.e., we work in the common-shot domain).

Using equation (D.7) along with the expression

$$h = \frac{vT \sin(\frac{\theta}{2})}{\sin\theta_0} \tag{D.8}$$

for the half-offset h allows us to follow Fomel (2003) to arrive at the DMO smile of Deregowski & Rocca (1981).

In a constant-velocity medium, one can also derive an expression for the AMO impulse response in closed form. This is done in Appendix B of de Hoop *et al.* (2003a), with the final result given in equation B.9.

Appendix E

On Amplitudes[1]

E.1 Modeling

We begin with the kernel of the Born modeling operator (de Hoop *et al.* (2003a); equation 7),

$$F[\delta c](\mathbf{r},\mathbf{s},t) = \int_X \int_0^t G(\mathbf{r},t-t',\mathbf{x})\, 2c^{-3}(\mathbf{x})\partial_{t'}^2 \delta c(\mathbf{x}) G(\mathbf{x},t',\mathbf{s})\, \mathrm{d}t'\mathrm{d}\mathbf{x}. \tag{E.1}$$

In the above equation, $G(\mathbf{r},t-t',\mathbf{x})$ is the Green's function for the ray from the scattering point to the receiver, and $2\,c^{-3}(\mathbf{x})\,\partial_{t'}^2\,\delta c(\mathbf{x})\,G(\mathbf{x},t',\mathbf{s})$ is the contrast source at the scattering point, generated by the true source at the surface. The background velocity is denoted by $c(\mathbf{x})$, $\delta c(\mathbf{x})$ is the velocity perturbation that contains the locations of the reflectors, and X is the set of scattering points in the subsurface. The notation $F[\delta c](\mathbf{r},\mathbf{s},t)$ indicates that the operator F acts on the perturbation δc, with the result being dependent on the variables $(\mathbf{r},\mathbf{s},t)$. We use the full Born theory; the amplitudes will change if the Kirchhoff approximation is used in place of Born. For example Biondi *et al.* (1998) use the Zhang-Black Black *et al.* (1993) amplitudes, which are different from those used in this paper. The amplitude in equation (7.2.1) of Bleistein *et al.* (2000) should be compared with that of equation (E.1). Equation (20) of Black *et al.* (1993) gives the comparison between Black's DMO amplitudes and Hale's DMO amplitudes. Equation (7.6.36) of Bleistein *et al.* (2000) compares the Bleistein amplitudes with those of Hale (1991).

From this point onward we will assume that the background velocity, c, of the medium is constant. Thus, the Green's function is given by

$$G(\mathbf{y},t,\mathbf{x}) = \frac{1}{2\pi}\int \frac{1}{4\pi|\mathbf{y}-\mathbf{x}|} e^{-i\omega(t-T(\mathbf{x},\mathbf{y}))}\mathrm{d}\omega, \tag{E.2}$$

where $T(\mathbf{x},\mathbf{y}) = \frac{|\mathbf{x}-\mathbf{y}|}{c}$ is the traveltime between $\mathbf{x}$ and $\mathbf{y}$. The Green's function, as written in equation (E.2), is the kernel of a Fourier integral operator Stolk & de Hoop (2002). To

[1]This appendix has been published, along with Chapter 3 and Appendices C, D, and F as:
Malcolm, A. E., de Hoop, M. V. and Le Rousseau, J. H. 2005. The applicability of DMO/AMO in the presence of caustics. *Geophysics* **70 S1-S17.**

construct F, we substitute the two Green's functions into equation (E.1), obtaining

$$\begin{aligned} F[\delta c](\mathbf{r},\mathbf{s},t) = \quad & \frac{1}{2\pi}\int_{\mathbb{R}}\frac{1}{2\pi}\int_{\mathbb{R}}\int_0^t\int_X \frac{2c^{-3}(-\omega^2)\delta c(\mathbf{x})}{4\pi|\mathbf{s}-\mathbf{x}|4\pi|\mathbf{x}-\mathbf{r}|} \\ & e^{-i\omega(t-t'-T(\mathbf{x},\mathbf{r}))-i\omega'(t'-T(\mathbf{s},\mathbf{x}))}\,\mathrm{d}\mathbf{x}\,\mathrm{d}t'\,\mathrm{d}\omega\,\mathrm{d}\omega'. \end{aligned} \tag{E.3}$$

Performing the integration with respect to t' results in $2\pi\delta(\omega-\omega')$ so that the final operator is given by

$$F[\delta c](\mathbf{r},\mathbf{s},t) = \frac{1}{2\pi}\int_{\mathbb{R}}\int_X \frac{-\omega^2\ 2c^{-3}}{16\pi^2|\mathbf{s}-\mathbf{x}||\mathbf{x}-\mathbf{r}|}e^{-i\omega(t-T(\mathbf{x},\mathbf{r})-T(\mathbf{s},\mathbf{x}))}\delta c(\mathbf{x})\,\mathrm{d}\mathbf{x}\,\mathrm{d}\omega. \tag{E.4}$$

E.2 Imaging

We use the adjoint operator (of the modeling operator) as the imaging/migration operator (first step toward inversion)

$$\begin{aligned} F^*[u](\mathbf{x}) = \quad & \frac{1}{2\pi}\int_{\mathbb{R}}\int_{O_r\times O_s}\int_{\mathbb{R}_+}\frac{-\omega'^2\ 2c^{-3}}{16\pi^2|\mathbf{s}-\mathbf{x}||\mathbf{x}-\mathbf{r}|} \\ & e^{i\omega'(t-T(\mathbf{x},\mathbf{r})-T(\mathbf{s},\mathbf{x}))}u(\mathbf{r},\mathbf{s},t)\,\mathrm{d}t\,\mathrm{d}\mathbf{s}\,\mathrm{d}\mathbf{r}\,\mathrm{d}\omega', \end{aligned} \tag{E.5}$$

where we use ω' since we will shortly compose this operator with the modeling operator given above. We use $O_r \times O_s$ as the domain of source and receiver positions.

E.3 Normal Operator

To obtain the correct amplitude characteristics of the output data, we construct the normal operator $N = F^*F$ so that we may use the left inverse, $(F^*F)^{-1}F^*$. To do this, we compose the modeling and imaging operators (recalling that c, the background velocity, is constant)

$$\begin{aligned} N[\delta c](\mathbf{y}) = \quad & \frac{1}{2\pi}\int_{\mathbb{R}}\mathrm{d}\omega'\frac{1}{2\pi}\int_{\mathbb{R}}\mathrm{d}\omega\int_{O_r\times O_s}\int_{\mathbb{R}_+}\int_X \big[\omega^2\ 4c^{-6}A(\mathbf{s},\mathbf{x},\mathbf{r})\omega'^2A(\mathbf{s},\mathbf{y},\mathbf{r}) \\ & e^{-i\omega(t-T(\mathbf{r},\mathbf{x},\mathbf{s}))+i\omega'(t-T(\mathbf{r},\mathbf{y},\mathbf{s}))}\big]\,\delta c(\mathbf{x})\,\mathrm{d}\mathbf{x}\,\mathrm{d}t\,\mathrm{d}\mathbf{s}\,\mathrm{d}\mathbf{r}, \end{aligned} \tag{E.6}$$

where $A(\mathbf{s},\mathbf{x},\mathbf{r}) = \frac{1}{16\pi^2|\mathbf{x}-\mathbf{s}||\mathbf{x}-\mathbf{r}|}$ and $T(\mathbf{r},\mathbf{x},\mathbf{s}) = T(\mathbf{x},\mathbf{r}) + T(\mathbf{s},\mathbf{x})$. The integration in t results in $2\pi\delta(\omega-\omega')$. Performing both this integration and that in ω' results in

$$\begin{aligned} N[\delta c](\mathbf{y}) = \quad & \frac{1}{2\pi}\int_{\mathbb{R}} \mathrm{d}\omega \int_{O_r\times O_s}\int_X \left[\omega^4\, 4c^{-6} A(\mathbf{s},\mathbf{x},\mathbf{r})A(\mathbf{s},\mathbf{y},\mathbf{r})\right. \\ & \left. e^{i\omega(T(\mathbf{r},\mathbf{x},\mathbf{s})-T(\mathbf{r},\mathbf{y},\mathbf{s}))}\right] \delta c(\mathbf{x})\, \mathrm{d}\mathbf{x}\, \mathrm{d}\mathbf{s}\, \mathrm{d}\mathbf{r}. \end{aligned} \tag{E.7}$$

We now change variables to the ray directions at the scattering point ($\boldsymbol{\alpha}^s$ and $\boldsymbol{\alpha}^r$). We will use subscripts $1,2,3$ to denote the components of a vector in the x_1, x_2, x_3 direction respectively. To change from $(\mathbf{s},\mathbf{r})$ to $(\boldsymbol{\alpha}^s,\boldsymbol{\alpha}^r)$, we compute the Jacobian

$$\frac{\partial(\alpha_1^s,\alpha_2^s)}{\partial(s_1,s_2)}\frac{\partial(\alpha_1^r,\alpha_2^r)}{\partial(r_1,r_2)} = \frac{y_3^2}{|\mathbf{y}-\mathbf{s}|^4}\frac{y_3^2}{|\mathbf{y}-\mathbf{r}|^4} \tag{E.8}$$

since

$$\alpha_{1,2}^s = \frac{y_{1,2}-s_{1,2}}{|\mathbf{y}-\mathbf{s}|} \quad \text{and} \quad \alpha_{1,2}^r = \frac{y_{1,2}-r_{1,2}}{|\mathbf{y}-\mathbf{r}|}.$$

Performing this change of variables we obtain

$$\begin{aligned} N[\delta c](\mathbf{y}) \simeq \quad & \frac{1}{2\pi}\int_{\mathbb{R}} \mathrm{d}\omega \int_{S_s^2\times S_r^2}\int_X \left[\omega^4\, 4c^{-6} A(\underline{\mathbf{s}},\mathbf{y},\underline{\mathbf{r}})^2 \frac{|\mathbf{y}-\underline{\mathbf{s}}|^4|\mathbf{y}-\underline{\mathbf{r}}|^4}{y_3^4}\right. \\ & \left. e^{i\omega(T(\underline{\mathbf{r}},\mathbf{x},\underline{\mathbf{s}})-T(\underline{\mathbf{r}},\mathbf{y},\underline{\mathbf{s}}))}\right] \delta c(\mathbf{x})\, \mathrm{d}\mathbf{x}\, \mathrm{d}\boldsymbol{\alpha}^s\, \mathrm{d}\boldsymbol{\alpha}^r. \end{aligned} \tag{E.9}$$

Underlined symbols are used to indicate that a variable is a function of other variables and S_s^2 (S_r^2) is the unit sphere on which the direction of the source (receiver) ray lies. We have expanded $A(\underline{\mathbf{s}},\mathbf{x},\underline{\mathbf{r}})$ about $\mathbf{y}$, using that $\mathbf{x}\approx\mathbf{y}$ at stationarity in $\boldsymbol{\alpha}^r$ and $\boldsymbol{\alpha}^s$ (see de Hoop & Brandsberg-Dahl (2000, p. 553) and Beylkin (1985)).

Expanding $T(\underline{\mathbf{r}},\mathbf{x},\underline{\mathbf{s}})$ to first order in a Taylor series about $\mathbf{y}$, we can write the phase as

$$\boldsymbol{\Gamma}\cdot(\mathbf{x}-\mathbf{y}), \tag{E.10}$$

where $\boldsymbol{\Gamma} = \nabla_{\mathbf{y}} T(\underline{\mathbf{r}},\mathbf{y},\underline{\mathbf{s}})$. We will also scale the ω variable by $|\boldsymbol{\Gamma}|^{-1}$ and introduce $\boldsymbol{\nu} = \boldsymbol{\Gamma}/|\boldsymbol{\Gamma}|$. Note that $\boldsymbol{\nu}$ corresponds to the migration dip. The expression thus becomes

$$N[\delta c](\mathbf{y}) \simeq \frac{1}{2\pi}\int_{\mathbb{R}} \mathrm{d}\omega \int_{S_s^2\times S_r^2}\int_X \left[4c^{-6}\omega^4 \mu_{LS}(\underline{\mathbf{r}},\boldsymbol{\alpha}^r,\underline{\mathbf{s}},\boldsymbol{\alpha}^s,\mathbf{y}) e^{i\omega\boldsymbol{\nu}\cdot(\mathbf{x}-\mathbf{y})}\right] \delta c(\mathbf{x})\, \mathrm{d}\mathbf{x}\, \mathrm{d}\boldsymbol{\alpha}^s\, \mathrm{d}\boldsymbol{\alpha}^r, \tag{E.11}$$

letting $\mu_{LS}(\underline{\mathbf{r}},\boldsymbol{\alpha}^r,\underline{\mathbf{s}},\boldsymbol{\alpha}^s,\mathbf{y}) = A(\underline{\mathbf{s}},\mathbf{y},\underline{\mathbf{r}})^2 \frac{\partial(\mathbf{s},\mathbf{r})}{\partial(\boldsymbol{\alpha}^s,\boldsymbol{\alpha}^r)}|\boldsymbol{\Gamma}|^{-5}$.

We now change variables again, to the scattering angle θ, scattering azimuth ψ and migration dip $\boldsymbol{\nu}$ (these quantities are defined in terms of $\boldsymbol{\alpha}^s$ and $\boldsymbol{\alpha}^r$ by de Hoop & Brandsberg-Dahl (2000, eqn (127))). This introduces a Jacobian, $\frac{\partial(\boldsymbol{\alpha}^s,\boldsymbol{\alpha}^r)}{\partial(\boldsymbol{\nu},\theta,\psi)}$, which is computed for the general case by Burridge & Beylkin (1988) and for the homogeneous, isotropic case by Bur-

ridge & Beylkin (1988). In a three-dimensional (homogeneous and isotropic) space, this Jacobian is simply $\sin\theta$. Thus,

$$N[\delta c](\mathbf{y}) \simeq \frac{1}{2\pi}\int_{\mathbb{R}} \mathrm{d}\omega \int_{E_\nu} \quad \int_{E_\theta\times E_\psi}\int_X \Big[4c^{-6}\omega^4 \mu_{LS}(\underline{\mathbf{r}},\underline{\boldsymbol{\alpha}}^r,\underline{\mathbf{s}},\underline{\boldsymbol{\alpha}}^s,\mathbf{y})\sin\theta e^{i\omega\boldsymbol{\nu}\cdot(\mathbf{y}-\mathbf{x})}\Big]$$

$$\delta c(\mathbf{x})\ \mathrm{d}\mathbf{x}\,\mathrm{d}\boldsymbol{\nu}\,\mathrm{d}\theta\,\mathrm{d}\psi, \tag{E.12}$$

where we have changed the sign of ω noting that $\int_{\mathbb{R}} e^{i\omega(\mathbf{x}-\mathbf{y})}\mathrm{d}\omega = \int_{\mathbb{R}} e^{i\omega(\mathbf{y}-\mathbf{x})}\mathrm{d}\omega$, and that the amplitude is an even function of ω. We denote by E_ν the set of migration dips, by E_θ the set of scattering angles and by E_ψ the set of scattering azimuths.

Letting $\Lambda(\mathbf{y},\boldsymbol{\nu}) = \int_{E_\theta\times E_\psi} \frac{1}{2}\mu_{LS}(\underline{\mathbf{r}},\underline{\boldsymbol{\alpha}}^r,\underline{\mathbf{s}},\underline{\boldsymbol{\alpha}}^s,\mathbf{y})\sin\theta\ \mathrm{d}\psi\ \mathrm{d}\theta + (\ldots)(\mathbf{y},-\boldsymbol{\nu})$, $((\ldots)(\mathbf{y},-\boldsymbol{\nu})$ indicates the same expression evaluated at $(\mathbf{y},-\boldsymbol{\nu})$, noting that $\boldsymbol{\alpha}^r$ and $\boldsymbol{\alpha}^s$ are related to $\boldsymbol{\nu}$) we may write

$$N[\delta c](\mathbf{y}) \simeq \left(\frac{1}{2\pi}\right)^3 \int_{\mathbb{R}_+} \omega^2\ \mathrm{d}\omega \int_{E_\nu} \omega^2 4c^{-6}8\pi^2\Lambda(\mathbf{y},\boldsymbol{\nu}) \int_X e^{i\omega\nu\cdot(\mathbf{y}-\mathbf{x})}\delta c(\mathbf{x})\ \mathrm{d}\mathbf{x}\,\mathrm{d}\boldsymbol{\nu}, \tag{E.13}$$

from which we recognize $\omega^2\mathrm{d}\omega\mathrm{d}\boldsymbol{\nu}$ as a measure of integration in spherical coordinates, where ω takes the place of radial length and $\nu_{1,2}$ of directions. We see also that $\omega^2 4c^{-6}8\pi^2\Lambda(\mathbf{y},\boldsymbol{\nu})$ is the principal symbol[2] (Treves, 1980b; de Hoop *et al.*, 2003b, Appendix A) of the normal operator. Since we associate ω with a length, the ω integration should be over only $\mathbb{R}_+$. By noting that the argument is an even function of ω, we have replaced the integration over $\mathbb{R}$ with integration over $\mathbb{R}_+$ introducing a factor of 2. The remaining ω^2 term is the (scaled) second derivative operator. The kernel of the parametrix[3] (Treves, 1980b; de Hoop *et al.*, 2003b, Appendix A) of the normal operator is

$$P(\mathbf{x},\mathbf{y}) \simeq \left(\frac{1}{2\pi}\right)^3 \int_{\mathbb{R}_+}\int_{E_\nu} (4c^{-6}8\pi^2\Lambda(\mathbf{y},\boldsymbol{\nu}))^{-1} e^{i\omega\boldsymbol{\nu}\cdot(\mathbf{x}-\mathbf{y})}\ \mathrm{d}\boldsymbol{\nu}\,\mathrm{d}\omega. \tag{E.14}$$

To construct the linear inversion operator, we compose P with the original imaging operator to form $(F^*F)^{-1}F^*$

$$\begin{aligned} PF^*[u](\mathbf{y}) \quad &= \left(\frac{1}{2\pi}\right)^4 \int_{E_\nu}\int_X\int_{\mathbb{R}_+}\int_{O_r\times O_s} A(\mathbf{s},\mathbf{x},\mathbf{r})2c^{-3}(4c^{-6}8\pi^2\Lambda(\mathbf{x},\boldsymbol{\nu}))^{-1}e^{i\omega\boldsymbol{\nu}\cdot(\mathbf{x}-\mathbf{y})} \\ &\int_{\mathbb{R}} (-\omega'^2)e^{-i\omega' T(\mathbf{r},\mathbf{x},\mathbf{s})}u(\mathbf{r},\mathbf{s},\omega')\ \mathrm{d}\omega'\mathrm{d}\mathbf{s}\,\mathrm{d}\mathbf{r}\,\mathrm{d}\omega\,\mathrm{d}\mathbf{x}\,\mathrm{d}\boldsymbol{\nu}, \end{aligned} \tag{E.15}$$

where the data, u, are now in the frequency domain. By expanding $T(\mathbf{r},\mathbf{x},\mathbf{s})$ to first order

[2]The principal symbol of an operator is the highest order term in the asymptotic expansion of its amplitude in the Fourier domain.

[3]The parametrix of an operator is an asymptotic approximation to its inverse.

in a Taylor series about $\mathbf{x} = \mathbf{y}$, we can write the phase of the above operator as

$$i\omega\boldsymbol{\nu}\cdot(\mathbf{x}-\mathbf{y}) - i\omega'\nabla_y T(\mathbf{r},\mathbf{y},\mathbf{s})\cdot(\mathbf{x}-\mathbf{y}) - i\omega' T(\mathbf{r},\mathbf{y},\mathbf{s}).$$

We can now perform the integration in $\mathbf{x}$ (noting that $\mathbf{x}\approx\mathbf{y}$ at stationarity), giving

$$(2\pi)^3\delta(\omega\boldsymbol{\nu} - \omega'\nabla_y T(\mathbf{r},\mathbf{y},\mathbf{s})) = \frac{(2\pi)^3}{\omega'^2|\boldsymbol{\Gamma}|^2}\delta(\omega-\omega'|\Gamma|)\delta(\boldsymbol{\nu}-\mathbf{v}), \tag{E.16}$$

where $\mathbf{v} = \nabla_y T(\mathbf{r},\mathbf{y},\mathbf{s})/|\nabla_y T(\mathbf{r},\mathbf{y},\mathbf{s})|$. This allows us to integrate out both the $\boldsymbol{\nu}$ and ω variables resulting in

$$\begin{aligned} PF^*[u](\mathbf{y}) &= \frac{1}{8\pi^2}\int_{O_r\times O_s}\frac{1}{|\boldsymbol{\Gamma}|^2}(\Lambda(\mathbf{y},\mathbf{v}))^{-1}\frac{1}{2}c^3 A(\mathbf{s},\mathbf{y},\mathbf{r}) \\ &\quad \frac{1}{\pi}\mathrm{Re}\left[\int_{\mathbb{R}_+} u(\mathbf{s},\mathbf{r},\omega')e^{-i\omega' T(\mathbf{r},\mathbf{y},\mathbf{s})}\,\mathrm{d}\omega'\right]\mathrm{d}\mathbf{s}\,\mathrm{d}\mathbf{r}. \end{aligned} \tag{E.17}$$

Changing variables from $(\mathbf{s},\mathbf{r})$ to $(\boldsymbol{\alpha}^s,\boldsymbol{\alpha}^r)$ as before and substituting $\mu_{LS}(\underline{\mathbf{r}},\boldsymbol{\alpha}^r,\underline{\mathbf{s}},\boldsymbol{\alpha}^s,\mathbf{y})$ gives

$$\begin{aligned} I[u](\mathbf{y}) = PF^*[u](\mathbf{y}) &= \frac{1}{16\pi^2}\int_{S_s^2\times S_r^2}\frac{c^3|\boldsymbol{\Gamma}|^3(\Lambda(\mathbf{y},\mathbf{v}))^{-1}\mu_{LS}(\underline{\mathbf{r}},\boldsymbol{\alpha}^r,\underline{\mathbf{s}},\boldsymbol{\alpha}^s,\mathbf{y})}{A(\underline{\mathbf{s}},\mathbf{y},\underline{\mathbf{r}})} \\ &\quad \frac{1}{\pi}\mathrm{Re}\left[\int_{\mathbb{R}_+} e^{-i\omega' T(\underline{\mathbf{r}},\mathbf{y},\underline{\mathbf{s}})}u(\underline{\mathbf{s}},\underline{\mathbf{r}},\omega')\,\mathrm{d}\omega'\right]\mathrm{d}\boldsymbol{\alpha}^s\,\mathrm{d}\boldsymbol{\alpha}^r. \end{aligned} \tag{E.18}$$

We can then perform the integration with respect to ω', obtaining

$$I[u](\mathbf{y}) = \frac{1}{16\pi^2}\int_{S_s^2\times S_r^2}\frac{c^3|\boldsymbol{\Gamma}|^3(\Lambda(\mathbf{y},\mathbf{v}))^{-1}\mu_{LS}(\underline{\mathbf{r}},\boldsymbol{\alpha}^r,\underline{\mathbf{s}},\boldsymbol{\alpha}^s,\mathbf{y})}{A(\underline{\mathbf{s}},\mathbf{y},\underline{\mathbf{r}})}u(\underline{\mathbf{s}},\underline{\mathbf{r}},T(\underline{\mathbf{s}},\mathbf{y},\underline{\mathbf{r}}))\,\mathrm{d}\boldsymbol{\alpha}^s\,\mathrm{d}\boldsymbol{\alpha}^r. \tag{E.19}$$

In equation (E.18), we recognize the form of equation (27) of Miller *et al.* (1987), by noting that

$$|\boldsymbol{\Gamma}| = \frac{2\cos\left(\frac{\theta}{2}\right)}{c},$$

and setting $\mu_{LS} = 1$. The two equations are not exactly the same however; our equation contains a factor, $\frac{\sin\theta}{\Lambda}$. The $\sin\theta$ is introduced by changing to the same coordinates as used by Miller et al. The factor Λ^{-1} is present since we construct the least squares inverse and is equal to $\int_{E_\theta}\sin\theta\,\mathrm{d}\theta$.

E.4 Continuation

To compute the continuation operator, we now compose I with the modeling operator

$$FI[u](\mathbf{s},\mathbf{r},t) = \frac{1}{2\pi}\int_{\mathbb{R}}\int_X \frac{1}{16\pi^2}\int_{S^2_{\underline{s}}\times S^2_{\underline{r}}}\frac{1}{2\pi}\int_{\mathbb{R}}|\mathbf{\Gamma}|^3(\Lambda(\mathbf{x},\mathbf{v}))^{-1}\frac{-\omega^2 A(\mathbf{s},\mathbf{x},\mathbf{r})}{A(\underline{\mathbf{s}}',\mathbf{x},\underline{\mathbf{r}}')} \tag{E.20}$$

$$\mu_{LS}(\underline{\mathbf{r}}',\boldsymbol{\alpha}^{r\prime},\underline{\mathbf{s}}',\boldsymbol{\alpha}^{s\prime},\mathbf{x})e^{-i\omega(t-T(\mathbf{r},\mathbf{x},\mathbf{s}))-i\omega' T(\underline{\mathbf{r}}',\mathbf{x},\underline{\mathbf{s}}')}u(\underline{\mathbf{s}}',\underline{\mathbf{r}}',\omega')\,\mathrm{d}\omega'\,\mathrm{d}\boldsymbol{\alpha}^{s\prime}\,\mathrm{d}\boldsymbol{\alpha}^{r\prime}\,\mathrm{d}\mathbf{x}\,\mathrm{d}\omega$$

or, in $(\theta',\psi',\boldsymbol{\nu}')$ variables, exchanging the order of integration,

$$FI[u](\mathbf{s},\mathbf{r},t) = \frac{1}{2\pi}\int_{\mathbb{R}}\frac{1}{16\pi^2}\int_{\nu'}\int_{E_{\theta'}\times E_{\psi'}}\int_X\frac{1}{2\pi}\int_{\mathbb{R}}\sin\theta'|\mathbf{\Gamma}|^3(\Lambda(\mathbf{x},\mathbf{v}))^{-1}\frac{-\omega^2 A(\mathbf{s},\mathbf{x},\mathbf{r})}{A(\underline{\mathbf{s}}',\mathbf{x},\underline{\mathbf{r}}')}$$

$$\mu_{LS}(\underline{\mathbf{r}}',\underline{\boldsymbol{\alpha}}^{r\prime},\underline{\mathbf{s}}',\underline{\boldsymbol{\alpha}}^{s\prime},\mathbf{x})e^{-i\omega(t-T(\mathbf{r},\mathbf{x},\mathbf{s}))-i\omega' T(\underline{\mathbf{r}}',\mathbf{x},\underline{\mathbf{s}}')}u(\underline{\mathbf{s}}',\underline{\mathbf{r}}',\omega')\,\mathrm{d}\omega'\,\mathrm{d}\mathbf{x}\,\mathrm{d}\boldsymbol{\nu}'\,\mathrm{d}\theta'\,\mathrm{d}\psi'\mathrm{d}\omega. \tag{E.21}$$

We now approximate the $\mathbf{x}$-integration using the method of stationary phase. To do this, we will first change variables to $(\tau',\sigma_1',\sigma_2')$, where (σ_1',σ_2') are coordinates on the level sets of $T(\underline{\mathbf{r}}',\mathbf{x},\underline{\mathbf{s}}')$ and τ' is the value of $T(\underline{\mathbf{r}}',\mathbf{x},\underline{\mathbf{s}}')$, which fixes the level set on which we perform the computations. This transformation is accomplished by noting that de Hoop & Bleistein (1997)

$$\mathrm{d}\mathbf{x} = \frac{|\partial_{\sigma_1'}\underline{\mathbf{x}}\wedge\partial_{\sigma_2'}\underline{\mathbf{x}}|}{|\nabla_{\underline{x}}T'|}\,\mathrm{d}\tau'\,\mathrm{d}\sigma_1'\,\mathrm{d}\sigma_2', \tag{E.22}$$

where $T' = T(\mathbf{r}',\mathbf{x},\mathbf{s}')$.

If $\underline{\mathbf{r}}'$ and $\underline{\mathbf{s}}'$ were independent parameters then the level sets of T' would define standard isochrons and the stationary phase analysis can be found in Bleistein *et al.* (2000). If instead we want the level sets of T' to be the angle isochrons shown in the text of this paper, we must change our variables of integration from $(\boldsymbol{\nu}',\psi',\theta')$ to $(\mathbf{s}',\psi',\theta')$, which introduces the Jacobian $\frac{\partial(\boldsymbol{\nu}',\boldsymbol{\psi}',\theta')}{\partial(\mathbf{s}',\boldsymbol{\psi}',\theta')}$. In this case, $\mathbf{s}'$ is an independent parameter but $\underline{\mathbf{r}}'$ is no longer independent since

$$\underline{\mathbf{r}}'(\mathbf{x},\mathbf{s}',\theta',\psi') = \mathbf{x} - (\underline{x}_3/\underline{\alpha}_3')\underline{\boldsymbol{\alpha}}^{r'},$$

using the definitions of $\underline{\boldsymbol{\psi}'}$ and $\underline{\boldsymbol{\alpha}'}$ from de Hoop & Brandsberg-Dahl (2000)

$$\underline{\boldsymbol{\alpha}}^{r\prime} = \frac{\mathbf{x}-\mathbf{s}'}{|\mathbf{x}-\mathbf{s}'|} - \frac{\boldsymbol{\psi}'\cos\left(\frac{\theta'}{2}\right)}{\sin\theta'},\quad \underline{\boldsymbol{\psi}'} = \frac{(\underline{\boldsymbol{\alpha}}^{s\prime}\cdot\boldsymbol{\nu}')\underline{\boldsymbol{\alpha}}^{r\prime} - (\underline{\boldsymbol{\alpha}}^{r\prime}\cdot\boldsymbol{\nu}')\underline{\boldsymbol{\alpha}}^{s\prime}}{\sin\theta'}. \tag{E.23}$$

In this parameterization $D_{x_j}T' = \partial_{x_j}T' + \partial_{\underline{r}_i'}T'\partial_{x_j}\underline{r}_i'$ due to the $\mathbf{x}$ dependence of $\underline{\mathbf{r}}'$. In the isochron variables, the phase of the continuation operator becomes

$$\Phi = T(\mathbf{r},\underline{\mathbf{x}}(\sigma_1',\sigma_2',\tau'),\mathbf{s}) - t - \frac{\omega'}{\omega}\tau'. \tag{E.24}$$

We now continue with the stationary phase analysis in (σ_1', σ_2'), following Bleistein *et al.* (2000). The stationary phase condition

$$\partial_{\sigma_{1,2}'}\Phi = \nabla_{\underline{x}} T \cdot \frac{\partial \underline{\mathbf{x}}}{\partial \sigma_{1,2}'} = 0,$$

gives that $\nabla_{\underline{x}} T$ is parallel to $\nabla_{\underline{x}} T'$ or equivalently, the unit normal to the input angle isochron $\hat{\mathbf{n}}'$ is equal to the unit normal, $\hat{\mathbf{n}}$, to the output standard isochron. The Hessian of second derivatives is

$$\mathbf{H} = \det\left[\frac{\partial^2 T}{\partial \sigma_1' \partial \sigma_2'}\right] = |\nabla_{\underline{x}} T|^2 det[\mathbf{B}_{kl}' - \mathbf{B}_{kl}]$$

where we have used the relation

$$\frac{\partial^2 T}{\partial \sigma_l' \partial \sigma_k'} = \frac{\partial^2 T}{\partial \underline{x}_i \partial \underline{x}_j}\frac{\partial \underline{x}_i}{\partial \sigma_k'}\frac{\partial \underline{x}_j}{\partial \sigma_l'} + \frac{\partial T}{\partial \underline{x}_i}\frac{\partial^2 \underline{x}_i}{\partial \sigma_k' \partial \sigma_l'} \tag{E.25}$$

and

$$\frac{\partial T}{\partial \underline{x}_i}\frac{\partial^2 \underline{x}_i}{\partial \sigma_k' \partial \sigma_l'} = \hat{\mathbf{n}} \cdot \frac{\partial^2 \underline{x}}{\partial \sigma_k' \partial \sigma_l'}|\nabla_{\underline{x}} T| = \mathbf{B}_{kl}'|\nabla_{\underline{x}} T(\underline{\mathbf{r}}', \underline{\mathbf{x}}, \mathbf{s}')|, \tag{E.26}$$

using the fact that $\hat{\mathbf{n}}' = \hat{\mathbf{n}}$ at stationarity. $\mathbf{B}_{kl}$ is the second fundamental tensor, which is a rotation of the matrix of principle curvatures for the level sets (standard isochrons) of the function T. $\mathbf{B}_{kl}'$ denotes $\mathbf{B}_{kl}$ in the input parameters (i.e., a rotation of the matrix of principle curvatures for the level sets (angle isochrons) of T'). Equation (E.26) gives $\mathbf{B}_{kl}'$ because the (σ_1', σ_2') are coordinates on the angle isochrons (level sets of T'). The transformation of the first term in equation (E.25) to $\mathbf{B}_{kl}$ is explained in section 7.7 of Bleistein *et al.* (2000).

We note at this point that the preceding stationary phase analysis is applicable only when the Hessian, $\mathbf{H}$, is nonzero. One example of when $\mathbf{H} = 0$ is when the input and output configurations are the same, in which case $\mathbf{B}_{kl} = \mathbf{B}_{kl}'$. Assuming that $\mathbf{H} \neq 0$ we may write the final continuation operator as

$$\begin{aligned} FI[u](\mathbf{s}, \mathbf{r}, t) \quad = & \int_{E_{\theta'} \times E_{\psi'}} \frac{-1}{2\pi} \int_{\mathbb{R}_+} \int_{\mathbb{R}} \frac{1}{4\sqrt{2\pi}} \int_{S'} \omega \sin\theta' |\mathbf{\Gamma}|^3 (\Lambda(\underline{\mathbf{x}}_0, \mathbf{v}))^{-1} \\ & \mu_{LS}(\underline{\mathbf{r}}', \underline{\boldsymbol{\alpha}}^{r\prime}, \mathbf{s}', \underline{\boldsymbol{\alpha}}^{s\prime}, \underline{\mathbf{x}}_0) |\partial_{\sigma_1} \underline{\mathbf{x}} \wedge \partial_{\sigma_2} \underline{\mathbf{x}}| \left| \frac{\partial(\boldsymbol{\nu}', \boldsymbol{\psi}', \theta')}{\partial(\mathbf{s}', \boldsymbol{\psi}', \theta')} \right| \frac{A(\mathbf{s}, \underline{\mathbf{x}}_0, \mathbf{r})}{A(\mathbf{s}', \underline{\mathbf{x}}_0, \underline{\mathbf{r}}')\sqrt{\overline{\mathbf{H}}} |\nabla_{\underline{x}_0} T'|} \\ & u(\mathbf{s}', \underline{\mathbf{r}}', T(\underline{\mathbf{r}}', \underline{\mathbf{x}}_0, \mathbf{s}')) e^{i\omega(T(\mathbf{r}, \underline{\mathbf{x}}_0, \mathbf{s}) - t) + i\frac{\pi}{4} sig(\mathbf{H})} \mathrm{d}\mathbf{s}' \, \mathrm{d}\omega \, \mathrm{d}\tau' \, \mathrm{d}\theta' \, \mathrm{d}\boldsymbol{\psi}'. \end{aligned} \tag{E.27}$$

In this expression, $\underline{\mathbf{x}}_0$ is the stationary point (in σ_1' and σ_2', i.e., $\underline{\mathbf{x}}_0 = \underline{x}(\sigma_1'^0, \sigma_2'^0, \tau')$, $\nabla_{\underline{x}_0} T' = \nabla_{\underline{x}} T(\underline{\mathbf{r}}', \underline{\mathbf{x}}, \mathbf{s}')|_{\underline{x}=\underline{x}_0}$, and $sig(\mathbf{H})$ is not evaluated as this will depend on the exact input and output configuration.

Equation (E.27) can be reduced to equation 7.7.13 of Bleistein et al., again by setting $\mu_{LS} = 1$, and noting that $|\mathbf{\Gamma}|^3$ is the obliquity factor. This comparison is possible only after noting the differences between the definitions of the modeling and inversion operators between this work and that of Bleistein et al. As in the comparison of the inversion formula with that of Miller *et al.* (1987) the final two formulas differ by a factor $\frac{\sin\theta'}{\int_{E_\theta}\sin\theta'}$.

Other authors have done similar computations to that shown here for particular input and output geometries. For example Biondi *et al.* (1998) compute the operator that maps general input data to single azimuth output data, Black *et al.* (1993), Liner (1991) and Bleistein (1990) compute the DMO operator and more general continuation is given in Fomel & Bleistein (2001); Fomel (2003); Stolt (2002); Bleistein *et al.* (1999); Bleistein & Jaramillo (2000).

Appendix F

Properties of FF^* for Common Offset[1]

A formal definition of a pseudodifferential operator is beyond the scope of this paper; we refer the reader to either Treves (1980b) or Appendix A of de Hoop *et al.* (2003b) for the mathematical details. Roughly speaking, however, an operator is pseudodifferential if it can be written in the form of a forward and inverse Fourier transform along with a multiplication by an amplitude in the Fourier domain. In general FF^* is not a pseudodifferential operator. In certain cases, however, when the input and output offsets are constrained to be equal for example, FF^* does have this property. In this particular case, we write the kernel of FF^* as that of a pseudodifferential operator and extract its amplitude behavior.

The phase of FF^* is given by (cf. equation (E.20))

$$\Phi = -\omega(t - T(\mathbf{r}, \mathbf{x}, \mathbf{s})) + \omega'(t' - T(\mathbf{r}', \mathbf{x}, \mathbf{s}')), \tag{F.1}$$

in which $\mathbf{x}$, ω and ω' are identified as phase variables. Subjecting equation (F.1) to the common offset condition, the travel time, T, and phase function, Φ, can be rewritten in terms of midpoints, $\mathbf{y} = \frac{\mathbf{s}+\mathbf{r}}{2}$, $\mathbf{y}' = \frac{\mathbf{s}'+\mathbf{r}'}{2}$ and offset, $\mathbf{h} = \frac{\mathbf{s}-\mathbf{r}}{2} = \frac{\mathbf{s}'-\mathbf{r}'}{2}$, as

$$\Phi = -\omega(t - T(\mathbf{x}, \mathbf{h}, \mathbf{y})) + \omega'(t' - T(\mathbf{x}, \mathbf{h}, \mathbf{y}')). \tag{F.2}$$

Treatment of phase variables

The representation of the kernel of the operator FF^* will contain integrations over $\mathbf{x}$, ω and ω'. The application of this operator to input data will result in integrations over $\mathbf{y}'$ and t', the input midpoint and time (but not over $\mathbf{h}$ as this is fixed). For this phase to be that of a pseudodifferential operator, we must be able to write it in the form

$$\omega'(t' - t) + \boldsymbol{\eta}' \cdot (\mathbf{y} - \mathbf{y}'), \tag{F.3}$$

where $\omega' t'$ and $-\boldsymbol{\eta}' \cdot \mathbf{y}'$ are associated with Fourier transforms and $-\omega' t$ and $\boldsymbol{\eta}' \cdot \mathbf{y}$ are associated with inverse Fourier transforms. Thus the oscillatory integral representation of

[1]This appendix has been published, along with Chapter 3 and Appendices C, D, and E as:
Malcolm, A. E., de Hoop, M. V. and Le Rousseau, J. H. 2005. The applicability of DMO/AMO in the presence of caustics. *Geophysics* **70 S1-S17.**

the kernel of FF^* must contain integrations over $(\omega', \boldsymbol{\eta}')$, the Fourier duals of $(t', \mathbf{y}')$. To reduce the phase (F.2) to the form in equation (F.3) we apply the method of stationary phase to (x_3, ω), and then change variables of integration, $(x_1, x_2) \rightarrow (\eta_1, \eta_2)$.

To begin we perform stationary phase in (x_3, ω), the depth and the output frequency. The stationary phase conditions are

$$\frac{\partial \Phi}{\partial \omega} = T(\mathbf{x}, \mathbf{h}, \mathbf{y}) - t = 0, \tag{F.4}$$

$$\frac{\partial \Phi}{\partial x_3} = \omega \partial_{x_3} T(\mathbf{x}, \mathbf{h}, \mathbf{y}) - \omega' \partial_{x_3} T(\mathbf{x}, \mathbf{h}, \mathbf{y}') = 0. \tag{F.5}$$

Equation (F.4) determines the isochron on which the scattering point, $\mathbf{x}$, lies, through its solution $\underline{x}_3^0(x_1, x_2, \mathbf{y}, t; \mathbf{h})$ and (F.5) gives the scaling between the input and output frequencies at stationarity through its solution

$$\underline{\omega}^0(\omega', x_1, x_2, \mathbf{y}, \mathbf{y}', h) = \omega' \frac{\partial_{x_3} T(\mathbf{x}, \mathbf{h}, \mathbf{y}')}{\partial_{x_3} T(\mathbf{x}, \mathbf{h}, \mathbf{y})}. \tag{F.6}$$

The determinant of the Hessian, $\mathbf{H}$, is

$$-(\partial_{x_3} T(\mathbf{x}, \mathbf{h}, \mathbf{y}))^2, \tag{F.7}$$

which is unequal to zero since we exclude the direct ray between the source and receiver (i.e. we require $x_3 \neq 0$ in a constant medium). As this (2×2) determinant is negative, $\text{sig}(\mathbf{H}) = 0$.

The phase at stationarity can be written as

$$\Phi = \omega'(t' + T(x_1, x_2, \underline{x}_3^0(x_1, x_2, \mathbf{y}, t; \mathbf{h}), \mathbf{h}, \mathbf{y}')) \tag{F.8}$$

$$= -\omega'(\underbrace{T(x_1, x_2, \underline{x}_3^0, \mathbf{h}, \mathbf{y})}_{=t} - T(x_1, x_2, \underline{x}_3^0, \mathbf{h}, \mathbf{y}) - t' + T(x_1, x_2, \underline{x}_3^0, \mathbf{h}, \mathbf{y}')) \tag{F.9}$$

$$= -\omega'(t - T(x_1, x_2, \underline{x}_3^0, \mathbf{h}, \mathbf{y}) - t' + T(x_1, x_2, \underline{x}_3^0, \mathbf{h}, \mathbf{y}')) \tag{F.10}$$

$$= \omega'(t' - t) + \omega'(T(x_1, x_2, \underline{x}_3^0, \mathbf{h}, \mathbf{y}) - T(x_1, x_2, \underline{x}_3^0, \mathbf{h}, \mathbf{y}')). \tag{F.11}$$

We expand $T(x_1, x_2, \underline{x}_3^0, \mathbf{h}, \mathbf{y}')$ in a Taylor series about the point $\mathbf{y}' = \mathbf{y}$, which results in

$$T(x_1, x_2, \underline{x}_3^0, \mathbf{h}, \mathbf{y}') \simeq T(x_1, x_2, \underline{x}_3^0, \mathbf{h}, \mathbf{y}) + \nabla_{y'} T(x_1, x_2, \underline{x}_3^0, \mathbf{h}, \mathbf{y}')|_{\mathbf{y}'=\mathbf{y}} \cdot (\mathbf{y}' - \mathbf{y}). \tag{F.12}$$

Thus, using the shorthand notation $\nabla_y T$ for $\nabla_{y'} T(x_1, x_2, \underline{x}_3^0, \mathbf{h}, \mathbf{y}')|_{\mathbf{y}'=\mathbf{y}}$ we have,

$$\Phi \simeq \omega'(t' - t) + \omega' \nabla_y T \cdot (\mathbf{y} - \mathbf{y}'). \tag{F.13}$$

To obtain an explicit representation of a pseudodifferential operator, we change variables $(x_1, x_2) \rightarrow (\eta_1', \eta_2')$ in accordance with

$$\boldsymbol{\eta}' = \omega' \nabla_{y'} T(x_1, x_2, \underline{x}_3^0(x_1, x_2, \mathbf{y}, t; \mathbf{h}), \mathbf{h}, \mathbf{y}')|_{\mathbf{y}'=\mathbf{y}}, \tag{F.14}$$

for given $(\mathbf{y}, t)$ and $\mathbf{h}$ still fixed (note that the $\underline{x}_3^0$ dependence contains implicitly a dependence on x_1, x_2). With this definition, equation (F.13) gives (F.3). To compute the Jacobian associated with the transformation $(x_1, x_2) \to (\eta_1', \eta_2')$, we compute

$$\mathbf{J} = \frac{\partial(\eta_1', \eta_2')}{\partial(x_1, x_2)} = \frac{\omega'^2}{c^2} \begin{vmatrix} \partial_{x_1}\eta_1' + \partial_{x_3}\eta_1' \dfrac{\partial \underline{x}_3^0}{\partial x_1} & \partial_{x_2}\eta_1' + \partial_{x_3}\eta_1' \dfrac{\partial \underline{x}_3^0}{\partial x_2} \\ \partial_{x_1}\eta_2' + \partial_{x_3}\eta_2' \dfrac{\partial \underline{x}_3^0}{\partial x_1} & \partial_{x_2}\eta_2' + \partial_{x_3}\eta_2' \dfrac{\partial \underline{x}_3^0}{\partial x_2} \end{vmatrix}. \tag{F.15}$$

Introducing the vectors $\mathbf{p} = (\mathbf{x} - \mathbf{y} - \mathbf{h})$ and $\mathbf{q} = (\mathbf{x} - \mathbf{y} + \mathbf{h})$, and orienting the system of coordinates so that $\mathbf{h} = (h_1, 0, 0)$, we have, upon substituting $T = \frac{|\mathbf{q}|+|\mathbf{p}|}{c}$,

$$J = \frac{\omega'^2}{c^2} \begin{vmatrix} \frac{-|\mathbf{q}|^2+q_1^2}{|\mathbf{q}|^3} + \frac{-|\mathbf{p}|^2+p_1^2}{|\mathbf{p}|^3} + \left(\frac{q_1 q_3}{|\mathbf{q}|^3} + \frac{p_1 p_3}{|\mathbf{p}|^3}\right)\frac{\partial \underline{x}_3^0}{\partial x_1} & \frac{q_1 q_2}{|\mathbf{q}|^3} + \frac{p_1 p_2}{|\mathbf{p}|^3} + \left(\frac{q_1 q_3}{|\mathbf{q}|^3} + \frac{p_1 p_3}{|\mathbf{p}|^3}\right)\frac{\partial \underline{x}_3^0}{\partial x_2} \\ \frac{q_1 q_2}{|\mathbf{q}|^3} + \frac{p_1 p_2}{|\mathbf{p}|^3} + \left(\frac{q_1 q_3}{|\mathbf{q}|^3} + \frac{p_1 p_3}{|\mathbf{p}|^3}\right)\frac{\partial \underline{x}_3^0}{\partial x_1} & \frac{-|\mathbf{q}|^2+q_2^2}{|\mathbf{q}|^3} + \frac{-|\mathbf{p}|^2+p_2^2}{|\mathbf{p}|^3} + \left(\frac{q_2 q_3}{|\mathbf{q}|^3} + \frac{p_2 p_3}{|\mathbf{p}|^3}\right)\frac{\partial \underline{x}_3^0}{\partial x_2} \end{vmatrix}. \tag{F.16}$$

We solve equation (F.4) for $\underline{x}_3^0$,

$$\underline{x}_3^0 = \frac{1}{2ct}\sqrt{-2p_1^2c^2t^2 - 4q_2^2c^2t^2 + p_1^4 + q_1^4 - 2p_1^2q_1^2 - 2q_1^2c^2t^2 + c^4t^4}, \tag{F.17}$$

noting that $q_2 = p_2$ and $q_3 = p_3 = \underline{x}_3^0$ and taking the positive square-root as x_3 is constrained to be greater than zero. We then compute

$$\frac{\partial \underline{x}_3^0}{\partial x_1} = \frac{k_1}{p_3}, \qquad \text{where} \quad k_1 = \frac{-(p_1+q_1)(q_2^2 + x_3^2 + q_1q_2 + |\mathbf{q}||\mathbf{p}|)}{c^2t^2} \tag{F.18}$$

$$\frac{\partial \underline{x}_3^0}{\partial x_2} = \frac{-q_2}{p_3}, \tag{F.19}$$

where we have again used the stationarity condition (F.4) in the numerator of (F.18). Substituting (F.18) and (F.19) into (F.16) reduces the Jacobian matrix to

$$\begin{vmatrix} -\frac{1}{|\mathbf{q}|} + \frac{q_1^2+q_1k_1}{|\mathbf{q}|^3} - \frac{1}{|\mathbf{p}|} + \frac{p_1^2+p_1k_1}{|\mathbf{p}|^3} & 0 \\ * & -\frac{1}{|\mathbf{q}|} - \frac{1}{|\mathbf{p}|}, \end{vmatrix} \tag{F.20}$$

where the $*$ represents a term that we do not need to compute as it is multiplied by 0 in the Jacobian. Thus we have for the Jacobian

$$\mathbf{J} = \frac{\omega'^2}{c^2}\left(\frac{1}{|\mathbf{p}|^2} + \frac{1}{|\mathbf{q}|^2} - \frac{p_1^2 + k_1p_1}{|\mathbf{p}|^3}\left(\frac{1}{|\mathbf{p}|} + \frac{1}{|\mathbf{q}|}\right) - \frac{q_1^2 + k_1q_1}{|\mathbf{q}|^3}\left(\frac{1}{|\mathbf{p}|} + \frac{1}{|\mathbf{q}|}\right) + \frac{2}{|\mathbf{q}||\mathbf{p}|}\right). \tag{F.21}$$

After some algebra, it can be shown that

$$-\frac{p_1^2 + k_1p_1}{|\mathbf{p}|^3}\left(\frac{1}{|\mathbf{p}|} + \frac{1}{|\mathbf{q}|}\right) + \frac{1}{|\mathbf{q}||\mathbf{p}|} = \frac{\mathbf{p}\cdot\mathbf{q}}{|\mathbf{p}|^3|\mathbf{q}|}, \tag{F.22}$$

which gives

$$\mathbf{J} = \frac{\omega'^2}{c^2}\left(\frac{1}{|\mathbf{p}|^2} + \frac{1}{|\mathbf{q}|^2} + \frac{\mathbf{p}\cdot\mathbf{q}}{|\mathbf{p}|^3|\mathbf{q}|} + \frac{\mathbf{q}\cdot\mathbf{p}}{|\mathbf{q}|^3|\mathbf{p}|}\right). \tag{F.23}$$

Since we are going to map from (x_1, x_2) to (η_1', η_2'), we require J^{-1}. Since $\mathbf{J} \neq 0$, we find that

$$\mathbf{J}^{-1} = \frac{\partial(x_1, x_2)}{\partial(\eta_1', \eta_2')} = \frac{c^2(|\mathbf{q}|^2|\mathbf{p}|^2)}{\omega'^2(|\mathbf{q}|^2 + |\mathbf{p}|^2)(1+\cos\theta)}, \tag{F.24}$$

where θ is the angle between the source and receiver rays at the scattering point (i.e., $\cos\theta = (\mathbf{q}\cdot\mathbf{p})|\mathbf{q}|^{-1}|\mathbf{p}|^{-1}$).

Treatment of amplitudes

To compute the final amplitude function, we begin with the initial amplitude, the product of the imaging and modeling amplitudes

$$Amp = \frac{1}{4\pi^2}\omega'^2\omega^2 A(\mathbf{x}, \mathbf{s}, \mathbf{r})A(\mathbf{x}, \mathbf{s}', \mathbf{r}'), \tag{F.25}$$

where $A(\mathbf{x}, \mathbf{s}, \mathbf{r}) = \frac{1}{8\pi^2 c^3 |\mathbf{s}-\mathbf{x}||\mathbf{x}-\mathbf{r}|}$.

We now follow the same steps as performed on the phase, beginning by changing to the midpoint-offset coordinates and the stationary phase in (x_3, ω) changing the amplitude function to

$$Amp' = \frac{1}{4\pi^2}\omega'^4\left(\frac{\partial_{x_3}T(x_1, x_2, \underline{x}_3^0, \mathbf{y}, \mathbf{h})}{\partial_{x_3}T(x_1, x_2, \underline{x}_3^0, \mathbf{y}', \mathbf{h})}\right)^2 \frac{A(x_1, x_2, \underline{x}_3^0, \mathbf{y}, \mathbf{h})A(x_1, x_2, \underline{x}_3^0, \mathbf{y}', \mathbf{h})}{\sqrt{|\partial_{x_3}T(x_1, x_2, \underline{x}_3^0, \mathbf{y}, \mathbf{h})|^2}}. \tag{F.26}$$

Up to the principal part (for which symbols and amplitudes are equal) we can assume $\mathbf{y} \approx \mathbf{y}'$ (Treves, 1980b, p 37), giving

$$\frac{1}{4\pi^2}\frac{\omega'^4 A^2(x_1, x_2, \underline{x}_3^0, \mathbf{y}, \mathbf{h})}{|\partial_{x_3}T(x_1, x_2, \underline{x}_3^0, \mathbf{y}, \mathbf{h})|}. \tag{F.27}$$

It is possible to write $\partial_{x_3}T$ in the notation defined above as

$$\partial_{x_3}T = \frac{q_3}{c|\mathbf{q}|} + \frac{p_3}{c|\mathbf{p}|}. \tag{F.28}$$

The product of the Jacobian of equation (F.24) with $\partial_{x_3}T$ from equation (F.28) gives equation (B-25) of de Hoop *et al.* (1999).

Multiplying equation (F.27) by the Jacobian $\frac{\partial(x_1,x_2)}{\partial(\eta_1',\eta_2')}$, and combining with the phase yields the kernel of the final operator

$$FF^*(\mathbf{y}, t, \mathbf{y}', t') = \frac{1}{4\pi^2}\int\int\int \frac{\omega'^4 A^2(\underline{x}_1, \underline{x}_2, \underline{x}_3^0, \mathbf{y}, \mathbf{h})}{|\partial_{x_3}T(\underline{x}_1, \underline{x}_2, \underline{x}_3^0, \mathbf{y}, \mathbf{h})|}\frac{\partial(x_1, x_2)}{\partial(\eta_1', \eta_2')}e^{i\omega'(t'-t)+i\boldsymbol{\eta}'\cdot(\mathbf{y}-\mathbf{y}')}\,\mathrm{d}\omega'\,\mathrm{d}\eta_1'\,\mathrm{d}\eta_2', \tag{F.29}$$

where $\underline{x}_1$ and $\underline{x}_2$ are underlined as they are now functions of (η_1', η_2'). It can be shown that the amplitude of this operator is the reciprocal of that of Miller *et al.* (1987) equation (27), upon changing variables in that equation from $\boldsymbol{\xi}$ to $\mathbf{y}$, using the Jacobian given in de Hoop *et al.* (1999). This amplitude construction can be used to correctly account for the amplitudes in offset continuation. For that case, one would simply fix both the output offset, $\mathbf{h} = \frac{\mathbf{s}-\mathbf{r}}{2}$, and the input offset, $\mathbf{h}' = \frac{\mathbf{s}'-\mathbf{r}'}{2}$ and follow the same procedure as for the case $\mathbf{h} = \mathbf{h}'$.

Appendix G

A Comparison of the Lippmann-Schwinger and Bremmer Series

The reason that internal multiples cause artifacts in imaging is that they violate the single scattering assumption, also known as the Born approximation. Two series to move beyond this assumption have been proposed in the literature, the Bremmer series (Bremmer, 1951) and the Lippmann-Schwinger series (Lippmann, 1956). Both of these series are designed to approximate the Green's function or Green's operator solving the wave equation. The wave equation is given by

$$c(\mathbf{x})^{-2}\partial_t^2 u(\mathbf{x},t) - \partial_x^2 u(\mathbf{x},t) - \partial_y^2 u(\mathbf{x},t) - \partial_z^2 u(\mathbf{x},t) = f(\mathbf{x},t)\,, \tag{G.1}$$

where c is the velocity, $\mathbf{x} = (x, y, z)$ is a spatial position vector and f is the source of waves. The Green's function, g, solves the wave equation in the sense that

$$\begin{aligned} c(\mathbf{x})^{-2}\partial_t^2 g(\mathbf{x},t-t',\mathbf{x}') - \partial_x^2 g(\mathbf{x},t-t',\mathbf{x}') - \partial_y^2 g(\mathbf{x},t-t',\mathbf{x}') - \partial_z^2 g(\mathbf{x},t-t',\mathbf{x}') \\ = \delta(\mathbf{x}-\mathbf{x}')\delta(t-t')\,, \end{aligned} \tag{G.2}$$

where δ is the dirac-delta function. Equation (G.1) can also be written in operator form, defining the wave operator, L, as

$$Lu = f\,. \tag{G.3}$$

This allows the definition of the Green's operator, G, via

$$LG = I\,, \tag{G.4}$$

where I is the identity operator. The Green's function is the kernel of the Green's operator so

$$[G\phi](\mathbf{x},t) = \int \mathrm{d}\mathbf{x}' \int \mathrm{d}t' g(\mathbf{x},t-t',\mathbf{x}')\phi(\mathbf{x}',t')\,, \tag{G.5}$$

where ϕ is the test function on which the operator acts. Thus the Green's operator propagates the wavefield, ϕ, from the position $(\mathbf{x}', t')$ to the position $(\mathbf{x}, t)$, which is why it is also referred to as a propagator. From the result that

$$g * f = u\,, \tag{G.6}$$

it follows that

$$Gf = u\,, \tag{G.7}$$

relating the source and the field via the Green's operator.

Both the Lippmann-Schwinger series and the Bremmer series couple Green's operators to approximate the higher-order scattering components of the wavefield. The following two sections describe these two series and the last section of this appendix discusses briefly the hybrid series developed in Chapter 4.

G.1 The Lippmann-Schwinger Series

The Lippmann-Schwinger series is an expansion in the contrast operator, V, between the wave operator in a known background, L_0 and the wave operator in the true medium, L. Thus,

$$V = L - L_0 \tag{G.8}$$

where

$$L = c(\mathbf{x})^{-2}\partial_t^2 - \partial_x^2 - \partial_y^2 - \partial_z^2 \tag{G.9}$$

$$L_0 = c_0(\mathbf{x})^{-2}\partial_t^2 - \partial_x^2 - \partial_y^2 - \partial_z^2\,, \tag{G.10}$$

where c_0 is the, known, velocity in the background medium and c is the, unkown, velocity in the true medium. Note that $V = (c(\mathbf{x})^{-2} - c_0(\mathbf{x})^{-2})\partial_t^2$ is an operator, not simply a difference in medium properties. Each successive term in the series is of higher order in this contrast operator. The series is derived, through a resolvent equation, from the Lippmann-Schwinger equation

$$G = G_0 + G_0 V G\,, \tag{G.11}$$

where G is the Green's operator, which is the solution operator for a partial differential operator (PDO) in the true medium, and G_0 is the Green's operator for the same PDO in a background medium. Lippmann (1956) derives this equation for the quantum scattering case, where G_0 is the solution before the particles interact and G is the solution containing the interaction term. Weglein *et al.* (1997) have used this idea extensively in the attenuation of both surface and internal multiples as well as other areas of seismic processing. Ten Kroode (2002) puts this theory in a mathematical framework, describing the conditions under which the Weglein *et al.* (1997) theory can be applied. The Born approximation is that $G \approx G_0 + G_0 V G_0$.

Re-arranging terms in (G.11) gives

$$G_0 = (I - G_0 V)G\,. \tag{G.12}$$

Equation (G.12) is a resolvent equation, the theory of which can be found in Yosida (1995). For the purpose of this appendix, the relevant result of this theory is that if the background medium is chosen such that $\|G_0 V\| < 1$ the Green's function G may be expanded into the

Lippmann-Schwinger series

$$G = \left(\sum_{n=0}^{\infty}(-G_0V)^n\right)G_0 = G_0 - G_0VG_0 + G_0VG_0VG_0 - \dots . \tag{G.13}$$

To my knowledge there are no references that investigate the choice of background model to ascertain whether or not $\|G_0V\| < 1$, meaning that this series is not, in general, convergent.

An advantage of the Lippmann-Schwinger series is that, unlike the Bremmer series, it has a corresponding inverse series that expresses difference operator, V, in terms of the Green's operator, which is directly related to the data. To express the medium contrast in terms of the data, assume the medium contrast can be decomposed into a series,

$$V = \sum_{j=1}^{\infty} V_j \,, \tag{G.14}$$

where V_j is of order j in the data. So, while the forward series expresses the Green's operator as a series with each term being of higher order in the medium contrast, the inverse series expresses the medium contrast in terms of a series in which each term is of higher order in the data.

This assumption is then substituted into (G.13), and terms of equal order in the data are equated, giving the following relations:

$$\begin{aligned} d &= G - G_0 = -G_0V_1G_0 && \text{(G.15)}\\ 0 &= -G_0V_2G_0 + G_0V_1G_0V_1G_0 && \text{(G.16)}\\ 0 &= -G_0V_3G_0 + G_0V_1G_0V_2G_0 + G_0V_2G_0V_1G_0 - G_0V_1G_0V_1G_0V_1G_0 && \text{(G.17)} \end{aligned}$$

etc. .

Equation (G.15) serves to define the data (or the scattered field as in Weglein *et al.* (1997)). This difference is directly related to seismic data because the difference between G and G_0 is in the reflections from differences between the true and reference media. The terms in (G.15) are first-order in the data, those in (G.16) are second-order in the data, and so on. By substituting (G.16) into (G.17) and continuing to higher order in the series it is found that

$$G_0V_jG_0 = \underbrace{G_0V_1G_0V_1\cdots G_0V_1}_{j \text{ times}}G_0 \,. \tag{G.18}$$

Since the Green's operators, G_0, are in the background medium, they are known and V_j can be estimated in this manner.

To estimate V_j from equation (G.18) requires an operator to estimate V_j from $G_0V_jG_0$, but this is the only inverse operator needed to estimate all of the V_j. The single-scattering case,

$$d = -G_0V_1G_0 \tag{G.19}$$

illustrates that this operator is the standard migration operator, M,

$$V_1 = M(d) = M(-G_0 V_1 G_0)\,. \tag{G.20}$$

This operator estimates the position in the subsurface of reflectors given the background velocity model, which in this case is embedded in G_0. From (G.20) and (G.18) the inverse series is rewritten as

$$V = \sum_{j=1}^{\infty} V_j = \underbrace{M(d)}_{V_1} + M\left(\sum_{j=1}^{\infty} \underbrace{G_0 V_1 G_0 V_1 \cdots G_0 V_1}_{j \text{ times}} G_0\right)\,, \tag{G.21}$$

by applying M to (G.14) inserting the recursion relation between the V_j given in (G.18).

G.2 The Bremmer Series

The Bremmer series was developed by Bremmer (1951). In his work, he suggests the solving of wave propagation in a layered medium by considering the solution in two parts: one that estimates the wavefield on one side of the layer, given the wavefield at the opposite side, and another that couples the propagation between layers. Later authors (Atkinson, 1960; Gray, 1983) extended this series and interpreted it as a splitting of the wavefield into and up- and downward propagating waves. Aminzadeh & Mendel (1980, 1981) used this theory used to attenuate surface-related multiples, also under the assumption of horizontal layers. The generalization of the Bremmer series to media varying in all spatial directions can be found in de Hoop (1996). It is this generalization that is used throughout the thesis and is discussed here.

Rather than solving two equations in different media as in Lippmann-Schwinger, the Bremmer series works from a decomposition of the wavefield into its up- and down-going constituents. (There is nothing fundamental about the up-down decomposition; the decomposition into opposite-going constituents can be done in any spatial direction.) The idea behind this decomposition is similar to the way in which a matrix is diagonalized using its eigenvalues and eigenvectors. The wave equation, written as a first-order system (equation (4.2)) is the starting matrix. The $B_\pm$ operators, from equation (4.7) are the analog of the eigenvalues of this matrix and the Q and Q^{-1} matrices from equation (4.6) are the analog of the matrices of eigenvectors used in a standard matrix diagonalization. This decomposition is discussed in more detail in Section 4.3.

The starting point for deriving the Bremmer series is from equation (4.6), restated here

$$(I\partial_z + \mathsf{Q}(z)\partial_z \mathsf{Q}(z)^{-1} + \mathsf{B})U = X\,, \tag{G.22}$$

where the cut-offs in the Green's functions that remove horizontal propagation are assumed to have been applied. Recall from Chapter 4 that the Q matrix diagonalizes the wave equation in a known background, B is a matrix with diagonal entries that are the one-way wave operators or single-square-root operators, U is a vector of the up- and down-going wave constituents, u_+, u_- and X is the source vector consisting of the up- and down-going

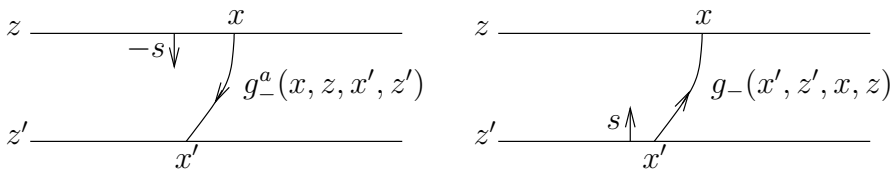

Figure G.1. Illustration of the reciprocity relation given in (G.26).

source constituents.

The Bremmer series is derived by considering the following derivative

$$\partial_z(g^a U) = \partial_z(g^a)U + g^a \partial_z U\,, \tag{G.23}$$

using the notation

$$g^a = \begin{pmatrix} g^a_+ & 0 \\ 0 & g^a_- \end{pmatrix} \tag{G.24}$$

for the matrix of adjoint Green's functions. The adjoint Green's functions are defined by taking the adjoint of the diagonalized wave equation

$$I\partial_z g^a + g^a \mathsf{B}^T = \delta(\mathbf{x} - \mathbf{x_0})\delta(z - z_0)\,; \tag{G.25}$$

where I is the identity operator. In this section $\mathbf{x} = (x, y)$ because the z dependence has been separated due to the up-down decomposition of the wavefield. The adjoint Green's function is related to the Green's function by

$$g^a(x, z, x', z') = -g(x', z', x, z)\,. \tag{G.26}$$

Recall that G_+ is the down-going propagator and G_- is the up-going propagator (with g_+ and g_- as their associated kernels). The adjoint operator propagates backward in time. Thus, G^a_+ propagates waves upward and G^a_- downward. The minus sign in (G.26) follows from reciprocity as in Remark 4.4.2. This is illustrated in Figure G.1.

Equation (G.23) can be expanded, by substituting (G.25) for the first term and (G.22) for the second, to

$$\begin{aligned} \partial_z(g^a U) &= (\delta(\mathbf{x} - \mathbf{x_0})\delta(z - z_0) + g^a \mathsf{B}^T)U + g^a(X - \mathsf{Q}(z)\partial_z \mathsf{Q}(z)^{-1}U - \mathsf{B}U) \\ &= \delta(\mathbf{x} - \mathbf{x_0})\delta(z - z_0)U + g^a X - g^a \mathsf{Q}(z)\partial_z \mathsf{Q}(z)^{-1}U\,, \end{aligned} \tag{G.27}$$

recalling that $\mathsf{B}^T = \mathsf{B}$ because the $B_+ = -B_-$ in the flux normalization. Defining G^a as the matrix of Green's operators associated with the matrix, g^a, of Green's functions and

integrating both sides of (G.27) over all space gives

$$0 = U + G^a X - G^a \mathsf{Q}(z)\partial_z \mathsf{Q}(z)^{-1} U \,, \tag{G.28}$$

where the left-hand side is zero because of causality of the Green's function (see Remark 4.4.1) and the limited region of investigation (sources exist over only a finite depth range). The reciprocity relation in (G.26) gives the resolvent equation for the Generalized Bremmer series

$$(I - G\mathsf{Q}(z)\partial_z \mathsf{Q}(z)^{-1})U = GX \,, \tag{G.29}$$

which can be solved for the wavefield U, assuming $(I - G\mathsf{Q}(z)\partial_z \mathsf{Q}(z)^{-1})$ is invertible, to give

$$U = (I - G\mathsf{Q}(z)\partial_z \mathsf{Q}(z)^{-1})^{-1} GX \,. \tag{G.30}$$

It has been shown (de Hoop, 1996) that under appropriate conditions, this resolvent equation allows a convergent series expansion

$$U = \sum_{j=0}^{\infty} (GS)^j GX \,, \tag{G.31}$$

defining the scattering matrix $S = \mathsf{Q}(z)\partial_z \mathsf{Q}(z)^{-1}$. Putting the scattering matrix into the familiar form of reflection (R) and transmission (T) coefficients

$$S = \begin{pmatrix} T & R \\ R & T \end{pmatrix} ,$$

and denoting the up- and down-going source constituents by X_- and X_+ respectively, the first few terms of the series are

$$\begin{aligned} U_1 &= \begin{pmatrix} G_+ X_+ \\ G_- X_- \end{pmatrix} \\ U_2 &= \begin{pmatrix} G_+ T G_+ X_+ + G_- R G_+ X_+ \\ G_- R G_+ X_+ + G_- T G_- X_- \end{pmatrix} \\ U_3 &= \begin{pmatrix} G_+ T G_+ T G_+ X_+ + G_+ T G_+ R G_- X_- + G_+ R G_- R G_+ X_+ + G_+ R G_- T G_- X_- \\ G_- R G_+ T G_+ X_+ + G_- R G_+ R G_- X_- + G_- T G_- R G_+ X_+ + G_- T G_- T G_- X_- \end{pmatrix} \end{aligned} \tag{G.32}$$

denoting by U_j the j^{th} term in the series.

The equations in (G.32) are illustrated in Figure G.2. The source term X generates waves that are propagated either upward by G_+ or downward by G_-. These waves are then coupled at some depth by either the reflection operator, R, or the transmission operator, T, after which the propagation continues. The reflection and transmission coefficients result from the changes in medium properties with depth, through the derivative ∂_z.

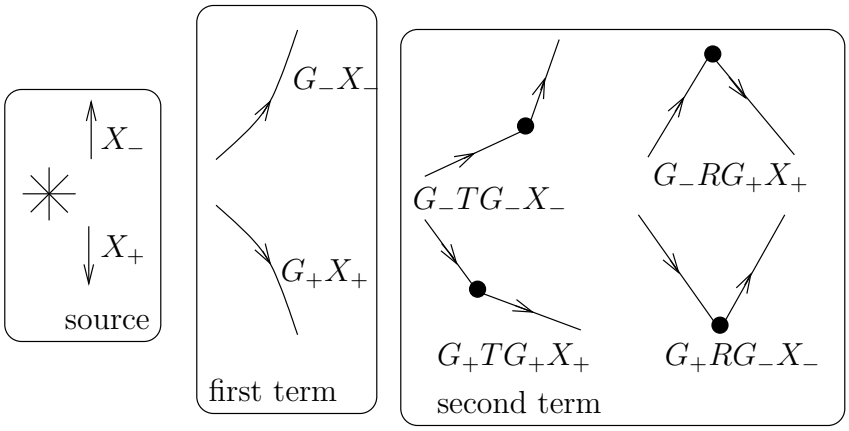

Figure G.2. Illustration of the first two terms of the Bremmer series.

G.3 The Hybrid Series

Chapter 4 describes a hybrid series between the Lippmann-Schwinger and Bremmer series. This is done in an attempt to capture the advantages of both series. The Lippmann-Schwinger series has the advantage that its form admits both a forward and inverse series. The advantage of the Bremmer series is that it is convergent and the splitting of the wavefield into its up- and down-going constituents fits naturally in a downward continuation or wavefield extrapolation migration. The hybrid series first separates the wavefield into its up- and down-going constituents as in the Bremmer series. This is done in a known background model. The diagonalization operators computed in the known background are then applied to the wavefield in the true medium, whose difference from the background medium is unknown, creating two equations in two different media, as in the Lippmann-Schwinger series.

Perhaps the most fundamental difference is in the writing of the series as a set of matrix equations rather than scalar operator equations. The Lippmann-Schwinger series is a series of operators applied to a single wavefield; each term of the series is of higher order in the contrast between the true and reference media, parameterized by the operator V. The hybrid series is a series of matrix operators applied to two wavefields; the up- and down-going constituents of the wavefield on which the operators of the Lippmann-Schwinger series acts. Each term of the series is of higher-order in the difference operator, which is now a matrix, and each term of the series also contains higher order scattering than does the previous term. The reflection and transmission operators of the hybrid series are different from those of the Bremmer series because the reflection operators in the Bremmer series are vertical derivatives of the medium whereas in the hybrid series these operators are based on differences between the true and background media.

The inverse hybrid series is constructed in exact parallel to the Lippmann-Schwinger

series. The reconstructed contrast operators V_j are now matrices with entries corresponding to reflection and transmission coefficients for scattering between up-to-up, down-to-down, up-to-down, and down-to-up going waves. Thus the hybrid series consists of the splitting of the wavefield into its up- and down-going constituents and then coupling those constituents through reflection and transmission coefficients derived from Lippmann-Schwinger type coupling of terms.

Appendix H

A comparison of different boundary conditions and edge effects in migration

The goal of this appendix is to show that boundary effects can be a source of significant artifacts in imaging. An understanding of the basics of wave-equation migration algorithms is assumed, although brief descriptions are given of the most important points.

Estimating multiples in the image space requires a better estimate of the image than is required for ordinary imaging. The reason for this is twofold. First, multiples have smaller amplitude than do primaries because they have reflected three times rather than once. Second, the process of migration focusses energy from primaires in time at $t = 0$ and in offset at $h = 0$, but energy from multiples is not correctly focussed, and thus does not make as strong a contribution to the image. The purpose of this appendix is to illustrate, primarily through examples, some of the imaging problems that need to be taken into account when imaging with multiples that may not be as important for standard imaging.

The migration algorithm used in Chapter 5 works by extrapolating the wavefield, sampled in midpoint, offset and time, in depth using a propagator provided by Total. The propagator begins with a standard Stolt phase shift (Stolt, 1978), followed by a lens correction to correct for lateral velocity variations and a wide angle correction using a tridiagonal matrix solve. The precise details of the propagator are not important. The essential point is that the propagator estimates the data at depth $z + \Delta z$ from the data at depth z. The zero time, zero offset imaging condition is then applied resulting in the final image. (The energy recorded at $h = 0$ and $t = 0$ is the reflected energy from a reflector at the current depth.) The entire algorithm works in the temporal frequency domain. The phase shift is applied in the spatial frequency or wavenumber domain. Each propagation step therefore requires Fourier transforms in both offset and wavenumber. To use the prime factor Fast Fourier Transform (FFT) the input data are padded with zeros to a length that is a product of the factors available to the FFT routine. (In this case, these factors are: 2,3,4,5,7,8,9,11,13 and 16.)

The model used throughout this appendix consists of a homogeneous velocity of 6 km/s with a low-velocity layer from 1.5 to 2.5 km depth with velocity 2 km/s. The model is sampled every 10 m, with 40 km lateral extent and 12 km depth. This model was chosen because the strong velocity contrast results in a strong internal multiple. Data were generated for this model using standard explicit second-order finite differences, using the program *sufdmod2*. A single shot at the center of the model was simulated with receivers spaced every 10 m; the source and receivers were at 300 m depth in the model. Four seconds

of data were recorded at 4 ms intervals (1001 time points). A range of offsets, $h = \frac{s-r}{2}$, were extracted from this shot resulting in a single shot record with 101 offsets ranging from 0 to 1.5 km at a spacing of 15 m. Since the model is laterally homogeneous, the recorded response depends only on the vertical velocity profile and the offset. Thus a shot record is identical to a common-midpoint (CMP) gather. The single CMP was then duplicated to form a data set of 101 CMPs.

Creating an image in this model is not difficult, such an image is shown in Figure H.1, with the amplitudes scaled so that nothing is clipped. When the amplitudes of this image are scaled so that the imaged multiple can be seen, as in Figure H.2 (where data above the 85^{th} percentile are clipped) artifacts begin to appear making it difficult to separate the multiple from other effects such as aliasing in both space and frequency and boundary reflections. These difficulties are enhanced in this model because everything is flat making it hard to distinguish the different artifacts from one another. Figure H.2 is an image made with enough padding to image the primaries correctly and is the basis to which the following figures are compared.

To attenuate the artifacts seen above, I tried several different things, which are illustrated below. I leave the description of parameters used to create each image to the figure caption and here describe briefly the tapers and boundary conditions applied.

To reduce computational cost, a bandpass filter is applied to the data to reduce the number of frequencies it is necessary to migrate. (Each frequency is migrated independently.) Although a cosine squared taper is used on this filter, there is still a lot of ringing if too many frequencies are filtered out. To avoid this, I found it best to migrate all frequencies present in the data. This still amounts to migrating only a small fraction of the frequencies obtained on FFTing the data from time to frequency because the temporal sampling is denser than required by the Nyquist sampling criteria. For comparison, a different filter is used in Figure H.3.

In any frequency domain method, both aliasing in time, caused by sampling the data with too large a time step, and aliasing in frequency, caused by sampling too sparsely in frequency, are possible sources of error. Aliasing in time is avoided by not migrating higher than the Nyquist frequency determined from the sampling of the input data. Aliasing in frequency does occur however, and is avoided by padding the input data set with more zeros to decrease the frequency sampling interval. The time padding is greatly increased in Figure H.4.

To reduce the effects of wrap-around, I applied a fifth-order polynomial taper to the edge of the data. The coefficients of the polynomial are chosen so that the taper function as well as its first and second derivatives are continuous at the start and end of the taper. To minimize the decay in amplitude at the edges of the image caused by the taper, I taper in the padding region at each depth step. The taper extends throughout the padding region, reaching zero in the center (the taper is applied for both small and large values). Figures H.6, H.7, H.8 show the affects of tapering in offset and midpoint. Since the offset taper seems to be most effective it will be kept in later plots whereas the y taper is left out.

Since the taper was not entirely successful in attenuating the artifacts, I also implemented a Robin boundary condition, as explained in van Stralen (1997, Section 5.4).

A Robin boundary condition is a mix of a Neumann and Dirichlet boundary condition; van Stralen (1997) found this particular boundary condition to be accurate in wave propagation problems. Because of the structure of the propagator used here, I chose to implement this boundary condition by propagating the wavefield from one depth to the next and then replacing the boundary elements of the wavefield with the solution of the boundary condition equations. The affects of the boundary conditions are shown in Figure H.5.

Finally, I came to the conclusion that tapering and boundary conditions is simply not sufficient and I simply padded the wavefield with zeros to approximately two and a half times its original size. This seems to attenuate the artifacts to the point where the image is sufficiently clean to analyze the contribution to the image from internal multiples. Padding in different variables is shown in Figures H.9,H.10 and H.11.

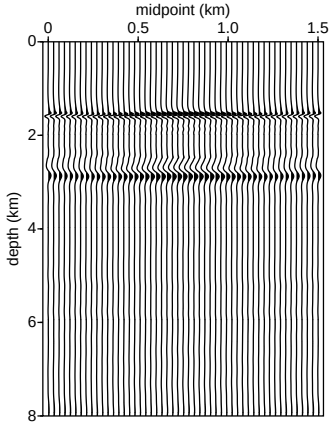

Figure H.1. Corner frequencies of bandpass filter: 1,3,20,30; padding of 25 points in both offset and midpoint; padding of 7 points in time; no tapers; no boundary conditions. Standard amplitude display.

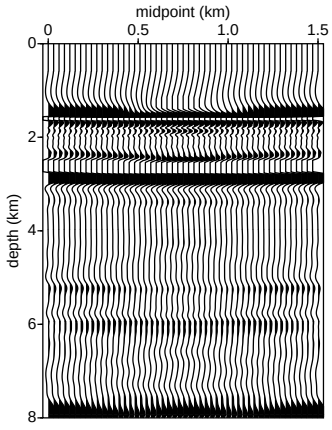

Figure H.2. Corner frequencies of bandpass filter: 1,3,20,30; padding of 25 points in both offset and midpoint; padding of 7 points in time; no tapers; no boundary conditions.

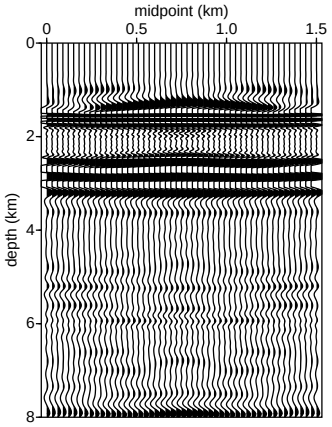

Figure H.3. Corner frequencies of bandpass filter: 5,10,20,30; padding of 25 points in both offset and midpoint; padding of 7 points in time; no tapers; no boundary conditions.

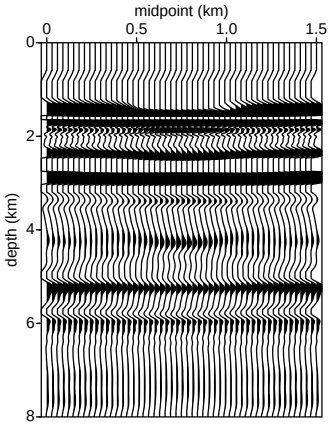

Figure H.4. Corner frequencies of bandpass filter: 1,3,20,30; padding of 25 points in both offset and midpoint; padding of 2079 points in time; no tapers; no boundary conditions.

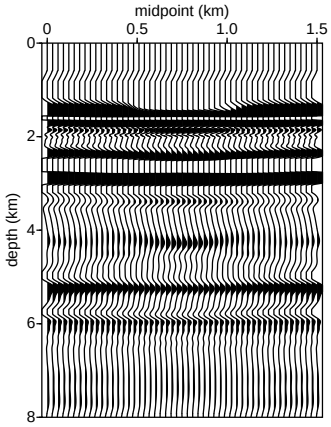

Figure H.5. Corner frequencies of bandpass filter: 1,3,20,30; padding of 25 points in both offset and midpoint; padding of 2079 points in time; no tapering; boundary conditions applied in both midpoint and offset.

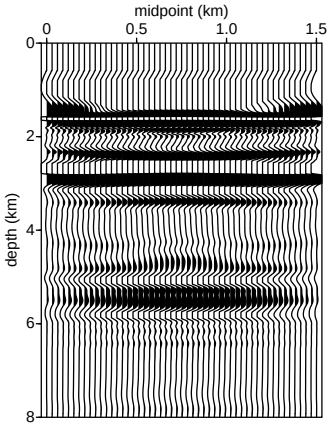

Figure H.7. Corner frequencies of bandpass filter: 1,3,20,30; padding of 25 points in both offset and midpoint; padding of 2079 points in time; taper in midpoint; no boundary conditions.

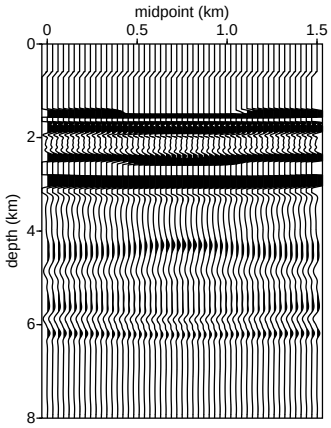

Figure H.6. Corner frequencies of bandpass filter: 1,3,20,30; padding of 25 points in both offset and midpoint; padding of 2079 points in time; taper in offset; no boundary conditions.

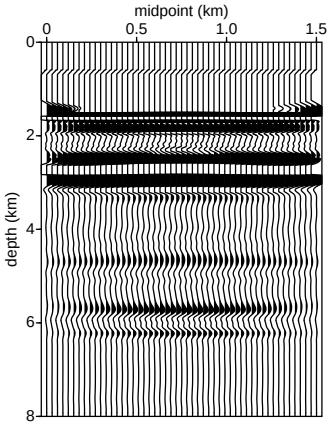

Figure H.8. Corner frequencies of bandpass filter: 1,3,20,30; padding of 25 points in both offset and midpoint; padding of 2079 points in time; taper in both midpoint and offset; no boundary conditions.

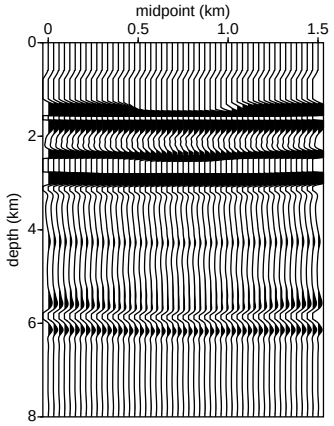

Figure H.9. Corner frequencies of bandpass filter: 1,3,20,30; padding of 151 points in offset and 25 in midpoint; padding of 2079 points in time; taper in offset; no boundary conditions.

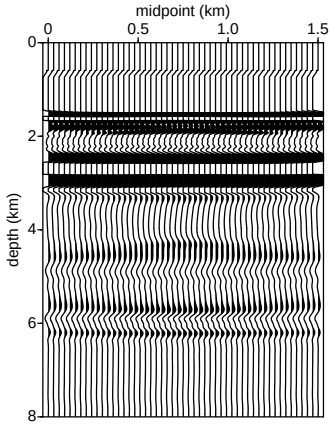

Figure H.10. Corner frequencies of bandpass filter: 1,3,20,30; padding of 25 points in offset and 151 in midpoint; padding of 2079 points in time; taper in offset; no boundary conditions.

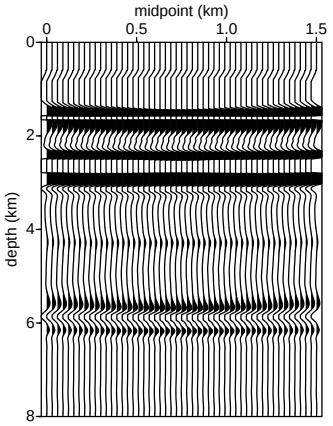

Figure H.11. Corner frequencies of bandpass filter: 1,3,20,30; padding of 151 points in both offset and midpoint; padding of 2079 points in time; taper in offset; no boundary conditions.

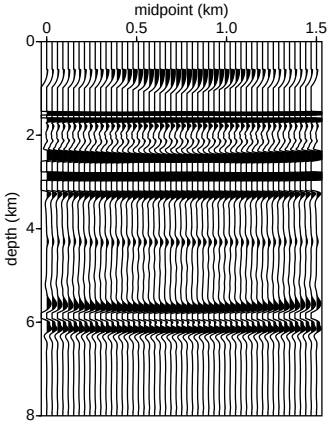

Figure H.12. Same as Figure H.11 except that this image has the Q and Ξ amplitude factors discussed in Appendix I applied.

Appendix I

Amplitude correction factors used in imaging

Chapter 4 gives a theory for predicting artifacts caused by internal multiples in imaging. In order to estimate these artifacts accurately, the various amplitude factors discussed must be implemented and applied to the data. In this appendix, I discuss the implementation of these factors and illustrate their application to two synthetic data sets. I describe their application as part of the standard imaging procedure rather than in the context of multiple estimation because this is the simplest application of these operators.

I.1 Algorithm

The goal of this appendix is to bridge the gap between the theory described by Stolk & de Hoop (2004a) for amplitude preserved wave-equation migration and the implementation of these ideas. I thus begin directly with Stolk & de Hoop (2004a, proposition 3.2), in which the following expression for the wave-equation angle transform is given,

$$(A_{\mathrm{WE}}d)(z,x,p) = j^{-1}R_3\bar{\Xi}^{-1}Q_{-,s}(z)^{-1}Q_{-,r}(z)^{-1}H^*(z,0) \\ Q_{-,s_0}(0)^{-1}Q_{-,r_0}(0)^{-1}D_t^{-2}d(s_0,r_0,t)\,. \quad \text{(I.1)}$$

In the above expression, d is the data, as a function of the source position, s_0, receiver position, r_0 and time, t. The Q operators are the elements of generalized operator eigenvectors which arise in the diagonalization of the wave-equation written as a first order system of differential equations (see Section 4.3 for more details). The propagator H is the downward continuation operator which is the Green operator of the double-square-root (DSR) equation (the DSR equation was introduced by Claerbout (1985)). The pseudo-differential operator $\bar{\Xi} = \bar{K}^*\bar{K}$ is the normal operator, where

$$\bar{K} = LE_2\,, \quad \text{(I.2)}$$

$$E_2 : b(z,r,s) \mapsto \delta(t)b(z,r,s)\,, \quad \text{(I.3)}$$

and

$$\bar{L}g = \int_0^Z H(0,z)g(z,\cdot,\cdot,\cdot)\,\mathrm{d}z. \quad \text{(I.4)}$$

The restriction operator R_3 is the beam-forming operator which gives the wavefield as a function of angle. The j^{-1} operator is a jacobian applied to the final image gather.

Using the semi-group property, $H^*(z,z_1) = H^*(z,z')H^*(z',z_1)$ (I.1) becomes

$$(A_{\mathrm{WE}}d)(z,x,p) = j^{-1}R_3\bar{\Xi}^{-1}Q_{-,s}(z)^{-1}Q_{-,r}(z)^{-1}H^*(z,z-\Delta z)\dots \\ H^*(2\Delta z,\Delta z)H^*(\Delta z,0)Q_{-,s_0}(0)^{-1}Q_{-,r_0}(0)^{-1}D_t^{-2}d(s_0,r_0,t)\,, \quad \text{(I.5)}$$

which shows the splitting of the propagator into depth steps. From this expression, the procedure required to generate an image gather is split into four steps. First, the term $Q_{-,s_0}(0)^{-1}Q_{-,r_0}(0)^{-1}D_t^{-2}$ is applied to the data. Next the data are propagated to the depth at which the image gather is to be formed, through H^*. Following this the data are corrected with the $\bar{\Xi}^{-1}Q_{-,s}(z)^{-1}Q_{-,r}(z)^{-1}$ term and an image gather is computed with R_3. This image gather is corrected with the term j^{-1}; this term is more difficult to implement as it involves variables both at the surface and at depth. Its implementation is not discussed here. The following subsections describe the implementation of the Q and $\bar{\Xi}$ operators.

I.1.1 Pre-conditioning

The preconditiong step is that portion of the imaging procedure which occurs before propagation begins. This section gives a procedure and approximations for the application of the $Q_{-,r_0}(0)^{-1}$ and D_t^{-2} terms to the data. The application of $Q_{-,s_0}(0)^{-1}$ follows directly from this case. First write

$$Q_{-,r_0}(0)^{-1}D_t^{-2}d(s_0,r_0,t)\,, \quad \text{(I.6)}$$

in the form of a pseudodifferential operator. It is well known that D_t^{-2} can be applied in the frequency domain through a division by ω^2. The derivation of this result is given to highlight that the procedure is the same as that used to apply $Q_{-,r_0}(0)^{-1}$. The symbol[1] of D_t^{-2} is ω^{-2} and is applied via

$$\frac{1}{2\pi}\int\mathrm{d}\omega\int\mathrm{d}s\;\omega^{-2}d(s_0,r_0,s)e^{\mathrm{i}\omega(t-s)}\,. \quad \text{(I.7)}$$

Since the symbol is independent of time,

$$\begin{aligned}\frac{1}{2\pi}\int\mathrm{d}\omega\;\omega^{-2}\int\mathrm{d}s\;d(s_0,r_0,s)e^{\mathrm{i}\omega(t-s)} &= \frac{1}{2\pi}\int\mathrm{d}\omega\;\omega^{-2}\widehat{d}(s_0,r_0,\omega)e^{\mathrm{i}\omega t} \quad \text{(I.8)}\\ &= \mathcal{F}^{-1}[\;\omega^{-2}\widehat{d}(s_0,r_0,\omega)]\,,\end{aligned}$$

where the hat indicates that the Fourier transform of a quantity has been taken and $\mathcal{F}$ represents the Fourier transform.

The application of $Q_{-,r_0}(0)^{-1}$ is done in essentially the same way; the symbol of $Q_{-,r}(z)$ is $q(z,r,\rho,t,\omega) = (c(z,r_0)^{-2}\omega^2 - \|\rho\|^2)^{\frac{1}{4}}$, where ρ is the cotangent variable associated with r and z is a parameter (i.e. Q does not act in this variable). Applying $Q_{-,r_0}(0)$ to the final

[1]The symbol of the differential operator, $P(x,D_x)$, is defined as $P(x,\xi)$ in which the D_x has been simply replaced with the ξ variable dual to x. The principle symbol, is the highest order component of the symbol as is generally denoted with the same symbol in lower case, i.e., $p(x,\xi)$.

equation in (I.8) gives

$$\left(\frac{1}{2\pi}\right)^2 \int \mathrm{d}\rho_0 \int \mathrm{d}\omega \int \mathrm{d}r_0' \int \mathrm{d}t' (c(0,r_0')^{-2}\omega^2 - \rho_0^2)^{\frac{1}{4}} \mathcal{F}_t^{-1}[\omega^{-2}\widehat{d}(s_0,r_0,\omega)](s_0,r_0',t') e^{\mathrm{i}\omega(t-t')+\mathrm{i}\rho_0(r_0-r_0')}\,, \quad \text{(I.9)}$$

where the subscript t to $\mathcal{F}$ to indicates that it is a Fourier transform only in time. This is equivalent to

$$\begin{aligned} & \left(\frac{1}{2\pi}\right)^2 \int \mathrm{d}\rho_0 \int \mathrm{d}\omega \int \mathrm{d}r_0' (c(0,r_0')^{-2}\omega^2 - \rho_0^2)^{\frac{1}{4}} e^{\mathrm{i}\rho_0(r_0-r_0')+e^{\mathrm{i}\omega t}} \int \mathrm{d}t' \quad \text{(I.10)} \\ & \qquad \mathcal{F}_t^{-1}[\omega^{-2}\widehat{d}(s_0,r_0,\omega)](s_0,r_0',t') e^{-\mathrm{i}\omega t'} \\ = & \left(\frac{1}{2\pi}\right)^2 \int \mathrm{d}\rho_0 \int \mathrm{d}\omega \int \mathrm{d}r_0' (c(0,r_0')^{-2}\omega^2 - \rho_0^2)^{\frac{1}{4}} \omega^{-2}\widehat{d}(s_0,r_0,\omega) e^{\mathrm{i}\rho_0(r_0-r_0')+\mathrm{i}\omega t}\,. \end{aligned}$$

There are several ways to approximate the above form, although its direct application is quite costly. One possible approximation scheme is discussed in the following section.

Screen approximation In (I.10) the forward and inverse Fourier transforms in the (r_0,ρ_0) variables cannot be separated because q depends on both variables. Because it is more efficient to apply the operator if this can be done, I approximate the symbol of Q by a phase screen. The idea of a phase screen is to approximate the symbol of an operator by a product of two symbols, one depending only on r_0 and the other only on ρ_0. Further details on screens and generalized screens can be found in de Hoop *et al.* (2003b). The slowness contrast is

$$u(z,x) = c(x,z)^{-2} - c_0(z)^{-2}\,, \quad \text{(I.11)}$$

where c_0 is the laterally invariant reference velocity. Using this define

$$q_0(z,\rho,\omega) = \left(\left(\frac{\omega}{c_0(z)}\right)^2 - \rho^2\right)^{\frac{1}{4}}\,, \quad \text{(I.12)}$$

as the symbol of Q in a background velocity model. Substituting this into the expression above for q gives

$$\begin{aligned} q(z,\rho,\omega) &= (q_0(z,\rho,\omega)^4 + u(z,x))^{\frac{1}{4}} \quad \text{(I.13)} \\ &= q_0(z,\rho,\omega)\left(1 + \frac{u(z,x)}{q_0(z,\rho,\omega)^4}\right)^{\frac{1}{4}}\,. \end{aligned}$$

Performing a first order Taylor expansion about $u=0$ of the term in brackets gives

$$q(z,\rho,\omega) \approx q_0(z,\rho,\omega)\left(1 + \tfrac{1}{4}\frac{u(z,x)}{q_0(z,\rho,\omega)^4}\right)\,. \quad \text{(I.14)}$$

In (I.14) q_0 depends only on cotangent variables (recalling that z is a parameter) whereas the term in parantheses depends on both space and cotangent variables. Thus one more approximation is required, expanding q_0 about vertical propagation ($\rho = 0$). The zero-order Taylor approximation is

$$q_0(z,\rho,\omega)^{-1} \approx c_0(z)^{\frac{1}{2}}\,, \tag{I.15}$$

giving

$$q(z,\rho,\omega) \approx q_0(z,\rho,\omega)(1+\tfrac{1}{4}c_0(z)^2u(z,x))\,. \tag{I.16}$$

Substituting this expression into (I.10) for the symbol of q gives

$$\begin{aligned}
&\left(\frac{1}{2\pi}\right)^2\int \mathrm{d}\rho_0 e^{\mathrm{i}\rho_0 r_0}\int\mathrm{d}\omega\ e^{\mathrm{i}\omega t}q_0(0,\rho_0,\omega)\int\mathrm{d}r_0'\ (1+\tfrac{1}{4}c_0(0)^2u(0,r_0))\omega^{-2}\widehat{d}(s_0,r_0,\omega)e^{\mathrm{i}\rho_0 r_0'}\\
&\quad= \left(\frac{1}{2\pi}\right)^2\int\mathrm{d}\rho_0 e^{\mathrm{i}\rho_0 r_0}\int\mathrm{d}\omega e^{\mathrm{i}\omega t}q_0(0,\rho_0,\omega)\\
&\qquad\qquad \mathcal{F}_{r_0}\left[(1+\tfrac{1}{4}c_0(0)^2u(0,r_0))\omega^{-2}\widehat{d}(s_0,r_0,\omega)\right](s_0,\rho_0,\omega)\\
&\quad= \left(\frac{1}{2\pi}\right)^2\mathcal{F}_{\rho_0}^{-1}\mathcal{F}_{\omega}^{-1}\Big[q_0(0,\rho_0,\omega)\\
&\qquad\qquad \mathcal{F}_{r_0}\left[(1+\tfrac{1}{4}c_0(0)^2u(0,r_0))\omega^{-2}\widehat{d}(s_0,r_0,\omega)\right]\Big](s_0,r_0,t)\,.
\end{aligned}$$

It follows from this that the Q operators can be applied, in the phase screen approximation, by first taking the Fourier Transform of the data, then multiplying by an amplitude factor in space, taking the Fourier Transform in space, then multiplying by a factor in wavenumber and returning to space and time through the inverse Fourier Transform. The output of this procedure is corrected data at the Earth's surface, which is denoted by d_c in the following section.

I.1.2 Propagation

These corrected data can then be propagated to any depth through successive applications of the H^* operator. Both H and its adjoint H^* are Fourier Integral Operators (FIOs). The symbol of $H^*(0,z)$ is

$$h^*(z,s,\sigma,r,\rho,t,\omega) = -\sqrt{\left(\frac{\omega}{c(z,r)}\right)^2-\rho^2}-\sqrt{\left(\frac{\omega}{c(z,s)}\right)^2-\sigma^2}\,.$$

It is applied to data by

$$\begin{aligned}
&\int\mathrm{d}\omega\int\mathrm{d}\sigma\int\mathrm{d}\rho\int\mathrm{d}t'\int\mathrm{d}s'\int\mathrm{d}r' d_c(s',r',t')\\
&\qquad e^{\mathrm{i}z\left(-\sqrt{\left(\frac{\omega}{c(z,r)}\right)^2-\rho^2}-\sqrt{\left(\frac{\omega}{c(z,s)}\right)^2-\sigma^2}\right)}e^{\mathrm{i}\omega(t-t')+\mathrm{i}\sigma(s-s')+\mathrm{i}\rho(r-r')}\,.
\end{aligned} \tag{I.17}$$

The symbol of H also depends on both the space and phase variables, making its application computationally expensive. There are many methods of approximating this operator, a few of which are given in de Hoop *et al.* (2003b) and references therein. This completes the data propagatation to depth z, denoted in the following by $d_p(z,s,r,t)$.

I.1.3 Imaging condition

To generate a CIG at depth z, the second set of amplitude corrections and the restriction operator R_3 are applied to the data. The first two operators that must be applied to the data are again Q^{-1} operators whose approximate symbols are given in (I.16). Thus, they are applied via

$$-\left(\frac{1}{2\pi}\right)^2 \mathcal{F}_\rho^{-1}\mathcal{F}_\sigma^{-1}\mathcal{F}_\omega^{-1}\left[q_0(z,\rho,\omega)q_0(z,\sigma,\omega)\right.$$
$$\left.\mathcal{F}_r\mathcal{F}_s\left[(1+\tfrac{1}{4}c_0(z)^2u(z,r))(1+\tfrac{1}{4}c_0(z)^2u(z,s))\widehat{d}_p(z,s,r,\omega)\right]\right](z,s,r,t)\,. \quad \text{(I.18)}$$

Next $\bar{\Xi}$ must be applied to the data. It's symbol is given by

$$c(z,s)^{-2}(c(z,s)^{-2}-\omega^{-2}\sigma^2)^{-\frac{1}{2}}+c(z,r)^{-2}(c(z,r)^{-2}-\omega^{-2}\rho^2)^{-\frac{1}{2}} \quad \text{(I.19)}$$

the phase screen approximation of this symbol, computed as in section I.1.1, is

$$c_0(z)^{-2}(c_0(z)^{-2}-\omega^{-2}\sigma^2)^{-\frac{1}{2}}(1+u(s,z)c_0(z)^2)(1-\tfrac{1}{2}c_0(z)^2u(s,z))$$
$$+\,c_0(z)^{-2}(c_0(z)^{-2}-\omega^{-2}\rho^2)^{-\frac{1}{2}}(1+u(r,z)c_0(z)^2)(1-\tfrac{1}{2}c_0(z)^2u(r,z))\,. \quad \text{(I.20)}$$

To simplify notation define

$$\xi_p(z,\omega,\alpha)=c_0(z)^{-2}(c_0(z)^{-2}-\omega^{-2}\alpha^2)^{-\frac{1}{2}}$$

and

$$\xi_s(z,x)=(1+u(x,z)c_0(z)^2)(1-\tfrac{1}{2}c_0(z)^2u(x,z))\,.$$

The application of $\bar{\Xi}$ to the data can then be written as

$$d_o(z,s,r,t)=\mathcal{F}_t^{-1}\left[\mathcal{F}_s^{-1}\left[\xi_p(z,\omega,\sigma)\mathcal{F}_s\left[\xi_s(z,s)\widehat{d}_i(z,s,r,\omega)\right]\right]\right.$$
$$\left.+\mathcal{F}_r^{-1}\left[\xi_p(z,\omega,\rho)\mathcal{F}_r\left[\xi_s(z,r)\widehat{d}_i(z,s,r,\omega)\right]\right]\right]\,, \quad \text{(I.21)}$$

which gives the final corrected data at depth z. The CIG is now formed through the restriction operator R_3,

$$a(z,x,p)=\int_{\mathbb{R}} d_o(z,x-\tfrac{h}{2},x+\tfrac{h}{2},ph)\chi(z,x,h)\,\mathrm{d}h, \quad \text{(I.22)}$$

where $h = \frac{1}{2}(s+r)$ is the offset and $x = \frac{1}{2}(s-r)$ the midpoint and χ is a pseudodifferential cutoff with compact support containing the point $h = 0$. This gives the common image gather $a(z, x, p)$ as a function of the position (z, x) and the slowness p.

I.2 Examples

To illustrate the use of the operators, I apply them to two synthetic data sets in this section. The particular models were chosen to be included in Stolk *et al.* (2005), which illustrates that wave-equation imaging does not have the same kinematic artifacts as are present in Kirchoff migration. (See also Stolk & Symes (2004).) The goal of this section is to show the differences in relative amplitudes between different regions of the image; thus the images are displayed without clipping large amplitudes.

I.2.1 Simple lens model

This model was developed to illustrate the presence of kinematic artifacts in Kirchoff migration (Stolk & Symes, 2004). The velocity model is shown in Figure I.1; it consists of a low-velocity gaussian lens centered at the origin with a single reflector at a depth of 2 km. Figure I.2 shows a typical shot record from this data set.

Figure I.3 shows an image of this model without applying either the Q or Ξ operators (the D_t^{-2} is applied however). The reflector shows up well, at the correct depth. Figure I.4 shows a common image gather directly beneath the lens. As expected, this gather is flat as a function of angle and the reflector is imaged at the correct depth. Figures I.5 and I.6 repeat the same image and CIG with the Q operators applied both at the surface and at the image point. Note that the image has a more consistent amplitude as a function of midpoint with the Q operators applied than without (compare Figure I.3 with I.5). The CIG shown in Figure I.6 shows some additional high frequency noise as compared with Figure I.4. This is likely due to the ω factor in the Q operators which acts as a time derivative. Figures I.7 and I.7 show the image and CIG with the Ξ operator applied. This operator does not seem to have a large impact on the relative amplitudes of the image.

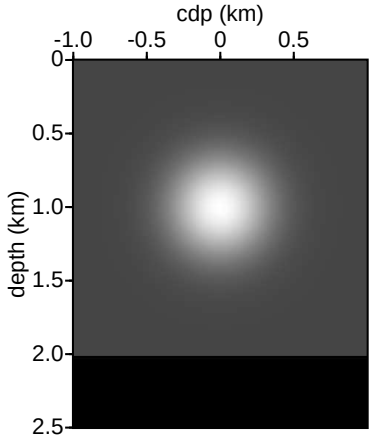

Figure I.1. Velocity model for the simple lens example. The low-velocity lens is described by $c(x,z) = 1 - 0.4e^{-9[x^2+(x-1)^2]}$; the velocity increases from 1 km/s to 1.15 km/s at a depth of 2 km to create a reflector.

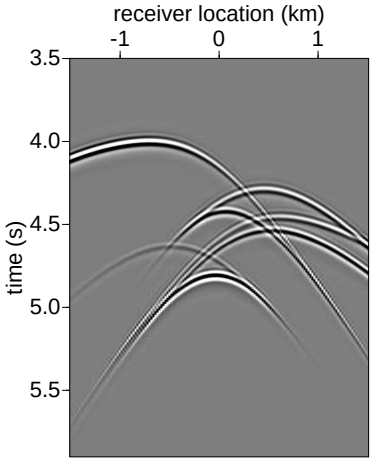

Figure I.2. Shot record from $x = -500m$ for the simple lens model.

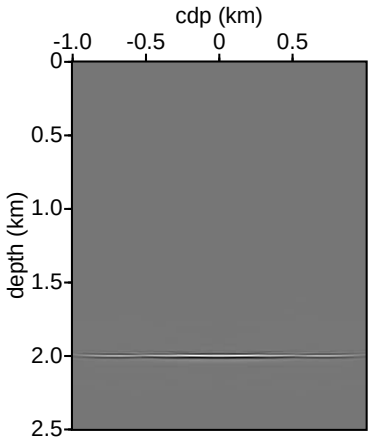

Figure I.3. Image in the simple lens model with no Q or Ξ operators applied.

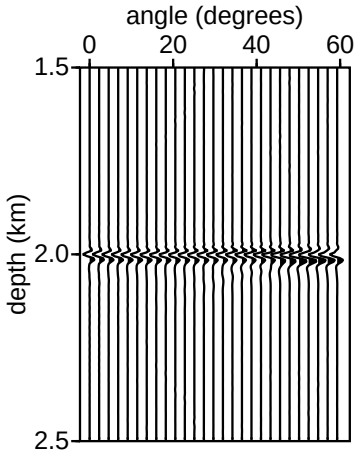

Figure I.4. Common image gather at $x = 0$ in the simple lens model with no Q or Ξ operators applied.

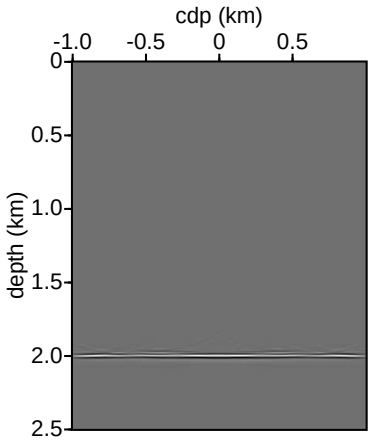

Figure I.5. Image in the simple lens model with Q operators applied.

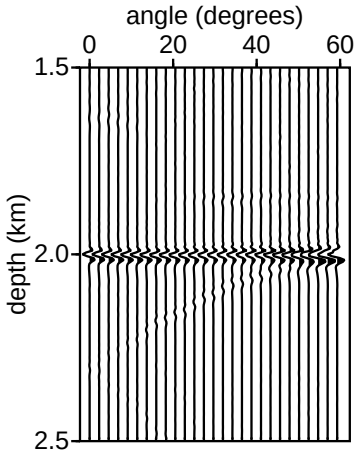

Figure I.6. Common image gather at $x = 0$ in the simple lens model with Q operators applied.

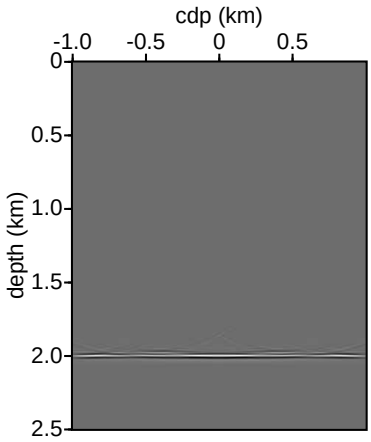

Figure I.7. Image in the simple lens model with both Q and Ξ operators applied.

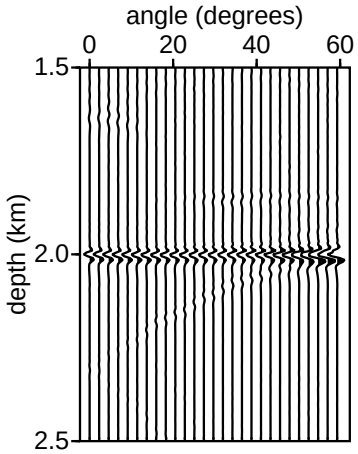

Figure I.8. Common image gather at $x = 0$in the simple lens model with both Q and Ξ operators applied.

I.2.2 Valhall toy lens model

This gas-lens model, shown in Figure I.9 consists of a vertical velocity gradient ($0.45\ \mathrm{s}^{-1}$) beginning at 1600 m/s, with a low-velocity circular lens with Gaussian parameter variations (maximum velocity contrast 800 m/s) located at lateral position 4600 m, and depth 600 m, with a diameter (Gaussian standard deviation) of 600 m. This model, introduced by Brandsberg-Dahl *et al.* (2003a), is based on a feature in the BP Valhall field; it is the same model used in Chapter 3. A typical shot record is shown in Figure I.10.

An image in this model is shown in Figure I.11 with no Q or Ξ operators applied. There are some imaging artifacts in this image, caused by edge reflections in the propagation (these show up as smiles near the edges). The dipping portion of the reflector is also spatially aliased. An image gather is shown in Figure I.12, at a position beneath the lens. As expected this image gather is flat with contributions only from the correct depth location.

Figures I.13 and I.14 show the image and CIG respectively with the Q operators applied both at the surface and the image point. The CIG in particular is sharper than without the Q operators, although once again high frequency noise is introduced. Figures I.15 and I.16 show the results of applying the Ξ operator. Again Ξ seems to have a small influence on the relative amplitudes, although the amplitudes at large angles are somewhat stronger.

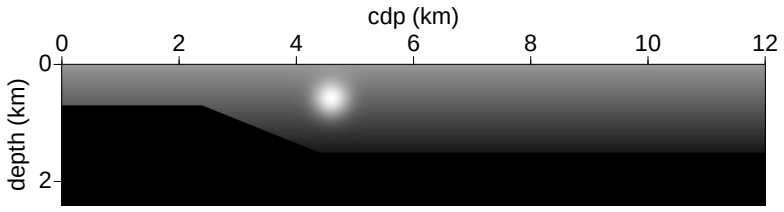

Figure I.9. Velocity model for the Valhall example, lighter colors represent lower velocities.

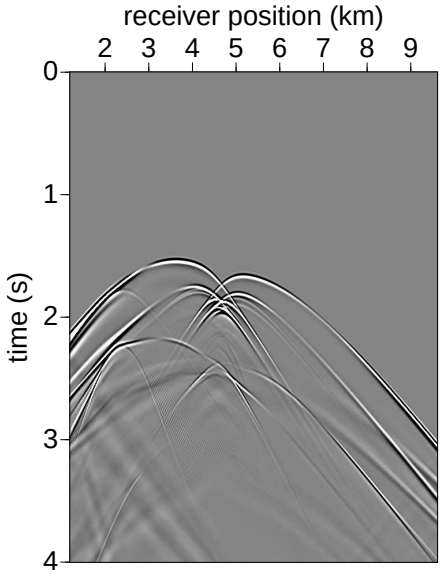

Figure I.10. Shot record in the Valhall model from $x = 4668$ m.

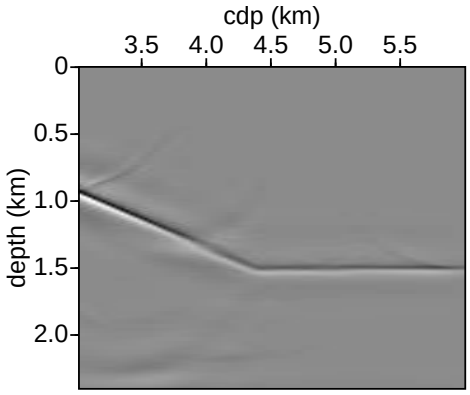

Figure I.11. Image in the Valhall model with no Q or Ξ operators applied.

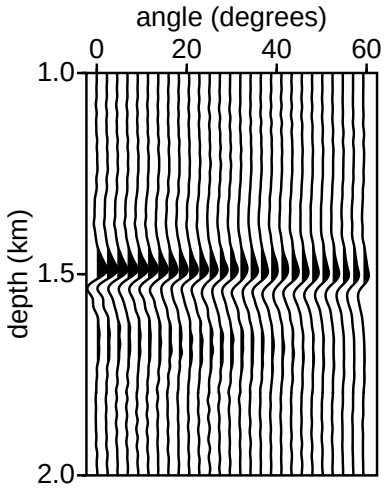

Figure I.12. Common image gather at $x = 4689$ m in the Valhall model with no Q or Ξ operators applied.

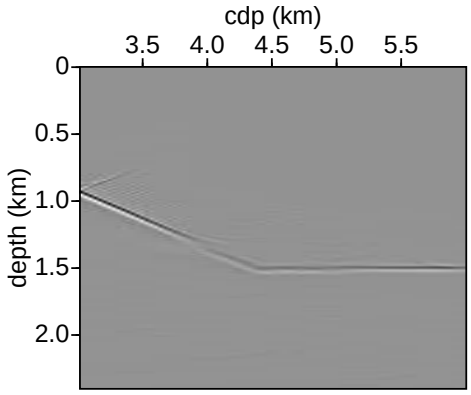

Figure I.13. Image in the Valhall model with Q operators applied.

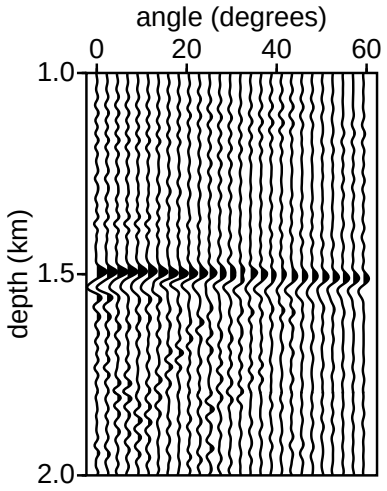

Figure I.14. Common image gather at $x = 4689$ m in the Valhall model with Q operators applied.

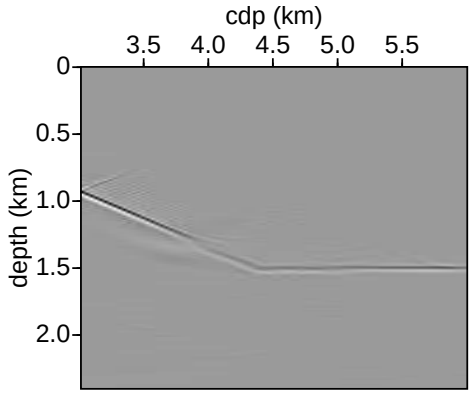

Figure I.15. Image in the Valhall model with both Q and Ξ operators applied.

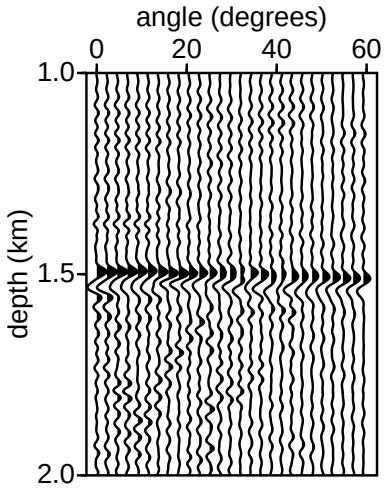

Figure I.16. Common image gather at $x = 4689$ m in the Valhall model with both Q and Ξ operators applied.

Appendix J

Proof of Theorem 4.7.1[1]

The proof rest on the semi-group property (4.23), discussed previously. The idea is to use this property to extend the two Green functions in (4.81 meeting at (z_1, m_s, m_r) to the surface (see Figure J.1). The resulting operators are then rearranged to pair the G_- operators to substitute the double-square-root Green function, H. We go through this procedure twice, once for $\delta u_{1,-}$ and once for the other elements of (4.81).

We start by applying the procedure outlined above to $\delta u_{1,-}$, beginning with the semi-group property applied to (4.77),

$$\begin{aligned}\delta u_{-,1}(z_1, m_r, t_a, 0, s_0) = -\tfrac{1}{4} D_t^2 Q^*_{-,s_0}(0) \int_{z_1}^{\infty} \mathrm{d}z_2 \int \mathrm{d}s_2 \int \mathrm{d}r_2 \int_{\mathbb{R}} \mathrm{d}t_0 \int_{\mathbb{R}} \mathrm{d}t' \int \mathrm{d}m'_r \int_{\mathbb{R}} \mathrm{d}t_{m'_r} \\ G^*_-(z_1, m_r, t_{m'_r}, 0, m'_r) G_-(0, m'_r, t_a + t_{m'_r} - t' - t_0, z_2, r_2) \\ G_-(0, s_0, t', z_2, s_2)\; Q_{-,r_2}(z_2) Q_{-,s_2}(z_2) (E_2 E_1 a)(z_2, s_2, r_2, t_0)\,, \quad \text{(J.1)}\end{aligned}$$

where $t_a + t_{m'_r}$ is the time required to travel from the source at s_0 to the pseudo-receiver at m'_r, as illustrated in Figure J.2. We now begin to rearrange the terms in preparation for the H substitution.

Since t' is independent of the other variables we bring this integration to the inside to replace the two G_- operators by the H operator

$$\begin{aligned}\delta u_{-,1}(z_1, m_r, t_a, 0, s_0) = -\tfrac{1}{4} D_{t_a}^2 Q^*_{-,s_0}(0) \int \mathrm{d}m'_r \int_{\mathbb{R}} \mathrm{d}t_{m'_r} G^*_-(z_1, m_r, t_{m'_r}, 0, m'_r) \\ \int_{z_1}^{\infty} \mathrm{d}z_2 \int \mathrm{d}s_2 \int \mathrm{d}r_2 \int_{\mathbb{R}} \mathrm{d}t_0 H(0, s_0, m'_r, t_a + t_{m'_r} - t_0, z_2, s_2, r_2) Q_{-,r_2}(z_2) Q_{-,s_2}(z_2) \\ (E_2 E_1 a)(z_2, s_2, r_2, t_0)\,. \quad \text{(J.2)}\end{aligned}$$

This completes the manipulations of $\delta u_{1,-}$.

[1]This appendix has been accepted, along with Chapter 4 and Appendix K, to Inverse Problems as: Malcolm, A. E. and de Hoop, M. V. A method for inverse scattering based on the generalized Bremmer coupling series.

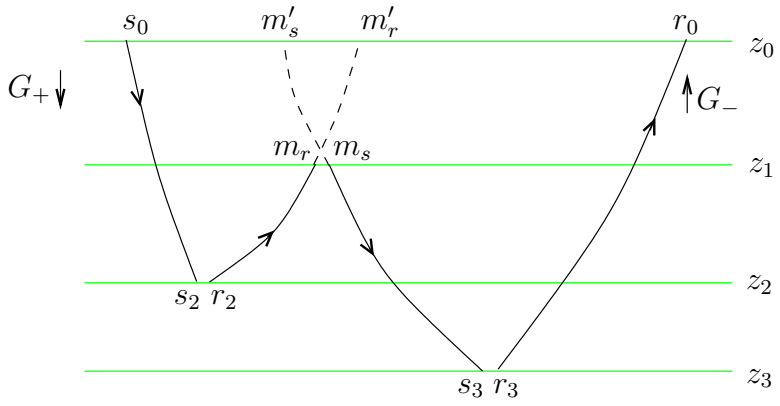

Figure J.1. Triple scattering notations and conventions for the extensions via G_-^* operators to propagate to the surface.

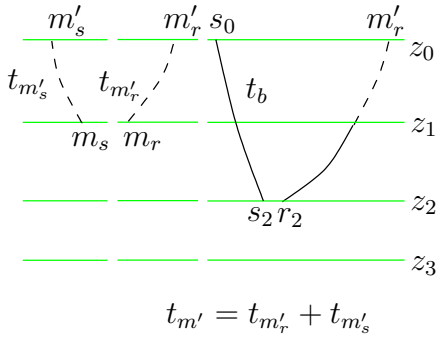

Figure J.2. Time variables used in the continuation of the G_- operators to the surface.

Next, we apply the same procedure to the second Green function in (4.81),

$$d_3(s_0,r_0,t_4) = -\tfrac{1}{4}D_t^4\int_0^\infty \mathrm{d}z_3\int \mathrm{d}s_3\int \mathrm{d}r_3\int_{\mathbb{R}}\mathrm{d}t_{30}\int_{\mathbb{R}}\mathrm{d}t_a\int_0^{z_3}\mathrm{d}z_1\int \mathrm{d}m_s\int \mathrm{d}m_r\int_{\mathbb{R}}\mathrm{d}t_3'$$
$$Q^*_{-,r_0}(0)G_-(0,r_0,t_4-t_a-t_3'-t_{30},z_3,r_3)Q_{-,r_3}(z_3)$$
$$Q^*_{-,m_s}(z_1)\int \mathrm{d}m_s'\int_{\mathbb{R}}\mathrm{d}t_{m_s'}G^*_-(z_1,m_s,t_{m_s'},0,m_s')G_-(0,m_s',t_3'+t_{m_s'},z_3,s_3)$$
$$Q_{-,s_3}(z_3)(E_2E_1a)(z_3,s_3,r_3,t_{30})(E_1a)(z_1,m_s,m_r)Q^*_{-,m_r}(z_1)$$
$$\delta u_{-,1}(z_1,m_r,t_a,0,s_0)\,, \quad \text{(J.3)}$$

where $t_{m_s'}$ is defined by analogy to $t_{m_r'}$ (see Figure J.2). We now begin to rearrange terms in (J.3) in preparation of the H substitution.

Since G^*_- and the propagator proceeding it do not have variables in common, we interchange their order. We also change variables from t_3' to $t_3'' = t_3' + t_{m_s'}$, interchanging the t_3' and $t_{m_s'}$ integrations. This results in

$$d_3(s_0,r_0,t_4) =$$
$$-\tfrac{1}{4}D_t^4\int_0^\infty \mathrm{d}z_3\int \mathrm{d}s_3\int \mathrm{d}r_3\int_{\mathbb{R}}\mathrm{d}t_{30}\int_{\mathbb{R}}\mathrm{d}t_a\int_0^{z_3}\mathrm{d}z_1\int \mathrm{d}m_s\int \mathrm{d}m_r\int_{\mathbb{R}}\mathrm{d}t_a\int \mathrm{d}m_s'\int_{\mathbb{R}}\mathrm{d}t_{m_s'}\int_{\mathbb{R}}\mathrm{d}t_3''$$
$$Q^*_{-,r_0}(0)Q^*_{-,m_s}(z_1)G^*_-(z_1,m_s,t_{m_s'},0,m_s')G_-(0,r_0,t_4-t_a-t_3''+t_{m_s'}-t_{30},z_3,r_3)$$
$$Q_{-,r_3}(z_3)G_-(0,m_s',t_3'',z_3,s_3)Q_{-,s_3}(z_3)$$
$$(E_2E_1a)(z_3,s_3,r_3,t_{30})(E_1a)(z_1,m_s,m_r)Q^*_{-,m_r}(z_1)\delta u_{-,1}(z_1,m_r,t_a,0,s_0)\,. \quad \text{(J.4)}$$

We now substitute H from (4.75) for the time convolution of the two G_- operators above, interchanging the order of integration, to obtain

$$d_3(s_0,r_0,t_4) = -\tfrac{1}{4}D_{t_4}^4Q^*_{-,r_0}(0)\int_0^\infty \mathrm{d}z_3\int_0^{z_3}\mathrm{d}z_1\int \mathrm{d}m_s\int \mathrm{d}m_r\int_{\mathbb{R}}\mathrm{d}t_a\int \mathrm{d}m_s'\int_{\mathbb{R}}\mathrm{d}t_{m_s'}$$
$$Q^*_{-,m_s}(z_1)G^*_-(z_1,m_s,t_{m_s'},0,m_s')\int \mathrm{d}s_3\int \mathrm{d}r_3\int_{\mathbb{R}}\mathrm{d}t_{30}$$
$$H(0,m_s',r_0,t_4-t_a+t_{m_s'}-t_{30},z_3,s_3,r_3)Q_{-,s_3}(z_3)Q_{-,r_3}(z_3)(E_1a)(z_1,m_s,m_r)$$
$$(E_2E_1a)(z_3,s_3,r_3,t_{30})Q^*_{-,m_r}(z_1)\delta u_{-,1}(z_1,m_r,t_a,0,s_0)\,. \quad \text{(J.5)}$$

We have now extended both Green operators to the surface, what remains is the combining of the G^*_- operators in (J.5) and (J.2) into an H^* operator.

To do this, we substitute (J.2) into (J.5). We then interchange operators to combine the two G^*_- terms, as well as changing the order of integration to move the t_a integral inside

the $t_{m'_s}$ one and also introduce E_2. This results in

$$\begin{aligned} d_3(s_0,r_0,t_4) = \tfrac{1}{16} D_{t_4}^6 Q^*_{-,r_0}(0) Q^*_{-,s_0}(0) \\ \int_0^\infty \mathrm{d}z_3 \int_0^{z_3} \mathrm{d}z_1 \int_{z_1}^\infty \mathrm{d}z_2 \int \mathrm{d}m_s \int \mathrm{d}m_r \int_{\mathbb{R}} \mathrm{d}t_{m_0} \int \mathrm{d}m'_s \int \mathrm{d}m'_r \int_{\mathbb{R}} \mathrm{d}t_{m'_s} \int_{\mathbb{R}} \mathrm{d}t_{m'_r} \\ Q^*_{-,m_s}(z_1)(E_2E_1a)(z_1,m_s,m_r,t_{m_0}) Q^*_{-,m_r}(z_1) \\ G^*_-(z_1,m_s,t_{m'_s},0,m'_s) G^*_-(z_1,m_r,t_{m'_r}-t_{m_0},0,m'_r) \\ \int_{\mathbb{R}} \mathrm{d}t_a \int \mathrm{d}s_3 \int \mathrm{d}r_3 \int_{\mathbb{R}} \mathrm{d}t_{30} H(0,m'_s,r_0,t_4-t_a+t_{m'_s}-t_{30},z_3,s_3,r_3) \\ Q_{-,s_3}(z_3) Q_{-,r_3}(z_3)(E_2E_1a)(z_3,s_3,r_3,t_{30}) \int \mathrm{d}s_2 \int \mathrm{d}r_2 \int_{\mathbb{R}} \mathrm{d}t_0 \\ H(0,s_0,m'_r,t_a+t_{m'_r}-t_{s_0}-t_0,z_2,s_2,r_2)\; Q_{-,r_2}(z_2) Q_{-,s_2}(z_2)(E_2E_1a)(z_2,s_2,r_2,t_0)\,. \end{aligned} \tag{J.6}$$

Interchanging the z_1 and z_3 integrals gives

$$\begin{aligned} d_3(s_0,r_0,t_4) = \tfrac{1}{16} D_{t_4}^6 Q^*_{-,r_0}(0) Q^*_{-,s_0}(0) \\ \int_0^\infty \mathrm{d}z_1 \int \mathrm{d}m_s \int \mathrm{d}m_r \int_{\mathbb{R}} \mathrm{d}t_{m_0} \int \mathrm{d}m'_s \int \mathrm{d}m'_r \int_{\mathbb{R}} \mathrm{d}t_{m'_s} \int_{\mathbb{R}} \mathrm{d}t_{m'_r} Q^*_{-,m_s}(z_1) \\ (E_2E_1a)(z_1,m_s,m_r,t_{m_0}) Q^*_{-,m_r}(z_1) G^*_-(z_1,m_s,t_{m'_s},0,m'_s) \\ G^*_-(z_1,m_r,t_{m'_r}-t_{m_0},0,m'_r) \int_{\mathbb{R}} \mathrm{d}t_a \int_{z_1}^\infty \mathrm{d}z_3 \int \mathrm{d}s_3 \int \mathrm{d}r_3 \int_{\mathbb{R}} \mathrm{d}t_{30} \\ H(0,m'_s,r_0,t_4-t_a+t_{m'_s}-t_{30},z_3,s_3,r_3) Q_{-,s_3}(z_3) Q_{-,r_3}(z_3) \\ (E_2E_1a)(z_3,s_3,r_3,t_{30}) \int_{z_1}^\infty \mathrm{d}z_2 \int \mathrm{d}s_2 \int \mathrm{d}r_2 \int_{\mathbb{R}} \mathrm{d}t_0 \\ H(0,s_0,m'_r,t_a+t_{m'_r}-t_0,z_2,s_2,r_2)\; Q_{-,r_2}(z_2) Q_{-,s_2}(z_2)(E_2E_1a)(z_2,s_2,r_2,t_0)\,. \end{aligned} \tag{J.7}$$

If we assume a point source, we identify the fictitious data $\mathbf{d}_1$ in this expression. (If the source is not a point source, then here is where knowledge of the wavelet becomes necessary to perform this substitution.)

Using the fictitious data set, $\mathbf{d}_1$ defined in (4.82) we simplify (J.7) to

$$\begin{aligned} d_3(s_0,r_0,t_4) = D_t^2 \int_0^\infty \mathrm{d}z_1 \int \mathrm{d}m_s \int \mathrm{d}m_r \int_{\mathbb{R}} \mathrm{d}t_{m_0} \int \mathrm{d}m'_s \int \mathrm{d}m'_r \int_{\mathbb{R}} \mathrm{d}t_{m'_s} \int_{\mathbb{R}} \mathrm{d}t_{m'_r} \\ Q^*_{-,m_s}(z_1)(E_2E_1a)(z_1,m_s,m_r,t_{m_0}) Q^*_{-,m_r}(z_1) G^*_-(z_1,m_s,t_{m'_s},0,m'_s) \\ G^*_-(z_1,m_r,t_{m'_r}-t_{m_0},0,m'_r) Q^*_{-,m'_r}(0)^{-1} Q^*_{-,m'_s}(0)^{-1} \\ \left\{ \int_{\mathbb{R}} \mathrm{d}t_a \mathbf{d}_1(z_1;m'_s,r_0,t_4-t_a+t_{m'_s}) \mathbf{d}_1(z_1;s_0,m'_r,t_a+t_{m'_r}) \right\}. \end{aligned} \tag{J.8}$$

In (J.8), the expression in braces is time a convolution of two fictitious data sets. By shifting time variables between the two $\mathbf{d}_1$ fictitious data sets (the time convolution structure is time

translation invariant) and changing time variables from t_a to $t_b = t_a + t_{m'_r}$ we arrive at a structure into which the distribution W defined in the theorem statement can be inserted. This W distribution is a new field constituent generated through the convolution of the two data sets on which the two Green functions in (J.8) act. The $\mathbf{d}_1$ data constituents cannot be extracted directly from the data unless ten Kroode's traveltime monotonicity assumption is satisfied. If this assumption is not satisfied one could generate $\mathbf{d}_1$ as $d_1 - \mathbf{D}\langle a\rangle$, where

$$(\mathbf{D}\langle a\rangle)(z_1, s_0, r_0, t) = -\tfrac{1}{4} D_t^2 Q^*_{-,r}(0) Q^*_{-,s}(0) \int_0^{z_1} \mathrm{d}z \int \mathrm{d}s \int \mathrm{d}r \int_{\mathbb{R}} \mathrm{d}t_0 \\ H(0, s_0, r_0, t - t_0, z, s, r) Q_{-,r}(z) Q_{-,s}(z) (E_2 E_1 \langle a\rangle)(z, s, r, t_0)\,, \quad \text{(J.9)}$$

is the data modeled from an estimate, $\langle a\rangle$, of the medium contrast down to the depth z_1.

Two changes are required to insert the W distribution into (J.8). First, the lower bound on the t_b integral is extended to 0, rather than $t_{m'_r}$ because $t_b > t_{m'_r}$ by definition. Second, to overlay the distribution W with the expression in braces in (J.8) we need only make the identification $t = t_4 + t_{m'_r} + t_{m'_s}$.

In the definition of W, we identify a new time variable $t_{m'} = t_{m'_r} + t_{m'_s}$ in the expression for t. To introduce this variable we change variables from $t_{m'_r}$ to $t_{m'}$, substituting the expression for W from (4.83) into (J.8)

$$d_3(s_0, r_0, t_4) = D_t^2 \int_0^{\infty} \mathrm{d}z_1 \int \mathrm{d}m_s \int \mathrm{d}m_r \int_{\mathbb{R}} \mathrm{d}t_{m_0} \\ Q^*_{-,m_s}(z_1)(E_2 E_1 a)(z_1, m_s, m_r, t_{m_0}) Q^*_{-,m_r}(z_1) \int \mathrm{d}m'_s \int \mathrm{d}m'_r \int_{\mathbb{R}} \mathrm{d}t_{m'} \int_0^{t'_m} \mathrm{d}t_{m'_s} \\ G^*_-(z_1, m_s, t_{m'_s}, 0, m'_s) G^*_-(z_1, m_r, t_{m'} - t_{m'_s} - t_{m_0}, 0, m'_r) \\ Q^*_{-,m'_r}(0)^{-1} Q^*_{-,m'_s}(0)^{-1} W(z_1; s_0, m'_r, t_4 + t_{m'}, m'_s, r_0)\,. \quad \text{(J.10)}$$

The two G^*_- operators in (J.10) along with the integration in $t_{m'_s}$ are nearly in the form of the H operator.

The integration in $t_{m'_s}$ is extended to ∞ as $t_{m'_s} > t_{m'}$ results in a negative time in the second G^*_- making it 0 by the anti-causality of G^*_- (Remark 4.4.1). This allows us to introduce the H operator, which gives the result.

Appendix K

Comparison with the Weglein/ten Kroode approach[1]

If no caustics form in the background medium, and the traveltime monotonicity of ten Kroode is satisfied, our results can be brought into correspondance with those of Weglein *et al.* (1997), and ten Kroode (2002). To facilitate this comparison, we will write (4.84) in terms of the data only.

We begin by recalling from the discussion following Theorem 4.7.1, that the integration in (m_r, m_s, t_m) is an inner product in these variables. We then identify $Q^*_{-,m_s}(z_1)$ $Q^*_{-,m_r}(z_1)(H(z_1,0))^*$ as an operator acting on $Q^*_{-,m'_r}(0)^{-1}Q^*_{-,m'_s}(0)^{-1}$ $W(z_1; s_0, m'_r, t_4 + t'_m, m'_s, r_0)$; this makes up the second entry in the inner product. The first entry in this inner product is $(E_2E_1a)(z_1, m_s, m_r, t_{m_0})$. An equivalent form of (4.84) is then

$$d_3(s_0,r_0,t_4) = D_t^2\int_0^\infty \mathrm{d}z_1\left(\int \mathrm{d}m'_s\int \mathrm{d}m'_r\int_{\mathbb{R}}\mathrm{d}t_{m'}\left\{\int \mathrm{d}m_s\int \mathrm{d}m_r\int_{\mathbb{R}}\mathrm{d}t_{m_0}\right.\right.$$
$$H(0,m'_s,m'_r,t_{m'}-t_{m_0},z_1,m_s,m_r)Q_{-,m_r}(z_1)Q_{-,m_s}(z_1)$$
$$\left.\left.(E_2E_1a)(z_1,m_s,m_r,t_{m_0})\right\}Q^*_{-,m'_r}(0)^{-1}Q^*_{-,m'_s}(0)^{-1}W(z_1;s_0,m'_r,t_4+t'_m,m'_s,r_0)\right)\,, \quad \text{(K.1)}$$

where $H(0,m'_s,m'_r,t_{m'}-t_{m_0},z_1,m_s,m_r)Q_{-,m_r}(z_1)Q_{-,m_s}(z_1)$ now acts on (E_2E_1a) and the inner product is in the (m'_s,m'_r,t'_m) variables. We define (for the expression in braces in (K.1)

$$\bar{d}_1(z_1,s,r,t) = -D_t^2Q^*_{-,s}(0)Q^*_{-,r}(0)\int \mathrm{d}s_1\int \mathrm{d}r_1\int_{\mathbb{R}}\mathrm{d}t_0$$
$$H(0,s,r,t-t_0,z_1,s_1,r_1)Q_{-,s_1}(z_1)Q_{-,r_1}(z_1)(E_2E_1a)(z_1,s_1,r_1,t_0)\,; \quad \text{(K.2)}$$

The quantity $\bar{d}_1$ is not one that can be measured directly from the data. To compute $\bar{d}_1$, the expression in (4.92) must be substituted for a to write it in terms of what can be measured, d.

[1]This appendix has been accepted, along with Chapter 4 and Appendix J, to Inverse Problems as: Malcolm, A. E. and de Hoop, M. V. A method for inverse scattering based on the generalized Bremmer coupling series.

Using the above definition and the expression for $\mathbf{d}_1$ in (4.82), we re-write (K.1) as

$$d_3(s_0,r_0,t_4) = \int_0^\infty \mathrm{d}z_1 \int \mathrm{d}m_s' \int \mathrm{d}m_r' \int_{\mathbb{R}} \mathrm{d}t_{m'} Q^*_{-,m_s'}(0)^{-1} Q^*_{-,m_r'}(0)^{-1} \bar{d}_1(z_1,m_s',m_r',t_{m'})$$
$$Q^*_{-,m_s'}(0)^{-1} Q^*_{-,m_r'}(0)^{-1} \int_{\mathbb{R}} \mathrm{d}t_b \; \mathbf{d}_1(z_1;m_s',r_0,t_4+t_{m'}-t_b)\mathbf{d}_1(z_1;s_0,m_r',t_b)\,, \quad \text{(K.3)}$$

Although this expression is in terms of three quantities that are directly related to data, we find that we cannot write (K.3) in terms of the actual data because of the z_1 dependence of each of $\bar{d}_1$ and $\mathbf{d}_1$. It is this z_1 dependence that separates our approach from that of Weglein and ten Kroode. In the following two remarks we summarize how the comparison to their work is made in the absence of caustics, when the traveltime monotonicity assumption introduced by ten Kroode is satisfied. This travel-time monotonicity assumption states that the traveltime for a ray leaving a position (z,x) in direction α arrives later than a ray leaving position (z',x') in direction α whenever $z > z'$. In his work, ten Kroode assumes this to hold for all x and α; of course this assumption can be violated.

If the traveltime monotonicity assumption is satisfied, we can replace the z_1 dependence of $\mathbf{d}$ in (K.3) with a time windowing procedure. In this case the z_1 integral in (K.3) can be combined with $\bar{d}_1$ resulting in

$$d_3(s_0,r_0,t_4) \approx \int \mathrm{d}m_s' \int \mathrm{d}m_r' \int_{\mathbb{R}} \mathrm{d}t_{m'} Q^*_{-,m_s'}(0)^{-1} Q^*_{-,m_r'}(0)^{-1} d(m_s',m_r',t_{m'})$$
$$Q^*_{-,m_s'}(0)^{-1} Q^*_{-,m_r'}(0)^{-1} \int_{t_m'}^\infty \mathrm{d}t_b \; d(m_s',r_0,t_4+t_{m'}-t_b)d(s_0,m_r',t_b)\,, \quad \text{(K.4)}$$

with the approximation $d \approx d_1$, substituting the definition of W.

Remark K.0.1. To show the correspondance of our method with that discussed in Weglein *et al.* (1997); ten Kroode (2002), we specifically compare (K.4) in this paper with (120) of ten Kroode (2002). To do this it is first necessary to establish a correspondence between our notation and ten Kroode's notation. To do this we compare Figure J.1 of this paper with Figure 4 of ten Kroode (2002). We then identify the t_1 variable of ten Kroode with the t_b variable here, the t_2 variable of ten Kroode with $t_{m'}$ and the t_3 variable with $t_4 + t_{m'} - t_b$. Then we note that $t_1 - t_2 + t_3$, which would be the time argument of d_3^{IM} in (117) of ten Kroode, is equal to t_4 here. This establishes the correspondence between the time dependence of the final result, (120) in ten Kroode, with (K.4) here.

To make the correspondence between the pseudo-data $\mathbf{d}$ here and the integration bounds on (117) of ten Kroode we observe that Z_2' of ten Kroode is a time parameterization of the scattering depth denoted here by z_1. Thus, as is done in ten Kroode, under the travel-time monotonicity assumption, we can replace the restrictions on the depth of the scattering points in the definition of $\mathbf{d}$ with the restriction $t_b > t_{m'}$ on the t_b integration. Using this we can replace $\mathbf{d}$ with d in (K.4), which brings it into correspondence with (120) of ten Kroode.

Ten Kroode performs stationary phase analysis in three sets of variables, corresponding

to the position of each of the scattering points. From this he finds that the ray from (in the notation used here) r_2 to m'_r (s_3 to m'_s) must follow the same path as that from r_2 to m_r (s_3 to m_s). In the formulation described here this condition is automatically applied through the relation (4.23) used to extend the modeled data from the scattering point at z_1 to the surface.